

# THE BELL SYSTEM TECHNICAL JOURNAL

DEVOTED TO THE SCIENTIFIC AND ENGINEERING  
ASPECTS OF ELECTRICAL COMMUNICATION

Volume 50

November 1971

Number 9

Copyright © 1971, American Telephone and Telegraph Company. Printed in U.S.A.

## Power Spectra of Multilevel Digital Phase-Modulated Signals

By B. GLANCE

(Manuscript received May 14, 1971)

*A formula is derived for computing the power spectrum of multilevel digital phase-modulated signals. The results apply to arbitrary pulse shapes and probability distributions providing that the pulses do not overlap and are independent. This formula can be applied easily to compute power spectra of signals phase-modulated by various pulse shapes. Several examples are given for rectangular and raised-cosine pulses.*

### I. INTRODUCTION

Power spectra of digital angle-modulated signals can be calculated in many ways. The direct way of defining the power spectrum is to find the Fourier transform of a sample of the signal on a finite time interval  $T_0$ . The magnitude square of this Fourier transform is then divided by  $T_0$  and averaged over all possible values of the signal. The power spectrum is finally obtained by taking the limit of the previous result as  $T_0$  tends to infinity. Power spectra of binary frequency shift-keyed signals have been calculated by this method by W. R. Bennett and S. O. Rice.<sup>1</sup> R. R. Anderson and J. Saltz<sup>2</sup> have extended the analysis to multilevel digital frequency-modulated signals by using the same technique.

Power spectra of digital phase-modulated signals can also be obtained

from the Fourier transform of the signal autocorrelation function. This second method has been used by L. Lundquist<sup>3</sup> to calculate the power spectra of signals phase-modulated by pulse stream  $\sum_k a_k g(t - kT)$ . The results obtained in his analysis apply to the case of overlapping pulses providing that the random discrete variables  $a_k$  are independent and have identical probability distributions.

In this paper, a general expression is derived for the power spectrum of multilevel digital phase-modulated signals by using the Fourier transform technique. The only restriction in these calculations is that the signal is modulated by independent non-overlapping pulses. Otherwise each level can be characterized by a different arbitrary pulse shape and have a different probability distribution. In order to simplify the spectral analysis, we show that a multilevel digital phase-modulated signal given by

$$v(t) = \cos [\omega_c t + \sum_k \sum_r a_k^r g_r(t - kT)] \quad (1)$$

can also be written in the case of non-overlapping pulses as

$$v(t) = \sum_k \sum_r a_k^r \gamma(t - kT) \cos [\omega_c t + P_r(t)]. \quad (2)$$

The  $g_r(t)$  in (1) define the pulse shapes of the different levels. The discrete variables  $a_k^r$  can take the values 0 or 1 and are mutually exclusive in the same time-slot  $T$ . In the equivalent expression (2),  $\gamma(t)$  is a unity rectangular pulse time-limited to one signaling interval  $T$ . The  $P_r(t)$  are periodic functions of period  $T$  and are respectively equal to the pulse shape functions  $g_r(t)$  in the interval  $T$ .

The spectral formula which is obtained has the same form as the expression found by H. C. Van Den Elzen<sup>4</sup> for data signals which can be written as a random process:

$$v(t) = \sum_k \sum_r g_{k,r}(t - kT). \quad (3)$$

Digital phase-modulated signals written as (2) can be seen as part of the class of signals given by (3). The same spectral distribution may therefore be expected, once the  $g_{k,r}(t)$  are made explicit.

The spectral analysis made in this paper follows the method developed by Bennett and Rice.<sup>1</sup> A simple compact formula is obtained which depends on the pulse shape functions  $g_r(t)$  and their probability distributions. The power spectra are found to be generally the sum of a continuous spectrum and of a spectrum made of discrete lines. These discrete lines occur at the carrier frequency  $\omega_c$  and at frequencies

shifted from  $\omega_c$  by multiples of the timing frequency. Several examples of application are given for

- (i) rectangular pulses of duration  $t \leq T$
- (ii) rectangular pulses with finite rise time and decay time
- (iii) raised-cosine pulses.

The asymptotic limit of the spectrum as  $f \rightarrow \infty$  is also given for these pulse shapes.

## II. LINEAR FORMULATION OF DIGITAL PHASE-MODULATED SIGNALS

Digital phase-modulation presents some similarity with amplitude modulation. For example, binary phase shift-keying by  $x(t)(\pi/2)$  radians is identical to amplitude modulation by  $x(t)$  if  $x(t)$  is a rectangular wave which takes the values 1 or  $-1$ , thus

$$\begin{aligned} v(t) &= \cos\left(\omega_c t + x(t) \frac{\pi}{2}\right) \\ &= x(t) \sin \omega_c t. \end{aligned} \quad (4)$$

The same signal can also be written with  $\Gamma(t) = [1 + x(t)/2]$  as

$$v(t) = \Gamma(t) \cos\left(\omega_c t + \frac{\pi}{2}\right) + [1 - \Gamma(t)] \cos\left(\omega_c t - \frac{\pi}{2}\right). \quad (5)$$

In a previous paper,<sup>5</sup> it has been shown that this expression can be generalized for any pulse shape which is time-limited to one timing period  $T$ . Equation (5) yields in the case of a binary encoding by two pulse shapes  $g_1(t)$  and  $g_2(t)$ :

$$v(t) = \Gamma(t) \cos[\omega_c t + P_1(t)] + [1 - \Gamma(t)] \cos[\omega_c t + P_2(t)]. \quad (6)$$

$P_1(t)$  and  $P_2(t)$  are two periodic functions equal respectively to  $g_1(t)$  and  $g_2(t)$  in a timing period  $T$ .

In order to extend this formulation to multilevel digital phase-modulated signals, let us consider the multilevel baseband-encoded signal

$$\phi(t) = \sum_{k=-\infty}^{+\infty} \sum_{r=1}^n a_k^r g_r(t - kT). \quad (7)$$

The pulse shape functions  $g_r(t)$  associated to the different levels can be arbitrary providing that

$$g_r(t) = 0 \text{ for } 0 > t > T \quad r = 1, 2, \dots, n. \quad (8)$$

The  $a_k^r$  are discrete variables which take the values 1 or 0 at each time slot  $T$ . The  $a_k^r$  relative to any time slot  $T$  are mutually exclusive since only one pulse can exist for each time interval  $T$ . These conditions lead to

$$\sum_{r=1}^n a_k^r = 1 \quad \text{for } kT \leq t \leq (k+1)T$$

$$k = -\infty, \dots, 0, \dots, +\infty. \quad (9)$$

For a signal made of independent pulses, the  $a_k^r$  relative to different time slots form a discrete stationary random process.

The baseband signal (7) can be seen as  $n$  mutually exclusive signals, each one related to a particular level as shown in Fig. 1. For example

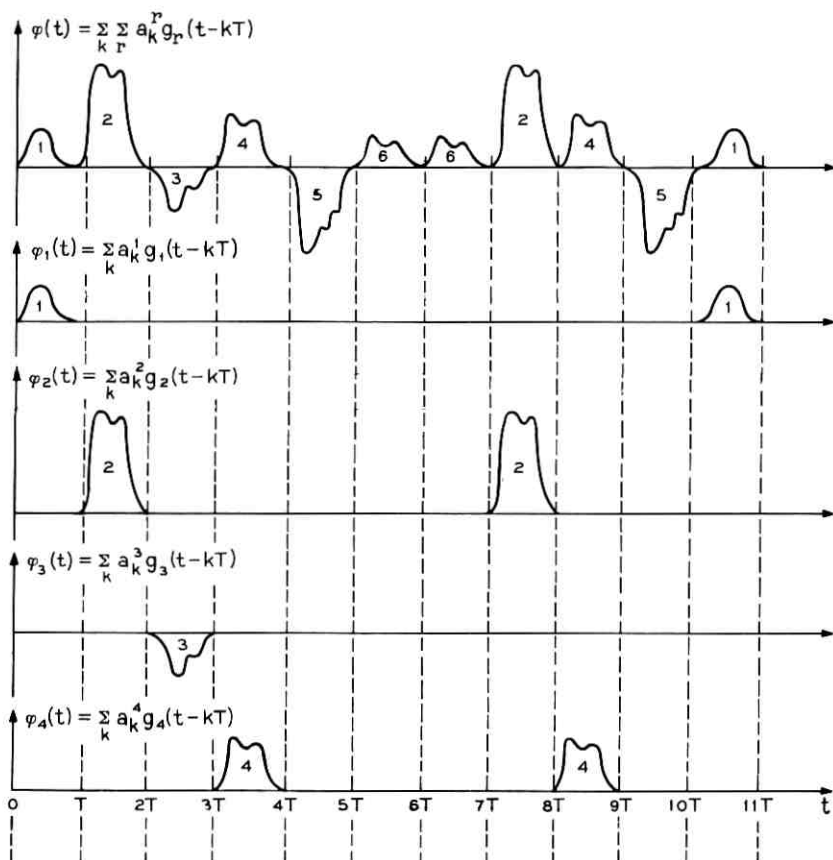


Fig. 1—Multilevel baseband-encoded signal.

the level  $r$  is given by

$$\phi_r(t) = \sum_k a_k^r g_r(t - kT). \quad (10)$$

Each  $\phi_r(t)$  can itself be seen in Fig. 2 as the product of a unity rectangular wave by a periodic function, thus

$$\phi_r(t) = P_r(t) \sum_k a_k^r \gamma(t - kT). \quad (11)$$

$P_r(t)$  is a periodic function of period  $T$  equal to  $g_r(t)$  in the interval  $T$ .  $\gamma(t)$  is a unity rectangular pulse time-limited to one interval  $T$ . Let us set

$$\Gamma_r(t) = \sum_k a_k^r \gamma(t - kT), \quad (12)$$

the baseband signal becomes

$$\phi(t) = \sum_r \Gamma_r(t) \cdot P_r(t). \quad (13)$$

A signal phase-modulated by an  $n$ -level digital signal such as (7) can be written from (13) as follows:

$$v(t) = \cos [\omega_c t + \sum_r \Gamma_r(t) \cdot P_r(t)]. \quad (14)$$

The  $n$  unity rectangular signals  $\Gamma_r(t)$  as given by (9) are mutually exclusive for all values of  $t$ :

$$\sum_r \Gamma_r(t) = 1. \quad (15)$$

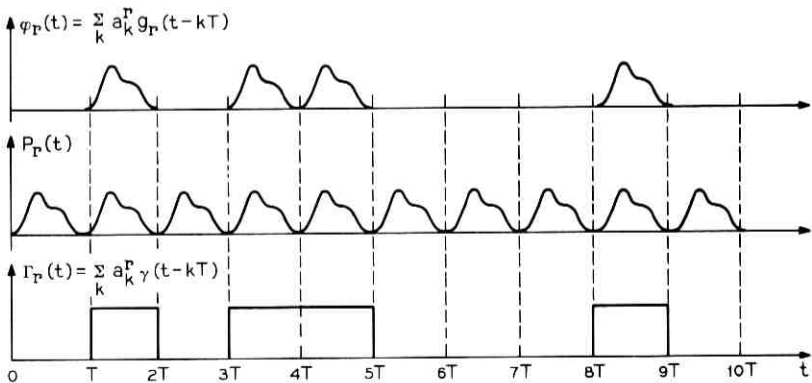


Fig. 2—Baseband signal corresponding to the level  $r$ .

As a result, (14) is also equal to

$$v(t) = \sum_r \Gamma_r(t) \cos [\omega_c t + P_r(t)]. \quad (16)$$

The modulated signal written in this form presents some similarity with amplitude modulation. Note that the argument is independent of the random variables  $a_k^r$ . This equivalent formulation simplifies greatly the spectral analysis of multilevel phase-modulated signals.

### III. POWER SPECTRA OF MULTILEVEL PHASE-MODULATED SIGNALS

#### 3.1 General Considerations

The spectrum calculations are made under the following conditions:

- (i) The baseband-encoded signal is made of independent pulses.
- (ii) The levels are defined by an ensemble of functions  $g_r(t)$  which are time-limited to an interval shorter than or equal to the timing period  $T$ .

Otherwise the  $g_r(t)$  are arbitrary and can have different probability distributions. Let  $p_r$  be the probability of occurrence of the level  $r$ . From (10) and (12)

$$p_r = \langle a_k^r \rangle, \quad (17)$$

and from (15)

$$\sum_r p_r = 1. \quad (18)$$

The power spectra, calculated by the Fourier transform method, are given by

$$G(f) = \lim_{NT \rightarrow \infty} \frac{1}{NT} \langle |X(f, NT)|^2 \rangle. \quad (19)$$

$X(f, NT)$  is the Fourier transform of a sample of the signal in the interval  $NT$ .  $\langle |X(f, NT)|^2 \rangle$  is the expectation taken over all possible values of the signal in the interval  $NT$ .

The Fourier transform  $X(f, NT)$  is calculated by using the linear formulation (16), thus

$$X(f, NT) = \sum_r \int_0^{NT} \Gamma_r(t) \cos [\omega_c t + P_r(t)] e^{-i\omega t} dt. \quad (20)$$

$X(f, NT)$  can be separated in two parts which correspond respectively to the positive and negative frequencies:

$$X(f_+, NT) = \frac{1}{2} \sum_r \int_0^{NT} \Gamma_r(t) e^{j[(\omega_c - \omega)t + P_r(t)]} dt \quad (21)$$

and

$$X(f_-, NT) = \frac{1}{2} \sum_r \int_0^{NT} \Gamma_r(t) e^{-j[(\omega_c + \omega)t + P_r(t)]} dt. \quad (22)$$

Note that  $X(f_-, NT) = X * (-f_+, NT)$  [ $*$  indicates that  $j$  is made  $-j$  in (22)].

The Fourier transform (22) relative to the positive frequencies can be written from (12) as

$$X(f_+, NT) = \frac{1}{2} \sum_{k=0}^{N-1} \sum_{r=1}^n a_k^r \int_{kT}^{(k+1)T} e^{j[(\omega_c - \omega)t + P_r(t)]} dt. \quad (23)$$

Let us set the new variable of integration  $y = t - kT$ . From the periodicity of the functions  $P_r(t)$

$$P_r(y + kT) = P_r(y), \quad (24)$$

which gives

$$X(f_+, NT) = \frac{1}{2} \sum_{k=0}^{N-1} \sum_{r=1}^n a_k^r e^{jkT(\omega_c - \omega)} \int_0^T e^{j[(\omega_c - \omega)y + P_r(y)]} dy. \quad (25)$$

In the limit of integration  $P_r(y) = g_r(y)$ ;  $g_r(y)$  can then be substituted to  $P_r(y)$ , thus

$$X(f_+, NT) = \frac{1}{2} \sum_{k=0}^{N-1} \sum_{r=1}^n a_k^r e^{jkT(\omega_c - \omega)} \int_0^T e^{j[(\omega_c - \omega)y + g_r(y)]} dy. \quad (26)$$

Let us set

$$F_r(f_+) = \frac{1}{2} \int_0^T e^{j[(\omega_c - \omega)y + g_r(y)]} dy \quad (27)$$

and

$$F_r(f_-) = \frac{1}{2} \int_0^T e^{-j[(\omega_c + \omega)y + g_r(y)]} dy. \quad (28)$$

The Fourier transform (20) takes the form

$$X(f, NT) = \sum_{k=0}^{N-1} \sum_{r=1}^n a_k^r \{ e^{jkT(\omega_c - \omega)} F_r(f_+) + e^{-jkT(\omega_c + \omega)} F_r(f_-) \}. \quad (29)$$

### 3.2 Power Spectrum Calculations

The power spectrum calculated from (19) is the sum of four terms given by

$$G(f) = \lim_{NT \rightarrow \infty} \frac{1}{NT} \left\langle \sum_{k=0}^{N-1} \sum_{\substack{r=1 \\ s=1}}^n a_k^r a_l^s \begin{pmatrix} F_r(f_+) \cdot F_s^*(f_+) e^{jT(k-l)(\omega_c - \omega)} \\ + F_r(f_-) \cdot F_s^*(f_-) e^{-jT(k-l)(\omega_c + \omega)} \\ + F_r(f_+) \cdot F_s^*(f_-) e^{j[kT(\omega_c - \omega) + lT(\omega_c + \omega)]} \\ + F_r(f_-) \cdot F_s^*(f_+) e^{-j[kT(\omega_c + \omega) + lT(\omega_c - \omega)]} \end{pmatrix} \right\rangle. \quad (30)$$

The third and fourth terms give the foldover between the positive and negative frequency parts of the spectrum. This effect is negligible when the bandwidth spectrum is much smaller than the carrier frequency which is the case in most applications. The spectral distributions are then accurately described by the first and the second terms of (30) which give respectively the power spectra relative to the positive and negative frequencies. The power spectrum relative to the positive frequencies yields in that case

$$G(f_+) = \lim_{NT \rightarrow \infty} \frac{1}{NT} \left\langle \sum_{k=0}^{N-1} \sum_{r=1}^n a_k^r a_l^s e^{jT(k-l)(\omega_c - \omega)} F_r(f_+) F_s^*(f_+) \right\rangle. \quad (31)$$

The ensemble average is taken on the random variables  $a_k^r a_l^s$ . The bracket sign can therefore be introduced on the summation as

$$G(f_+) = \lim_{NT \rightarrow \infty} \frac{1}{NT} \left\langle \sum_{k=0}^{N-1} \sum_{r=1}^n \langle a_k^r a_l^s \rangle e^{jT(k-l)(\omega_c - \omega)} F_r(f_+) \cdot F_s^*(f_+) \right\rangle. \quad (32)$$

From the definition given in Section II:

$$\langle a_k^r a_l^s \rangle = \begin{cases} p_r p_s & \text{if } k \neq l \text{ and } r \neq s \\ p_r^2 & \text{if } k \neq l \text{ and } r = s \\ p_r & \text{if } k = l \text{ and } r = s \\ 0 & \text{if } k = l \text{ and } r \neq s \end{cases} \quad (33)$$

where  $p_r$  and  $p_s$  are the probability distributions of the levels  $r$  and  $s$ .

After substitution of the terms  $\langle a_k^r a_l^s \rangle$  by their values given by (33), a summation is made on the variable  $l$ . The result gives

$$G(f_+) = \lim_{NT \rightarrow \infty} \left[ \sum_{r=1}^n \left\{ \frac{1}{T} \sqrt{p_r p_s} \delta_r^s + \frac{2}{T} p_r p_s \cdot \sum_{k=1}^{N-1} \frac{(N-k)}{N} \cos kT(\omega_c - \omega) \right\} F_r(f_+) F_s^*(f_+) \right], \quad (34)$$

$\delta_r^s$  is the Kronecker symbol given by

$$\delta_r^s = \begin{cases} 1 & \text{if } r = s \\ 0 & \text{if } r \neq s \end{cases}$$

Since the limit operation acts only on the second term of (34),  $G(f_+)$  can be rewritten as

$$G(f_+) = \left[ \sum_{r=1}^n \left\{ \frac{1}{T} \sqrt{p_r p_s} \delta_r^s + 2p_r p_s \operatorname{Lim}_{NT \rightarrow \infty} \frac{1}{NT} \right. \right. \\ \left. \left. \cdot \sum_{k=1}^{N-1} (N-k) \cos kT(\omega_c - \omega) \right\} F_r(f_+) F_s(f_+) \right]. \quad (35)$$

Summation on the discrete variable  $k$  yields for the series on  $k$

$$\operatorname{Lim}_{NT \rightarrow \infty} \frac{2}{NT} \sum_{k=1}^{N-1} (N-k) \cos kT(\omega_c - \omega) \\ = \operatorname{Lim}_{NT \rightarrow \infty} \frac{1}{NT} \left[ -N + \frac{\sin^2(\omega_c - \omega) \frac{NT}{2}}{\sin^2(\omega_c - \omega) \frac{T}{2}} \right] \\ = -\frac{1}{T} + \frac{1}{T^2} \sum_{m=-\infty}^{+\infty} \delta\left(f_c - f + \frac{m}{T}\right) \\ \sum_{m=-\infty}^{+\infty} \delta\left(f_c - f + \frac{m}{T}\right) \quad (36)$$

forms a set of Dirac functions which give a series of spikes:

$$\sum_{m=-\infty}^{+\infty} \delta\left(f_c - f + \frac{m}{T}\right) = \begin{cases} +\infty & \text{if } f = f_c + \frac{m}{T} \\ 0 & \text{if } f \neq f_c + \frac{m}{T} \end{cases}. \quad (37)$$

The substitution of (36) into (35) yields finally for the power spectrum relative to the positive frequencies

$$G(f_+) = \frac{1}{T} \left\{ \sum_{r=1}^n p_r |F_r(f_+)|^2 - \left| \sum_{r=1}^n p_r F_r(f_+) \right|^2 \right\} \\ + \frac{1}{T^2} \sum_{m=-\infty}^{+\infty} \left| \sum_{r=1}^n p_r F_r(f_+) \right|^2 \delta\left(f_c - f + \frac{m}{T}\right). \quad (38)$$

The first term of (38) gives the continuous power spectrum. The second

part gives the spectral discrete lines. These lines occur at the frequencies

$$f = f_c + \frac{m}{T} \quad (m = 0, \pm 1, \pm 2, \dots)$$

$$\text{if } \left| \sum_{r=1}^n p_r F_r(f_+) \right|^2 \neq 0 \quad \text{at } f = f_c + \frac{m}{T}.$$

The final formula (37) depends on two sets of parameters:

- (i) the probability distributions  $p_r$  of each level
- (ii) the pulse shape functions  $g_r(t)$  of each level from the Fourier transforms (27).

When the  $n$  levels have identical probability distributions, (38) becomes

$$G(f_+) = \frac{1}{T} \left\{ \frac{1}{n} \sum_{r=1}^n |F_r(f_+)|^2 - \frac{1}{n^2} \left| \sum_{r=1}^n F_r(f_+) \right|^2 \right\} + \frac{1}{T^2} \sum_{m=-\infty}^{+\infty} \frac{1}{n^2} \left| \sum_{r=1}^n F_r(f_+) \right|^2 \delta\left(f_c - f + \frac{m}{T}\right). \quad (39)$$

The pulse shape, in most cases, is given by a unique function  $g(t)$  for all the levels. Each level is then defined by a different pulse amplitude. In this case,  $g(t)$  can only have one maximum value which is assumed to be equal to one. The levels are then given by the ensemble  $\alpha_r g(t)$ ,  $r = 1, 2, \dots, n$ , where the  $\alpha_r$  are equal to the peak phase deviations. Several examples of power spectra will be calculated for this important case.

#### IV. EXAMPLE OF POWER SPECTRA

##### 4.1 Rectangular Pulse Shape of Duration $T$

The application of (38) to a signal phase-modulated by rectangular pulses of duration equal to the timing period  $T$  is straightforward. The Fourier transforms (27) are given in this case by

$$F_r(f_+) = \frac{1}{2} \int_0^T e^{j[(\omega_c - \omega)y + \alpha_r]} dy$$

$$= \frac{T}{2} e^{j\alpha_r} \cdot e^{j(\omega_c - \omega)(T/2)} \frac{\sin(\omega_c - \omega) \frac{T}{2}}{(\omega_c - \omega) \frac{T}{2}}, \quad (40)$$

where the  $\alpha_r$  are the phase deviations of the different levels. Equation (40) applied to (38) gives

$$G(f_+) = \frac{T}{4} \left[ \frac{\sin(\omega_c - \omega) \frac{T}{2}}{(\omega_c - \omega) \frac{T}{2}} \right]^2 \cdot \left\{ 1 - \left| \sum_{r=1}^n p_r e^{i\alpha_r} \right|^2 \right\} + \frac{1}{4} \left| \sum_{r=1}^n p_r e^{i\alpha_r} \right|^2 \delta(f_c - f). \quad (41)$$

The spectrum has only one line at the carrier frequency.

If one assumes that the levels are equidistant and equiprobable such that

$$\left. \begin{aligned} \alpha_r &= \alpha_0 + \frac{r-1}{n} \alpha \\ p_r &= \frac{1}{n} \end{aligned} \right\} \quad r = 1, 2, \dots, n \quad (42)$$

one obtains

$$\left| \sum_{r=1}^n p_r e^{i\alpha_r} \right|^2 = \frac{1}{n^2} \frac{\sin \frac{\alpha}{2} 2}{\sin \frac{\alpha}{2n}}, \quad (43)$$

and the spectrum is given by

$$G(f_+) = \frac{T}{4} \left[ \frac{\sin(\omega_c - \omega) \frac{T}{2}}{(\omega_c - \omega) \frac{T}{2}} \right]^2 \cdot \left\{ 1 - \frac{1}{n^2} \left[ \frac{\sin \frac{\alpha}{2}}{\sin \frac{\alpha}{2n}} \right]^2 \right\} + \frac{1}{4n^2} \left[ \frac{\sin \frac{\alpha}{2}}{\sin \frac{\alpha}{2n}} \right]^2 \delta(f_c - f). \quad (44)$$

In polar modulation, the  $\alpha_r$  can take positive and negative values. The term  $\sum_{r=1}^n p_r e^{i\alpha_r}$  can then become equal to zero for an infinite number of solutions. All these solutions give the same power spectrum, but without the discrete line:

$$G(f_+) = \frac{T}{4} \left[ \frac{\sin(\omega_c - \omega) \frac{T}{2}}{(\omega_c - \omega) \frac{T}{2}} \right]^2. \quad (45)$$

For example, the polar systems made of  $q$  pairs of equidistant and equiprobable levels such that

$$\sum_{r=1}^{2q} e^{j\alpha_r} = \sum_{r=1}^q \cos \alpha_r = 0$$

are given by

$$\begin{array}{l} 2 \text{ levels polar modulation} \\ 4 \text{ levels polar modulation} \\ 6 \text{ levels polar modulation} \\ \vdots \text{ etc.} \end{array} \left\{ \begin{array}{l} \alpha_{\pm 1} = \pm \frac{\pi}{2} \\ \alpha_{\pm 1} = \pm \frac{\pi}{4} \\ \alpha_{\pm 2} = \pm \frac{3\pi}{4} \\ \alpha_{\pm 1} = \pm \frac{\pi}{4} \\ \alpha_{\pm 2} = \pm \frac{\pi}{2} \\ \alpha_{\pm 3} = \pm \frac{3\pi}{4} \end{array} \right.$$

All these modes have the same spectrum given by (45).

#### 4.2 Rectangular Pulse of Duration $\tau < T$

Let us now consider a rectangular pulse shape of duration  $\tau < T$ . Assume the pulses are located symmetrically in the interval  $T$  as shown in Fig. 3. The Fourier transforms  $F_r(f_+)$  are equal in this case to

$$F_r(f_+) = \frac{1}{2} \left\{ \int_0^{(T-\tau)/2} e^{j(\omega_c - \omega)y} dy + e^{j\alpha_r} \int_{(T-\tau)/2}^{(T+\tau)/2} e^{j(\omega_c - \omega)y} dy + \int_{(T+\tau)/2}^T e^{j(\omega_c - \omega)y} dy \right\}. \quad (46)$$

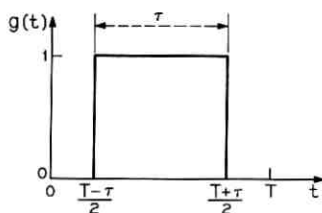


Fig. 3—Rectangular pulse with  $\tau < T$ .

The result of (46) applied to (38) yields for the continuous part of the spectrum

$$G_c(f_+) = \frac{T}{4} \left\{ \sum_{r=1}^n p_r \left| \frac{\sin(\omega_c - \omega) \frac{T}{2}}{(\omega_c - \omega) \frac{T}{2}} - \frac{\tau}{T} \frac{\sin(\omega_c - \omega) \frac{\tau}{2}}{(\omega_c - \omega) \frac{\tau}{2}} (1 - e^{j\alpha_r}) \right|^2 - \left| \frac{\sin(\omega_c - \omega) \frac{T}{2}}{(\omega_c - \omega) \frac{T}{2}} - \frac{\tau}{T} \frac{\sin(\omega_c - \omega) \frac{\tau}{2}}{(\omega_c - \omega) \frac{\tau}{2}} \left( 1 - \sum_{r=1}^n p_r e^{j\alpha_r} \right) \right|^2 \right\}. \quad (47)$$

The discrete lines are given by

$$G_d(f_+) = \frac{1}{4} \sum_{m=-\infty}^{+\infty} \left| \frac{\sin m\pi}{m\pi} - \frac{\tau}{T} \frac{\sin m\pi \frac{\tau}{T}}{m\pi \frac{\tau}{T}} \left( 1 - \sum_{r=1}^n p_r e^{j\alpha_r} \right) \right|^2 \delta\left(f_c - f + \frac{m}{T}\right). \quad (48)$$

There are always discrete lines in this case. As an example let us consider the case of a polar phase modulation with two equiprobable levels given by  $\alpha_r = \pm\pi/2$  radians. Equations (47) and (48) give in this case:

$$G(f_+) = \frac{T}{4} \left(\frac{\tau}{T}\right)^2 \left[ \frac{\sin(\omega_c - \omega) \frac{\tau}{2}}{(\omega_c - \omega) \frac{\tau}{2}} \right]^2 + \frac{1}{4} \sum_{m=-\infty}^{+\infty} \left[ \frac{\sin m\pi}{m\pi} - \frac{\tau}{T} \frac{\sin m\pi \frac{\tau}{T}}{m\pi \frac{\tau}{T}} \right]^2 \delta\left(f_c - f + \frac{m}{T}\right). \quad (49)$$

For  $T - \tau \ll T$  the continuous spectrum is practically the same as the one obtained for pulses of duration  $T$ , except for the discrete lines at  $f = f_c + m/T$  ( $m = \pm 1, \pm 2, \dots$ ). In both cases the spectrum decreases as  $1/f^2$  as  $f \rightarrow \infty$ .

#### 4.3 Rectangular Pulse Shape with Finite Rise Time and Decay Time

We consider in this example a rectangular pulse shape of duration  $T$

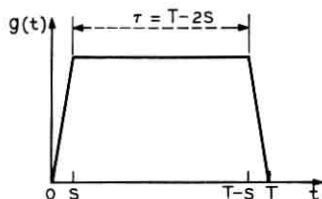


Fig. 4—Rectangular pulse with finite rise time and decay time.

with a finite rise time and decay time as shown in Fig. 4. The calculations are made for the case of two equiprobable levels with peak phase deviations equal to  $\pm\pi/2$  radians. We assume that the rise time and decay time are both equal to  $s = (T - \tau)/2$ ;  $\tau$  is the top pulse length. The Fourier transforms  $F_r(f_+)$  are given in this case by

$$F_1(f_+) = \frac{1}{2} \left\{ \int_0^s e^{j[(\omega_c - \omega) + (\pi/2s)]y} dy + e^{j(\pi/2)} \int_s^{T-s} e^{j(\omega_c - \omega)y} dy + e^{j(\pi/2)(T/s)} \int_{T-s}^T e^{j(\omega_c - \omega) - (\pi/2s)y} dy \right\}. \quad (50)$$

$F_2(f_+)$  can be obtained from (50) by changing the sign of  $\pi/2$ . The calculations yield for the continuous power spectrum:

$$G_c(f_+) = \frac{T}{4} \left( \frac{\pi}{4} \right)^2 \left\{ \frac{\frac{\tau}{T} \frac{\sin(\omega_c - \omega) \frac{\tau}{2}}{(\omega_c - \omega) \frac{\tau}{2}} + \frac{s}{T} \cos(\omega_c - \omega) \frac{T}{2}}{\left[ (\omega_c - \omega) \frac{s}{2} \right]^2 - \left( \frac{\pi}{4} \right)^2} \right\}^2. \quad (51)$$

The discrete lines are given by

$$G_d(f_+) = \frac{1}{4} \left( \frac{\pi}{4} \right)^2 \left( \frac{s}{T} \right)^2 \sum_{m=-\infty}^{+\infty} \frac{\cos^2 \left( 2\pi m \frac{s}{T} \right)}{\left[ \left( \pi m \frac{s}{T} \right)^2 - \left( \frac{\pi}{4} \right)^2 \right]^2} \delta \left( f_c - f + \frac{m}{T} \right). \quad (52)$$

The power spectrum decreases in this case as  $1/f^4$  as  $f \rightarrow \infty$ . Figure 5 shows the spectrum given by (51) and (52) which is calculated for  $s/T = 0.1$ .

#### 4.4 Raised-Cosine Pulse Shape

In the case of raised-cosine pulse shapes, the spectra are computed for polar modulation. We assume that the pulse duration is equal to

the timing period  $T$ . The pulse, of maximum height 1, is then given by  $g(t) = \sin^2 \Omega t/2$  with  $\Omega = 2\pi/T$ . A first example is calculated for a two-level system with different probability distributions. The second example is calculated for a multilevel system with equiprobable level distributions. The two-level and four-level cases are then compared for peak phase distributions which give  $\sum_1^n e^{j\alpha r} = 0$ .

#### 4.4.1 Two-Level Polar Phase Modulation with Raised-Cosine Pulses

Let  $\pm 2\alpha$  radians be the peak phase deviations of the two levels. The Fourier transforms  $F_r(f_+)$  are given in this case by

$$F_1(f_+) = \frac{1}{2} \int_0^T e^{j[(\omega_c - \omega)y + 2\alpha \sin^2 \Omega y/2]} dy. \quad (53)$$

$F_2(f_+)$  can be obtained from (53) by changing the sign of  $\alpha$ .

The term  $2j\alpha \sin^2 \Omega y/2$  of (53) expanded in Bessel series gives

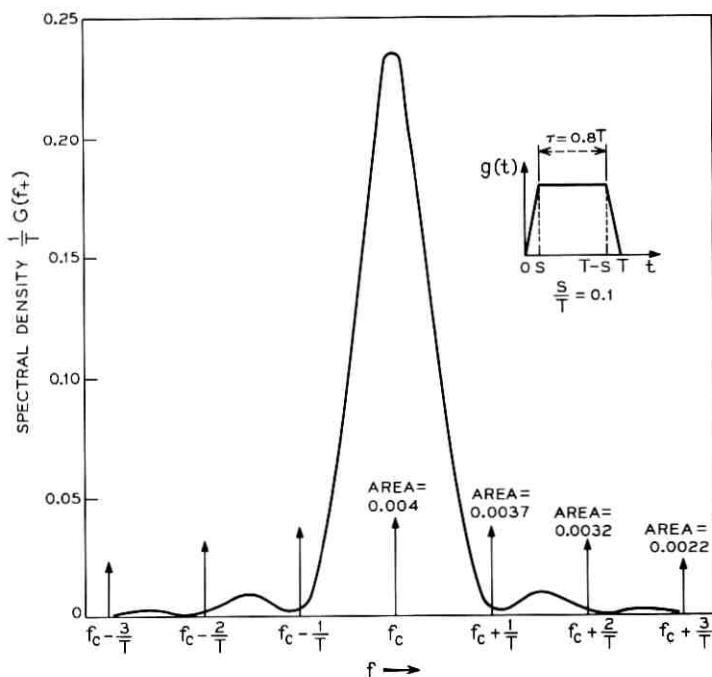


Fig. 5—Power spectrum for two-level polar phase modulation with rectangular pulses with finite rise time and decay time.

$$e^{2i\alpha \sin^2 \Omega y/2} = e^{i\alpha} \left\{ J_0(\alpha) + 2 \sum_{n=1}^{+\infty} (-1)^n J_{2n}(\alpha) \cos 2n\Omega y + 2j \cdot \sum_{n=1}^{+\infty} (-1)^n J_{2n-1}(\alpha) \cos (2n-1)\Omega y \right\}. \quad (54)$$

Substitution of  $e^{2i\alpha \sin^2 \Omega y/2}$  by its Bessel series expansion (54) into (53) yields

$$F(f_+, \pm\alpha) = \frac{T}{2} e^{i[(\omega_c - \omega)(T/2) \pm \alpha]} \left[ \frac{\sin(\omega_c - \omega) \frac{T}{2}}{(\omega_c - \omega) \frac{T}{2}} \right] \cdot \left\{ J_0(\alpha) + 2 \sum_1^{\infty} (-1)^n J_{2n}(\alpha) \frac{(\omega_c - \omega)^2}{(\omega_c - \omega)^2 - (2n\Omega)^2} \pm 2j \sum_1^{\infty} (-1)^n J_{2n-1}(\alpha) \frac{(\omega_c - \omega)^2}{(\omega_c - \omega)^2 - (2n-1)^2\Omega^2} \right\}. \quad (55)$$

Equation (55) applied to (38) yields for the continuous part of the power spectrum:

$$G_c(f_+) = p_1 p_2 T \left[ \frac{\sin(\omega_c - \omega) \frac{T}{2}}{(\omega_c - \omega) \frac{T}{2}} \right]^2 \cdot \left\{ \left[ J_0(\alpha) + 2 \sum_1^{\infty} (-1)^n J_{2n}(\alpha) \frac{(\omega_c - \omega)^2}{(\omega_c - \omega)^2 - (2n\Omega)^2} \right] \sin \alpha + 2 \sum_1^{\infty} (-1)^n J_{2n-1}(\alpha) \frac{(\omega_c - \omega)^2}{(\omega_c - \omega)^2 - [(2n-1)\Omega]^2} \cos \alpha \right\}^2. \quad (56)$$

Noting that

$$J_0(\alpha) + 2 \sum_1^{\infty} (-1)^n J_{2n}(\alpha) = \cos \alpha \quad (57)$$

and

$$2 \sum_1^{\infty} (-1)^n J_{2n-1}(\alpha) = -\sin \alpha,$$

(56) can be rewritten as

$$G_c(f_+) = 4p_1 p_2 T \left[ \frac{\sin(\omega_c - \omega) \frac{T}{2}}{(\omega_c - \omega) \frac{T}{2}} \right]^2 \left\{ \sum_{m=1}^{\infty} (-1)^m J_m(\alpha) \frac{\sin\left(\alpha + \frac{m\pi}{2}\right)}{1 - \left(\frac{\omega_c - \omega}{m\Omega}\right)^2} \right\}^2. \quad (58)$$

The discrete lines are given by

$$G_d(f_+) = \frac{1}{4} \sum_{m=-\infty}^{+\infty} J_m^2(\alpha) \left[ 1 - 4p_1 p_2 \sin^2 \left( \alpha + m \frac{\pi}{2} \right) \right] \delta \left( f_c - f + \frac{m}{T} \right). \quad (59)$$

The asymptotic limit of  $G_c(f_+)$  as  $f \rightarrow \infty$  is obtained by summing (58) for  $|\omega_c - \omega| > m\Omega$ , thus

$$\lim_{f \rightarrow \infty} G_c(f_+) = 4p_1 p_2 T \left\{ \frac{\left[ \pi \alpha \sin(\omega_c - \omega) \frac{T}{2} \right]^2}{\left[ (\omega_c - \omega) \frac{T}{2} \right]^3} \right\}, \quad (60)$$

which shows that  $G_c(f_+) \sim 1/f^6$  as  $f \rightarrow \infty$ .

The power sharing between  $G_c(f_+)$  and  $G_d(f_+)$  is a function of  $\alpha$  and  $p_1 p_2$ . Since  $p_1 + p_2 = 1$ ,  $G_c(f_+) = 0$  if  $p_1$  or  $p_2 = 1$  as expected. All the power is then contained in the discrete lines (case of a signal phase-modulated by a periodic function).

The condition  $p_1 = p_2 = \frac{1}{2}$  (identical probability distributions) gives a maximum for the continuous distributed power:

$$P_c(f_+) = \frac{1}{4} \sum_{m=-\infty}^{+\infty} J_m^2(\alpha) \sin^2 \left( \alpha + m \frac{\pi}{2} \right) \quad (61)$$

and

$$P_d(f_+) = \frac{1}{4} \sum_{m=-\infty}^{+\infty} J_m^2(\alpha) \cos^2 \left( \alpha + m \frac{\pi}{2} \right).$$

The power becomes equally divided between both parts of the spectrum for a peak phase deviation of  $\pm\pi/2$  radians and  $p_1 = p_2 = \frac{1}{2}$ . For this particular case,<sup>5</sup> the series expansion of (55) and (59) can be limited to the first two terms. A good approximation for the power spectrum is then obtained by

$$G_c(f_+) \cong \frac{T}{8} \left[ \frac{\sin(\omega_c - \omega) \frac{T}{2}}{(\omega_c - \omega) \frac{T}{2}} \right]^2 \cdot \left\{ J_0 \left( \frac{\pi}{4} \right) - 2(\omega_c - \omega)^2 \left[ \frac{J_1 \left( \frac{\pi}{4} \right)}{(\omega_c - \omega)^2 - \Omega^2} + \frac{J_2 \left( \frac{\pi}{4} \right)}{(\omega_c - \omega)^2 - (2\Omega)^2} \right] \right\}^2 \quad (62)$$

and

$$G_d(f_+) \cong \frac{1}{8} \sum_{m=-2}^{+2} J_m^2 \left( \frac{\pi}{4} \right) \delta \left( f_c - f + \frac{m}{T} \right). \quad (63)$$

Figure 6 shows the power spectrum given by (62) and (63).

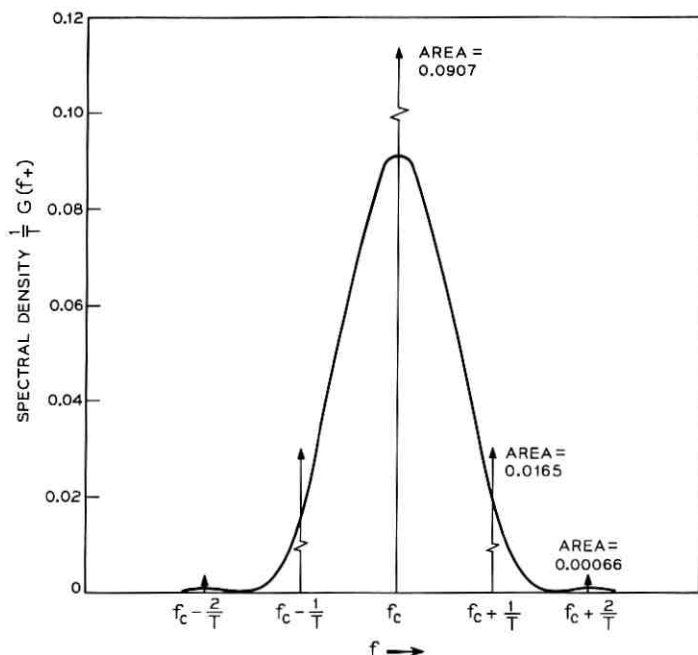


Fig. 6—Power spectrum for two-level polar phase modulation with raised-cosine pulses.

#### 4.4.2 Multilevel Polar Phase Modulation with Raised-Cosine Pulses

The results obtained in the previous section can be generalized in the case of multilevel polar phase modulation with identical probability distributions. Let  $\pm 2\alpha_r$  radians be the peak phase deviation of a multilevel system of  $q$  pairs of levels ( $r = 1, 2, \dots, q$ ). The Fourier transforms from (55) are equal to

$$F_r(f_+, \pm\alpha_r) = \frac{T}{2} e^{j1(\omega_c - \omega)(T/2) \pm \alpha_r} \frac{\sin(\omega_c - \omega) \frac{T}{2}}{(\omega_c - \omega) \frac{T}{2}} \{A_r \pm jB_r\}, \quad (64)$$

with

$$A_r = J_0(\alpha_r) + 2 \sum_1^{\infty} (-1)^n J_{2n}(\alpha_r) \frac{(\omega_c - \omega)^2}{(\omega_c - \omega)^2 - (2n\Omega)^2} \quad (65)$$

and

$$B_r = 2 \sum_1^{\infty} (-1)^n J_{2n-1}(\alpha_r) \frac{(\omega_c - \omega)^2}{(\omega_c - \omega)^2 - [(2n-1)\Omega]^2}.$$

The continuous power spectrum calculated from (38) with (64) and (65) yields

$$G_c(f_+) = \frac{T}{4} \left[ \frac{\sin(\omega_c - \omega) \frac{T}{2}}{(\omega_c - \omega) \frac{T}{2}} \right]^2 \cdot \left\{ \frac{1}{q} \sum_1^q [A_r^2 + B_r^2] - \frac{1}{q^2} \left[ \sum_1^{-q} (A_r \cos \alpha_r - B_r \sin \alpha_r) \right]^2 \right\}. \quad (66)$$

Taking into account (57),  $A_r$  and  $B_r$  can be rewritten as

$$A_r = \cos \alpha_r + 2 \sum_1^{\infty} (-1)^n \frac{J_{2n}(\alpha_r)}{1 - \left( \frac{\omega_c - \omega}{2n\Omega} \right)^2}$$

and (67)

$$B_r = -\sin \alpha_r + 2 \sum_1^{\infty} (-1)^n \frac{J_{2n-1}(\alpha_r)}{1 - \left[ \frac{\omega_c - \omega}{(2n-1)\Omega} \right]^2}.$$

Substituting of  $A_r$  and  $B_r$  by (67) into (66) yields

$$G_c(f_+) = T \left[ \frac{\sin(\omega_c - \omega) \frac{T}{2}}{(\omega_c - \omega) \frac{T}{2}} \right]^2 \cdot \sum_{r=1}^q \left\{ \frac{1}{q} \left[ \left[ \frac{\sum_1^{\infty} (-1)^n J_{2n}(\alpha_r)}{1 - \left[ \frac{\omega_c - \omega}{2n\Omega} \right]^2} \right]^2 + \left[ \frac{\sum_1^{\infty} (-1)^n J_{2n-1}(\alpha_r)}{1 - \left[ \frac{\omega_c - \omega}{(2n-1)\Omega} \right]^2} \right]^2 \right] - \frac{1}{q^2} \left[ \frac{\sum_1^{\infty} (-1)^n J_{2n}(\alpha_r) \cos \alpha_r}{1 - \left[ \frac{\omega_c - \omega}{2n\Omega} \right]^2} - \frac{\sum_1^{\infty} (-1)^n J_{2n-1}(\alpha_r) \sin \alpha_r}{1 - \left[ \frac{\omega_c - \omega}{(2n-1)\Omega} \right]^2} \right]^2 \right\}. \quad (68)$$

The discrete lines, obtained from the second term of (68), are given by

$$G_d(f_+) = \frac{1}{4q^2} \sum_{m=-\infty}^{+\infty} \left\{ \sum_{r=1}^q J_m(\alpha_r) \cos \left( \alpha_r + m \frac{\pi}{2} \right) \right\}^2 \delta \left( f_c - f + \frac{m}{T} \right). \quad (69)$$

For a four-level system given by

$$\begin{cases} 2\alpha_1 = \pm \frac{\pi}{4} \\ 2\alpha_2 = \pm \frac{3\pi}{4} \end{cases}$$

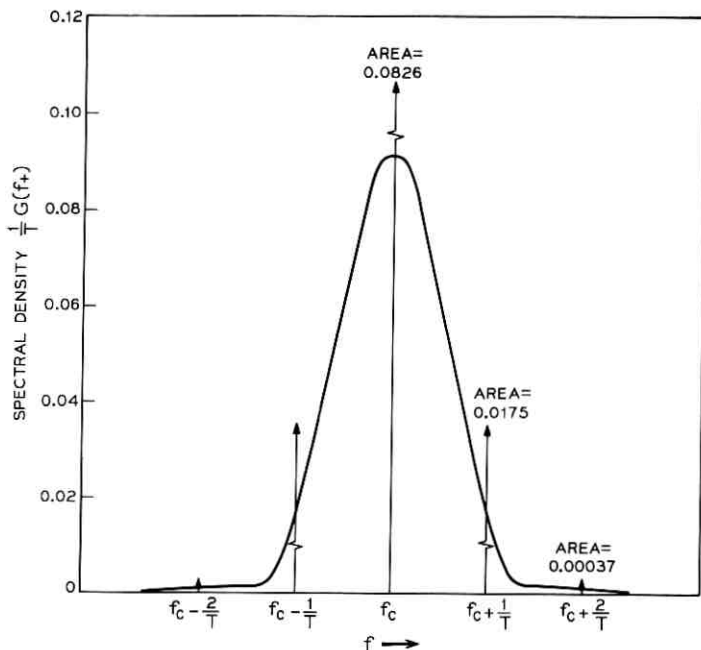


Fig. 7—Power spectrum for four-level polar phase modulation with raised-cosine pulses.

the series expansions in (68) and (69) can be limited to the second term. A good approximation of the power spectrum is then given by

$$\begin{aligned}
 G_c(f_+) \cong & \frac{T}{2} \left[ \frac{\sin(\omega_c - \omega) \frac{T}{2}}{(\omega_c - \omega) \frac{T}{2}} \right]^2 \\
 & \cdot \left\{ \frac{J_1^2\left(\frac{\pi}{8}\right) + J_1^2\left(\frac{3\pi}{8}\right)}{\left[1 - \left(\frac{\omega_c - \omega}{\Omega}\right)^2\right]^2} + \frac{J_2^2\left(\frac{\pi}{8}\right) + J_2^2\left(\frac{3\pi}{8}\right)}{\left[1 - \left(\frac{\omega_c - \omega}{2\Omega}\right)^2\right]^2} \right. \\
 & \left. - \frac{1}{2} \left[ \frac{J_2\left(\frac{\pi}{8}\right) \cos \frac{\pi}{8} + J_2\left(\frac{3\pi}{8}\right) \cos \frac{3\pi}{8}}{1 - \left(\frac{\omega_c - \omega}{2\Omega}\right)^2} - \frac{J_1\left(\frac{\pi}{8}\right) \sin \frac{\pi}{8} + J_1\left(\frac{3\pi}{8}\right) \sin \frac{3\pi}{8}}{1 - \left(\frac{\omega_c - \omega}{\Omega}\right)^2} \right]^2 \right\}
 \end{aligned}
 \tag{70}$$

and

$$G_d(f_+) \cong \frac{1}{16} \sum_{m=-2}^{+2} \left\{ J_m\left(\frac{\pi}{8}\right) \cos\left(\frac{\pi}{8} + m\frac{\pi}{2}\right) + J_m\left(\frac{3\pi}{8}\right) \cos\left(\frac{3\pi}{8} + m\frac{\pi}{2}\right) \right\}^2 \delta\left(f_0 - f + \frac{m}{T}\right). \quad (71)$$

The spectrum given by (70) and (71) is shown in Fig. 7. Note that this spectrum is almost identical to the spectrum of the two-level system calculated with  $2\alpha_r = \pm\pi/2$  and  $p_1 = p_2$ , shown in Fig. 6; in both cases  $\sum_{r=1}^q e^{\pm 2j\alpha_r} = 0$ . This result presents an analogy with the calculations made for rectangular pulses of duration  $T$  which satisfy the same condition.

## V. CONCLUSION

A formula has been derived for computing the power spectrum of multilevel digital phase-modulated signals. The results apply to arbitrary pulse shapes and probability distributions providing that the pulses do not overlap and are independent.

This formula is easy to apply to various pulse shapes. Several examples are given such as:

- (i) rectangular pulses of duration smaller than or equal to the timing period
- (ii) rectangular pulses with finite rise time and decay time
- (iii) raised-cosine pulses.

Approximate results can be obtained for more complex pulse shapes by the following method. The spectrum is a function of the pulse shapes  $g_r(t)$  by the Fourier transforms

$$F_r(f) = \frac{1}{2} \int_0^T e^{+j[\omega_c + g_r(t)]} e^{-j2\pi f} df.$$

$T$  can be segmented into a large number of intervals in which  $g_r(t)$  is approximated to its average value in this interval.  $F_r(f)$  is then given by the following series expansion

$$F_r(f) \cong \frac{T}{2n} e^{j(\omega_c - \omega)(T/2n)} \cdot \frac{\sin(\omega_c - \omega) \frac{T}{2n}}{(\omega_c - \omega) \frac{T}{2n}} \cdot \sum_{k=0}^n e^{j b k} \cdot e^{j(\omega_c - \omega)(kT/n)}$$

with

$$b_k = \frac{g_r\left(\frac{k+1}{n}T\right) + g_r\left(\frac{kT}{n}\right)}{2}.$$

#### VI. ACKNOWLEDGMENT

I am grateful to H. E. Rowe and V. K. Prabhu for helpful comments.

#### REFERENCES

1. Bennett, W. R., and Rice, S. O., "Spectral Density and Autocorrelation Functions Associated with Binary Frequency-Shift Keying," *B.S.T.J.*, 42, No. 5 (September 1963), pp. 2355-2385.
2. Anderson, R. R., and Salz, J., "Spectra of Digital FM," *B.S.T.J.*, 44, No. 6 (July-August 1965), pp. 1164-1189.
3. Lundquist, L., "Digital PM Spectra by Transform Techniques," *B.S.T.J.*, 48, No. 2 (February 1969), pp. 397-411.
4. Van Den Elzen, H. C., "Calculating Power Spectral Densities for Data Signals," *Proc. IEEE*, 58, No. 6 (June 1970), pp. 942-943.
5. Glance, B., "The Spectrum of Binary Digital Phase Modulation," unpublished work.

# A Microwave Feed-Forward Experiment

By H. SEIDEL

(Manuscript received April 12, 1971)

*Both one- and two-stage feed-forward control were applied to a 4-GHz, 461A, traveling-wave tube, used in the TD-3 radio relay system, to demonstrate the feasibility of reducing distortion to a sufficiently low level for single sideband transmission. With a single stage, and discounting extraneous losses, the third-order, M3, distortion measure was reduced by 38 dB over a selected 20-MHz channel, and the application of the second stage rendered distortion unobservable with our instruments. These results were time independent with continuous performance over several months.*

## I. INTRODUCTION

This paper describes an experimental microwave amplifier, designed around the Western Electric 461A traveling-wave tube, which operates with extremely low modulation products over a 20-MHz-wide microwave radio channel. The experimental results provide a fair assurance of the capability of such amplifiers for field use, with a prospect of significantly increasing the channel capacity of microwave radio systems by permitting the use of single sideband AM rather than FM transmission.

This work is part of a continuing effort to explore and exploit feed-forward error control techniques. Feed-forward error control was originated by Harold S. Black in 1924,<sup>1</sup> a precursor by several years to his more famous accomplishment of feedback control. Through 1960, it was viewed, somewhat, as a curiosity,<sup>2</sup> and was used only in the context of a McMillan circuit<sup>3</sup> which fused the two Black concepts of feedback and feed-forward.

Of interest in view of the present publication is U. S. Patent 2,592,716 issued in 1952 to W. D. Lewis, who extended McMillan's ideas to microwaves using traveling-wave tubes and other microwave hardware, to yield redundancy. As proposed, there are fundamental differences

to the results presented here, primarily with respect to unequal amplifier division, and the explicit equalization of signal path timing. Nevertheless, the failure of his ideas to achieve greater currency, leading ultimately to developments parallel to those presented here, probably reflects only to the difference of pressures spanning twenty years.

The essential feature of feed-forward is its total freedom from transit time limitations which seriously limit the application of negative feedback at high frequencies. H. Seidel, H. R. Beurrier, and A. N. Friedman,<sup>4</sup> in 1967, demonstrated the capabilities of feed-forward when applied to VHF amplifiers. Two separate high-power amplifiers, one operating between 25 and 35 MHz and the other between 60 and 90 MHz, were made to exceed dynamic ranges of well over 100 dB, using circuit features adapted to the requirements of feed-forward error control.

In 1969, the author demonstrated the capabilities of feed-forward control in improving an existing L-4 coaxial cable distribution amplifier. This amplifier, at the forefront of 1966 transistor and feedback art, yielded a 40-dB improvement of modulation products across the entire range of 0.5 to 20 MHz,<sup>5</sup> a 40:1 bandwidth. At this juncture, the cumulative evidence made clear the worth and tractability of feed-forward control, and interest arose in its applicability to microwaves.

Of particular interest in microwaves is the distortion of the power output stage of a radio relay repeater. It is well known that amplitude compression forces a frequency modulation, or PCM, or still other frequency redundant modulation schemes, to override the cross-modulation that would be otherwise produced. Redundant frequency solutions may, however, prove ultimately self-defeating. Spectrum width is not readily acquired in a climate of ever-accelerating communication traffic.

Under these circumstances, single sideband modulation is an attractive prospect assuming that, indeed, it is only the power stage limitation that excludes it. For example, the effect of atmospheric fluctuations on wideband single sideband transmission is, as yet, unevaluated, both with respect to fading and scintillation. Nevertheless, if one assumes the dominant limitation to be power stage compression and, assuming generally acceptable noise levels, talker statistics, path losses, etc., together with an assumption of 3600 circuits within a 20-MHz channel, linearity requirements for the power stage may be deduced. For the Western Electric 461A traveling-wave tube, the 10-watt saturation power stage used in the TD-3 system, calculation shows a required improvement in modulation products of between

40 and 47 dB.<sup>6,7</sup> The divergence in these numbers stems from the degree of phase decorrelation introduced into third-order intermodulation accumulation by transposing (frogging) master groups at various sites along the transmission route. To show the adequacy of feed-forward control independent of auxiliary techniques, it was the purpose of this experiment to show that distortion reduction could be accomplished beyond the higher, 47 dB, figure.

To make the linearity requirements precisely quantitative, let us momentarily review the definition of the intermodulation measure, M3. M3 is defined as the number of decibels relative to one milliwatt at which one will find a third-order product of the form  $A + B - C$ , with the amplifier emitting the three tones, A, B, and C, each at one milliwatt.<sup>8</sup> The 461A traveling-wave tube has an M3 rating of  $-78$  dB, so that a 47-dB improvement corresponds to an M3 value of  $-125$  dB.

Further specification on the experiment was that each tone in the third-order intermodulation test was to be set to a 22-dBm output power, and that the overall system was not to saturate fully below 38 dBm. Implicit in the specification of 22 dBm per tone is the recognition that third-order intermodulation products would be  $3 \times 22$ , or 66 dB, above the  $-125$ -dBm level. Therefore, it was the objective of this test to reduce third-order intermodulation below  $-59$  dBm with the specified three-tone excitation. A final specification required that the noise figure not be substantially increased from the present 461A value: a quantity of, roughly, 30 dB.

As we shall show, the various amplifier objectives have been met. There is a current study of atmospheric effects upon single sideband transmission. The combined results of the atmospheric study and the evaluation of the role of low-distortion amplifiers will form a basis for the determination of feasibility of single sideband transmission in microwave radio relay repeaters.

The body of this paper is contained in the following three sections. In Section II the essentials of feed-forward control are reviewed. While, in many respects, it repeats information contained in Refs. 4 and 5, it does contain new information in the form of a noise analysis of a feed-forward system. Embodiment of a feed-forward system is highly influenced by noise considerations and a full understanding of the noise process is important.

Feasibility of a microwave feed-forward amplifier requires, essentially, a demonstration of compatible co-existence of various microwave devices interacting in a fairly complex pattern. The very existence of individual devices capable of satisfying their requisite functions

must be investigated, and then their interaction must be shown to be predictable. While we attempt to separate Device Choices and Experimental Results in Sections III and IV, we cannot claim a fully successful separation. The choice of a device is, in the last analysis, an operational procedure in that its choice must make the total system operate acceptably, and this can only be done, convergently, in evaluating end results as part of the process of device choice.

Section V summarizes the various results of the study and suggests, possibly, profitable areas for further investigation.

## II. SHORT REVIEW OF FEED-FORWARD ERROR CONTROL

### 2.1 *General Features*

Feed-forward control, as we use it, has two major characteristics:

- (i) It recognizes time flow and provides appropriately adapted control circuitry.
- (ii) Error is determined relative to the source within each successive stage of growth, thereby not allowing any cumulative increase of error. To the contrary, an arbitrarily low error may be achieved with an ever-increasing number of stages.

Feedback, in comparing input with output, glosses over the fundamental distinction that input and output are not simultaneous events and, therefore, not truly capable of direct comparison. In practice, they are substantially simultaneous if device speed is far faster than the intelligence rate into the system. Device speed enters the problem, therefore, not in a fundamental sense, but only as a means of making the operational procedure of feedback acceptable. If we were to organize a system of error control which did not force a false requirement of simultaneity, not only would the problem of fabricating zero transit time devices disappear, but so would the entire problem of stability, another guise of the consequence of comparing incomparable events.

Using the first feature listed for feed-forward, we recognize the character of transit time in forming a proper error function. Rather than compare input with output, we form a delayed reference of the input, where the time delay employed sets a standard for the transit time of the amplifier. We assume that the amplifier deviates from this time value to only a small degree. Comparison of the output with the delayed input is made through a sampling coupler whose coupling loss is nominally the gain of the amplifier. Interfering the sampled amplifier output with the delayed reference, we form an error referred in time to the amplifier output.

In having both the amplifier output and the error component of the output in a frame properly referred to the source, we have an undegraded system. Thermodynamically there is no disorder added to the system by the amplifier since the error function provides the means to separate out what is desirable and what is undesirable in the amplifier output. This includes amplifier distortion, undesired variation in the transfer function, and thermal noise. In the sense of Brillouin,<sup>9</sup> the input signal information constitutes a "negative entropy" and we may employ it to cool the noise temperature of the amplifier. As indicated in the second feature of feed-forward, irrespective of complexity as the system grows, we may touch back again and again to this negative entropy to keep the system as cool in noise temperature as we may wish.

Having determined error, the next step in the process is to remove the error present in the amplified output. The process is, essentially, one of subtraction, implemented through a time compatible interference means. The detected error is amplified and brought back to the original error level in the amplifier output. During the transit period of amplification, both the signal and error in the amplifier output are appropriately delayed, so that the error of the main amplifier output and the amplified detected error may collide and annihilate in the final combining coupler.

In amplifying the detected error, we do degrade it somewhat in terms of the thermal noise and distortions of the correction amplifier so that error correction is not perfect. Further the annihilation of the original error is imperfect because of small transfer function perturbations within the error cancelling interferometer loop. While much reduced, the residual error is finite and circumstances may require greater reduction. Treating the two loops composing the error reduction stage as an algorithmic process, we may repeat that process arbitrarily by embedding the amplifier at each level of correction in still another two-loop error correcting stage. There is no cumulative error produced by multistaging since we touch back to the original signal, for reference, at each stage.

Two simplified feed-forward error control systems are shown in Fig. 1 following the lines of description given above. Figure 1a shows a single-stage correction system, where the term "stage" implies both an error detecting loop and an error cancelling injection loop. In this figure, we abstract the common phases produced by respectively equal time delays. The main amplifier is characterized by a small, relative complex error,  $\delta$ . The auxiliary amplifier, referred to at times as the subsidiary amplifier, or the correction amplifier, is characterized by

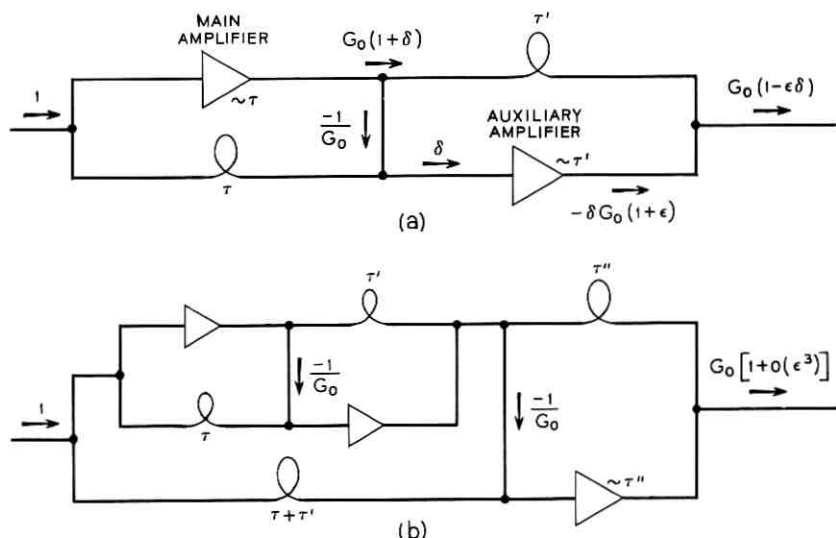


Fig. 1—Feed-forward error control systems: (a) single stage; (b) double stage.

a relative error  $\epsilon$ . Both of these quantities are small and we find the output to have an error of second-order smallness, equal, relatively, to  $\delta\epsilon$ .

Figure 1b shows a two-stage correction system in which the entire first stage is embedded in a second stage for another two-loop cycle of correction. The second-order error of the original single-stage amplifier is now rendered by the second stage into a third-order error through an identical iteration of the mechanics of the error cancellation circuit.

## 2.2 Thermal Noise

In its use here as a power stage output amplifier, thermal noise requirements on the amplifier are modest since it is driven at high level. Nevertheless, without appropriate caution, thermal noise could, inadvertently, become a major problem in a multistage feed-forward system. The crux of the matter lies in the specific means by which we extract information from the original source. If sampling at each correction stage depletes signal energy availability, signal-to-noise level reduces and the reference loses its quality as an information source. To understand the thermal noise aspects, let us calculate the observed noise system with ideal error cancellation.

A feed-forward correction stage is shown in Fig. 2 with noise sources

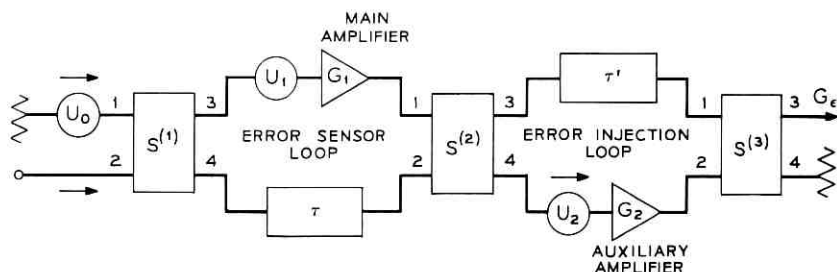


Fig. 2—Feed-forward stage with included noise sources.

included. The uncorrelated noise sources  $U_0$ ,  $U_1$ , and  $U_2$  represent the incident portions of the noise waves, respectively, of the matched termination of the input coupler  $S^{(1)}$ , the referred input noise of the main amplifier, and the referred input noise of the auxiliary amplifier.

If we assume ideal operation of both interferometer loops, we may immediately discount the effect of  $U_1$  since it is headed for ultimate annihilation in the final output. Consequently, we are concerned only with the black-body noise,  $U_0$ , and the auxiliary amplifier noise,  $U_2$ . A normalization to black-body emission will be taken in all that follows so that  $|\overline{U_0^2}| = 1$ . Lack of correlation between  $U_0$  and  $U_2$  provides a further condition that  $\text{Re}(\overline{U_0 U_2^*}) = 0$ .

Let us abstract time considerations from  $G_1$ , and  $G_2$  in all that follows, since that function is formed by the delay networks  $\tau$  and  $\tau'$ . To within these times, the interferometry conditions on the two loops of Fig. 1 are as follows:

$$S_{23}^{(1)} S_{14}^{(2)} G_1 + S_{24}^{(1)} S_{24}^{(2)} = 0, \quad (1)$$

$$S_{14}^{(2)} S_{23}^{(3)} G_2 + S_{13}^{(2)} S_{13}^{(3)} = 0. \quad (2)$$

These two equations permit major simplification in calculation. They assert, implicitly, that either  $G_1$  or  $G_2$ , exclusively, may be disabled without affecting ideal performance. We shall use these disabling features selectively, disabling  $G_2$  for gain calculation and disabling  $G_1$  for noise calculation.

For overall gain, we have,

$$\mathcal{G} = (S_{23}^{(1)} S_{13}^{(2)} G_1 + S_{24}^{(1)} S_{23}^{(2)}) S_{13}^{(3)}. \quad (3)$$

The couplers in Fig. 1 are all directional and forward scattering, having the general description,

$$S = \begin{bmatrix} 0 & 0 & S_{13} & S_{14} \\ 0 & 0 & S_{23} & S_{24} \\ S_{13} & S_{23} & 0 & 0 \\ S_{14} & S_{24} & 0 & 0 \end{bmatrix}. \quad (4)$$

Because of their lossless nature they satisfy the further condition that unitarity applies and

$$(S^T)^* S = 1. \quad (5)$$

Using (1), (4), and (5) in conjunction with (3), we obtain

$$\mathcal{G} = \frac{S_{24}^{(1)} S_{13}^{(3)}}{S_{23}^{(2)*}}, \quad (6)$$

where calculation details are shown in the Appendix. The noise output is given by

$$\epsilon = \{U_o[S_{14}^{(1)} S_{24}^{(2)}] + U_2\} G_2 S_{23}^{(3)} + U_o S_{14}^{(1)} S_{23}^{(2)} S_{13}^{(3)}. \quad (7)$$

Again using calculational details shown in the Appendix, we find

$$\epsilon = \frac{S_{13}^{(3)}}{S_{23}^{(2)*}} (U_o S_{14}^{(1)} + U_2 S_{24}^{(2)*}). \quad (8)$$

The relative noise temperature,  $T$ , of the feed-forward amplifier is given by<sup>†</sup>

$$T \equiv \frac{|\bar{\epsilon}^2|}{|\mathcal{G}|^2},$$

and the relative noise temperature of the auxiliary amplifier is  $T_2 \equiv |\bar{u}_2^2|$ . From (8), after minor transformation,

$$T = \frac{|S_{14}^{(1)}|^2 + T_2 |S_{13}^{(2)}|^2}{|S_{13}^{(1)}|^2}, \quad (9)$$

where the recognition is made that  $|S_{24}^{(m)}|^2 = |S_{13}^{(m)}|^2$ . A further relationship, easily deduced from (1) and (6), is

$$\frac{|G_1|^2}{|\mathcal{G}|^2} = \frac{1}{|S_{14}^{(1)}|^2} \frac{|S_{13}^{(2)}|^4}{|S_{13}^{(3)}|^2}. \quad (10)$$

The full noise design problem may be understood as a reconciliation between (9) and (10). We cannot afford to lose too much of the main

<sup>†</sup> The relative noise temperature,  $T$ , of the amplifier is defined such that the output noise contributed by the amplifier is  $290 \text{ kTBG}$ , where  $k$  is Boltzmann's constant given in joules/ $^\circ\text{C}$ .

amplifier output so that  $|S_{13}^{(2)}|$  and  $|S_{13}^{(3)}|$  must be quantities close to unity. Equation (10) states that a small value of  $|S_{14}^{(1)}|$  infers the need of a large main amplifier gain,  $G_1$ , to yield a specified system gain  $G$ . If, however,  $|S_{14}^{(1)}|$  were made too large,  $|S_{13}^{(1)}|$  would reduce, correspondingly, since these two matrix elements share the complete power flow of the coupler. Any significant reduction of  $|S_{13}^{(1)}|$  raises the noise temperature of the system, by virtue of (9), so that its value must be guarded.

The noise reconciliation with excessively large main amplifier gain requirements is as follows. Main amplifier noise does not enter into the final system noise temperature in principle, for an ideal error cancelling system. This holds in practice, as well, providing main amplifier noise is not allowed to achieve that level which can compete with the degree of cancellation in the last stage. In constructing a multistage system, therefore, we would allow the order of 6 dB noise increase per stage by making  $|S_{13}^{(1)}|^2$  correspond to about -6 dB, up until the last stage, losing about 1 dB gain per stage in the process. For the last stage, treating all previous stages as a new, noisy, main amplifier, we reverse the process, causing the final system noise temperature to exceed that of the last auxiliary amplifier by about 1 dB, but losing 6 dB of gain.

Equation (9) permits a simple, useful approximation. Typically,  $|S_{13}^{(2)}|^2$  deviates by less than 1 percent from unity and  $|S_{14}^{(1)}|^2$  is well less than unity.  $T_2$ , on the other hand, may range anywhere from a value of 3 or 4 in a practical system to well beyond 1000. A good approximation for (9) is

$$T = \frac{T_2}{|S_{13}^{(1)}|^2}, \quad (11)$$

which states that the noise temperature of a well-cancelled feed-forward system is given by the noise temperature of the final auxiliary amplifier times the transmission loss to the reference path produced by the reference coupler.

### 2.3 Criteria for Interferometer Balance

Each stage of correction requires two interferometer balances. The first, corresponding to (1), sets the standards for phase and gain of the main amplifier, while the second, corresponding to (2), cancels the imbalance products proceeding from the first. Nominally, the first loop comparison coupler and time delay closely approximates the transfer properties of the main amplifier, so that the error signal

due to small transfer function perturbation is small. If the standards of coupling loss and time delay were in small error, the system would operate to slightly different standards, with little consequence other than a somewhat higher average power operation of the auxiliary amplifier.

Alternatively, intermodulation and thermal noise are relatively incoherent with respect to the reference signal, so that they form imbalance products of the first interferometer loop independent of the precision of its balance with respect to the coherent portion of the signal. It is the second interferometer loop balance which is critical in cancelling these products from the output.

The relative precisions of the two interferometry relations, (1) and (2), are to be viewed from entirely different perspectives in system design. Given moderate dynamic range of the final auxiliary amplifier, the first loop must only possess that degree of cancellation to avoid any substantial manifestations of nonlinearity in the auxiliary amplifier. On the other hand, the entire figure of merit of the feed-forward error control system in yielding linearity improvement resides in the precision of balance of the second interferometer loop. Since this loop operates in relatively lightly loaded fashion, the potential for maintaining precise balance is good. As we shall show, major design effort is expended towards maintaining a time-independent excellence of this balance through the use of auxiliary controls.

### III. DEVICE CHOICES

#### 3.1 *First-Stage Devices*

Within a feed-forward microwave system we must seek acceptable choices of microwave amplifier, means of accommodating relatively large time delays, couplers adapted to the needs of precision interferometry, adjustment means for setup, adaptive controllers to maintain time-independent operation, etc. The adjective "acceptable" suggests not only the use of devices capable of meeting strictly technical objectives, but implies objectives, as well, of ultimate reproducibility, economic manufacture, and compact packaging.

While, in the longer term, one would think of microwave integration of many of the components used in the amplifier system, such integration is incompatible with the immediate needs of a feasibility demonstration. The microwave experiment, therefore, was performed entirely with waveguide and coaxial circuitry to provide for ease of modification. In general, a one-to-one correspondence exists between most of these

components and what exists within the present art of microwave integrated circuitry. Nevertheless, two devices would appear to except themselves, at this juncture, from realization within integrated format. They are:

- (i) main power amplifier, and
- (ii) error cancellation time delay section.

The main amplifier used in the experiment is a 461A traveling-wave tube capable of the order of 10 watts of saturated power at 4 GHz. While one may envision an ultimate solid-state replacement, such replacement is not now available. The time delay miniaturization problem is even less tractable than that of the main amplifier. The error cancellation time delay section, shown as  $\tau'$  in Fig. 1a, offsets the 13-ns transit time of the auxiliary amplifier, another 461A TWT. At 4 GHz this transit time corresponds to 52 cycles of storage, and the storage loss is absorbed from the output power of the main amplifier. Since the economics of generating distortion-free power is severe, it would seem unlikely that one would elect to waste that power through the use of a relatively lossy miniaturized delay line.

### 3.1.1 *Main Amplifier*

Two devices contended for the role of the main power amplifier: the 461A TWT used in the TD-3 system, and the 416C closed-spaced triode used in the transmitter amplifier in the TD-2 system. The 461A TWT was selected because of its superior gain and phase stability. In contrast to a transit-time-limited system the intrinsic functions of a traveling-wave tube (i.e., beam formation, drift, interaction, beam collection) are all well separated. While transit time may be large, nevertheless it is well characterized by a highly regulated helix potential as well as by the precision of the helix construction itself. Thermal heating of the helix through beam interception is imperceptible and its electrical phase is well maintained in a controlled ambient environment. Given a control of cathode current and a maintenance of beam synchronism, no significant aging problems appear evident. While some effect may be postulated of the accumulation of ionized gas molecules within the beam, estimations yield minor gain and phase level shifts, with no appreciable effect on time delay.

An attempt to grossly simulate TWT aging has been made varying beam-forming electrode potentials. While minor shifts were observed in gain and phase levels, these shifts were well within the corrective range of automatic controllers which we shall describe later. The essential result of this investigation is that transit time is unaffected

and that fixed feed-forward delay compensations retain their performance with time.

Measured performance over a 100-day period tends to support the favorable view of TWT capability. Figure 3 shows gain fluctuations of the order of  $\pm 0.05$  dB after a two-day stabilization period. The phase data of Fig. 4 show a stabilization period of, perhaps, ten days, followed by a drift of average phase of 1 degree in the remainder of the 100-day period. Short-term phase fluctuations appear to be within  $\pm 0.25$  degree.

To place these fluctuations within context, a 40-dB interferometer null implies either a gain imbalance of 0.08 dB or a phase imbalance of 0.6 degree, or a weighted combination of both. The small open-cycle fluctuations of the TWT lend themselves readily to active control means to provide for interferometer balance well beyond the 40-dB level.

### 3.1.2 *Subsidiary Amplifier-First Stage*

The subsidiary amplifier employed in the first stage was another 461A TWT. The determining factor in its choice was, primarily, that it was a standard device already employed in the Bell System, although its power capacity exceeded the needs of the experiment.

It is instructive, nevertheless, to consider the requirements on the first-stage subsidiary amplifier in the light of the M3 specifications for the entire feed-forward amplifier system. Relative to its own M3

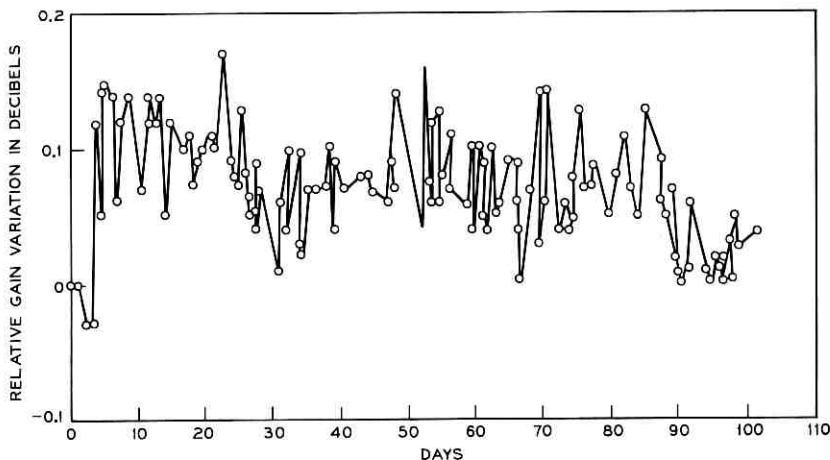


Fig. 3—Gain variation for 461A TWT amplifier.

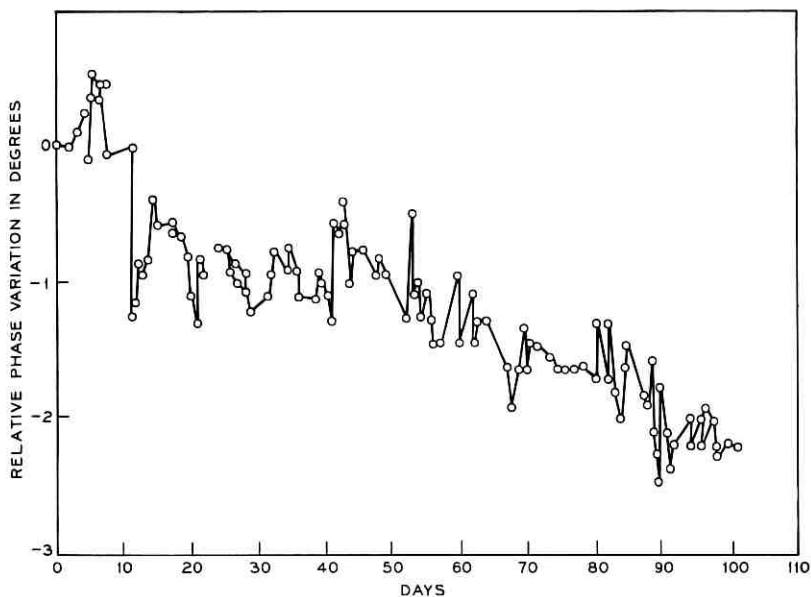


Fig. 4—Phase variation for 461A TWT amplifier.

rating of  $-78$  dB, the main amplifier produces third-order intermodulation tones of  $-12$  dBm for the three specified 22-dBm output tones. Thus, intermodulation tones are of order 34 dB below the main signal tones. If these tones form the substantial level of excitation into a subsidiary amplifier of capacity identical to the main amplifier, the new production of intermodulation would lie at about  $-96$  dBm taking into account the 6-dB transfer loss in the error combiner coupler.

The desired intermodulation level for the feed-forward system for 22 dBm/tone output is  $-59$  dBm, so that a margin exists of 37 dB. If we assume a first-stage reference loop imbalance of order 35 dB, the subsidiary amplifier must also handle this energy as if it were error. Such imbalance error is, roughly, at the same level as the intermodulation and diminishes the margin. Recognizing the three-for-one relation of intermodulation production, in dB, to power capacity, one might envision a new code of manufacture for the first-stage subsidiary amplifier designed to meet all the specifications as given having only 10 percent the capacity of the 461A.<sup>†</sup>

<sup>†</sup> Since the initial specifications were given, more recent requirements have stipulated an M3 of  $-125$  dB to the peak 38-dBm level. Calculation shows that this more demanding performance could still be handled by a subsidiary 461A TWT, but at 100 percent of its capacity.

However, even within these specifications, this degree of capacity reduction may be somewhat optimistic. Unlike a conventional amplifier, a singly corrected feed-forward system increases in intermodulation at a rate of 9 dB per dB with subsidiary amplifier saturation, and at a rate of 27 dB per dB for a doubly corrected system. Such precipitous distortion increase would suggest greater caution in establishing power margins.

### 3.1.3 *Delay Lines*

Both the error sensor loop and the error injector loop of the first stage house 461A traveling-wave tubes, each about 19,000 degrees in electrical length. Corresponding to each loop is an equivalent delay line designed to match its respective traveling-wave tube to within a precision of better than 1/2 degree.

By excellent helix design and construction techniques, phase distortion is maintained at minimal levels in the traveling-wave tube, and phase linearity is achievable within the level of precision sought. The onus falls on the matched delay section within each interferometer loop to match that degree of excellence. A problem arises of sheer bulk. The helix produces large attenuation because of its small cross section relative to physical length, but this is inconsequential because of electronic gain. There is no gain mechanism, however, in the sensor loop delay line, nor in the injector loop delay line. Large attenuation in the former increases system noise figure by that amount, whereas, attenuation in the latter dissipates expensively bought power.

There are some options on noise performance since we are discussing a high-level amplifier, and this should merit further investigation. We might accept some tolerably higher level of noise figure and allow a degree of compromise in miniaturizing the error sensor loop delay line. As stated, however, an excessively dissipative error cancellation delay line is unacceptable, since that line directly tandems the main power amplifier. Consequently, at least the error cancellation delay line is composed of standard cross-section waveguide. Having accepted the necessity for one large section delay line, for convenience, we made the second, corresponding to the error sensor loop, exactly similar.

With hardware pertinent to the system added, the actual time delay within each loop exceeds 15.5 ns. Using straight WR229 waveguide, this calls for a span of 11.93 feet for each delay line section. This length proves awkward to package, particularly with the knowledge that it must be used repeatedly within the feed-forward assembly.

The simultaneous need to retain waveguide cross section and to

make packaging practical suggests use of filter techniques to increase energy storage per unit length. Since the filter must not ripple or bow the phase linearity in any substantial manner, nor be permitted to distort the amplitude response substantially, we chose a moderately wide bandwidth, maximally flat, filter as a basis for design. Computation shows that one may realize the delay section to within 0.0002 dB amplitude and 0.1 degree phase ripples over the 20-MHz band with a 14-inch, six-section, asymmetric inductive iris, direct-coupled filter. The computation does not account for iris thickness, and physical realization with 1/32-inch-thick irises shows excellent preservation of relative shape of characteristics but modifies time delay by a small factor. As a practical matter, the time delay computed is designed at 15 percent lower than that required. This empirical determination has been found operational over a significant span of time delay. Residual errors are simply tailored by the addition of a small guide length so that accurate time control is easily achieved within a relatively compact package.

#### 3.1.4 *Directional Couplers*

Control of amplitude is the counterpart to the control of time delay in a broadband interferometer loop. Since amplitude levels are set, primarily, by directional coupling ratios in the feed-forward system's interferometer loops, one need only require flat coupler over a negligible 1/2-percent bandwidth. Given a fixed design ready for manufacture, such couplers are easily obtained. However, in the case of an experimental system requiring close, adjustable, control, it is impossible to think of a continuum of couplers made conveniently available.

Fortunately an adjustable directional coupler is readily available—but at a price. In essence, the coupler is composed of two circulators with an adjustable cutoff section intervening, and is shown in Fig. 5. The price to be paid is the dissipation of two passes through the circulator plus the small dissipation in reflecting from the cutoff section. These losses form part of the excess loss picture to which we shall refer later, but which would not be present in a final design.

In Fig. 5, wave energy incident upon port A impinges entirely upon the mismatch section in the first pass through the circulator. Most of that energy reflects via circulation to port B. That energy transmitted through the cutoff section circulates to port C. Energy reflected from B returns only to A and, similarly, all reflection from C returns only to D. The coupling ratio of this coupler system is, substantially, the insertion loss of the cutoff section which, as indicated, is controllable.

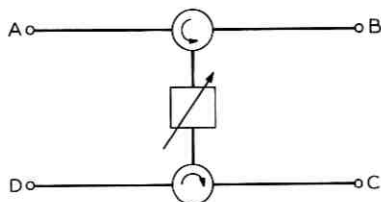


Fig. 5—Adjustable directional coupler.

As used throughout, the controllable cutoff section, shown in Fig. 6a, is composed of two inductive irises forming an off-resonance cavity, and three symmetrically located screws spanning  $1/4 \lambda_r$  of length of this cavity.

Scattering matrix properties of a reactive, reciprocal, symmetric two-port readily yield a phase quadrature relationship between the reflection and transmission coefficients. Since two passes through equivalent circulators is required to go from A to either B or C in Fig. 5, the 90-degree phase difference between these two ports is unaltered by symmetric adjustment of the cutoff section. Therefore, phase and gain adjustments of the interferometry conditions are entirely independent.

The two irises of the cavity are spaced essentially to be at a peak of the first rejection region, as shown in Fig. 6b, where the iris susceptance value defines a particular loss. Simultaneous motion of the two outer screws, without the presence of the center one, controls internal phase within the cavity. This tends to change the center frequency corresponding to peak loss, with only a minor interaction with that loss. The center screw operating by itself produces a dominant shift of peak loss, with only a minor interaction with center frequency. With both sets of controls operating, various intermediate control relations are obtained. Thus, control of amplitude and flatness is simply afforded without phase interaction.

### 3.1.5 Adaptive Control

The 461A traveling-wave tube has two types of drift, both slow but of widely differing time periods. There is a "breathing" effect which produces 1 degree and 0.1 dB changes throughout a day, probably attributable to thermal effects, and there is a larger term aging process which changes phase by 2 degrees and gain by 0.1 dB over a 100-day period. While these changes are not profound, they exceed the bounds set for the degree of interferometer balance sought. For continuous

operation of the system at target specifications an adaptive control system must be employed to maintain initial balance.

The phase and gain drift variations are nondispersive. For example, a 2-degree drift represents a microscopic change of transit time considering a total electrical length of 19,000 degrees. A simple phase shifter, having in itself a negligible transit time, suffices to compensate this drift across an entire 20-MHz band with fully adequate precision. Precisely the same consideration holds for gain drift control.

To set a test for balance, a continuous pilot tone is injected into the system at a position following the main amplifier in the manner shown in Fig. 7 (point 1). By hypothesis, since this signal appears as an uncorrelated emission of the main amplifier, the feed-forward system must operate to remove it through the interferometric cancellation of the error injector loop.

The quality of interferometric null can, of course, be observed at the output of the first stage, and a performance measure may be made. Unfortunately, it is difficult to discern within the degree of balance accomplished by the interferometer a quantitative evaluation of how much was attributable to phase and how much to gain in failing to achieve a more perfect balance. One may propose a variety of systems to achieve this determination, such as one operating by successively rocking phase and gain to achieve a deepest null. Several possibilities were considered, but we felt them to be more elaborate than the system finally used.

Assuming that the transfer characteristics of the final coupler in which the two paths destructively interfere are highly stable, we may measure the differential gain and phase, respectively, of the two paths

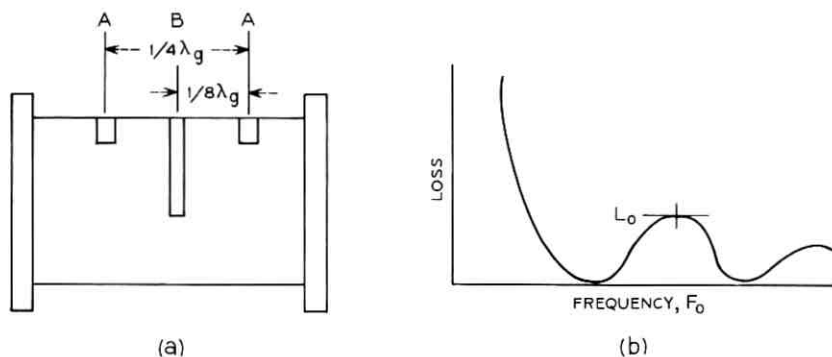


Fig. 6—Controllable cutoff section.

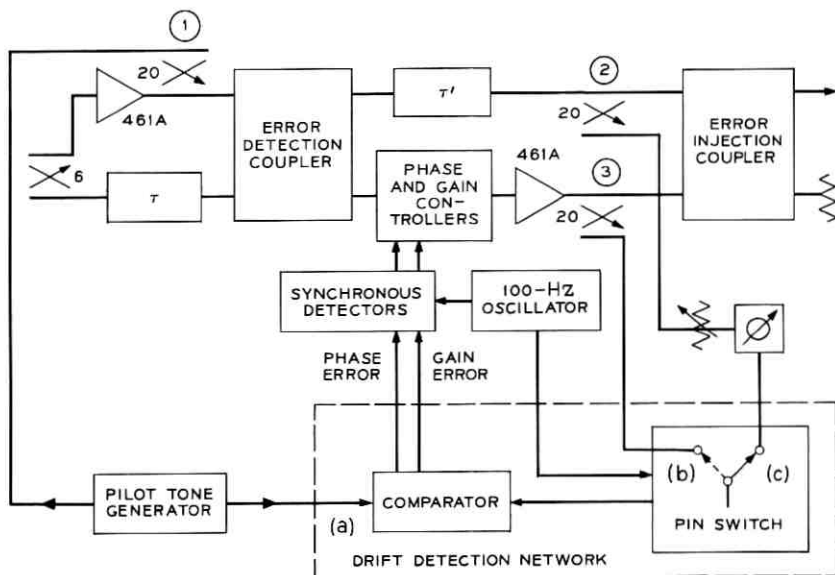


Fig. 7—Drift control in first stage.

prior to interference, and servomechanically correct those differential quantities relative to standards known to yield best destructive interference. Operating in this manner, we have recognized the relative identity of each path within the interferometer and are not confronted with an admixed relationship of these two paths, as we would be in testing the final null.

The two paths of the error injector loop are sampled, via directional couplers, at points 2 and 3 in Fig. 7. These two samplings are brought to points labeled *b* and *c* in the Drift Detector, while the original pilot tone reference connects at point *a*. Intervening in one of the sampled paths is an adjustably set attenuator, phase shifter combination.

The detection of drift is accomplished through means reminiscent of a Dicke radiometer.<sup>10</sup> A known reference to phase is given at point *a*. A switch, synchronously shuttling between *b* and *c* at a 110-Hz rate, samples each of the interferometer paths. By an internal phase discriminator arrangement, it compares the phase of *b* to *a* at one extreme of the switch, while comparing the phase of *c* to *a* at the other. Let the adjustable phase shift control in sampling path *b* be preset such that the output detector readings, corresponding to both *b* and *c*, are identical. With drift, a phase sensitive synchronous signal develops which tags the

direction of the drift and, with synchronous detection, generates a control signal. The attenuation drift detection is accomplished similarly, with the initial set attenuator in path *b* providing a zero amplitude error in the balanced state, and with the phase sensitive synchronous signal tagging the direction of amplitude drift.

The interferometer null drift is, relatively, very slow and the synchronous detection of gain and phase deviation may be made with long correlation times: a fraction of a second or longer. This yields excellent precision in detection, with negligible requirements on pilot tone power for good sensitivity. Given the narrow band nature of this signal, high feedback gain may be employed, and the loop null may be actively restored to limits far exceeding requirements on the feed-forward system.

The controllers employed within the experiment were mechanically driven devices. Electronic phase shift using varactors was ruled out because of the possibility of its generating intermodulation. By default, since an external electronic phase control could not be used, the electronic control of attenuation through a PIN diode was also excluded to avoid noncommon circuitry. Direct electrode control of the TWT was a considered possibility. Tests were made showing that small helix voltage perturbation about synchronous velocity produced phase shift with a negligible attenuation variation. Beam current control affects both phase and amplitude. Using a fast helix voltage feedback and a slow beam current feedback, gain and phase control may be individually achieved. While this may well prove an operational solution in ultimate use, such control meant tampering with a highly regulated power supply during an experiment, and we chose the least adventurous approach.

The mechanical controllers were of similar construction, using a resistive vane in a guillotine attenuator arrangement, and a dielectric vane in like manner for phase shift. To assure no interaction between attenuation and phase control, a shaped dielectric compensation was physically appended to the resistance card to maintain invariant phase with insertion. Each controller, corresponding either to the phase unit or the attenuation unit, was composed of two sections. The first was a manual set to assure initial adjustment, while the second contained a motorized section used in the servomechanical drift adjustment system discussed above. These units are shown in Fig. 8.

The precision of balance is the key to long-term feed-forward microwave error control. The synchronous sampling technique above is excellent for such control, but only if the sampling means is rigorously time independent. A serious question concerns the transmission qualities of the switch.

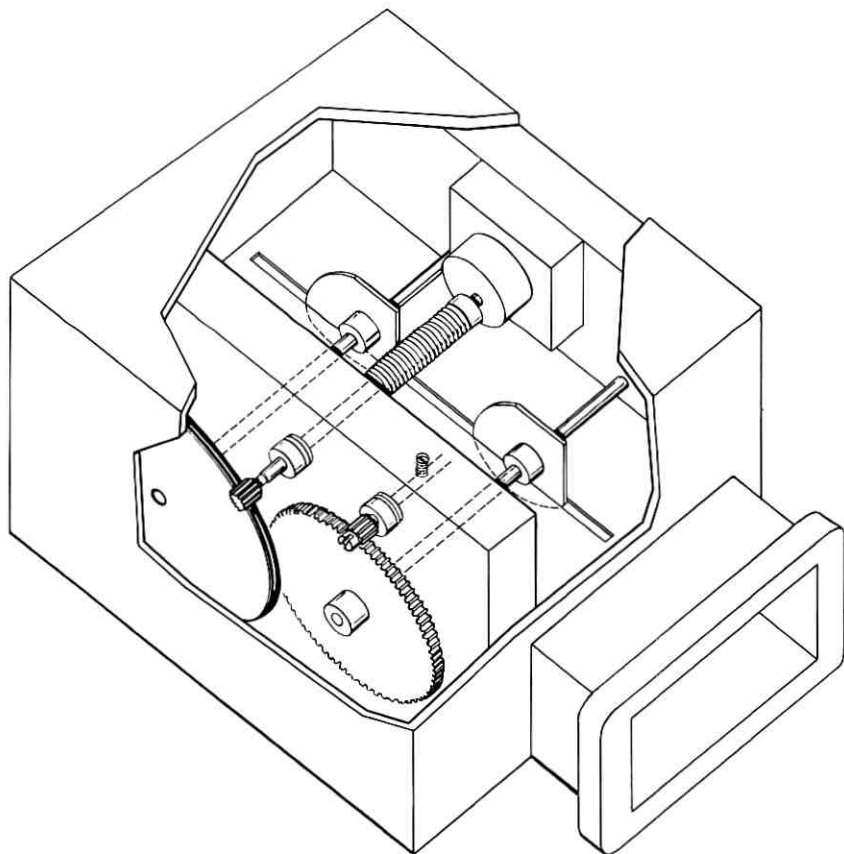


Fig. 8—Mechanical phase/gain controller.

Early in the experiment it was felt that microwave switching might prove complex. Under the circumstance, the sampling signals were individually heterodyned to IF, and all circuitry functions including that of switching were accomplished at IF. This control system worked badly; null balances of the fed-back interferometer loops ranged in time from greater than 50 dB over the band to less than 30 dB. The fault, after intensive examination, was found to lie in the mixers. Over the course of a day, with no overt evidence of thermal gradients between them, and for common fluctuations of local oscillator power and frequency supplied to them, evidence was found of greater than 3 degrees differential transfer phase variation between them in going from micro-

wave to intermediate frequency. The immediate cause of this effect is not understood, but it is probably thermal in origin.

Microwave switching was, thereupon, more rigorously examined and found to be capable of excellent reproducibility. The switch is composed of two oppositely switched sections, each section composed of a shunt PIN diode pair. Each section, individually, lies in the path of one of the sampled signals, and each is followed by an isolator. Both sampling paths are then brought to a common output port using a microwave hybrid combiner. During its transmission cycle, the PIN is strongly reverse biased, but well short of its avalanching. This causes the entire scattering of the diode to reside in its cartridge and to be independent of any semiconductor parameters. In its reflection cycle, the diode is strongly forward biased so that its impedance is dominated by its ohmic contact. Whatever small leakage occurs, at least, does so in a stable manner. The output isolator further stabilizes whatever effect fluctuating impedance might have on the other switching diode pair, although these individual switches are isolated by the conjugacy of the microwave hybrid.

Measurement failed to discern any differential phase or gain shift of the switch although resolvability could be made to within hundredths of a degree and thousandths of a dB. That switching had been the original source of the null softness was confirmed by the very tight system that resulted with the introduction of the PIN switches.

The existence of control circuitry with this caliber of performance was vital to the microwave experiment; without a control capability of this order, a microwave feed-forward system would prove impractical.

### 3.2 *Second-Stage Devices*

In undertaking this experiment, it was felt that an exploration should be made of the performance of an added second stage with no pre-conceived concerns as to ultimate system practicability. All the concerns of this section are rendered academic, if only a single stage is to be used. The construction of the second stage was, however, conditioned by the proviso that the first stage be optimally tailored for independent operation, whereas an intent to construct a two-stage system from the start would have led to different choices and, possibly, usages.

#### 3.2.1 *Second-Stage Subsidiary Amplifier*

Most of the elements of the second stage are essentially the same as those of the first, with a major exception being the second-stage subsidiary amplifier. We have recognized in our treatment of the first

subsidiary amplifier that, as a replica of the main amplifier, it possessed greater power capacity than needed. Since the first stage, a composite of these two amplifiers, requires orders of magnitude less correction power, we may properly look to a low-level or weak system for second-stage correction. Indeed, its very weakness is the key to ultimately low noise performance.

The second-stage correction system is shown schematically in Fig. 9. The second-stage subsidiary amplifier is a composite system comprised of a Schottky barrier down-converter, a baseband amplifier, and a varactor upconverter. This combination provides the noise figure of the Schottky barrier, the RF phase and gain stability of the majority carrier Schottky barrier and varactor devices, and the phase and gain stability of a 400-MHz wide baseband amplifier used at a relatively low 70-MHz centerband frequency. This arrangement has the advantage of providing a well-performing solid-state final reference standard to a feed-forward system, operable throughout the microwave spectrum.

The virtue of this arrangement as compared to, say, a microwave transistor amplifier, is clear.

- (i) Gain per stage is low in a microwave transistor amplifier, and a complex, expensive structure is required
- (ii) Thermal phase sensitivity is high.
- (iii) Dynamic range is very low, even for application as a subsidiary amplifier.
- (iv) General applicability beyond 4 GHz is questionable.

Noise considerations exclude IMPATT and Gunn devices, while

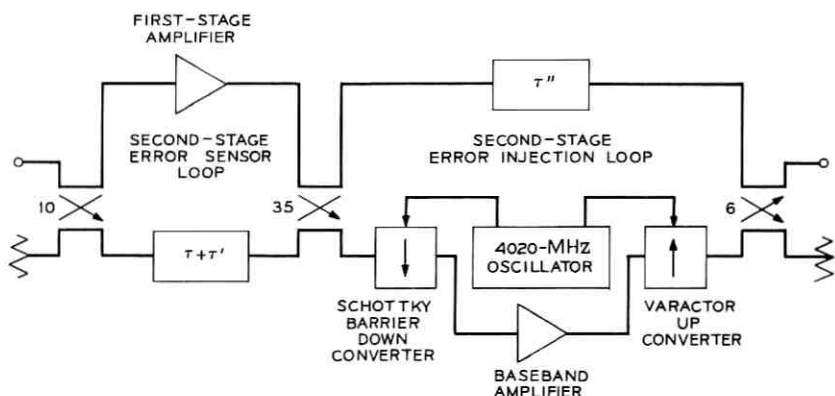


Fig. 9—Second stage.

complexity and/or stability problems make tunnel diode and parametric amplifier systems dubious, for long-term, dependable operation.

In express conflict with our discussion in Section II, Fig. 9 shows the reference arm signal to be dominantly transmitted to the first stage and decoupled by 10 dB from the input, while noise considerations would have it be the other way around. This situation is a direct consequence of the imposed constraint of keeping the first stage intact. Since the first stage was constructed for best noise performance, a substantial loss in gain was incurred in favoring signal into the first subsidiary amplifier. We could not afford to take this loss of gain a second time so that the second stage was run in a high-noise mode. While this rendered noise measurement meaningless, nevertheless, we were able to perform intermodulation measurements with a second-stage correction, and this remains a meaningful measurement irrespective of the noise connection.

With the configuration of Fig. 9 a subsidiary amplifier gain of 44 dB was required to yield a second-stage error cancellation loop balance. Because of overdrive considerations, the balance of the error sensor loop which drives the subsidiary amplifier was critical. A worst null figure was found of 38 dB, but we might expect even better performance with more fastidious equalization since such improved equalization is justified in light of the prior stabilization of the first stage. In contrast, such an attempt to improve error sensor loop balance in the first stage could not be justified in view of the relative softness of the main amplifier.

Accepting the 38-dB worst null figure, and accepting, further, a  $-1.5$ -dBm input necessary to drive the two-stage feed-forward system to its operating level, the 44-dB subsidiary amplifier gain in conjunction with the 10-dB loss through the input coupler and 0.3 dB of added loss in the second-stage time delay circuit implies a  $-8.5$ -dBm output level of the final second-stage upconverter due only to imbalance effects introduced by the first stage. This power far exceeds that required to handle first-stage intermodulation and, consequently, dominates the power capacity required for the upconverter.

In order to expedite the program we used, in the second stage of feed-forward, commercially available components which were marginal in their power handling ability. This necessitated the addition of a second pilot tone at 4110 MHz and a phase controller to offset overload-producing imbalances created by thermal effects in the second-stage, error-sensor-loop, delay line. These additions would probably not be needed in final design.

For completeness, Fig. 10 shows the detection and control system actually employed. In essence, operation is based on the principle that a

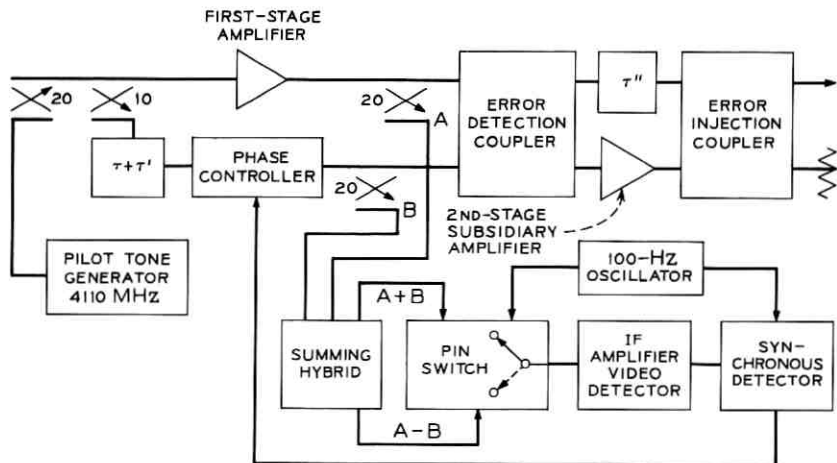


Fig. 10—Second-stage controller.

vector sum and a vector difference have the same magnitude only if the two component vectors are in perfect phase quadrature. This yields a phase sensing means for control feedback.

#### IV. EXPERIMENTAL RESULTS

A complete schematic of the full, two-stage system is given in Fig. 11, omitting third-loop correction features as irrelevant. Front and side photographic views of the system are given in Figs. 12 and 13.

As Fig. 11 shows, the experimental system leans heavily on ferrite loaded components for both adjustment and cautionary purposes. These would disappear, for the most part, substantially lowering losses appearing in an actual system. Conservative calculation of extraneous losses suggests that at least 2 dB of loss is recoverable in practice for a single stage over that achieved here, and twice that for a double correction stage.

##### 4.1 Saturation Curves

Figure 14 shows gain as a function of output power for the uncorrected, first-stage corrected, and second-stage corrected microwave amplifier. The uncorrected amplifier shows very soft gain characteristics, with gain deviation observed as early as 12 dB below its 40-dBm saturation. The first and second corrected stages appear relatively identically shaped, but differ in their saturation power by the circuit losses. With

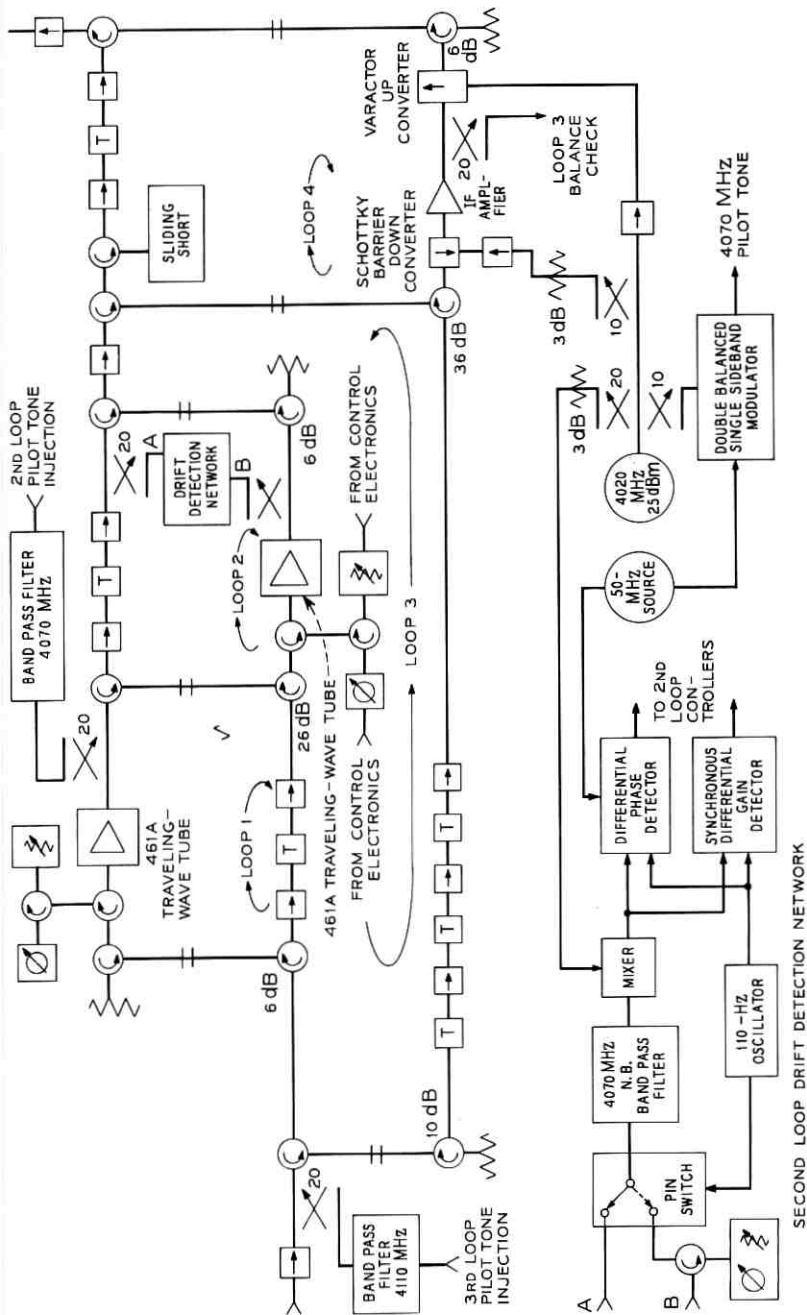


Fig. 11—Two-stage microwave feed-forward correction system.

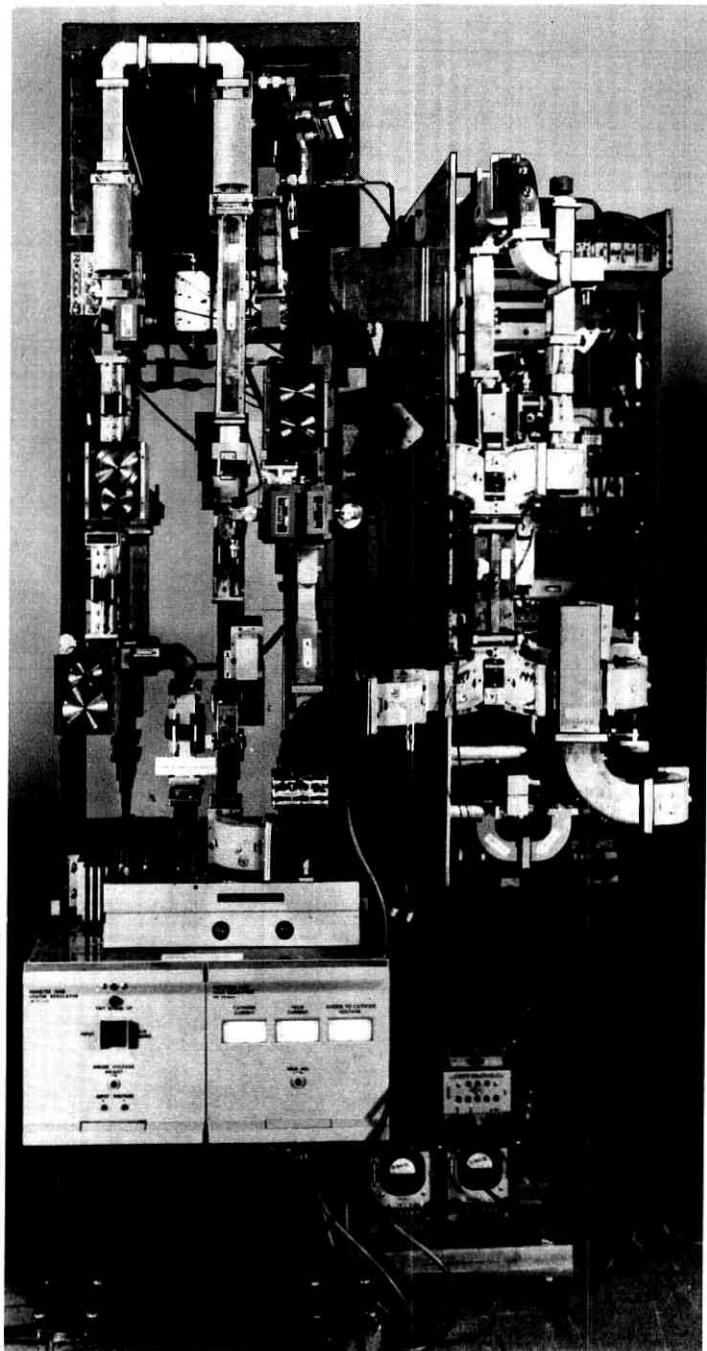


Fig. 12—Front view of system.

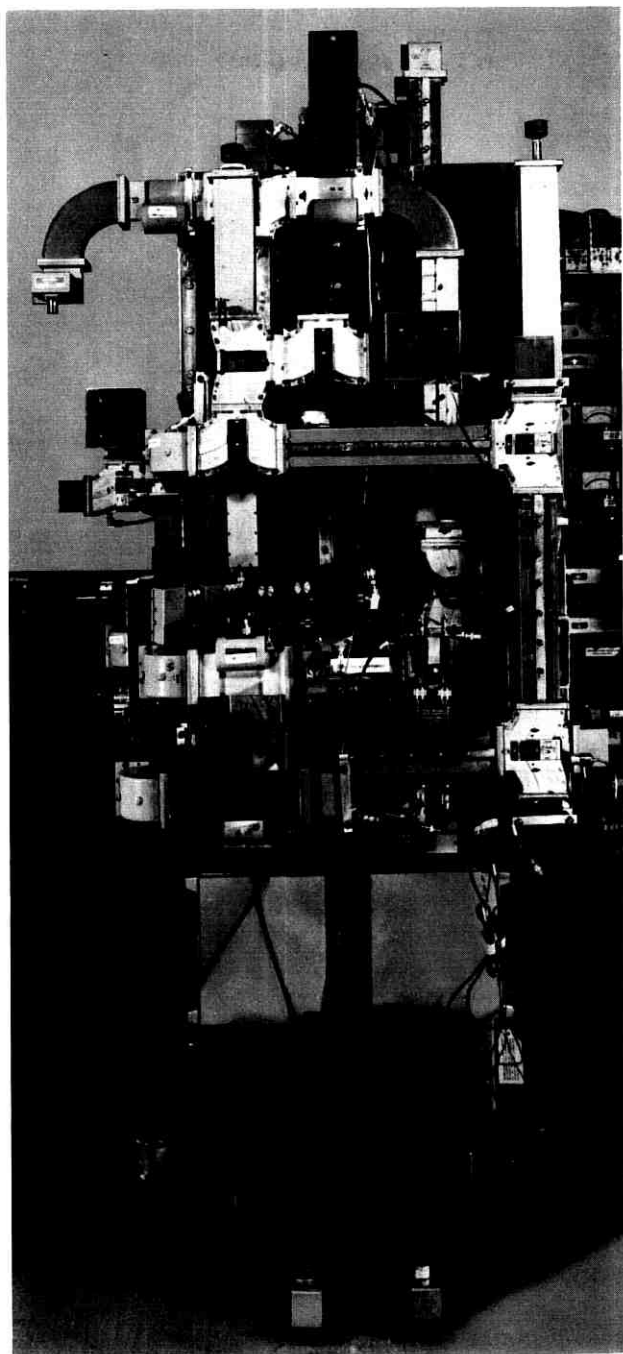


Fig. 13—Right-side view of system.

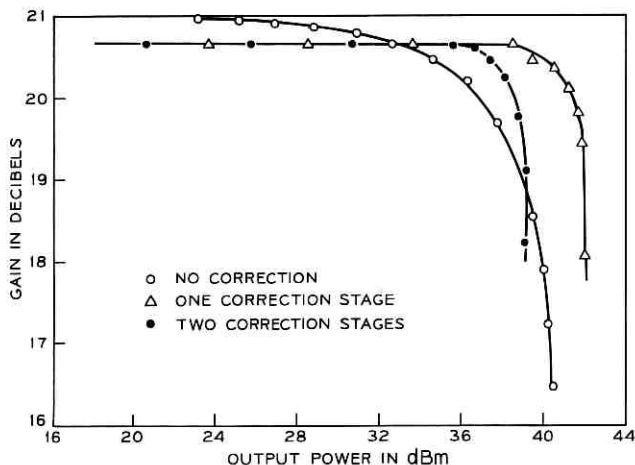


Fig. 14—Experimental gain characteristics.

first-stage correction, saturation occurs at about 42 dBm, while second stage correction reduces this to 39 dBm. Discounting extraneous losses of 2 dB per stage, these numbers would correspond in practice to 44 and 43 dBm, respectively. In contrast to the uncorrected amplifier, gain is a far flatter function in the corrected systems, showing the onset of gain deviation within only 3 dB of saturation.

Figure 15 shows corresponding phase characteristics. The phase curve of the uncorrected amplifier shows the same sort of softness as does the gain curve, while first- and second-stage correction yield a remarkable flattening. To within a phase variation of, perhaps, 1 degree peak to peak, there is no marked deviation from flatness until about 2 dB from saturation.

#### 4.2 Dump Port Power

First-stage error cancellation injection is performed via a 6-dB four-port coupler. Three ports are occupied with main path transmission and error injection, while the fourth is resistively terminated to assure the match and directivity properties of the coupler.

A serious concern is expressed in Ref. 4 about the use of a four-port for this function since the resistive termination operates to absorb 1 dB of main path power for a 6-dB coupler. It is easily shown, however, that by choosing the reference phase and gain appropriately in the first-stage error sensor loop, a destructive interference occurs into that termination

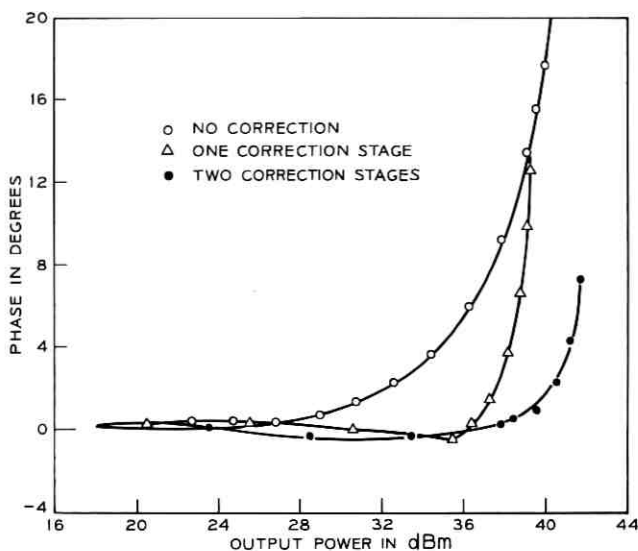


Fig. 15—Experimental phase characteristics.

of the wave portion coupled from the main amplifier and the portion transmitted from the error amplifier. Under this circumstance, with only small power entering the termination, most of the power lost by the main amplifier is recaptured and is further augmented by virtually all the power emitted by the subsidiary amplifier. We can, in principle, arrange this condition at some most critical operating point of the system, turning the injection coupler from a liability to an asset.

This process is made evident in Fig. 16 which shows dump-port power as a function of output power. At low levels, only small error power is generated and the dump power is dominated by main line coupling. This is evidenced by a linear dB for dB relationship. At 36 dBm output, however, the coupling into the termination is 9 dB below a linear coupling rate, representing a relatively minor system power loss with respect to the combined power emissions of both the main and subsidiary amplifiers.

#### 4.3 Intermodulation Results

The reduction of intermodulation is a function of the various interferometer loop balances. The first- and second-stage error injection nulls measured minimally 42 and 38 dB, respectively, across the band suggesting, ideally, an 80-dB two-stage distortion correction capability,

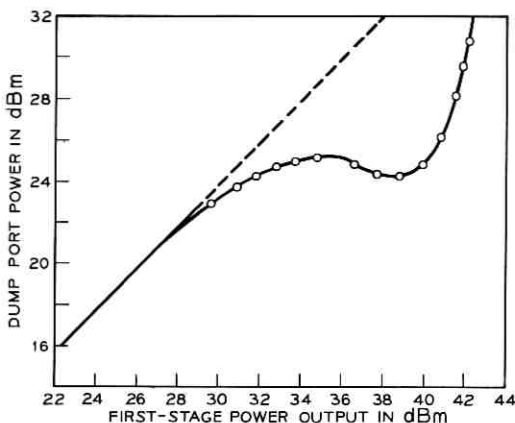


Fig. 16—First-stage dump port power.

disregarding losses added by the two stages. As measured, the error sensor null of the first stage exceeded 35 dB, which was ample to avoid observable distortion in the 461A TWT subsidiary amplifier. While the error sensor null of the second stage was 37 dB it proved only marginally adequate in avoiding saturation onset in the second-stage subsidiary amplifier. Estimation suggests, nevertheless, that greater than 50 dB distortion reduction was achieved with both correction stages operating.

The intermodulation tests were made with three tones, each driving the first-stage-corrected traveling-wave tube amplifier to a 22-dBm output. Taking actual losses into account, this corresponds to a 25-dBm/tone output of the uncorrected TWT. With the addition of the second stage, this output level was reduced by the additional loss to about 19 dBm/tone. Two of the tones were fixed at 4.080 and 4.100 GHz, respectively, while the third was adjusted to discrete positions across the 20-MHz band. To provide improved dynamic range of the intermodulation equipment a coherent main tone cancellation scheme was employed. The three input tones were sampled, individually processed, and reintroduced following the amplifier in a fashion to interfere destructively with the tones transmitted by the amplifier.

The intermodulation test set apparatus is depicted in Fig. 17. For simplicity of display while moving the variable tone signal a delay line was introduced in tandem with the combined cancellation signals to maintain a phase-tracked interference with the test amplifier. A minimum interference of 35 dB to the signal tones was obtained across the

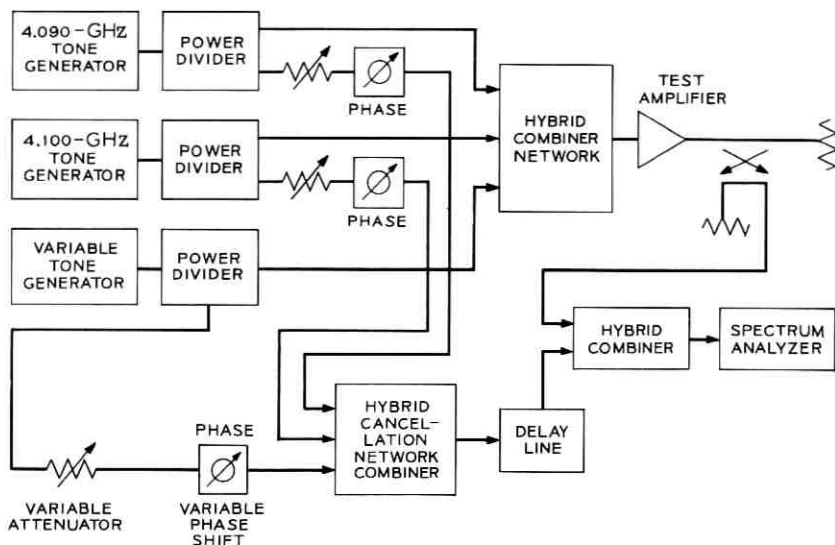


Fig. 17—Intermodulation test set.

4.080- to 4.100-GHz band with no observable interaction to the modulation tones.

Figure 18a shows the amplifier at what would normally be the second-stage output, but with both first and second correction stages disabled. The adjustable tone is set at 4.092 GHz and intermodulation products are observed ranging up to about  $-9$  dBm. Considering the 6-dB loss sustained from the output of the main line TWT to the second-stage output, this corresponds to an intermodulation production of  $-3$  dBm. This quantity is excellently consistent, at 25 dBm/tone excitation, with the  $-78$ -dB M3 measure given the 461A.

As we shall find in the tabulation to follow, one may identify products down to ninth order. The dominant term with which we are mostly concerned here is the third-order  $A + B - C$  product, given as the image with respect to band center of the adjustable tone. This product, shown at 4.088 GHz, has the  $-9$ -dBm value alluded to earlier. Visible in the figure are pilot tones at 4.070 and 4.110 GHz, respectively.

Figure 18b shows the effect of a single correction stage. The dominant third-order tone is reduced well beyond 40 dB, and all others in-band are rendered virtually invisible. We may observe that the 4.070-GHz pilot tone which lies well below band is reduced by 25 dB, showing that error degeneration is still somewhat effective at that frequency. The 4.110

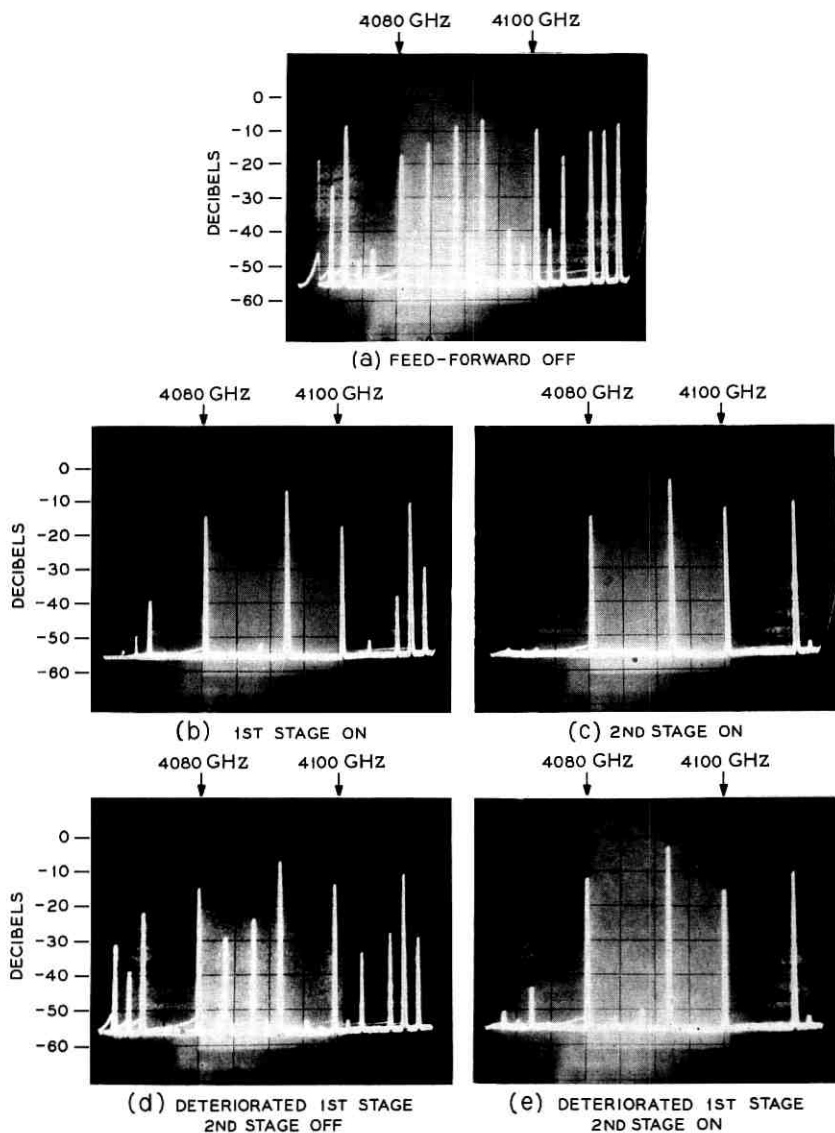


Fig. 18—Spectograms of modulation products.

tone, unlike that at 4.070, is not introduced in the fashion of simulating noise, but rather it enters the system as a spurious signal. It will be observed that it, like the signal tones, is unaffected by feed-forward correction.

Figure 18c, showing application of the second stage, reduces all intermodulation products into the base line. We observe that it wipes out the residue of the 4.070-GHz pilot, but it leaves some vestigial bumps at 4.088 and 4.085 which were visible with first-stage correction. The fact that the pilot was removed, and the bumps not, suggests that the second stage operates to remove previously generated products, but that it has generated new ones in the process. This corresponds with our concern over the weak upconverter stage.

To confirm this mode of second-stage operation, Fig. 18d shows the effect of fully disabling the second stage, but of only partially detuning the first-stage error injector loop. It resembles Fig. 18a but the intermodulation products are down by about 15 dB. Leaving the detuned first stage untouched, the second stage is reenergized, producing the result of Fig. 18e. We find cancellation exceeding 30 dB but, again, the telltale bumps suggest a residual level corresponding to newly generated intermodulation products.

To give a more quantitative measure to the results shown on the various spectrograms, these same results were tabulated point by point in Table I on a Western Electric 39A measuring set. The vestigial bumps with second-stage correction, barely observable visually, cannot be found at all in the measuring set. Therefore, no second-stage observations appear. This level of unresolvability within the 39A corresponded to about a  $-55$ -dBm amplifier output level and, consequently, accounts for the general vacancy of entries with first-stage correction as well.

The tabulation corresponds to output differences of 3 dB between the uncorrected and corrected stages, and mirrors losses, for the most part, attributable to experimental implementation. A realistic difference in practice would be close to 1 dB, losing 5 dB in distortion reduction for third-order products over that obtained by directly differencing the last two columns of Table I. Extrapolating to a system in practice, the results with the adjustable tone at 4.092 GHz, for example, would show a first-stage correction of 37.7 dB, an M3 value of  $-116.2$  dB, corresponding to a 28.8-dBm average power, and the peaking of a single 33.6-dBm tone.

From the first stage data it is observed that a reduction of greater than 40 dB occurs throughout with the first stage operating as opposed to its being disabled but remaining in position. This result is consistent

TABLE I—INTERMODULATION RESULTS

Adj. Freq.	Modulation Product Order	Produce Freq.	Uncorrected <sup>†</sup> (25 dBm Out)	1st Stage <sup>†</sup> (22 dBm Out)
4098	3	4082	-4.5 dBm	-47.5 dBm
		4096	-9.2	—
		4084	-34.5	—
	5	4094	-41.3	—
		4086	-41.5	—
		4092	-37.3	—
	7	4088	-34.5	—
		4090	-34.5	—
		4084	-3.5	-46
4096	3	4092	-8.2	—
		4088	-44.2	—
		4084	-9	—
4092	5	4088	-3.5	-46.2
		4096	-34.2	—
		4089	-5.1	-50.5
4089	3	4098	-14.4	—
		4082	—	—
	5	4087	-39.8	—
		4092	-12.9	—
		4094	-3.6	-50.5
4086	5	4088	-38.0	—
		4098	-44.5	—
	3	4086	-14.3	—
		4097	-5.4	-52
4083	5	4089	-45	—
		4094	-39	—

<sup>†</sup> The absence of datum indicates its unresolvability on the measuring equipment used and represents power < -54 dBm.

with the 42-dB minimum interferometer null of the error injector loop portion of the first stage. This correlation to measurement, although it could not be made with the second stage as well because of inadequate power capacity, is gratifying. First, it confirms the fundamental operations principles of feed-forward. Secondly, it demonstrates the sufficiency of a frequency swept interferometer null measurement and this is important in providing an intrinsically simple field procedure for setting up and maintaining a feed-forward microwave amplifier system.

#### V. COMMENTS AND SUMMARY

With first-stage correction, and at a 22-dBm power level per tone, with a three-tone excitation, all intermodulation products were reduced by the order of 40 dB or more over those of an uncorrected 461A traveling-wave tube amplifier. With second stage correction these products were unmeasurable with instruments available to us.

The use of feed-forward techniques in microwave applications suggests the need to review the precise nature and meaning of distortion measure in view of precipitous distortion increase with subsidiary amplifier saturation. Those specifications set for the present experiment might well have been met with a smaller first-stage subsidiary amplifier but recent, more rigid, specifications suggest ultimate use of the full power capacity of the 461A tube used.

Nowhere in the scope of the experiment was an attempt made to evaluate the economics of a higher performance single-stage versus an equally performing multistage correction system, with a lower quality of performance per stage. Nevertheless, the distortion reduction presently achievable with a single 461A TWT subsidiary amplifier correction stage is not too far from the objective of 47 dB sought. We feel this figure to be realistic with improved equalization, providing that the power supply is also improved in terms of the hum content that presently limits performance.

It is in the nature of the electronic art that a new device, initially viewed as a substitution for other devices which it overlaps, finds a niche quite apart from the one contemplated. The transistor, originally a substitute for the vacuum tube, proved amenable to a radical revamping of use, and shifted the very arts which employed it. Within this context, the new existence of a highly linear microwave amplifier suggests review by communication analysts as to the role of analog devices in this portion of the spectrum.

## VI. ACKNOWLEDGMENTS

It is a pleasure to acknowledge a laboratory-wide support in this traveling-wave experiment, and I regret any slight to many not mentioned. Most notably, major responsibilities for system integration and operation rested with H. R. Beurrier and C. H. Bricker. Mr. Beurrier was responsible for first-stage operation, and designed and constructed the control circuitry. Mr. Bricker built both the second stage and the intermodulation measurements equipment.

A. J. Giger's initial studies established the levels of device linearity necessary in single sideband transmission. His comments were much valued during the course of the experiment.

Finally, I am indebted to W. E. Danielson for stimulating this project and to F. H. Blecher and E. D. Reed for their kind encouragement and support.

## APPENDIX

*Scattering Matrix Simplifications*

The noise formulation in Section 2.2 is considerably simplified by the application of energy conservation and time reversibility relationships implicit in the couplers used. As stated in equations (4) and (5), and as a result of these relationships, a coupler scattering matrix,

$$S = \begin{bmatrix} 0 & 0 & S_{13} & S_{14} \\ 0 & 0 & S_{23} & S_{24} \\ S_{13} & S_{23} & 0 & 0 \\ S_{14} & S_{24} & 0 & 0 \end{bmatrix}, \quad (12)$$

must satisfy the unitary requirement,

$$\begin{bmatrix} 0 & 0 & S_{13}^* & S_{14}^* \\ 0 & 0 & S_{23}^* & S_{24}^* \\ S_{13}^* & S_{23}^* & 0 & 0 \\ S_{14}^* & S_{24}^* & 0 & 0 \end{bmatrix} \begin{bmatrix} 0 & 0 & S_{13} & S_{14} \\ 0 & 0 & S_{23} & S_{24} \\ S_{13} & S_{23} & 0 & 0 \\ S_{14} & S_{24} & 0 & 0 \end{bmatrix} = \begin{bmatrix} 1 & 0 & 0 & 0 \\ 0 & 1 & 0 & 0 \\ 0 & 0 & 1 & 0 \\ 0 & 0 & 0 & 1 \end{bmatrix}. \quad (13)$$

A series of relationships yielded by (13):

- (i)  $|S_{13}|^2 + |S_{14}|^2 = 1,$
- (ii)  $|S_{13}|^2 + |S_{23}|^2 = 1,$
- (iii)  $|S_{23}|^2 + |S_{24}|^2 = 1.$

From *i* and *ii*,

$$(iv) \quad |S_{14}|^2 = |S_{23}|^2,$$

and, using *iii*,

$$(v) \quad |S_{13}|^2 = |S_{24}|^2.$$

From the zero elements of the unit matrix we find:

- (vi)  $S_{13}S_{14}^* + S_{23}S_{24}^* = 0,$
- (vii)  $S_{13}S_{23}^* + S_{14}S_{24}^* = 0.$

We apply these relationships first to find a simplification for  $\mathcal{G}$ . From (1),

$$G_1 = -\frac{S_{24}^{(1)} S_{24}^{(2)}}{S_{23}^{(1)} S_{14}^{(2)}}. \quad (14)$$

Using this result in (3) we find

$$\mathcal{G} = \frac{S_{24}^{(1)} S_{13}^{(3)}}{S_{14}^{(2)}} (-S_{13}^{(2)} S_{24}^{(2)} + S_{14}^{(2)} S_{23}^{(2)}). \quad (15)$$

Recognizing from *vi* that

$$S_{13}^{(2)} = -\frac{S_{23}^{(2)} S_{24}^{(2)*}}{S_{14}^{(2)*}}, \quad (16)$$

yields

$$\mathcal{G} = \frac{S_{24}^{(1)} S_{13}^{(3)} S_{23}^{(2)}}{|S_{14}^{(2)}|^2} (|S_{24}^{(2)}|^2 + |S_{14}^{(2)}|^2). \quad (17)$$

Since the portion in parenthesis is unity by virtue of the unitary relations, and using the equality of *iv*, we obtain the result given in (6); namely,

$$\mathcal{G} = \frac{S_{24}^{(1)} S_{13}^{(3)}}{S_{23}^{(2)*}}. \quad (18)$$

Simplification of the noise formulation follows easily along the same lines. Equation (7) yields

$$\epsilon = U_o [S_{14}^{(1)} S_{24}^{(2)} G_2 S_{23}^{(3)} + S_{14}^{(1)} S_{23}^{(2)} S_{13}^{(3)}] + U_2 G_2 S_{23}^{(3)}. \quad (19)$$

From (2),

$$G_2 = -\frac{S_{13}^{(2)} S_{13}^{(3)}}{S_{14}^{(2)} S_{23}^{(3)}}. \quad (20)$$

Combining, we find

$$\epsilon = \frac{S_{13}^{(2)} S_{13}^{(3)}}{S_{14}^{(2)}} \left[ U_o \left( -S_{24}^{(2)} + \frac{S_{14}^{(2)} S_{23}^{(2)}}{S_{13}^{(2)}} \right) S_{14}^{(1)} - U_2 \right]. \quad (21)$$

From *vi*,

$$\frac{S_{23}^{(2)}}{S_{13}^{(2)}} = -\frac{S_{14}^{(2)*}}{S_{24}^{(2)*}},$$

so that

$$\epsilon = -\frac{S_{13}^{(2)} S_{13}^{(3)}}{S_{14}^{(2)} S_{24}^{(2)*}} [U_o S_{14}^{(1)} + U_2 S_{24}^{(2)*}]. \quad (22)$$

Since, by *vii*,  $S_{14}^{(2)} S_{24}^{(2)*} = -S_{13}^{(2)} S_{23}^{(2)*}$ , we find

$$\epsilon = \frac{S_{13}^{(3)}}{S_{23}^{(2)*}} | U_0 S_{14}^{(1)} + U_2 S_{24}^{(2)*} |, \quad (23)$$

in agreement with (8).

The noise, normalized by the gain to yield an amplifier noise temperature, is found from combining the results of (18) and (23). We have

$$\frac{\epsilon}{G} = \frac{U_0 S_{14}^{(1)} + U_2 S_{24}^{(2)*}}{S_{24}^{(1)}}. \quad (24)$$

The autocorrelation of the above yields

$$\frac{|\overline{\epsilon^2}|}{|G^2|} = \frac{|S_{14}^{(1)}|^2 + T_2 |S_{24}^{(2)}|^2}{|S_{24}^{(1)}|^2}, \quad (25)$$

which agrees with (9) to within the recognition that  $|S_{24}|^2 = |S_{13}|^2$ .

#### REFERENCES

1. Black, H. S., U. S. Patent 1, 686, 792, issued October 9, 1929.
2. Bode, H. W., Proceedings of the Symposium on "Active Networks and Feedback Systems," Vol. X, Polytech Press of the Polytechnic Institute of Brooklyn, April 1960, pp. 1-17.
3. McMillan, B., U. S. Patent 2, 748, 201, issued May 29, 1956.
4. Seidel, H., Beurrier, H. R., and Friedman, A. N., "Error-Controlled High Power Linear Amplifiers at VHF," B.S.T.J., 47, No. 5 (May-June 1968), pp. 651-722.
5. Seidel, H., "A Feedforward Experiment Applied to an L-4 Carrier System Amplifier," IEEE Trans. Commun. Tech., COM-19, No. 3 (June 1971), pp. 320-325.
6. Giger, A. J., private communication.
7. Hensel, W. G., and Sheets, L. L., individual private communications.
8. Members of Technical Staff, Bell Telephone Laboratories, *Transmission Systems for Communications*, Fourth Edition, February 1970, p. 252.
9. Brillouin, L., *Science and Information Theory*, New York: Academic Press, 1956, p. 153.
10. Dicke, R. H., Beringer, R., Kyhl, R. L., and Vane, A. B., Phys. Rev., 70, 1946, p. 340.

# An Experimental MM-Wave Path Length Modulator

By W. J. CLEMETSON, N. D. KENYON, K. KUROKAWA,  
B. OWEN, and W. O. SCHLOSSER

(Manuscript received June 3, 1971)

*A modulation scheme in which the transmission path length of the mm-wave signal is digitally modulated by means of a PIN diode switch has been proposed for the waveguide transmission system. To demonstrate the feasibility of this proposal, a complete transmitter has been developed in the 50 ~ 60-GHz range, consisting of an IMPATT oscillator, circulator, PIN diode switch, and its driver circuit. The model can handle signals at 300 Mb/s and deliver 100 mW of modulated power at the output. This paper describes the design considerations of each component in detail, together with the experimental results.*

## I. INTRODUCTION

The availability of mm-wave silicon IMPATT diodes<sup>1</sup> with several hundred milliwatts of output power makes practical the construction of reliable all-solid-state mm-wave communication systems. Several candidate schemes have been proposed.<sup>2-9</sup> They can be divided into two broad categories, depending on whether the modulation is achieved within the oscillator circuit or separately.

The varactor tuned oscillator and the direct deviator are examples of achieving the modulation within the oscillator.

A method by which the path length of the mm-wave is modulated by a PIN diode switch is described in this paper and is an example of externally modulating a fixed-frequency oscillator. It represents the best compromise with respect to the required driving power, insertion loss, speed, and power handling capability at mm-wave frequencies. In particular, we have concentrated on two-level Path Length Switched Differentially Coherent Phase Shift Keying, in short, PLS-DCPSK. This paper describes the development of an experimental mm-wave PLS-DCPSK transmitter in the 50 ~ 60-GHz range. The model is

capable of handling signals at a rate of 300 Mb/s and delivers 100 mW of modulated power at the output port.

## II. PLS-DCPSK

The principle of PLS-DCPSK is best illustrated by referring to Fig. 1. The mm-wave power from a fixed oscillator is fed into a PIN diode switch through a circulator. When the switch is closed, the wave is reflected at the diode position, and when it is open, the wave is reflected at the short circuit a quarter-wavelength behind the diode. The phase of the transmitted mm-wave, therefore, changes by 180 degrees whenever the switch changes its state<sup>10,11</sup> corresponding to incoming signal "1" as illustrated in Fig. 2. At the receiver, the RF phases one time interval (3.33 ns for 300-megabaud signals) apart are compared by means of a delay line and hybrid circuits. When the phase difference is 180 degrees the detector output becomes "1" and when there is no phase difference, the output becomes "0." Thus, the receiver output becomes a duplicate of the original signal. In addition to the phase switching, the amplitude can be modulated to send, for example, a timing signal, if so desired.

The two principal advantages of this modulation scheme are separation of generation and modulation functions, and digital operation of the modulator. Because of the first feature, the oscillator and modulator can be optimized independently. No compromises are required between conflicting factors in the oscillator design, such as low  $Q$  for modulation sensitivity and high  $Q$  for low noise and frequency stability. The oscillation frequency can be made very stable and the oscillation noise low by using a high  $Q$  stable oscillator circuit. Should a more efficient

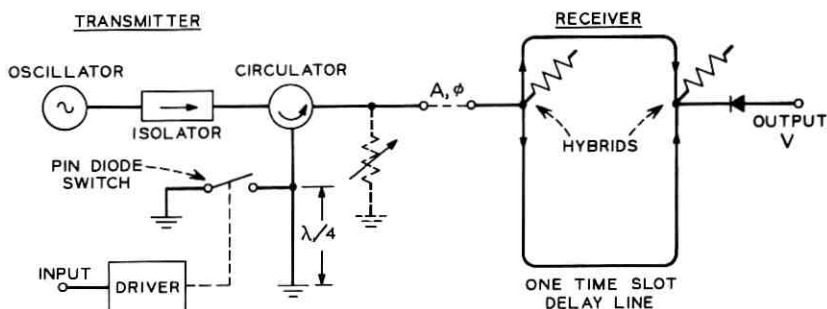


Fig. 1—A schematic diagram of PLS-DCPSK transmitter and receiver.

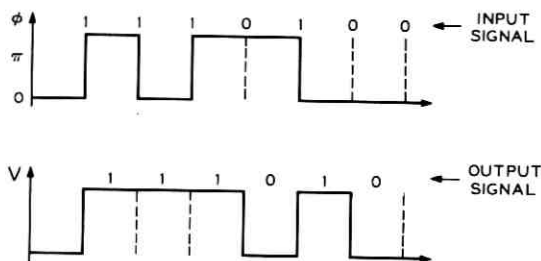


Fig. 2—The RF phase  $\phi$  and the detector output  $V$  in relation with the input and output signals.

oscillator (with the same output power) be developed in the future, the original oscillator can be replaced by the new one without redesigning the modulator, since it is independent of the oscillator tuning characteristics. Because of the digital operation, the characteristics of the modulator are not sensitive to small changes in the environmental temperature or in the bias voltage. The modulator has additional flexibility: by adding a 90-degree phase switch, we can extend the two-level operation of PLS-DCPSK to four-level operation, increasing the information rate by a factor of two.

On the other hand, the path length modulator system needs two semiconductor devices: an IMPATT diode and a PIN diode, plus a circulator or a 3-dB coupler. In addition, we have to accept an insertion loss due to the modulator, which in the 50 ~ 60-GHz range is of the order of 1 dB.

In the following sections, we discuss, in turn, the oscillator, the circulator, the PIN diode, and the driver circuit.

### III. THE OSCILLATOR

It is possible to build mm-wave IMPATT oscillators with sufficient output power for mm-wave communication systems by providing several tuning elements and adjusting them by trial and error. However, frequency jumps and sudden increases of noise being common during the circuit and bias adjustment, it is difficult to predict the performance of such oscillators or to establish a systematic tuning procedure. These complications occur when the impedance locus  $Z(\omega)$  intersects the device line  $\bar{Z}(A)$  more than once, indicating more than one possible mode of oscillation. [ $Z(\omega)$  is the circuit impedance presented to the device and  $\bar{Z}(A)$  is the negative of the device impedance as a function of

the RF current amplitude  $A$ .] For a stable oscillator circuit with predictable performance,<sup>12</sup> the impedance locus must intersect the device line once and only once over the active frequency range of the device. Attempts to realize such an oscillator circuit with lossless elements have not succeeded, and hence the lossless restriction is relaxed.

We will next describe the evolution of an equivalent circuit which gives a suitable impedance locus.

### 3.1 Equivalent Circuit and Hardware

In the design of oscillator circuits, a dc bias has to be applied to the diode. The bias connection inevitably forms a part of the RF circuit, so it is desirable to select a geometric form whose microwave transmission properties are well known. This leads one to choose a uniform two-conductor transmission line shown in Fig. 3a. In this form, the open-circuit to the right will cause an undesired frequency dependent reflection; the only way to prevent this is to add a matched termination shown in Fig. 3b as  $Z_0$ . This approach is legitimate only if the useful load, which may be thought of as coupled in some way to the transmission line, presents a series resistance much higher than the characteristic impedance of the transmission line. This situation is depicted in Fig. 3c. A small fraction of the output power may be wasted in the bias line termination, but in return we obtain a truly single-tuned stable circuit free from multiple-intersections between the impedance locus and the device line.<sup>13-15</sup> A similar approach was first used by E. T. Harkless.<sup>16</sup>

Since we require operation only at a single frequency and need a high

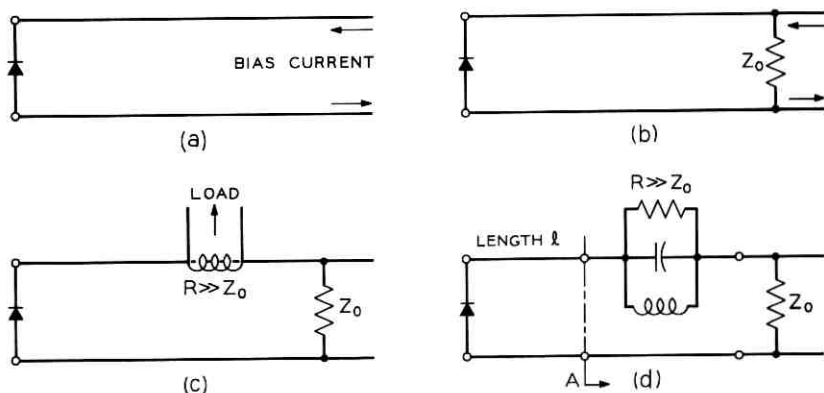


Fig. 3—Step-by-step construction of the equivalent circuit.

resistance at the operation frequency, the natural approach is to make the load in Fig. 3c look like a parallel resonant circuit as shown in Fig. 3d. The combined impedance, load and termination, has an impedance locus like the solid circle on the Smith chart of Fig. 4; at resonance the resistance of the load circuit is much greater than  $Z_0$  while away from resonance only the termination is effective. On this chart, we have also shown the device line and the optimum operating point. In order to reach this point at resonance, we first change the diameter of the resonance circle, in this case to the dotted one at the right. Secondly, we interpose a length  $l$  of the uniform transmission line, displacing the circle by an angle  $\theta = 4\pi l/\lambda$  ( $\lambda =$  wavelength) clockwise about the center of the chart to the required point. The clockwise rotation is easy to understand. To explain the change of circle diameter, let us expand the parallel resonant load in a more realistic form. Referring to Fig. 5, it takes a form of a high  $Q$  microwave cavity, coupled by some coupling  $K_2$  into the main waveguide, and itself coupled at  $K_1$  onto the transmission line. The external  $Q$  of the oscillator will be almost exactly the loaded  $Q$  of this cavity. The loaded  $Q$  must be much smaller than the unloaded  $Q$ , in order to minimize the power wasted in the cavity and to maximize the circuit efficiency. The external loading is adjusted by  $K_2$ , leaving  $K_1$  to control the diameter of the impedance circle. As  $K_1$  is tightened, the diameter of the circle increases; thus  $K_1$  is in the nature of a power optimizing element. However, it may happen that  $K_1$  has some natural maximum and we may still not have enlarged the circle diameter enough to reach the optimum operating point. Then, it is necessary to move the optimum operating point towards the center of the chart, which can be accom-

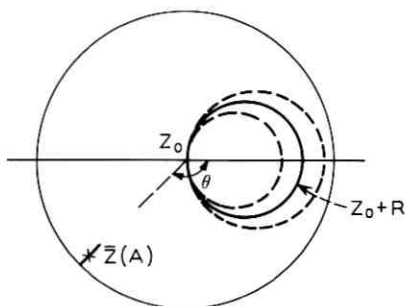


Fig. 4—Impedance locus looking from reference plane  $A$  in Fig. 3d and device line. The optimum operating point is indicated by  $x$ .

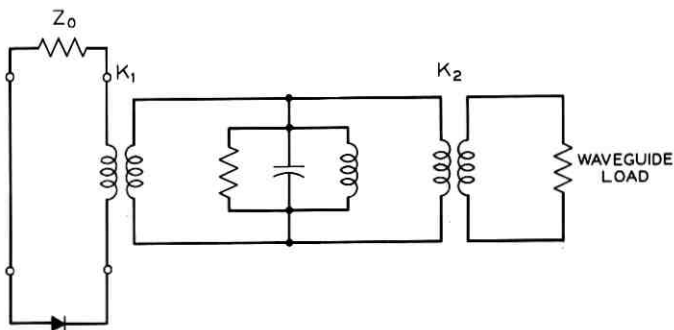


Fig. 5—Oscillator equivalent circuit.

plished by inserting a transformer close to the diode in such a way as to improve its effective resistance level by a factor of two or three. It was necessary to do this for the mm-wave diodes.

Figure 6 shows a physical realization of the equivalent circuit. The transmission line is shown as a terminated coaxial line of about  $50 \Omega$  impedance with a place for the IMPATT diode; it passes through a half-wavelength rectangular waveguide cavity which is coupled by an iris to the output waveguide,  $K_2$ . The coupling  $K_1$  is adjustable over a limited range by a movable short-circuit placed immediately behind the center conductor. Figure 7 is the actual circuit used at 57 GHz. It has some features not shown in Fig. 6: the transformer previously mentioned is inserted immediately above the diode, and the length  $l$  of transmission line is adjusted by means of spacers, so shaped that mechanical pressure gives good electrical contact to avoid losses. The quartz rod serves to compensate the cavity resonance for changes in temperature and, independently, as a fine frequency control.

The rectangular waveguide cavity resonates in the  $TE_{101}$  mode. The cavity will also resonate in higher modes such as  $TE_{201}$ ,  $TE_{102}$ , etc. However, at these resonant frequencies, the impedance locus  $Z(\omega)$  will be located so far from the device line that no multiple intersections will occur. This is because the rotation  $\theta = 4\pi l/\lambda$  of the resonant impedance is now too large (small values of  $\lambda$ ) and overshoots the position of the device line at the corresponding frequencies. Also, the coupling coefficients  $K_1$  and  $K_2$  for most higher modes do not lead to intersection of the circuit impedance with the device line. At the higher resonant frequencies the diode will cease to show a negative resistance.

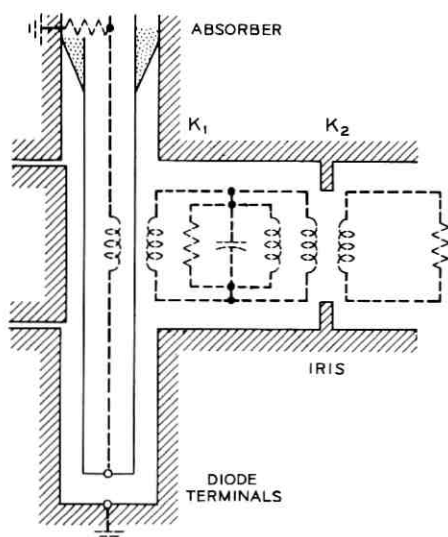


Fig. 6—Hardware around the equivalent circuit of Fig. 5.

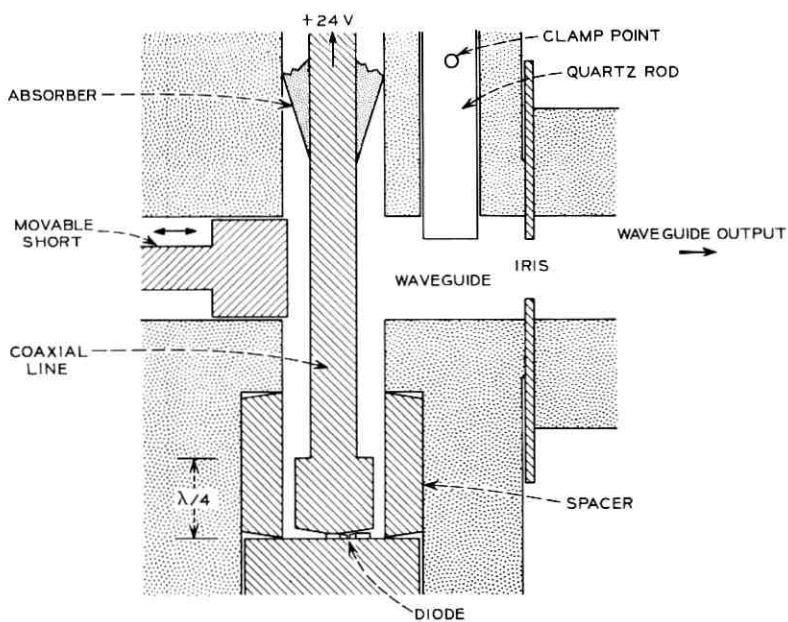


Fig. 7—Oscillator structure.

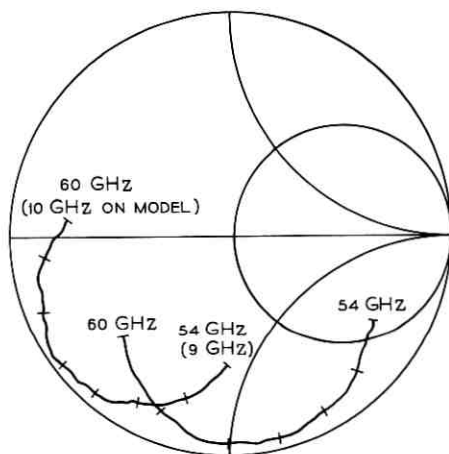


Fig. 8—Impedance seen at diode position on X-band model for two values of the transmission line length.

### 3.2 Experimental Results

In order to check that the mechanical configuration shown in Fig. 6 gives the desired impedance locus, a scale model was built in X-band and a network analyzer was used to measure the impedance seen from the diode terminals. The examples in Fig. 8 show that we obtained the smooth single-tuned behavior desired. Figure 9 shows how the mm-wave oscillator output power and frequency varied with the position of the sliding short; there is a power optimum at about 0.3 mm, and the frequency actually rises as the short is withdrawn. The more

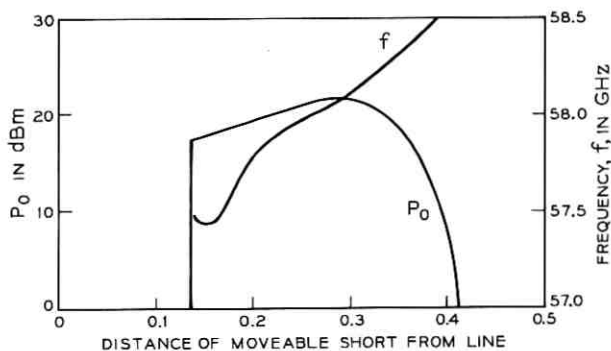


Fig. 9—Output power and frequency vs short position.

extensive impedance measurements on the X-band model show that such behavior is to be expected.

Results from a variety of mm-wave diodes are listed in Table I. The bias current was adjusted to produce 125 ~ 130 mW. The diode temperature was measured by momentarily pulsing down the bias voltage and measuring the breakdown voltage, which is a function of the diode temperature. The efficiencies are somewhat low because the diodes were being operated well below the current density needed for maximum efficiency. The external Q's were of the order of 100. Should a higher external Q be desired, further improvement of the unloaded Q of the cavity would be necessary. However, the performance of these oscillators was already quite satisfactory for this application.

#### IV. THE CIRCULATOR

A symmetrical three-port junction circulates when the reflection coefficients of its three characteristic excitations are of the same magnitude and are mutually phase displaced by  $2\pi/3$  radians. These excitations are the eigenvectors of the junction scattering matrix, and the reflection coefficients are the corresponding eigenvalues.<sup>17</sup> One excitation has its components in phase in all three ports. The other two have their components displaced by  $2\pi/3$  radians from port to port, and rotate in opposite directions. The reflection coefficients are determined by the internal modes associated with these excitations and by their interaction with the enclosed ferrite.

In the compact turnstile circulator,<sup>18</sup> dielectric spacers are used to couple the rotating excitations to circularly polarized modes which propagate along the ferrite axis. These modes experience different permeabilities when the ferrite is magnetized, and the phases of their reflection coefficients are essentially determined by the ferrite length

TABLE I—TYPICAL CHARACTERISTICS OF IMPATT OSCILLATOR

Diode No.	Power mW	Efficiency %	Current mA	Temp. °C	$\Delta f/\Delta T$ kHz/°C	Freq. GHz
1	125	3.8	150	175	—	—
2	125	3.7	150	175	—	—
3	125	3.3	165	230	+200	57.4
4	125	4.1	142	210	-100	56.4
5	125	3.9	142	210	—	57.4
6	130	5.3	100	225	-600†	57.4

† Insufficient quartz clamping length.

and applied magnetic field. They are affected only slightly by the ferrite diameter. The in-phase excitation, on the other hand, cannot couple to an axially propagating mode. It sees the ferrite simply as a dielectric resonator, and the phase of its reflection coefficient is largely determined by the ferrite diameter. By adjusting the ferrite length, diameter, and applied magnetic field, the three reflection coefficients may be phase displaced from one another by  $2\pi/3$  radians and circulator operation is achieved.

A cross section of the circulator developed for the path length modulator is shown in Fig. 10. The ferrite was recessed into the metal junction both to provide a secure mount and to assure its symmetrical disposition. An air gap was used to provide the dielectric discontinuity required to couple the rotating excitations to axially propagating modes. The use of air simplified the coupling adjustment in development and avoided any dependence on dielectric properties such as loss and dielectric constant. A quarter-wave transformer was used as an aid in matching into the junction.

The ferrite chosen was a nickel-zinc material with a 5000-gauss saturation magnetization. The ferrite diameter and length were approximately  $3/4$  wavelengths and  $5/4$  wavelengths respectively, as measured in the infinite ferrite medium. The circulator could in principle operate with any odd number of quarter wavelengths for the ferrite length. In this case the rectangular waveguide height dictated the choice of  $5/4$  wavelengths. A biasing field of approximately 600 gauss was required.

The measured characteristics are shown in Fig. 11. Isolation of 20 dB was achieved over a 4-percent bandwidth, and the insertion loss was less than 0.25 dB across this band.

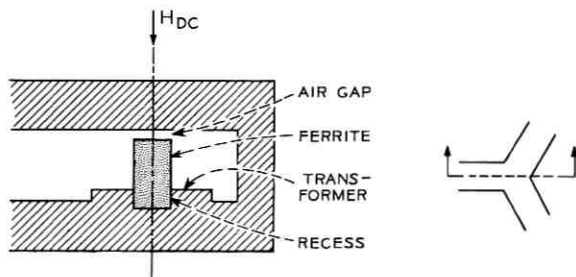


Fig. 10—Circulator cross section.

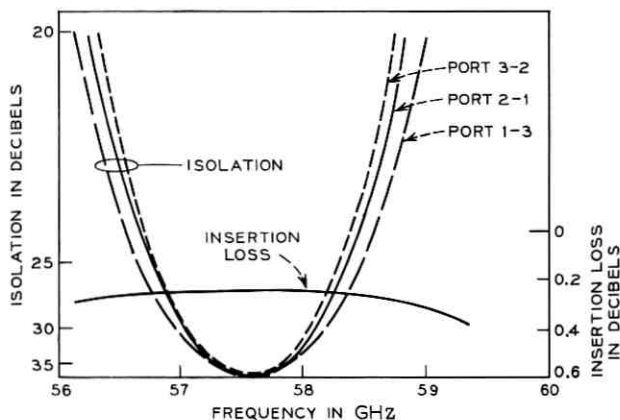


Fig. 11—Circulator characteristics.

## V. THE PIN DIODE

PIN diodes can support RF current substantially greater than the forward bias current. In the reverse bias state, the capacitance per unit area of PIN diodes is relatively small and independent of the bias voltage. This means that the impedance level of the switch circuit can be made relatively high (for a specified power handling capability) and the switch characteristic is approximately independent of the bias voltage. Neither Schottky barrier diodes nor p-n junction diodes have these desirable features.

Schottky barrier diodes will probably provide the fastest switching action among available semiconductor devices. However, when a switching time of the order of a half ns is acceptable, PIN diodes are superior with respect to power handling capability, insertion loss, impedance level, and harmonic content. The use of a transferred-electron diode<sup>19,20</sup> or avalanche diode as a switching element cannot be justified in our case because of the high driving power required; for these devices, high bias current and high voltage must be applied simultaneously.

We now discuss the design of a PIN diode for the mm-wave switch application.<sup>21</sup>

### 5.1 Design

The design of the PIN diode is so intimately related to both the driver and the mm-wave circuit that the three must be jointly designed.

The  $i$  layer thickness of the diode is primarily determined by the available pulse voltage from the driver. A pulse amplitude of the order of 10 V is a reasonable target for any transistorized driver for mm-wave repeater applications. Then the RF peak voltage one can apply to the reverse biased PIN diode without introducing too much loss is also approximately 10 V; so the breakdown voltage must be larger than 20 V to realize the full advantage of the available driver pulse voltage. Taking into account possible field nonuniformity in the  $i$  layer, especially during the switching transient, a breakdown voltage of 40 V was considered to be a good objective. Since the breakdown field is  $2 \times 10^5$  V/cm in silicon, 40 V breakdown voltage requires a  $2 \mu$  thick  $i$  layer.

The cross-sectional area of the diode is determined by the practical impedance level of the mm-wave circuit. In order to get 180-degree phase differences with equal insertion losses in the two switching states, the real and imaginary parts of the mm-wave circuit impedance presented to the diode must each be approximately one-half of the impedance of the  $i$  layer capacitance, assuming that the series resistance stays the same in the two states [see equation (5) in Appendix]. Suppose that we can present approximately  $(50 + j50)\Omega$  to the diode without introducing too much loss, then the desired  $1/\omega C$  is  $100 \Omega$  or  $C$  is approximately 0.026 pF at 60 GHz. With a  $2 \mu\text{m}$  thick  $i$  layer, the diode diameter is calculated to be of the order of  $25 \mu\text{m}$ .

Now, we have to check the power handling capability of the 180-degree phase switch. A simple equivalent circuit shows that, if the RF voltage swing across the  $i$  layer is limited to  $\pm 10$  V as previously assumed, the switch can handle about 125 mW provided that the forward bias state can support sufficient RF current (see Appendix). In the forward bias state the diode should be almost short circuited. The peak RF current under this condition is calculated to be approximately 100 mA. This value of RF current can be used to determine the forward bias current and is considered next.

Suppose that the carrier (electron) velocity is  $10^6$  cm/s (about one-tenth of the saturation velocity), then the transit time for the  $2 \mu\text{m}$  thick layer becomes 0.2 ns. The required forward bias current is equal to the peak RF current multiplied by the ratio of the electron transit time to lifetime (neglecting the contribution of holes to the RF current). If we assume the lifetime to be about 10 ns, the forward bias current is calculated to be 2 mA which is a quite reasonable value for a transistorized driver. However, before fixing the bias current, it is necessary to check the RF series resistance of the  $i$  layer. If the electron mobility in the  $i$  layer is conservatively assumed to be 1000

$\text{cm}^2/\text{V}\cdot\text{s}$ ,<sup>†</sup> the RF field corresponding to a velocity of  $10^6$  cm/s is 1000 V/cm; thus, the RF voltage across the  $i$  layer is 0.2 V, and the RF resistance of the  $i$  layer under the forward bias condition is  $2 \Omega$ , which is rather high. To reduce the series resistance, the bias current has to be increased. In fact, bias current up to 10 mA is used depending on the wafer. The corresponding RF series resistance is about  $0.4 \Omega$ .

Finally, we have to check the switching times. The forward switching time is limited by the  $i$  layer thickness divided by the saturation velocity. This is about 20 ps. After the carriers reach the other sides of the  $i$  layer, it takes a relatively long time (of the order of lifetime) before steady state is reached. However, during this period the RF impedance does not change appreciably and for all practical purposes the forward switching time of the PIN diode is negligible compared to the time constant of transistorized drivers. The reverse switching time is determined by how quickly the charge stored in the  $i$  layer can be removed. Since the stored charge is given by the forward bias current multiplied by the lifetime of the carriers, the reverse switching time is given by the product of the lifetime and ratio of the forward bias current to the driving current.<sup>22</sup> If we assume 10 V pulse height and  $20 \Omega$  output impedance for the driver, the initial driving current becomes 500 mA, so that a reverse switching time of the order of a half nanosecond should be achievable.

In the above calculation, it is assumed that the diode works as a PIN diode rather than a p-n junction diode. The validity of this assumption may be questioned because of the extremely thin  $i$  layer. Fortunately, the forward dc characteristic, the backward capacitance characteristic, and the RF behavior all indicate that most of the diodes are working as PIN diodes in the bias range mentioned above.

It is assumed that the RF current distribution is uniform over the entire cross section. Since the resistivity to give  $0.4 \Omega$  RF series resistance with the given dimensions is calculated to be  $0.01 \Omega\cdot\text{cm}$  and the corresponding skin depth approximately  $20 \mu\text{m}$ , the uniform current assumption seems to be appropriate.

Finally, the above calculation is based on an assumed lifetime of 10 ns. If the lifetime is longer, the forward bias current should be decreased to get similar switching characteristics. If it is shorter, the bias current should be increased. In fact, our experiments indicate that the lifetime varies over a wide range from one wafer to another

---

<sup>†</sup> No particular significance should be attached to this value used for the rough estimate of the RF resistance.

and the bias current is best determined experimentally after diodes are fabricated.

### 5.2 Fabrication

In the preceding discussion of PIN diode design, we have neglected the detrimental effects of contact resistance, substrate resistance, and resistance in doping tails. The substrate resistance is kept low by minimizing its thickness, and the contact resistance by optimizing metallization and bonding techniques. The doping tails occur in practice at both ends of the  $i$  layer, where ideally we would prefer abrupt transitions to the  $p$  and  $n$  regions. In the reverse biased state, these doping tails are not completely depleted and present a relatively high resistance in series with the  $i$  layer capacitance. To reduce this effect, the fabrication of the diode should be such that the doping tails are short compared to the total thickness of the  $i$  layer which is  $2\ \mu\text{m}$  in our case.

The actual fabrication of diodes starts with the epitaxial growth of the  $2\ \mu\text{m}$  thick  $i$  layer on an arsenic-doped silicon substrate with resistivity about  $0.001\ \Omega\text{-cm}$ . The transport reaction responsible for the epitaxial growth is hydrogen reduction of  $\text{SiCl}_4$ . Special care must be taken to use a high-resistivity silicon susceptor to achieve a relatively high resistivity of the order of  $10\ \Omega\text{-cm}$  in the  $i$  layer. The substrate is kept at  $1170^\circ\text{C}$ . The typical doping tail obtained is  $0.4 \sim 0.6\ \mu\text{m}$  long, which seems to be acceptable for switches at least in the  $50 \sim 60\text{-GHz}$  range.

Boron is then diffused to a depth of  $0.25\ \mu\text{m}$  by placing the slice in a furnace at  $875^\circ\text{C}$  for 60 minutes. The relatively low temperature and short time are used both to prevent further out-diffusion from the highly doped substrate into the  $i$  layer and to make the doping profile sharp on the  $p$  side.

The substrate is then lapped to a thickness of approximately  $10\ \mu\text{m}$ . The stresses developed by lapping are removed by a light etch. The slice must then be thoroughly cleaned before metallization. Extreme care must be exercised in this step; otherwise, good metal adherence will not be achieved in the subsequent process. After cleaning,  $200\ \text{\AA}$  of titanium and  $1000\ \text{\AA}$  of gold are evaporated on both sides of the slice. The gold is then plated up to a thickness of  $5\ \mu\text{m}$ . A photoresist pattern of approximately  $70\text{-}\mu\text{m}$  diameter dots is applied and the slice is etched apart into diode chips.

Each diode is then thermocompression bonded onto a burnished,

gold-plated copper stud 3.2 mm in diameter, using a pressure of 700 Kg/cm<sup>2</sup> at about 330°C. These parameters have been carefully optimized by experiment. Two quartz standoffs, metallized on the top and bottom surfaces, are also bonded to the stud as close as possible to the diode. These standoffs are connected to the diode with a short thin gold ribbon. The diode is then etched to the final diameter and baked in a nitrogen atmosphere to dry it thoroughly. This completes the diode fabrication. Figure 12 shows an electron microscope picture of a finished diode. The silicon has been etched back to an appropriate diameter and appears as the black column at the center. The discs at both ends of the column are thin gold dots. To distinguish the top and bottom of the diode, the bottom disc is made squarish. The gold ribbon is bonded on the upper circular disc.

### 5.3 *The Diode Mount*

As we mentioned earlier, the 180-degree phase shift is obtained when the waveguide impedance, transformed to a value determined by the diode impedance, is presented to the diode. Since the external circuit

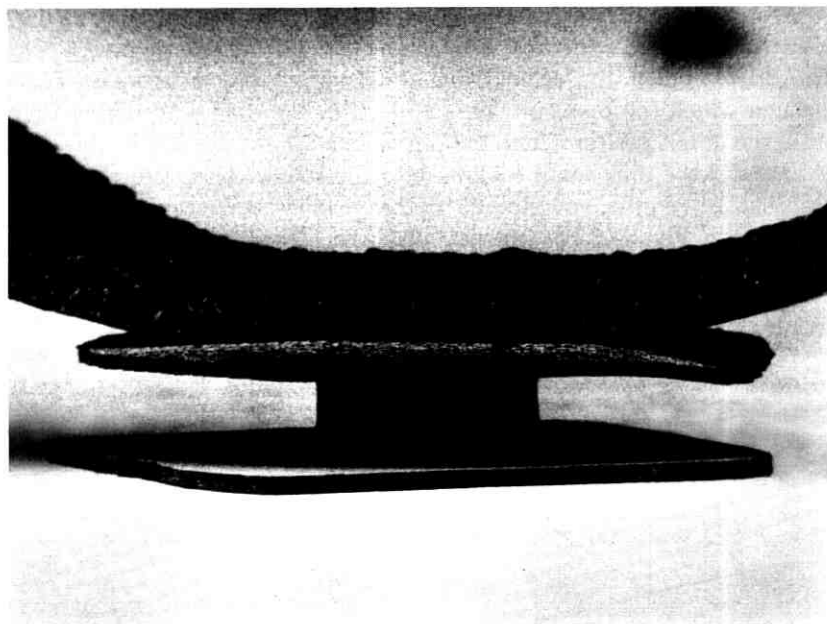


Fig. 12—Electron microscope picture of a PIN diode.

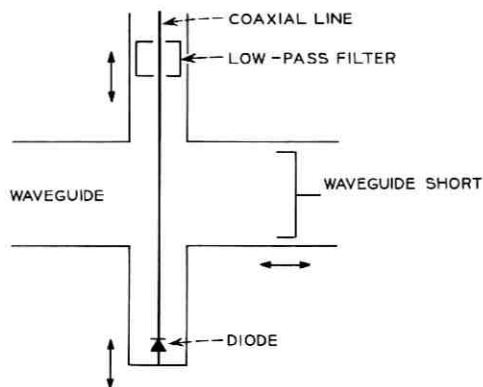


Fig. 13—Schematic diagram of the diode mount.

is connected to the diode at the top of the quartz standoffs and it is not obvious what kind of transformation is performed by that part of the circuit (consisting of the gold ribbon and the standoffs), the diode mount is designed in such a way as to permit all possible impedance transformations. The diode is mounted at one end of a coaxial line cross coupled to a short-circuited waveguide as illustrated in Fig. 13. The other end of the coaxial line is terminated by a low-pass filter through which the bias voltage is applied to the diode. Assuming that both the filter position and the waveguide short are adjustable, let us consider the impedance looking into the coaxial line from the diode position. An equivalent circuit of the coaxial-to-waveguide junction is shown in Fig. 14. The coaxial line is in series with the waveguide

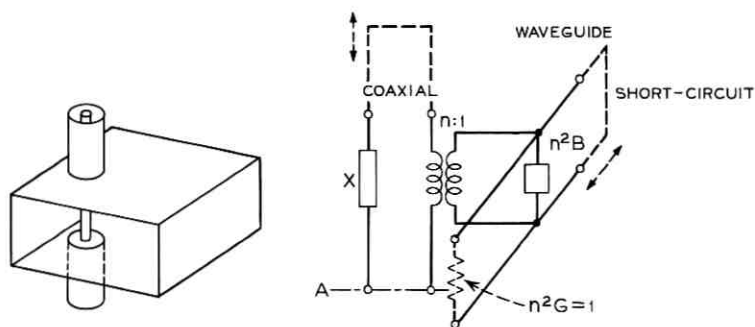


Fig. 14—Equivalent circuit of coaxial-to-waveguide symmetrical junctions.

which is in turn a parallel connection of the characteristic admittance  $Y_0 = G$  and some susceptance due to  $B$  and the short-circuited waveguide. From this equivalent circuit, the possible range of impedance which is realizable at reference plane  $A$  by adjusting the waveguide short and the coaxial filter position is given by the shaded area in the Smith chart of Fig. 15. If we avoid the coaxial position too close to the waveguide sidewall,  $G$  becomes less than one. Thus, any impedance on the Smith chart becomes realizable at the diode position (which is also adjustable along the coaxial line).

A cross section of the actual diode mount is shown in Fig. 16. The tuning spacers are replaceable and the retaining screws secure good electrical contact. The coaxial line is located about a quarter of the waveguide width off the center in order to reduce  $B$  and  $X$  in Fig. 14 so that the circuit adjustment becomes less critical.

#### 5.4 Diode Characteristics

The same type of diode mount is used for the diode  $\hat{Q}$  measurement. The quality factor  $\hat{Q}$  of switching diodes is defined by<sup>23</sup>

$$\hat{Q} = \frac{|Z_1 - Z_2|}{\sqrt{r_1 r_2}}$$

where  $Z_1$  and  $Z_2$  are the diode impedances under the reverse and forward bias conditions to be used in the switch (+10 mA forward and -10 V

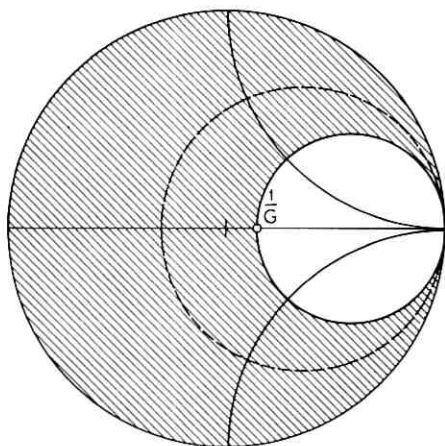


Fig. 15—Possible range of impedance at reference  $A$  in Fig. 14 (solid line  $G < 1$ , dotted line  $G > 1$ ).

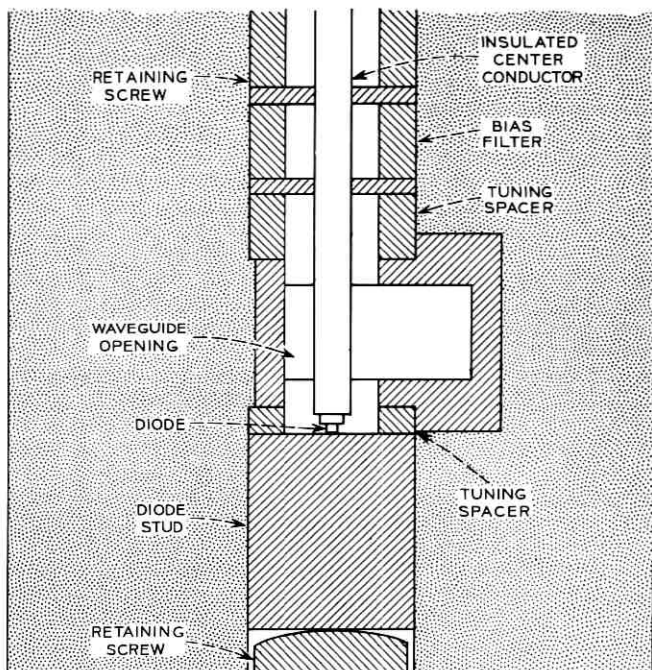


Fig. 16—PIN diode mount for 180-degree phase switch.

reverse in our case) and  $r_1$  and  $r_2$  are the real parts of  $Z_1$  and  $Z_2$ . The best PIN diode yet tested showed  $\hat{Q}$  to be about 40 at 57 GHz, corresponding to an insertion loss of about 0.4 dB for a 180-degree phase shifter. In addition to  $\hat{Q}$ , we usually measure the breakdown voltage at a reverse current of  $0.1 \mu\text{A}$ , the packaged capacitance at  $-10 \text{ V}$ , and the dc incremental resistance at 10 mA and 100 mA of forward bias current. Table II shows typical results. The correlation between  $\hat{Q}$  and the incremental resistance is fair.

## VI. THE DRIVER

A high-speed driver circuit is needed to activate the PIN diode switch. It is also necessary to convert the input binary information into a differential binary signal before driving the PIN diode as is evident from Fig. 2. A driver circuit which incorporates a step-recovery diode pulse generator, a high-speed flip-flop, and a high-speed pulse amplifier was developed. A detailed description of the circuit and of

TABLE II—TYPICAL CHARACTERISTICS OF PIN DIODE

Diode No.	Q	BV (V)	Packaged Capacitance (pF)	Forward Resistance ( $\Omega$ )	
				at 10 mA	at 100 mA
1	35	42	0.087	3.3	0.3
2	25	30	0.098	11.8	1.3
3	20	42	0.104	6.6	1.0
4	30	42	0.086	4.2	0.9
5	40	42	0.100	5.0	0.35

experimental results obtained with the complete path length modulator follows.

### 6.1 Circuit Description

A block diagram of the driver circuit is shown in Fig. 17. The high-speed flip-flop circuit requires that the trigger pulse be narrow ( $\cong 1.2$  ns). The step-recovery diode pulse generator provides this narrow pulse to ensure reliable triggering of the flip-flop. The flip-flop converts the binary information into a differential binary signal. This signal is then amplified to drive the PIN diode switch which shifts the phase of the RF carrier by 180 degrees.

The step-recovery diode pulse generator and the high-speed flip-flop were originally designed by D. Koehler<sup>24</sup> and modified by T. O'Shea and W. E. Ballentine. The technique they used to obtain the high-speed operation of the flip-flop was the utilization of pulse routing which provides a sufficiently high-current trigger source. Also, an emitter follower was used in the collector-to-base feedback loop of the flip-flop to provide a base current spike necessary for fast switching without overloading the collector circuit.

The complete driver schematic is shown in Fig. 18. The binary input is applied to the pulse generator which consists of a charge-storage step-recovery diode  $D_1$  and a Schottky barrier diode  $D_2$ . Diode  $D_2$  provides a forward-current charging path for the step-recovery

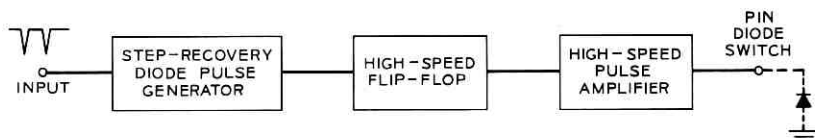


Fig. 17—Block diagram of the driver circuit.

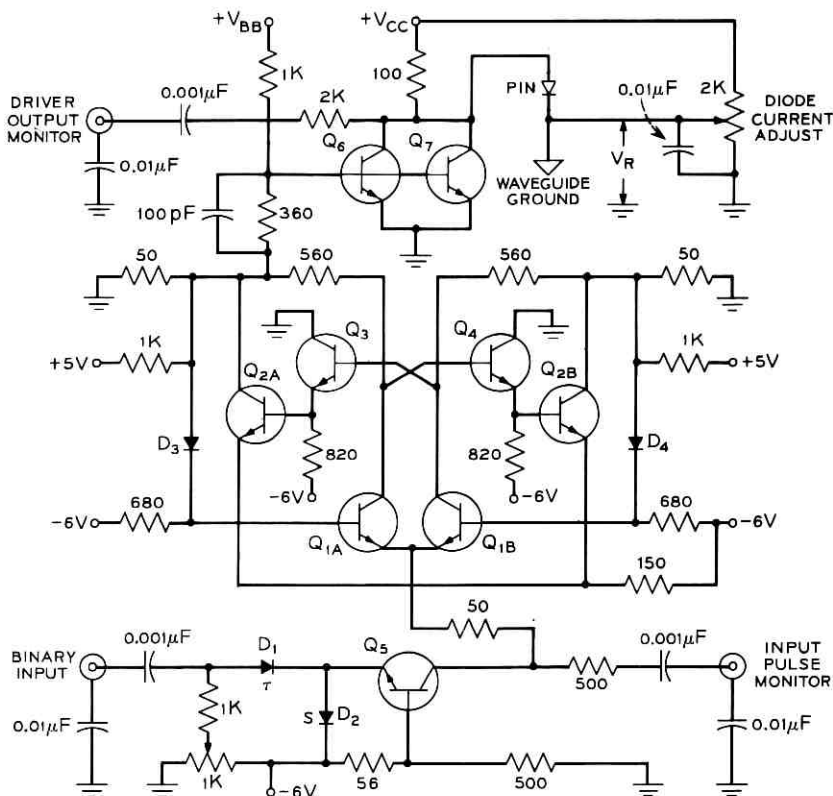


Fig. 18—Schematic diagram of the driver circuit.

diode. A negative input pulse will cut  $D_2$  off and remove the charge stored in  $D_1$  to obtain the step-recovery effect. The common base amplifier ( $Q_5$ ) amplifies the resulting fast pulse. This provides a trigger pulse of about 1.2 ns width and 10 mA amplitude, which drives the steering transistors ( $Q_{1A}$  and  $Q_{1B}$ ). The state of the flip-flop is fed back to the steering transistors by level shifting diodes  $D_3$  and  $D_4$ . The trigger pulse is then routed to the emitter followers ( $Q_3$  or  $Q_4$ ) which provide the base current spike to switch the flip-flop transistors ( $Q_{2A}$  or  $Q_{2B}$ ). The flip-flop output is then applied to the pulse amplifiers ( $Q_6$  and  $Q_7$ ).

In order to drive the PIN diode from forward conduction to reverse bias, the driver circuit is floated by a voltage corresponding to the diode reverse voltage ( $V_R$ ). The output drive transistor operates

basically as a switch. When the flip-flop output is zero, the transistor is forward-biased by  $V_{BB}$  and the reverse voltage  $V_R$  is applied to the PIN diode. When the flip-flop output is  $-1$  V, this provides a negative bias which turns off the drive transistor and the PIN diode is forward-biased. The forward current is determined by the difference between  $V_{CC}$  and  $V_R$ .

The output drive amplifier requires fairly high collector breakdown voltage  $BV_{CE}$  and maximum collector current  $I_{C\max}$  ratings which are difficult parameters to meet for a high-speed switching transistor. However, by paralleling two transistors, an adequate  $I_{C\max}$  rating was obtained. Also, by proper selection, transistors having similar current gain  $\beta$  and sufficient  $BV_{CE}$  rating were obtained for the parallel pair. The average power dissipation is low because of the short time spent in the active region and because of the low values of grounded-emitter saturation voltage  $V_{CE(\text{sat})}$  and collector leakage current  $I_{CO}$ . For a continuous train of input pulses at a 300-megabaud rate, the average power dissipation is approximately 20 mW in each transistor.

Improvement in the speed of the output pulse amplifier was accomplished by peaking the base current with an RC network in the

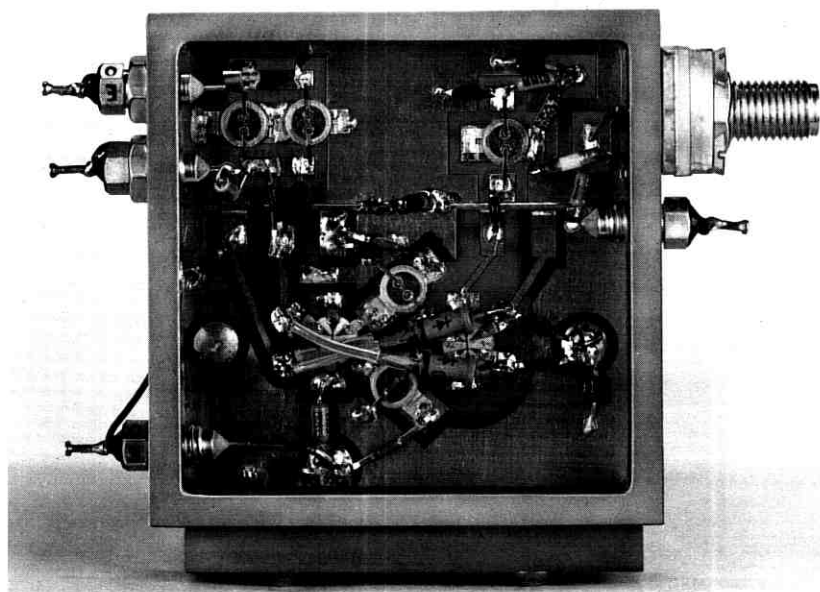


Fig. 19—A photograph of the driver.

base circuit. Reasonably close starting values for  $R_b$  and  $C_b$  were calculated by the standard formula.<sup>25</sup> These values were then adjusted experimentally to obtain the optimum waveshape. Typical values for  $R_b$  and  $C_b$  are  $360 \Omega$  and  $100 \text{ pF}$ . This provides an output waveform with rise and fall times of less than  $1 \text{ ns}$  and a voltage swing of  $10 \text{ volts}$ .

These circuits were constructed on epoxy glass printed circuit boards and mounted on a brass frame. Standard discrete high-frequency components are used. A photograph of the complete driver is shown in Fig. 19. A fully developed version of the driver would use hybrid integrated circuit techniques.

### 6.2 Experimental Results

In order to measure the speed of RF switching, the driver is connected to the PIN diode which is used as a transmission on-off switch. A typical result is shown in Fig. 20. RF switching times from the reverse to forward state and forward to reverse state are approximately  $0.5 \text{ ns}$ .

The amplitude characteristic of the  $180\text{-degree}$  phase switch can be checked by monitoring the mm-wave output directly with a crystal detector. Figure 21 shows such a detector output. This indicates that the imbalance of the insertion losses in the two switching states is less than  $0.2 \text{ dB}$ . Further testing of the PLS-DCPSK modulator is done using a differential phase detector which compares the RF phases one time interval apart. The block diagram of this equipment is shown in Fig. 22 and a photograph in Fig. 23. The input signal to the differential phase detector is split by hybrid No. 1 and in one branch the delay line stores a pulse for one time interval ( $3.33 \text{ ns}$  for  $300\text{-megabaud}$  signals). The output hybrid No. 2 compares the phase of this previous pulse with the following pulse as was explained in Section II.

To demonstrate that the complete path length modulator performs properly at a  $300\text{-Mb/s}$  rate, a simple word generator was constructed using high-speed pulse circuitry. Good reproduction of the input words



Fig. 20—Detected output of the PIN diode on-off switch.

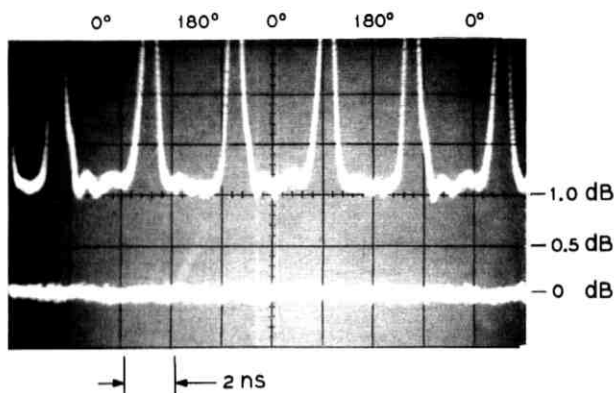


Fig. 21—Amplitude characteristic of 180-degree phase switch (circulator loss included).

was obtained at the output. The example of Fig. 24 shows the input waveform to the flip-flop circuit and the output waveform from the phase detector, corresponding to the pattern 000111000111 . . . . The average power consumption of the driver is about 0.8 W.

Table III summarizes the characteristics of the path length modulators that have been built.

## VII. CONCLUSION

Considering the various factors involved in the design of mm-wave solid-state repeater systems, including the present state of device technology, the path length modulator has been proposed as one of

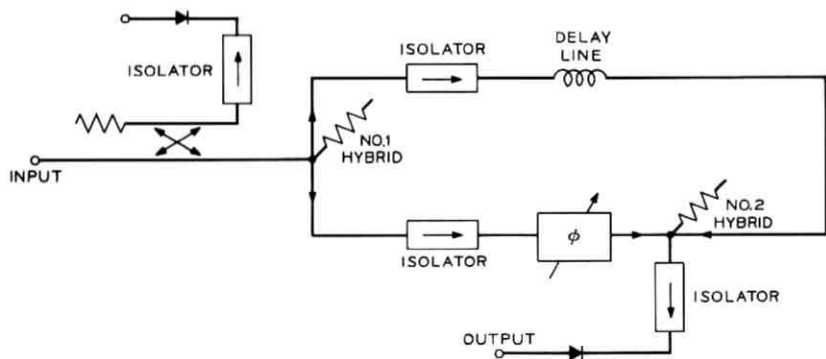


Fig. 22—A block diagram of the mm-wave phase detector.

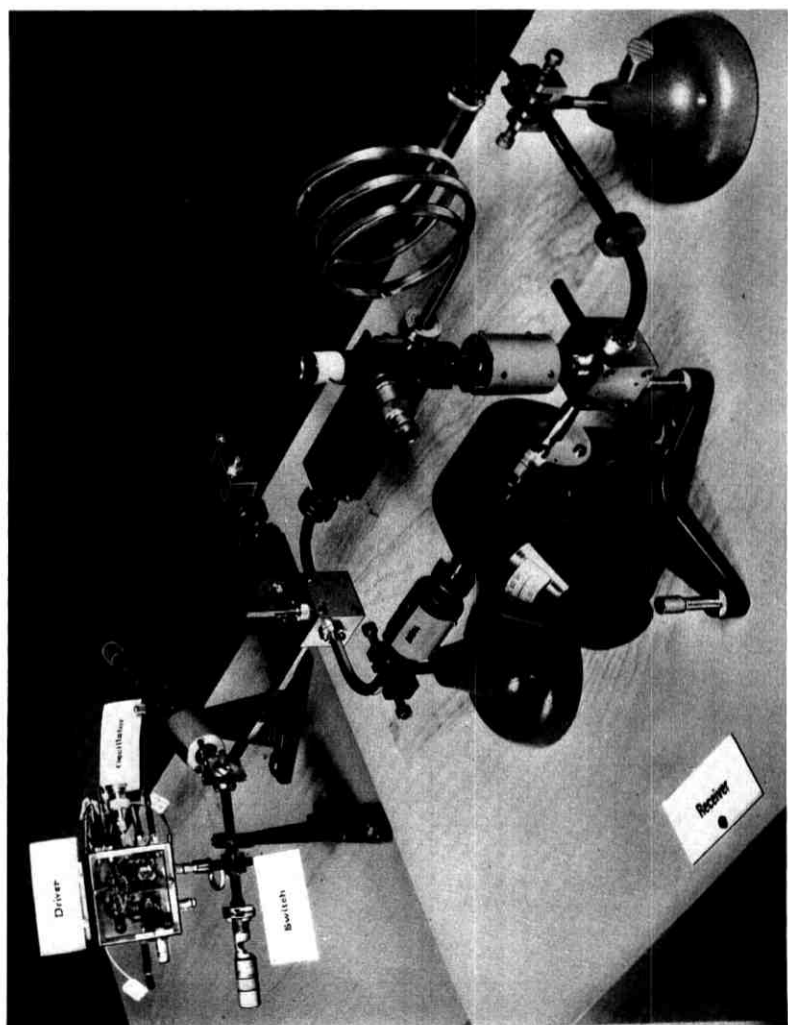


Fig. 23—A photograph of the mm-wave phase detector with Model I.

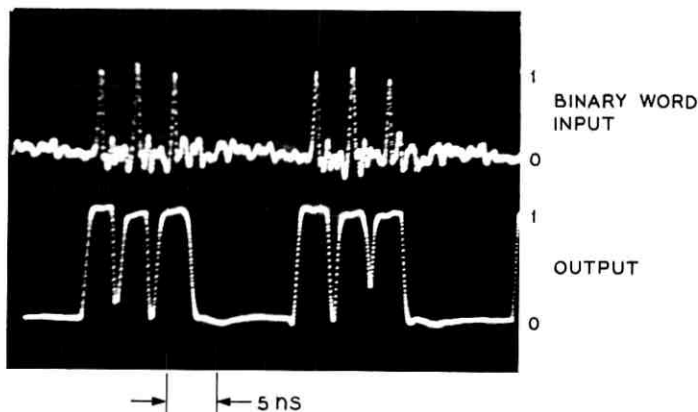


Fig. 24—Input and detected output waveform of the path length modulator.

the most promising practical modulation schemes in the mm-wave range. To demonstrate the feasibility of this proposal, three models, each consisting of an IMPATT oscillator, circulator, PIN diode switch, and its driver circuit were built. The experimental results show that the path length modulator can handle signals at 300 Mb/s. The total

TABLE III—PATH LENGTH MODULATOR CHARACTERISTICS

Characteristic		Model I <sup>†</sup>	Model II	Model III
Oscillator				
Frequency		56.4 GHz	56.4 GHz	57.4 GHz
Output Power		85 mW	135 mW	138 mW
Efficiency		2.2 %	4.1 %	4.2 %
Temperature Coefficient		—	-250 kHz/°C	-150 kHz/°C
Isolator				
Insertion Loss <sup>‡</sup>		1.0 dB	<0.3 dB	<0.3 dB
Modulator				
Insertion Loss	Switch	0.7 dB	0.5 dB	0.6 dB
	Circulator	0.5 dB	0.5 dB	0.5 dB
Output Power		50 mW	100 mW	100 mW
Switching Time <sup>§</sup>				
To Forward		1.7 ns	<0.8 ns	<0.8 ns
To Reverse		1.0 ns	<0.7 ns	<0.7 ns
DC Power		0.8 W	0.8 W	0.8 W

<sup>†</sup> An early developmental model to demonstrate feasibility.

<sup>‡</sup> A circulator with its one port terminated is used as the isolator in Model II and in Model III. For Model III, this circulator and the circulator in the modulator are integrated to form a four-port circulator.

<sup>§</sup> Measured with the differentially coherent phase detector.

insertion loss of the modulator including two circulator passes is about 1 dB in the 50 ~ 60-GHz range, and 100 mW of output power is obtained at the output port of the circulator.

#### VIII. ACKNOWLEDGMENTS

Acknowledgments are due to R. Edwards who supplied the IMPATT diodes; W. Bleickardt who made the high-speed flip-flop circuit design available to us; R. E. Fisher, F. M. Magalhaes, and H. W. Thim who contributed to the initial phase of this project; and J. P. Beccone, E. E. Becker, and R. S. Riggs who assisted in the experiments. The authors wish to thank C. Barnes, F. H. Blecher, R. S. Engelbrecht, L. Moose, and K. M. Poole for their support and encouragement.

#### APPENDIX

##### *An Equivalent Circuit of a PIN Diode Switch*

In this appendix, we discuss the transformation necessary to get 180 degrees phase shift by a PIN diode. Suppose that the waveguide impedance is  $R_0$  and a reciprocal two-port network is inserted between  $R_0$  and the diode as illustrated in Fig. 25. Let the impedance looking into the two-port from the diode position be  $Z_a^*$  and define power waves at ports 1 and 2 with reference impedances  $R_0$  and  $Z_a$  respectively. For example, the incident and reflected power waves at port 2 are given by<sup>26</sup>

$$a_2 = \frac{V_2 + Z_a I_2}{2\sqrt{\text{Re } Z_a}}, \quad b_2 = \frac{V_2 - Z_a^* I_2}{2\sqrt{\text{Re } Z_a}}. \quad (1)$$

The two-port network is characterized by a scattering matrix as follows:

$$\begin{bmatrix} b_1 \\ b_2 \end{bmatrix} = S \begin{bmatrix} a_1 \\ a_2 \end{bmatrix} = \begin{bmatrix} 0 & s \\ s & 0 \end{bmatrix} \begin{bmatrix} a_1 \\ a_2 \end{bmatrix}. \quad (2)$$

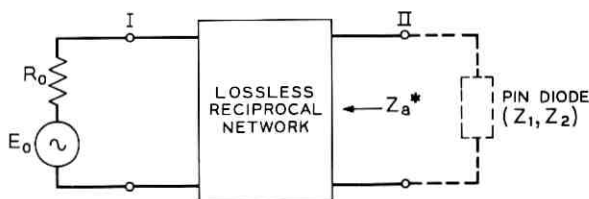


Fig. 25—Two-port network representing the switch circuit.

In the scattering matrix  $S_{11} = S_{22} = 0$ , since both ports are matched when the reference impedances are connected, and  $S_{12} = S_{21} = s$ , since reciprocity is assumed. When  $Z_1$  is connected to port 2,  $V_2 = -Z_1 I_2$ . Substituting into (1), we have

$$a_2 = \frac{Z_1 - Z_a}{Z_1 + Z_a^*} b_2. \quad (3)$$

From (2) and (3), the reflected wave at port 1 is given by

$$b_1 = sa_2 = s \frac{Z_1 - Z_a}{Z_1 + Z_a^*} b_2 = s \frac{Z_1 - Z_a}{Z_1 + Z_a^*} sa_1.$$

Consequently, when the diode impedance is  $Z_1$ , the reflection coefficient at port 1 becomes

$$\frac{b_1}{a_1} = s^2 \frac{Z_1 - Z_a}{Z_1 + Z_a^*}.$$

Similarly, when the diode impedance is  $Z_2$ , the same reflection coefficient becomes  $s^2(Z_2 - Z_a)/(Z_2 + Z_a^*)$ . To get 180 degrees phase shift with equal losses in the two bias states, therefore, we have

$$\frac{Z_1 - Z_a}{Z_1 + Z_a^*} = -\frac{Z_2 - Z_a}{Z_2 + Z_a^*}. \quad (4)$$

Assuming that the denominators are not equal to zero, (4) is equivalent to

$$2Z_1Z_2 + (Z_1 + Z_2)(Z_a^* - Z_a) - 2Z_aZ_a^* = 0.$$

Suppose  $Z_1 = r_1 + jx_1$ ,  $Z_2 = r_2 + jr_2$ , and  $Z_a = r_a + jx_a$ , then the above equation shows that

$$x_a = \frac{r_1x_2 + r_2x_1}{r_1 + r_2}, \quad r_a = \sqrt{r_1r_2} \sqrt{1 + \frac{(x_1 - x_2)^2}{(r_1 + r_2)^2}}.$$

Figure 26 shows the equivalent circuit. If the magnitude of  $x_1 = -1/\omega C$  is much larger than  $|x_2|$  and  $r_1$  and  $r_2$  are small quantities of the same order of magnitude, we have

$$x_a \cong \frac{x_1}{1 + \frac{r_1}{r_2}}, \quad r_a \cong \frac{|x_1|}{\sqrt{\left(1 + \frac{r_1}{r_2}\right)\left(1 + \frac{r_2}{r_1}\right)}}. \quad (5)$$

Since the exchangeable power is invariant to lossless transformations, if the two-port is lossless, the incident power  $P_i$  at port 1 in Fig. 25 can be calculated from the equivalent circuit in Fig. 26. Under the

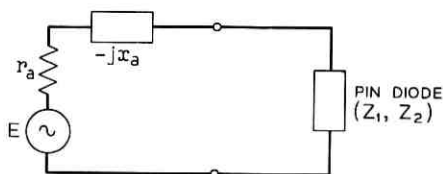


Fig. 26—Equivalent circuit of the PIN diode switch.

same approximation as (5), we obtain

$$P_i = \frac{|E_p|^2}{4R_o} = \frac{|E|^2}{4r_a} \cong \frac{|E_p|^2}{8|x_1|} \sqrt{\frac{r_1}{r_2}} \quad (6)$$

where  $E_p$  is the peak RF voltage applied to the diode. Equation (6) gives the maximum power handling capability of the 180-degree phase switch when  $E_p$  is limited. It is worth noting that (6) is quite different from the formula derived by M. E. Hines<sup>27</sup> without taking into account the insertion loss condition in the two switching states.

When  $E_p$  is equal to 10 V and  $|x_1|$  is 100  $\Omega$  and  $r_1 = r_2$ ,

$$x_a \cong -50 \Omega, \quad r_a \cong 50 \Omega, \quad P_i \cong -125 \text{ mW.}$$

These numbers are used in the design of the PIN diode.

#### REFERENCES

- Misawa, T., "CW Millimeter-Wave IMPATT Diodes with Nearly Abrupt Junction," *Proc. IEEE*, 56, No. 2 (February 1968), pp. 234-235.
- Harkless, E. T., and Vincent, R., "A Solid-State Modulator for Millimeter Waves," *ISSCC Digest of Technical Papers* (1960), pp. 44-45.
- Hubbard, W. M., and Mandeville, D. G., "Experimental Verification of the Error-Rate Performance of Two Types of Regenerative Repeaters for Differentially Coherent Phase-Shifted Keyed Signals," *B.S.T.J.*, 46, No. 6 (July 1967), pp. 1173-1202.
- Hubbard, W. M., Goell, J. E., Warters, W. D., Mandeville, G. D., Lee, T. P., Shaw, R. C., and Clouser, P. L., "A Solid State Regenerative Repeater for Guided Millimeter Wave Communication Systems," *B.S.T.J.*, 46, No. 9 (November 1967), pp. 1977-2018.
- Lee, T. P., Standley, R. D., and Misawa, T., "A 50 GHz Silicon IMPATT-Diode Oscillator and Amplifier," *IEEE Trans. Elec. Devices*, ED-15, No. 10 (October 1968), pp. 741-747.
- Lee, T. P., and Standley, R. D., "Frequency Modulation of a Millimeter-Wave IMPATT Diode Oscillator and Related Harmonic Generator Effects," *B.S.T.J.*, 48, No. 1 (January 1969), pp. 143-161.
- Brenner, H. E., "FM Modulation of mm-Wave IMPATT Oscillators with PCM Baseband Pulses," *Proc. IEEE*, 57, No. 9 (September 1969), pp. 1683-1684.
- Hubbard, W. M., Mandeville, G. D., and Goell, J. E., "Multilevel Modulation Techniques for Millimeter Guided Waves," *B.S.T.J.*, 49, No. 1 (January 1970), pp. 33-54.
- Miyauchi, K., Kita, S., Shimada, S., and Sushi, N., "Design and Performance of an Experimental 400 MB-4PSK Guided Millimeter-Wave Transmission System," *Electrical Communication Laboratory Report*, NTT, Japan, 1970.

10. Nakamura, S., and Inoue, Y., "Digital 4-Phase Modulation Using Diode Switches in 2 GC Band," *J. IECE*, 50, No. 6 (June 1967), pp. 127-134.
11. Murotani, M., and Tachikawa, K., "Microwave PCM System," *Japan Telecommun. Rev.*, 9, (November 3, 1967), pp. 126-136.
12. Kurokawa, K., "Some Basic Characteristics of Broadband Negative Resistance Oscillator Circuits," *B.S.T.J.*, 48, No. 6 (July-August 1969), pp. 1937-1955.
13. Pulfer, J. K., "Voltage Tuning in Tunnel Diode Oscillators," *Proc. IRE*, 48, No. 6 (June 1960), p. 1155.
14. Magalhaes, F. M., and Kurokawa, K., "A Single-Tuned Oscillator for IMPATT Characterization," *Proc. IEEE*, 58, No. 5 (May 1970), pp. 831-832.
15. Kenyon, N. D., "A Circuit Design for MM-Wave IMPATT Oscillators," *G-MTT Symposium Digest* (1970), pp. 300-303.
16. Private communication from P. T. Hutchison.
17. Kurokawa, K., *An Introduction to the Theory of Microwave Circuits*, New York: Academic Press, 1969, pp. 247-253.
18. Owen, B., and Barnes, C. E., "The Compact Turnstile Circulator," *G-MTT Symposium Digest* (1970), pp. 388-392.
19. Sugimoto, S.; and Sugiura, T., "Microwave Switching with Gunn-Effect Diodes," *Proc. IEEE*, 56, No. 3 (March 1968), p. 371.
20. Sterzer, F., "Amplitude Modulation of Microwave Signals Using Transferred Electron Diodes," *Proc. IEEE*, 57, No. 1 (January 1969), pp. 86-87.
21. Schlosser, W. O., Beccone, J. P., and Riggs, R. S., "A PIN Diode for MM-Wave Digital Modulation," *G-MTT Symposium Digest* (1970), pp. 114-117.
22. White, J. F., "Review of Semiconductor Microwave Phase Shifters," *Proc. IEEE*, 56, No. 11 (November 1968), pp. 1924-1931.
23. Kurokawa, K., and Schlosser, W. O., "Quality Factor of Switching Diodes for Digital Modulation," *Proc. IEEE*, 58, No. 1 (January 1970), pp. 180-181.
24. Koehler, D., "Semiconductor Switching at High Pulse Rates," *IEEE Spectrum*, 12, No. 11 (November 1965), pp. 50-66.
25. Gillie, A. C., *Pulse and Logic Circuits*, New York: McGraw-Hill, 1968, Section 9.7.
26. Reference 17, pp. 33-38 and pp. 211-224.
27. Hines, M. E., "Fundamental Limitations in RF Switching and Phase Shifting Using Semiconductor Diodes," *Proc. IEEE*, 52, No. 6 (June 1964), pp. 697-708.



## Traffic Analysis of a Ring Switched Data Transmission System

By J. F. HAYES and D. N. SHERMAN

(Manuscript received April 12, 1971)

*This paper is concerned with a study of traffic and message delay in a ring switched data transmission system. The system, by asynchronous multiplexing and data storage, shares transmission facilities among many users. It is the random component of message delay due to buffering that is the focal point of our study.*

*The basic configuration of the system is a ring connecting stations where traffic enters or leaves the system. A mathematical model of the ring is developed which accommodates an arbitrary number of stations and any given pattern of traffic between stations. Studied in detail is the uniform traffic pattern in which each user is identical and communicates equally to all others. Intrinsic to the model is a recognition of the bursty nature of data sources. Other factors that are taken into account are line and source rates as well as the blocking of data into fixed size packets. Formulas are derived from which average message delay induced by traffic in the ring can be calculated.*

*The results of the study are presented in a set of curves where normalized delay due to traffic within specific system configurations is plotted as a function of the number of stations and source activity. The delay here is normalized to average message lengths. An important parameter of these curves is the ratio of source rate to line rate. The results show that, in certain quite reasonable circumstances, the delay is less than two average message lengths.*

*Rings of 10, 50, and 100 users have been simulated on a digital computer. Data obtained from these investigations are presented and compared to the theoretical estimates for line busy and idle periods and message delay. The results of simulated average message delay show that, for interstation link utilizations of about 60 percent, the difference between the theoretical estimates and experimental observations is small.*

## I. INTRODUCTION AND BACKGROUND

In a recent paper<sup>1</sup> J. R. Pierce has proposed a data communication network in which users are connected in a ring or loop topology. In this paper we study the behavior of this network. We examine the relationship between source and line utilizations and the message delay within the system. We propose mathematical models of station behavior and, by making use of reasonable input data traffic models, predict the average delay as a function of network parameters. A principal result of our study shows that, in many cases of interest, average delay in storage is less than two message lengths.

The network is *buffered*, operates on a *distributed control* philosophy, and user entry is gained by *asynchronous* multiplexing into the line bit stream. Other systems have used the ring topology. For example, IBM offers a synchronous, nonbuffered system<sup>2</sup> in which a central controller monitors the loop and allows access by the users. Buffered, centrally controlled systems have been proposed by W. D. Farmer and E. E. Newhall<sup>3</sup> and A. G. Fraser.<sup>4</sup> In the first a computer controls several peripheral devices, while in the second, several computers are interconnected.

The characteristics of data sources and the requirements of users make the technique of message switching applicable to data communications. One important characteristic is that data sources are often bursty; i.e., relatively short sequences of bits followed by long pauses. A basic need of many data customers is rapid response to data bursts. One way to meet this need is by devoting a line to a source for a long period of time. However, because of the long pauses between data bursts the line will be underutilized. On the other hand, dropping the line between data bursts may be inefficient because of long setup times. For the line switching techniques that are currently used, the setup time will often be longer than the holding time.

Message switching provides a way of efficiently using the line and obtaining rapid response. The idea is to asynchronously multiplex several sources onto the same line. For example, in the present system, data from each source are formed into fixed size packets and supplied with a header. The header contains source and destination addresses as well as bookkeeping information. Packets from all sources are buffered and fed onto the line according to some scheduling algorithm. (One such algorithm will be seen presently when the detailed operation of the ring is described.) Clearly as more packets seek access to the same line, more storage is required. The storage requirements and the at-

tendant buffering delay are important characteristics of system operation. It is precisely these characteristics that are the focal point of our study.

A sketch of the basic ring system is shown in Fig. 1. As indicated, traffic flows in one direction around the ring from station to station. The stations are indicated as B-boxes in Fig. 1. For purposes of explanation let us begin with the operation of the B-box before considering the other components of the loop (A-box and C-box). The data source is connected to the B-box where its output is formed into fixed size blocks or packets and supplied with header. A message from a source may consist of several packets. If the line is free a packet is multiplexed on the line immediately. The packet is then passed from B-box to B-box to its destination. At each B-box on its itinerary the address of a packet is examined to determine whether the packet's destination is at that particular B-box. This examination entails a fixed delay for each B-box which can be calculated given the source and destination. It is, however, the random delay encountered by the last bit of a message before it gets on the loop that commands our

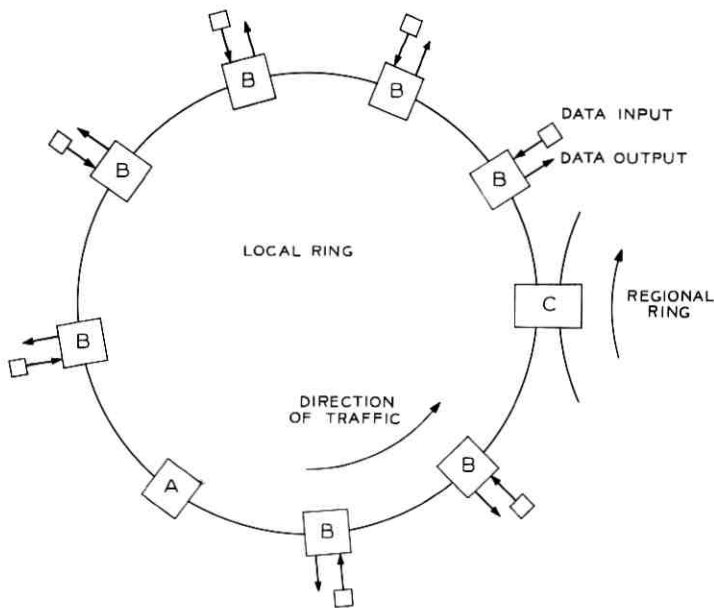


Fig. 1—Pierce ring.

attention. A fundamental property of the system is that traffic presently in transmission has priority over traffic seeking entrance to the ring. If the line at a B-station is busy with information packets passing through it, the packets produced at that station are buffered until the line is free. The reading onto the line of a message consisting of more than one packet will be interrupted when packets from another station pass through. The reading of the message is resumed from the point of interruption when the line is free again.

In order to explain the mechanism of multiplexing packets on and off the line, it is helpful to draw an analogy between the ring and a conveyer belt (see Fig. 2 for an illustration). Time slots into which packets may be placed circulate around the loop. The A-box insures that synchronism is maintained (see below). At the beginning of each time slot is a marker indicating whether the ensuing packet slot is empty or full. The B-box senses this marker and acts accordingly. In a full packet, address bits follow the occupancy marker. If a B-box senses its own address the packet is removed from the line and sent to its destination. This same B-box may take advantage of the empty slot to feed its own packet on the line. Of course if a packet slot is full and destined for a source beyond a particular B-box, then the line is momentarily blocked for that B-box.

While there are many B-boxes in a ring, there is only one A-box. The A-box has two basic functions. The first, as mentioned earlier,

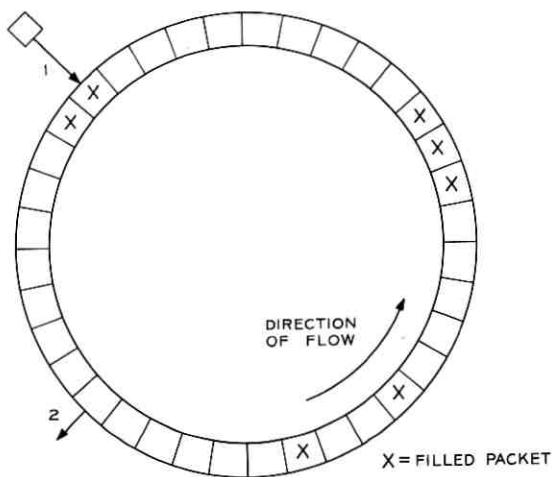


Fig. 2—Conveyor belt. Packets enter at 1 and leave at 2.

is synchronization of the ring. The second function is that of preventing the buildup of traffic in the ring due to undeliverable packets. The header of each packet passing through an A-box is marked. If a packet tries to pass through an A-box a second time it is either destroyed, creating an empty packet slot, or sent back to its destination. Sending a packet back to its destination is done simply by interchanging source and destination addresses. In this way a busy signal is provided.

The C-box shown in Fig. 1 provides interconnection of rings (see Fig. 3). Packets destined for a station outside a particular ring have addresses indicating this and are picked off by the C-box in exactly the same way that intraring traffic is picked off by B-boxes. This traffic is buffered and multiplexed onto the next ring in the same way that traffic from a local station is multiplexed on a ring. Since traffic already on a loop has priority, inter-ring traffic will suffer some delay. A likely realization of the C-box suggested by W. J. Kropff<sup>5</sup> is the tandem connection of buffer and B-boxes shown in Fig. 4.

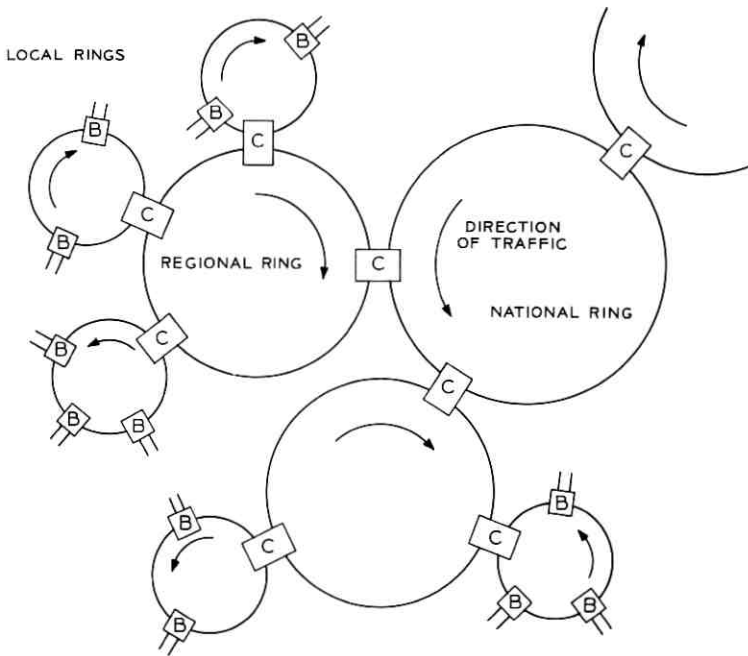


Fig. 3—Three-stage hierarchy of Pierce ring.

In the remainder of this paper a mathematical model of the ring will be developed and analyzed. The results of this study will be presented in the form of sets of curves which illustrate the behavior of normalized delay as a function of either the number of stations in the ring or the utilization of the source.

In order to carry this analysis forward it was necessary to make several assumptions and approximations. Thus in order to verify our results and to refine our model, a simulation program was developed. Simulation results have been obtained for rings ranging from 10 stations to 100 stations. These results are compared to the results of analysis.

## II. GLOSSARY OF TERMS

- $C_b$ —Line rate in bits per second.
- $C_p$ —Line rate in packets per second.
- $b_i$ —Bit rate during the activity period of the  $i$ th source.
- $B_p$ —Number of information bits per packet.
- $H$ —Number of header bits per packet.
- $1/\lambda_i$ —Average duration of idle period of  $i$ th source in seconds.
- $1/\mu_i$ —Average duration of active period of  $i$ th source in seconds.
- $Q_i$ —Average number of packets per message at  $i$ th source.
- $\gamma_i$ —Ratio of source packet rate to the line packet rate.
- $u_i$ —Utilization of source  $i$  [see equation (3)].
- $\theta_i$ —Intensity of source  $i$  [see equation (4)].
- $r_i$ —Average number of packets per second from source  $i$ .
- $N$ —Number of stations in ring.
- $P_{ij}$ —Portion of traffic from station  $i$  to station  $j$ .
- $R_k^*$ —Traffic passing through station  $k$  in packets per second.
- $R_k$ —Traffic out of station  $k$  in packets per second.
- $U_k^*$ —Line utilization as seen by station  $k$  [see equation (9a)].
- $\Theta_k^*$ —Line intensity as seen by station  $k$  [see equation (10)].
- $U_k$ —Line utilization after station  $k$  [see equation (9b)].
- $\Theta_k$ —Line intensity after station  $k$  [see equation (10b)].
- $1/\Lambda_k^*$ —Average duration of line idle period in seconds as seen by station  $k$ .
- $1/M_k^*$ —Average duration of line busy period in seconds as seen by station  $k$ .

## III. SYSTEM MODEL

### 3.1 Source Input Model

In this section a mathematical model for a ring is presented thereby

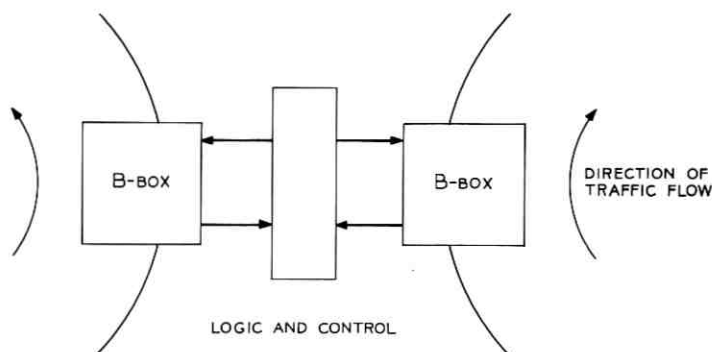


Fig. 4—Tandem connection of B-boxes for ring switching.

laying a foundation for succeeding sections where the model is analyzed. We are primarily interested in the traffic characteristics of the ring and the attendant delay. In order to focus on this aspect of ring operation, we assume that there are no equipment failures or transmission errors so that, once on the ring, a packet is ultimately delivered to its destination. Thus the action of the A-box in destroying packets or providing a busy signal is not part of the model. At present the study is confined to an analysis of a single ring. Finally the study was predicated on light to moderate loading of the system. In a heavily loaded system long queues of messages form and the response time of the system may be excessive for data applications.

Throughout the analysis the parameter  $N$  designates the number of B-boxes or stations that are on the ring. The capacity of the line connecting the stations to one another is designated as  $C_b$  bits/second.

To each B-box is connected a source, which as we have noted above, is bursty in nature. The output of the  $i$ th data source is modeled as consisting of alternate idle and active periods. During the latter, transmission is at a constant rate of  $b_i$  bits/second. The durations of the source activity and idle periods are assumed to be exponentially distributed and statistically independent of one another. Successive idle and busy periods are also independent of one another. The average durations in seconds of the active and idle periods of the source connected to the  $i$ th station in the loop are denoted as  $1/\mu_i$  and  $1/\lambda_i$ , respectively. Studies of computer user statistics<sup>6,7</sup> indicate that the foregoing is a reasonable, if somewhat simplified, model of a data source.<sup>†</sup>

<sup>†</sup> An initial study of this model of the data stream is due to R. J. Pile.<sup>8</sup>

Each message (bits generated in a source activity period) is bundled into an integral number of fixed size packets. The maximum number of information bits in each packet is  $B_p$ . The number of header bits that accompany each packet is denoted by the parameter  $H$ . In Appendix A it is shown that the number of packets in a message is geometrically distributed with mean

$$Q_i = \frac{1}{1 - \exp(-B_p \mu_i / b_i)}, \quad i = 1, 2, \dots, N. \quad (1)$$

During an active period of a source, the rate at which packets are produced is  $\mu_i Q_i$ . The rate at which packets can be transmitted on the line is  $C_b / (B_p + H)$ . An important quantity in our consideration is the ratio of source packet rate to line packet rate,

$$\gamma_i = \frac{\mu_i Q_i}{C_p}, \quad i = 1, 2, \dots, N. \quad (2a)$$

It may well be that in some applications a typical message consists of many packets, i.e.,  $b_i / \mu_i \gg B_p$ . In this case we have

$$\gamma_i \cong \frac{b_i / B_p}{C_p}. \quad (2b)$$

Other source parameters that are important in our study can be derived. The utilization of source  $i$  or the fraction of time that source  $i$  is active is

$$u_i = \frac{\lambda_i}{\lambda_i + \mu_i}, \quad i = 1, 2, \dots, N. \quad (3)$$

The intensity of source  $i$  is defined as

$$\theta_i = \frac{\lambda_i}{\mu_i}, \quad i = 1, 2, \dots, N. \quad (4)$$

The average number of packets/second transmitted from source  $i$  is

$$r_i = \frac{Q_i}{1/\lambda_i + 1/\mu_i} = \mu_i Q_i u_i. \quad (5)$$

#### IV. LINE TRAFFIC

##### 4.1 Line Utilization

From the way in which traffic is multiplexed onto the line it is clear that message delay is dependent upon the line traffic. As a prelude to the calculation of delay, the relevant characteristics of line traffic are

considered in this section. A precise mathematical characterization of line traffic is extremely difficult. In fact, for reasons that will be explained presently, we encounter the most difficulty in this phase of the analysis.

We begin by calculating the average line utilization at each point in the ring. The basic assumption in this calculation is that a conservation law holds so that, over a sufficiently long time period, the average packet rate into a station is equal to the average packet rate out of a station. The traffic into and out of a station includes data to and from a customer connected to the station as well as line traffic. The implication is that there is no continuous buildup of packets in storage at a station, which is as it should be for normal ring operation.

Let the number of packets/second emanating from the source connected to station  $i$  ( $i = 1, 2, \dots, N$ ) be designated as  $r_i$ . In terms of parameters defined earlier  $r_i = Q_i[1/\lambda_i + 1/\mu_i]^{-1}$ .  $P_{ij}$  is defined as the portion of traffic originating at station  $i$  that is destined for station  $j$  with  $P_{ii} = 0$ . The average number of packets per second going from station  $i$  to station  $j$  is  $P_{ij}r_i$ . All of these packets pass through each station on the ring between stations  $i$  and  $j$ . The average number of packets per second from station  $i$  passing through station  $k$  is given by

$$R_{ik}^* = \begin{cases} r_i \sum_1^{i-1} P_{ij} + r_i \sum_{k+1}^N P_{ij} & \text{if } 1 < i < k, k \neq N \\ r_i \sum_1^{i-1} P_{ij} & \text{if } 1 < i < k, k = N \\ r_i \sum_{k+1}^N P_{ij} & \text{if } i = 1, k \neq N \\ r_i \sum_{k+1}^{i-1} P_{ij} & \text{if } k + 1 < i \leq N \\ 0 & \text{otherwise.} \end{cases} \quad (6)$$

The total volume of traffic passing through station  $k$  is given by

$$R_k^* = \sum_{i=1}^N R_{ik}^* . \quad (7)$$

The total volume of traffic out of station  $k$ , including traffic from the local source, is

$$R_k = R_k^* + r_k, \quad k = 1, 2, \dots, N. \quad (8)$$

Perhaps the distinction between  $R_k$  and  $R_k^*$  here can be emphasized

by referring to Fig. 5. Here a B-box is shown as being split into its two functions, viz., taking data off the line and reading data onto the line. At point *Z* the line carries all of the traffic out of station *k* at an average rate of  $R_k$  packets/second. At point *Y* the average traffic rate seen by the local source as it attempts to multiplex data on the line is  $R_k^*$  packets/second. (Throughout the remainder of the analysis an asterisk on a line traffic parameter denotes a quantity as seen by the location station after message deletion.) Since the packet capacity of the line is  $C_p$ , the line utilization as seen by the source at station *k* is

$$U_k^* = R_k^*/C_p. \quad (9a)$$

The line intensity at this point is

$$\Theta_k^* = R_k^*/(C_p - R_k^*). \quad (10a)$$

The utilization and intensity on the line after station *k* are given by

$$U_k = R_k/C_p \quad (9b)$$

$$\Theta_k = R_k/(C_p - R_k). \quad (10b)$$

In the case where ring traffic is symmetric, i.e.,

$$P_{ij} = \begin{cases} 0 & i = j \\ 1/(N - 1) & i \neq j \end{cases} \quad (11)$$

and  $r_i = r$ ,  $i = 1, 2, \dots, N$ , these expressions simplify greatly. We have

$$R_k^* = r\left(\frac{N}{2} - 1\right). \quad (12)$$

#### 4.2 Busy Period

We turn now to the calculation of the average duration of idle and busy periods on the line. An exact calculation of either quantity is

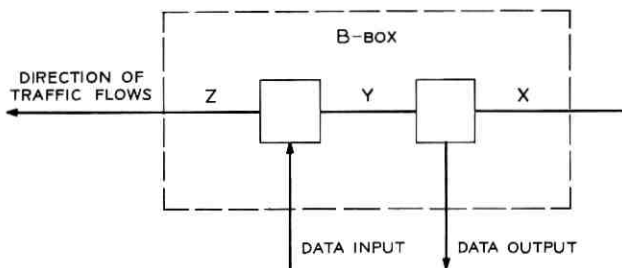


Fig. 5—Station decomposition.

difficult for all but very specific cases. The reason for this difficulty can be seen by examining the mechanism for multiplexing traffic on and off the line. Packets destined for a particular station may be interspersed in a sequence of contiguous packets. This sequence is broken up at random when the packets are delivered. On the other hand, the packets with the same destination may be concentrated at the beginning of a long sequence. In this case the long sequence will be scarcely affected when the packets in question are taken off the line.

In the remainder of this section are presented two approaches to the problem of calculating the average duration of the line busy period. While neither calculation is exact, both take into account the various factors involved, and, in those special cases where the answer is known, the same correct result is obtained. The basic difference between the two methods lies in the kind of line traffic that they are designed to model. As we proceed in the calculation this will be pointed out.

Both of these approaches draw on a result from storage theory concerning the data sequence out of a buffer. Suppose that  $n$  sources feed into a common buffer. The sources turn on and off at random transmitting at a constant rate during the active period, and data are read out of the buffer at a constant rate. The output will consist of successive idle and busy periods. Suppose that the durations of input idle periods are exponentially distributed with mean  $1/\alpha_i$ ,  $i = 1, 2, \dots, n$ . By definition, the probability of an input idle period terminating in any incremental interval  $dt$  is  $\alpha_i dt$ . An output idle period terminates when any one of the input idle periods terminate. Thus the probability of an output idle period terminating in any incremental interval  $dt$  is  $\sum_{i=1}^n \alpha_i dt$ ; consequently the duration of the output idle period is exponentially distributed with mean  $1/\sum_{i=1}^n \alpha_i$ .

In both calculations the line traffic intensity [see equations (10a) and (10b)] is assumed to be equal to the ratio of the average durations of the line busy period to the line period. It is implicit in this assumption that the active and idle periods on the line are independent of one another and that they are stationary in the mean.

The first method that calculates the average duration of the busy period looks at each station individually. In equation (6) an expression for  $R_{ik}^*$ , the number of packets per second from station  $i$  passing through station  $k$ , is given. If this were the only source active, the line intensity at station  $k$  would be

$$\Theta_{ik}^* = \frac{R_{ik}^*}{C_n - R_{ik}^*}.$$

The average length of a message from source  $i$  is  $Q_i$  packets. We take the average duration of the idle period of the packet stream in seconds from the  $i$ th source as

$$1/\Lambda_{ik}^* = Q_i/C_p\Theta_{ik}^* = \frac{Q_i(C_p - R_{ik}^*)}{C_p R_{ik}^*}. \quad (13)$$

Now the assumption is made that the durations of the idle periods in the packet streams are exponentially distributed. To find the average duration of the idle period of the packet stream as seen by the source connected to station  $k$ , we call upon the result from storage theory quoted earlier. The duration of the idle period is exponentially distributed with mean

$$1/\Lambda_k^* = 1 / \sum_{\substack{i=1 \\ i \neq k}}^N \Lambda_{ik}^*. \quad (14)$$

The average duration of the busy period of the line in seconds as seen by the source at station  $k$  is given by

$$\frac{1}{M_k^*} = \frac{\Theta_k^*}{\Lambda_k^*}. \quad (15)$$

Combining (13), (14), and (15) we obtain

$$\frac{1}{M_k^*} = \frac{\Theta_k^*}{\sum_{\substack{i=1 \\ i \neq k}}^N \frac{C_p R_{ik}^*}{Q_i(C_p - R_{ik}^*)}}. \quad (16)$$

When the ring traffic is symmetric [see equation (11)], these results simplify. We have

$$\Lambda_k^* = \sum_{j=2}^{N-1} \frac{\lambda u((j-1)/(N-1))}{1 - \gamma u((j-1)/(N-1))}, \quad (17)$$

where  $\mu = \mu_i$ ,  $\Theta = \Theta_i$ , and  $u = u_i$ ,  $i = 1, 2, \dots, N$ . In many cases of interest  $\gamma$  is small so that the term  $\gamma u((j-1)/(N-1))$  in the denominator of (17) contributes little and may be ignored. In this case we may make a convenient approximation:

$$\Lambda_k^* \cong \mu u \left( \frac{N}{2} - 1 \right), \quad k = 1, 2, \dots, N \quad (18)$$

and

$$\frac{1}{M_k^*} = \frac{\gamma}{\left[ 1 - \gamma u \left( \frac{N}{2} - 1 \right) \right]}. \quad (19a)$$

This expression may be put in the alternate form

$$1/M_k^* = \gamma(1 + \Theta^*)/\mu. \quad (19b)$$

The key assumption in this calculation suggests the region of application of this model. In the packet stream from station  $i$  passing through station  $k$ , at average rate  $R_{ik}^*$ , it is assumed that the messages stay together. Thus the average busy period of this stream is  $Q_i$  packets long. The model is not valid when the messages from individual sources are broken up in the act of multiplexing. Thus the model should hold best when the sources emit short messages or when line utilization is low.

The foregoing method of calculating the duration (length) of the average busy period on the line essentially ignores the ring and treats each station as a separate entity. In contrast the second method makes explicit use of the ring structure. The algorithm begins with the assumption that the length of the line busy period at the input to a station is known. Based on this assumption the length of the busy period on the line out of the station is calculated. The process continues all the way around the ring until one returns to the starting point. The ring is closed by setting the duration of the final busy period equal to that of the initial busy period.

The algorithm for calculating the change in the busy period is best explained by referring to Fig. 5. The line intensities at points  $X$  and  $Y$  are  $\Theta_{k-1}$  and  $\Theta_k^*$  respectively. The assumption, fundamental to this approach, is that whole busy periods are deleted from the data stream. While there may be fewer busy periods at point  $Y$ , the average length of a busy period is the same from  $X$  to  $Y$ . The average durations of the idle periods are related by

$$\frac{1}{\Lambda_k^*} = \frac{\Theta_{k-1}}{\Theta_k^*} \frac{1}{\Lambda_{k-1}}. \quad (20)$$

The durations of the idle periods between  $Y$  and  $Z$  can be related by calling upon the previously quoted result from storage theory. If the length of the idle period at point  $Y$  is assumed to be exponentially distributed with mean  $1/\Lambda_k^*$ , and the length of the source idle period is exponentially distributed with mean  $1/\lambda_k$ , then the duration of the idle period at point  $Z$  is exponentially distributed with parameter

$$\Lambda_k = \Lambda_k^* + \lambda_k. \quad (21)$$

The average duration of the busy period at point  $X$  is given by

$$\frac{1}{M_k} = \frac{\Theta_k}{\Lambda_k}. \quad (22)$$

One can continue in this fashion until the starting point is reached.

In the case of a ring with a symmetric distribution of traffic the solution simplifies considerably since, by assumption, we have

$$\frac{1}{M_{k-1}} = \frac{1}{M_k}.$$

Substituting into equations (20), (21), and (22) we have that

$$\frac{1}{M_k} = \frac{\theta - \theta^*}{\lambda} = \frac{\theta - \theta^*}{\mu\theta}, \quad (23a)$$

where  $\lambda = \lambda_i$ , and  $\theta = \theta_i$ ,  $i = 1, 2, \dots, N$ . This result can be put into the form

$$\frac{1}{M_k} = \frac{\gamma}{(\lambda + \mu)[1 - \gamma u(N/2)][1 - \gamma u(N/2 - 1)]}. \quad (23b)$$

The key assumption in this calculation is that entire busy periods are destined for a single station. As the line traffic begins to build up, messages from different stations will tend to cluster in the same sequence and the validity of the model is weakened. The model should hold well when messages are multiplexed into light to moderate traffic.

## V. DELAY CALCULATIONS

In this section we shall consider models for calculating message delay. As mentioned earlier we are primarily interested in calculation of message delay that is induced by traffic in the ring. Other delays such as propagation and processing delays are invariant with traffic intensity and are fixed for a given implementation of the ring.

Two separate approaches to the calculation of message delay have been considered. These approaches are complementary in the sense that they apply to different kinds of source traffic while neither approach is applicable to the whole range of source traffic. The exponential on-off model of the source as presented in the foregoing is difficult to handle analytically. The difference in the two approaches lies in the way this exponential on-off model is approximated.

The first approach that we shall consider uses a classical queueing theory model for the source.<sup>†</sup> Messages arriving at a terminal are viewed as customers arriving for service. An analogy is drawn between the length of the message (in bits or packets) and the service time of

<sup>†</sup> The queueing theory model of a source in message switched networks is widely used, e.g., Refs. 9 and 10.

a customer in queueing theory. Thus the exponential on-off source is approximated by messages with exponential length which arrive at a Poisson rate.

The queueing theory model is well suited to sources that are not very active. (However the line into which these sources are multiplexed may be very active if many sources are connected to the ring.) When the source is more active the queueing model has some inherent inaccuracies. The queueing model implies that the distribution of time between messages is an exponentially distributed random variable and there is a nonzero probability of successive messages overlapping. In contrast for the exponential on-off model, the distribution between beginnings of successive messages is the convolution of two exponential distributions and the probability of message overlap is zero.

The second approach to delay calculation uses a smoothed version of the traffic out of a source. Thus if the *average* number of bits per second out of a source is  $X$  bits/second, the calculation assumes that bits emanate from the source at a *constant* rate of  $X$  bits/second. This model of the source is meant to take up where the previous model leaves off, i.e., active sources. The effect of smoothing the bit flow will be less deleterious for more active sources.

The analysis of message delay based on a modified  $M/G/1$  queue<sup>†</sup> is based on work by B. Avi-Itzhak and P. Naor.<sup>11</sup> The line into which a message is multiplexed is viewed as a server that is subject to random breakdown. As the line is either idle or busy the server is operating or under repair. Four assumptions on probability distributions are necessary in order to carry out the analysis: messages arrive at a Poisson rate, the interval between message arrivals is independent of the message size, the duration of the line idle period is exponentially distributed, and the lengths of line idle and busy periods are statistically independent. The distributions of the size of a message and of the duration of a line busy period are arbitrary.

We take the arrival rate of messages from source  $i$  as  $\lambda_i$ . The amount of time required to multiplex a message onto a completely free line at station  $i$  is denoted by the random variable  $S_i$ . It is assumed that the duration of the idle period on the line is exponentially distributed with parameter  $\Lambda_i^*$  [see equations (17) and (21)]. The random variable  $L_i$  denotes the duration of the line busy period as seen by the source at station  $i$ . In Appendix B it is shown that the Laplace-Stieltjes

<sup>†</sup> According to standard queueing theory notation an  $M/G/1$  queue is one where a single server accommodates customers that arrive at a Poisson rate with an arbitrarily distributed service time per customer.

transform of  $T_i$ , the delay suffered by a message at station  $i$ , is given by

$$\mathcal{L}_{T_i}(v) = (1 - U_i^* - \gamma\theta_i) \frac{[\Lambda_i^* \mathcal{L}_{L_i}(v) - \Lambda_i^* - v] \mathcal{L}_{S_i}(\Lambda_i^* - \Lambda_i^* \mathcal{L}_{L_i}(v))}{\lambda_i - v - \gamma_i \mathcal{L}_{S_i}(v + \Lambda_i^* - \Lambda_i^* \mathcal{L}_{L_i}(v))}, \quad (24)$$

where  $\mathcal{L}_{L_i}(v)$  and  $\mathcal{L}_{S_i}(v)$  denote the  $L-S$  transforms of  $L_i$  and  $S_i$ , respectively. By differentiating  $\mathcal{L}_{T_i}(v)$  with respect to  $v$  and allowing  $v$  to approach zero, one obtains the following expression for the expected value of  $T_i$ ,

$$\begin{aligned} E[T_i] &= E[S_i] \Theta_i^* \\ &+ E[S_i^2] \frac{\lambda_i(1 + \Theta_i^*)^2}{2[1 - \gamma_i \theta_i(1 + \Theta_i^*)]} \\ &+ E[L_i^2] \frac{\Lambda_i^*}{2(1 + \Theta_i^*)[1 - \gamma_i \theta_i(1 + \Theta_i^*)]}. \end{aligned} \quad (25)$$

Now the mean number of packets per message is  $Q_i$ . Since the line packet rate is  $C_p$  packets per second, the average time that it takes to multiplex a message onto a clear line is

$$E[S_i] = Q_i/C_p = \frac{\gamma_i}{\mu_i}.$$

In the previous section we have made estimates of the line busy period which we have designated as  $1/M_i^*$ . These quantities can be substituted into (25) yielding

$$\begin{aligned} E[T_i] &= \frac{\gamma_i \Theta_i^*}{\mu_i} + \frac{\gamma_i^2 \theta_i (1 + \Theta_i^*)^2 (1 + \beta_{S_i})}{\mu_i 2[1 - \gamma_i \theta_i (1 + \Theta_i^*)]} \\ &+ \frac{1}{M_i^*} \frac{U_i^* (1 + \beta_{L_i})}{2[1 - \gamma_i \theta_i (1 + \Theta_i^*)]}, \end{aligned} \quad (26)$$

where

$$\beta_{S_i} = \frac{\text{Var}(S_i)}{E^2(S_i)}$$

and

$$\beta_{L_i} = \frac{\text{Var}(L_i)}{E^2(L_i)}.$$

The quantities  $\beta_{S_i}$  and  $\beta_{L_i}$  indicate the sensitivity of the calculation of delay to assumptions about probability distributions. In the next section sample calculations are presented in which we assume that

$\beta_{L_i} = \beta_{S_i} = 1$  as would be the case if  $S_i$  and  $L_i$  were exponentially distributed.

By taking a second derivative of equation (24) and letting  $v$  approach zero, the second moment of delay can be found. For brevity we have omitted this expression; however, calculations based on it will be presented in Section VII.

$\mathcal{L}_{T_i}(v)$  can also be used to calculate the probability that a message has zero delay. Let us assume that  $\lim_{v \rightarrow \infty} \mathcal{L}_{L_i}(v) = 0$  and that  $S$  is exponentially distributed. Then

$$\begin{aligned} \text{Pr [zero message delay]} &= \lim_{v \rightarrow \infty} \mathcal{L}_{T_i}(v) \\ &= (1 - U_i^* - \gamma\theta_i) \left[ \frac{\gamma\mu_i}{\gamma\mu_i + \Lambda_i^*} \right]. \end{aligned} \quad (27)$$

As mentioned previously, the second calculation of delay is predicated on the assumption that the data flow from the source is at a *constant* rate equal to the average rate from a source. Thus we assume that the source associated with station  $i$  generates data at a constant rate of  $r$  packets per second. Because the line is not continuously available to receive these packets buffering is required. It is the content of the buffer that is the key element in the calculation of delay.

As stated earlier, the line traffic consists of alternate busy and idle periods. In the following it is assumed that the durations of the busy and idle periods are independent and exponentially distributed. The mean values of these quantities are known from the calculations in the previous section. Under these assumptions, constant input rate and exponentially distributed durations of line idle and busy periods, it can be shown<sup>12†</sup> that the probability density of the content of the buffer in packets of the  $i$ th station is given by

$$f(B_i) = K_i \delta(B_i) + (1 - K_i) \alpha_i \exp(-\alpha_i B_i), \quad (28)$$

where  $\delta(\cdot)$  is the Dirac delta function and  $K_i$  and  $\alpha_i$  are related to the parameters of the system by

$$K_i = \frac{C_p - r_i(1 + \Theta_i^*)}{(C_p - r_i)(1 + \Theta_i^*)} \quad (29a)$$

and

$$\alpha_i = \frac{M_i^*}{r_i} - \frac{\Lambda_i^*}{C_p - r_i}. \quad (29b)$$

<sup>†</sup> In the reference, the solution was obtained for a hyper-exponential density. In the present work the density is exponential, which can be obtained from the hyper-exponential density.

Notice that  $K_i$  is the probability that buffer  $i$  is empty. The average content of buffer  $i$  in packets is

$$E[B_i] = \frac{1 - K_i}{\alpha_i}. \quad (30)$$

The delay suffered by a packet is the amount of time that it spends in the buffer while waiting to be put on the line. From Little's Theorem<sup>13</sup> the average delay of a packet is the average content of the buffer divided by the arrival rate:

$$E[T_i] = E[B_i]/r_i, \quad i = 1, 2, \dots, N. \quad (31)$$

Substituting (29) and (30) into (31) yields

$$E[T_i] = \frac{1}{M_i^*} \left[ \frac{U_i^*}{1 - \gamma_i u_i (1 + \Theta_i^*)} \right]. \quad (32)$$

## VI. RESULTS—AVERAGE DELAY

This section is devoted to numerical examples of the foregoing results. We shall look at two contrasting modes of system operation, complete symmetry and complete asymmetry. In the symmetric case all stations transmit equally to all other stations and the destination matrix is given by equation (11). All stations in this case are precisely alike in their traffic characteristics. This symmetric traffic pattern may be encountered on a national ring which connects regional rings. The presumption here is that each of the regional rings to which it is connected receives and transmits the same volume of traffic.

The asymmetric case models the situation where one station on the ring receives all of the output of the other stations. This singular station, in turn, distributes its traffic equally among the remaining stations. The asymmetric traffic pattern will be encountered in a ring which is composed of inquiry response users connected to a computer through a C-box.

Let us begin with the symmetric ring. Calculations were made for two separate models of delay. Model 1 is based on the queueing model of delay that resulted in equation (26). The model of line busy period here is that which led to equations (16)–(19). The combination of these two models is best suited to the situation where there are many lightly loaded sources on the line which send short messages. Model 2 is a combination of the smoothed approximation to the source that led to equation (32) and the calculation of line busy period lengths that resulted in equation (23).

The estimates of average delay yielded by Models 1 and 2 are given in terms of average message lengths. Presumably, in a particular application, the duration of an average message is known and the delay in seconds due to line traffic can be evaluated.

The results of the calculation for the symmetric ring are shown in Figs. 6-10. On Figs. 6 and 7 delay normalized to the average message duration is shown as a function of the number of stations for two different values of source utilization. The difference between these curves lies in the factor  $\gamma$  which is equal to 1 on Fig. 6 and  $1/30$  on Fig. 7. The value of  $1/30$  for  $\gamma$  corresponds roughly to sources with  $50 \times 10^3$ -bit-per-second active rate feeding into a  $1.5 \times 10^6$ -bit-per-second line. The results predict that, for  $\gamma = 1/30$ , the ring can accommodate many stations with delay less than one average message length.

Another view of system performance is shown on Figs. 8-10, where delay is shown as a function of source utilization for 10-, 50-, and 100-station rings when  $\gamma = 1$ . We see from these curves that, for moderate line loading, delays are not large. For example, when the line utilization on a 50-station ring (see Fig. 9) is 0.5, the delay is less than two average message lengths. Also shown on Figs. 8-10 are the results of simulations which will be discussed presently.

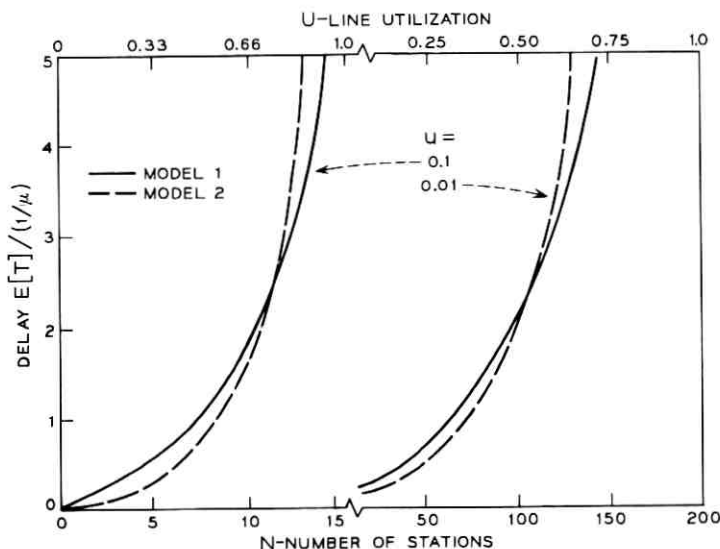


Fig. 6—Normalized delay for  $u = 0.1$  and  $0.01$  (uniform inputs),  $\gamma = 1$ .

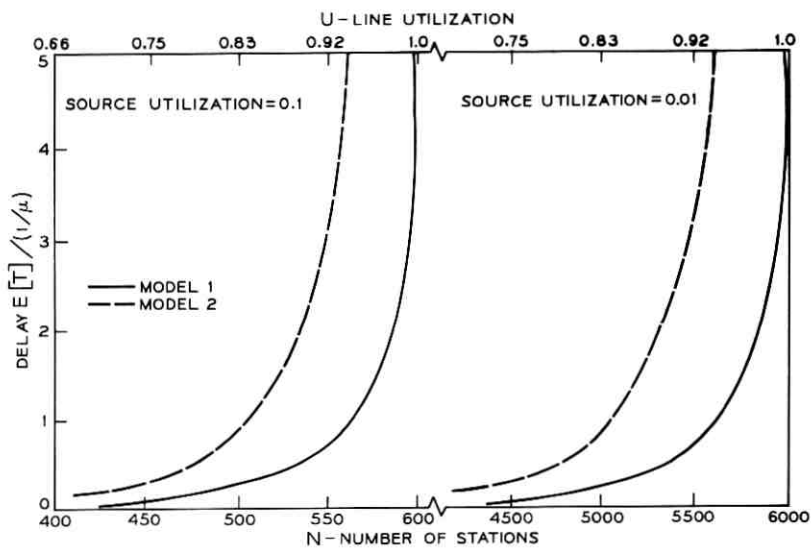


Fig. 7—Normalized delay for  $u = 0.1$  and  $0.01$  (uniform inputs),  $\gamma = 1/30$ .

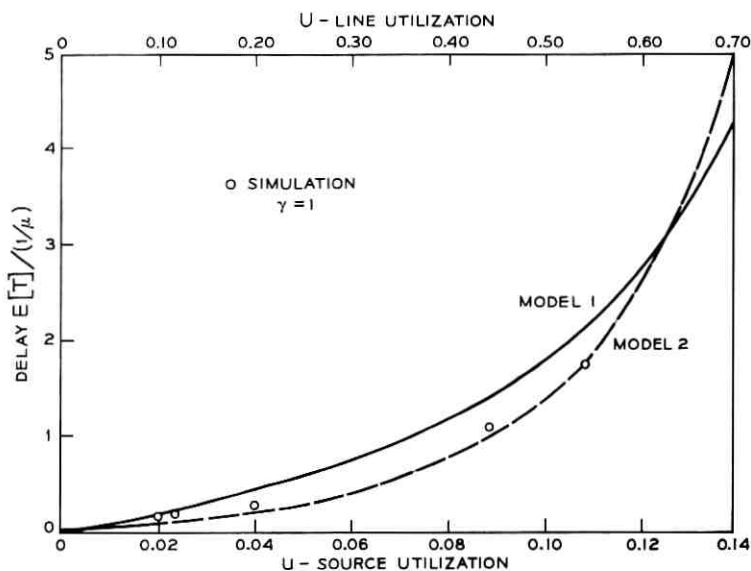


Fig. 8—Normalized delay for 10-station ring (uniform inputs).

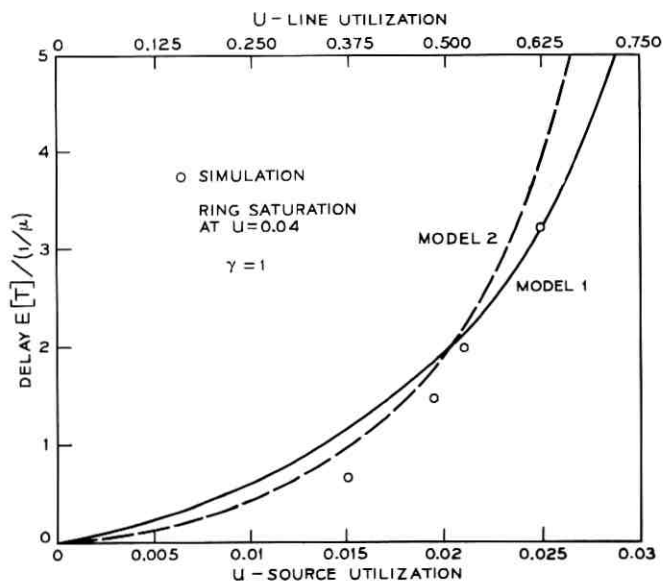


Fig. 9—Normalized delay for 50-station ring (uniform inputs).

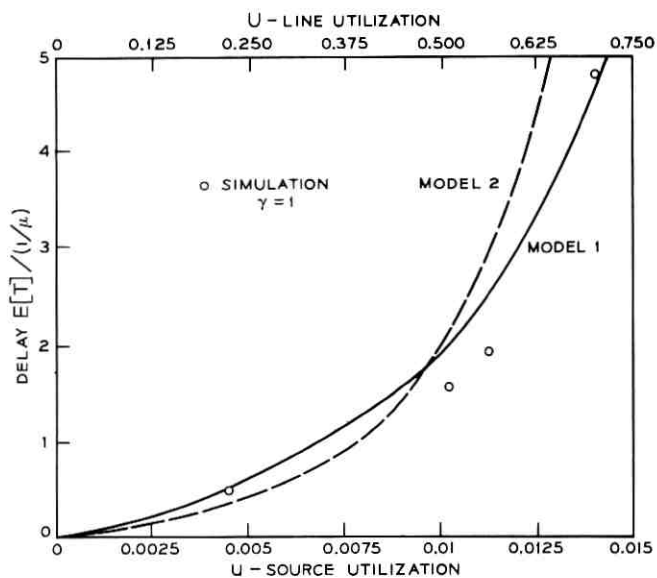


Fig. 10—Normalized delay for 100-station ring (uniform inputs).

A comparison of Figs. 10 and 11 shows the impact of different values of  $\gamma$ . On both figures delay is shown as a function of line utilization for 100-station rings. The difference between them is that  $\gamma = 1$  on Fig. 10 and  $\gamma = 1/30$  on Fig. 11. For  $U = 0.5$  and  $\gamma = 1$  (Fig. 10), we find that the delay is two message units. In contrast, for  $\gamma = 1/30$  and the same line loading (Fig. 11), the delay is near zero. When  $\gamma = 1/30$ , the line has very large capacity compared to the source data rates, even when the line is moderately loaded.

It is convenient to use Model 2 to examine the asymmetric case of many users communicating with a single computer on the ring. Let  $u_c$  denote the utilization of the computer and  $u_s$  denote the utilization of the customer in each of the  $N$  stations connected to the computer. We assume that the computer distributes its traffic equally among all the other stations. Applying equations (7) and (9) the line utilization as seen by the  $i$ th station after the computer is

$$U_i^* = \gamma_c u_c \frac{(N - i)}{N} + \gamma_s u_s (i - 1), \quad i = 1, 2, \dots, N, \quad (33)$$

where  $\gamma_c$  and  $\gamma_s$  are the ratios of source packet rate to line packet rate for the computer and the user, respectively [see equation (2)].

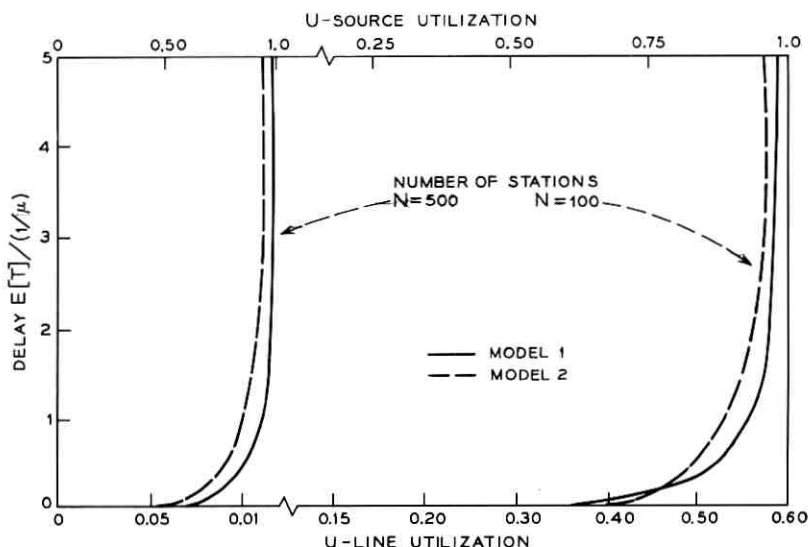


Fig. 11—Normalized delay for 100 and 500 stations (uniform inputs),  $\gamma = 1/30$ .

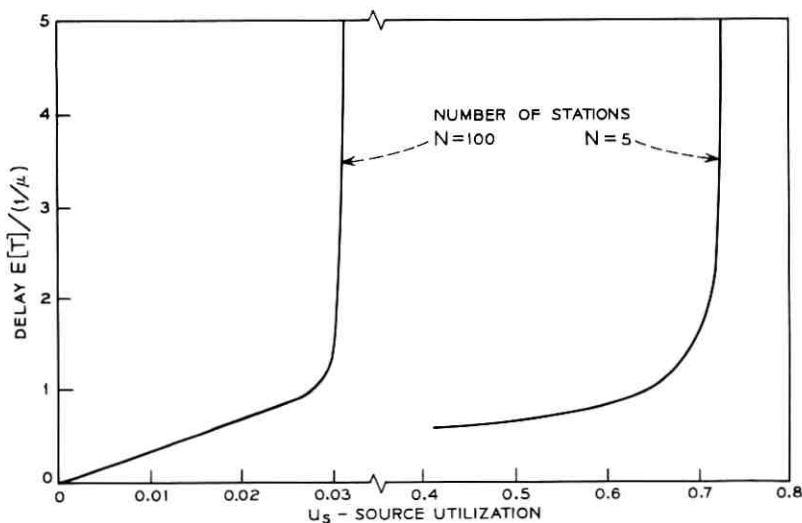


Fig. 12—Normalized delay at most critical station for  $N = 5$  and 100 stations,  $\gamma = 1/30$  (asymmetric case).

In our computations we assume that the computer-to-user traffic is ten times the user-to-computer traffic ( $u_c \gamma_c = 10 \gamma_s N u_s$ ).<sup>†</sup> Equation (33) leads us to conclude that under this assumption the most critical station in the ring is the one right after the computer ( $i = 1$ ) since the line traffic at this point is heaviest.

Equation (33) may be used in conjunction with equation (32) to find the delay normalized to the line busy period at the most critical station. Because of the way the line busy period is calculated in Model 2, we may in turn normalize the line busy period to the activity time of the computer. The results are shown in Fig. 12 where delay, normalized to the computer busy period, is shown as a function of  $u_s$  and  $u_c$  and the number of stations as parameters. In Fig. 12 we have taken  $\gamma_s = 1/30$  and  $\gamma_c = 1$ .

## VII. SIMULATION RESULTS AND COMPARISON WITH THEORY

An investigation of the system was carried out by means of simulation as well as analysis. Single rings comprising the one A-box and from 10 to 100 B-boxes were simulated. All of the simulation results were for symmetric rings in which each station has identical traffic

<sup>†</sup> Studies of computer traffic support this assumption.<sup>6</sup>

characteristics and transmits equal portions of its traffic to the other stations.

In the simulation, as in the analysis, our attention was focused on average delay. Nevertheless, as we shall see, the simulation yielded information on other characteristics of delay which can be compared to analytical results.

The simulations attempted to mirror as closely as possible the actual operation of the ring. At each station a sequence of message and idle period lengths are chosen randomly from exponential distributions. As the messages are generated they are assembled into an integral number of packets. Bit stuffing is used to round out the last packet in a message. The destination of each message is found by a random selection from  $N - 1$  equally probable choices.

After packets are generated they are given an initial time tag and sent to a buffer. The packets are stored in the buffer until they are multiplexed on the line. When a packet is multiplexed on the line, the time is noted and a difference in multiples of packets is taken with the initial time for each packet. It may happen, especially in a lightly loaded system, that a packet is multiplexed on the line immediately. In this case the time difference is zero.

These time differences indicate the delay suffered by a packet due to line traffic. By noting the time difference for the last packet in a message, we have a measurement of message delay. Histograms of message delay were compiled and results drawn from these histograms will be presented in the sequel.

A key step in the theoretical calculation was the estimation of line busy and idle period durations. Accordingly, in order to check the consistency of the models, measurements were made of line busy and idle period durations. These measurements will also be presented in the sequel.

In order to keep the simulation effort within reasonable bounds, it was necessary to fix some of the parameters of the system. Thus for most of the data that follow the average message length was fixed at 100 bits. The messages were quantized into 125-bit packets ( $B_p = 125$ ). Header information was neglected ( $H = 0$ ). Source utilization was varied by choosing appropriate idle durations. In this case 70 percent of the messages are of one packet duration. As a check, selected simulations were run with different ratios of message length to packet size.

As seen in the previous section, the theoretical models estimated average delays of one or two average message lengths for light to

moderate line loadings. For  $\gamma = 1/30$ , estimates of average delay were small even for reasonably heavy line loadings. In Figs. 8, 9, and 10 average delays yielded by simulation are shown in comparison with theoretical results. These averages were taken over all stations for each of the line loadings shown. In Fig. 8 we see that for the 10-station ring the theoretical estimates given by Model 2 are quite close to simulation results, differing by substantially less than a message duration. The estimates produced by Model 1 for moderate line loads are also fairly good, overestimating delay by about 0.3 message duration. Theoretical estimates compare well with simulation results for the 50- and 100-station ring as well. In general both models overestimate the simulation delays somewhat. For line loadings below 0.5, Model 1's estimates are within 0.5 message duration above simulation values, while Model 2's estimates are somewhat closer. For line loadings above 0.5, Model 1's estimates are closer to simulation results.

It is significant that delay estimates obtained for line loadings below the knee of the curve ( $U \cong 0.5$  for the 10-station ring) are well within an average message duration. Since the system would probably be operated in this region, delay estimates for these line loadings are important.

Each of the simulation points presented above is an average of between 7000 and 14,000 data points obtained through simulation. Along with average delay the standard deviation of delay was estimated. Estimates of the standard deviation of average delay were obtained by assuming that the standard deviation obtained from simulation was equal to the standard deviation of the underlying distribution of delay. The results showed that standard deviations of the averages are reasonably low. For example, for a 10-station ring at a line loading of 0.43, 10,000 data points were taken and the standard deviation was estimated to be 1.61 average message durations. The standard deviation of the mean is estimated to be 0.016 average message duration which is less than 2 percent of the average delay. The situation is the same on the 100-station ring. At a line loading of 0.52 where 7000 data points were taken, the standard deviation of the mean was estimated to be approximately 2 percent of the average delay.

Average delay is clearly not the only characteristic of delay that is important in judging the performance of a system. Both the simulation and the analysis provided results on characteristics of delay beyond averages. As mentioned earlier, histograms of message delay were compiled by the simulation program. On Fig. 13 the cumulative probability graph of message delay is shown. Also shown on Fig. 13 is the

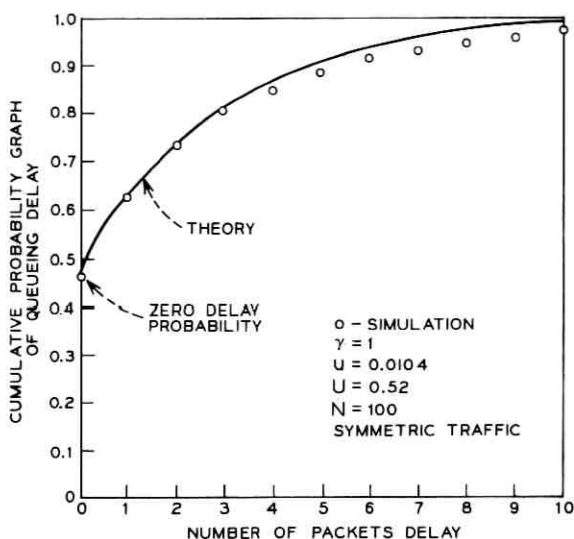


Fig. 13—Cumulative probability graph of queueing delay in a 100-station ring. Data compared with estimates from Model 2.

probability distribution predicted by Model 2 from the same line loading and system configuration [see equation (28)]. The probability distribution for Model 1 was not readily obtainable. The cumulative probability graph shown here is typical of other system configurations and line loadings. It shows a nonzero component at zero delay with diminishing probabilities of larger packet delays.

In order to summarize simulation results along these lines, three sets of numbers will be presented. They are probability of zero delay and a conditional mean and standard deviation of delay. The mean and standard deviation of message delay here are conditioned on the message having nonzero delay.

In Table I are shown the probability of zero delay given by simulation and by Model 1 [equation (27)] and Model 2 [equation (29a)]. For the smallest utilization in the 10-station ring the error between simulation and theory is within 15 percent. For the other line loadings the estimate obtained from Model 2 is within 10 percent of simulation values while Model 1 considerably underestimates zero message delay probability. For the highest loading considered,  $U = 0.7$  on the 100-station ring, neither model predicts the simulation value very well.

Estimates of means and standard deviations of delay conditioned

TABLE I—PROBABILITY OF ZERO MESSAGE DELAY

N—Number of Stations	U—Line Utilization	Simulation	Theory	
			Model 1	Model 2
10	0.10	0.906	0.833	0.918
10	0.20	0.80	0.688	0.833
10	0.43	0.565	0.418	0.624
10	0.54	0.464	0.311	0.514
100	0.235	0.773	0.622	0.769
100	0.52	0.454	0.318	0.485
100	0.54	0.418	0.264	0.420
100	0.70	0.252	0.178	0.304

on nonzero delay for both simulation and theory are presented in Table II. Comparison of the theoretical estimates of the mean shows that for the lightest loading in both the 10- and the 100-station rings the analysis estimates the delay within 3 percent. For the heavier loadings, excluding the  $U = 0.7$  loading on the 100-station ring, the error is about 20 percent of the simulated results for Model 1 and about 25 percent for Model 2.

In summary, the data presented in Tables I and II indicate that a substantial portion of the messages (i.e., those that have no delay) are accounted for, and that the remaining messages have an average delay that is predictable, in the lighter loads, within 3 percent. For example, in the 10-station ring with a line loading of 0.1, 90.6 percent

TABLE II—MEAN AND STANDARD DEVIATION FOR DELAYED MESSAGES (IN AVERAGE MESSAGE LENGTHS)

N—Number of Stations	U—Line Utilization	Simulation		Theory		
		Mean, $E[T   T > 0]$	Standard Deviation $\sigma[T   T > 0]$	Model 1		Model 2 <sup>†</sup>
				Mean	Std Dev	Mean
10	0.10	1.18	0.79	1.19	1.22	1.18
10	0.20	1.34	0.99	1.44	1.46	1.44
10	0.43	2.06	1.89	2.33	2.48	2.58
10	0.54	2.66	2.75	3.12	3.34	3.78
100	0.235	1.57	1.59	1.61	1.61	1.69
100	0.52	2.95	3.20	3.13	3.16	4.26
100	0.54	3.29	3.55	3.78	3.81	4.83
100	0.70	6.48	7.89	5.60	5.65	10.72

<sup>†</sup> The density in this case is exponential, and thus the mean and standard deviation are equal.

of the messages have no delay and the remaining 9.4 percent have an average delay of 1.18 average message durations.

One observed difference between theory and simulation lies in the prediction of zero message delay by Model 1, which, for moderate line loadings, noticeably underestimates this quantity. There is evidence that the difficulty here may lie in the way that Model 1 treats quantization effects. For example, message lengths were taken to be exponentially distributed when, in fact, they are geometrically distributed. As pointed out in the beginning of this section, most of the simulation results are carried out for an average message length of 100 bits and a packet length of 125 bits. Investigations of the effect of quantizing messages into packets are continuing.

As mentioned earlier in this section, data were gathered on line busy and idle periods in order to check the consistency of our models. In Table III are shown the average durations of line busy periods for different loadings measured at one station in the ring. For comparison the average line busy periods predicted by Models 1 and 2 are also shown. Model 1 underestimates the length of the busy period by approximately 10 percent. The estimates given by Model 2 consistently overestimate the duration of the line busy period. For line loadings greater than 0.5, the estimate is poor.

The average durations of line idle periods as found in simulation are shown in Table IV. Again Model 1 underestimates while Model 2 overestimates. The error for Model 1 is higher than for the corresponding line busy periods. For line loadings greater than 0.5, Model 2 yields high estimates.

If the data on the durations of line busy periods obtained from

TABLE III—LINE BUSY PERIODS<sup>†</sup> (PACKETS)

No. of Stations	U-Line Utilization	Simulation		Theory	
		Mean	Standard Deviation	Mean (Model 1)	Mean (Model 2)
10	0.10	1.58	1.02	1.53	1.65
10	0.20	1.81	1.41	1.70	1.98
10	0.43	2.66	2.74	2.24	3.36
10	0.54	3.20	3.64	2.80	4.76
100	0.235	1.94	1.52	1.78	2.36
100	0.52	2.96	3.07	2.80	5.87
100	0.54	3.32	3.87	3.24	7.9
100	0.70	5.08	7.32	4.49	14.5

<sup>†</sup> The results shown here are averages for a single station. The line utilization is averaged over the entire ring.

TABLE IV—LINE IDLE PERIODS<sup>†</sup> (PACKETS)

No. of Stations	<i>U</i> -Line Utilization	Simulation		Theory	
		Mean	Standard Deviation	Mean (Model 1)	Mean (Model 2)
10	0.10	14.07	13.30	17.60	18.90
10	0.20	7.22	6.80	6.80	7.93
10	0.43	3.40	2.97	2.84	4.48
10	0.54	2.74	2.24	2.34	3.95
100	0.235	6.34	5.71	5.95	7.70
100	0.52	2.96	2.75	2.54	5.85
100	0.54	2.78	2.39	2.3	5.65
100	0.70	2.05	1.58	1.95	6.20

<sup>†</sup> The results shown here are averages for a single station. The line utilization is averaged over the entire ring.

simulation are used in the calculation of average delay the conclusions do not change substantially. Except for the  $U = 0.7$  load point in the 100-station ring, the average delays predicted by Model 1 increase by less than 10 percent. Below line loadings of  $U = 0.5$ , the predictions of Model 2 decrease but are still fairly close to simulation points. Regions where the line loading is light to moderate are of greatest interest since it is most likely that systems would be operated in this region. For higher line loadings, delay in terms of average message lengths is large and small changes in loading lead to large changes in delay.

#### VIII. CONCLUSION

We conclude with a summary of our results. The analysis and the simulation of 10-, 50-, and 100-station rings show that for  $\gamma = 1$ , i.e., source rate and line rate equal, message delay is less than 2 average message durations for line loading up to 0.5 of capacity. For line loadings greater than 0.5, delay increases substantially. For  $\gamma = 1/30$ , i.e., a low-speed source feeding into a high-speed line, average delay in terms of average message durations is low for line loadings up to 0.8. Analytical and simulation results indicate that there is a nonzero probability of zero message delay at all line loadings. The probability of zero message delay is greater than 0.5 for line loadings less than 0.5. Analysis and simulation indicate that the probability of a specific message delay decreases monotonically with the value of delay. The rate of decrease is similar to that of an exponential distribution (see Fig. 13).

For light to moderate line loads the theoretical models of average message delay show good agreement with the simulation results. For high line loads some of the approximations used in the theoretical models are weakened and agreement is not as good. However, even for heavy loading, there is meaningful agreement between analysis and simulation since both predict large delay and large shifts in delay with small shifts in line loading.

Some of the discrepancy between analysis and simulation may be due to the fact that the analysis did not take into account quantizing effects. For example, line busy periods must be an integral number of packets in duration, whereas the analysis treated line busy periods as a continuous random variable. Investigation of these effects on message delay will be carried out in the future.

The simulation program is capable of simulating systems where the traffic pattern is not symmetric and work will continue in this direction.

#### IX. ACKNOWLEDGMENTS

The authors wish to thank M. J. Ferguson for many fruitful discussions. Acknowledged also is the assistance of B. Avi-Itzhak and M. Segal in deriving results on the server with breakdown queueing model.

The simulation programming was done by R. R. Anderson, who is also responsible for coaxing from the computer all of the simulation points that are shown here. The authors are deeply appreciative of his efforts.

#### APPENDIX A

##### *Effect of Quantization*

In the text we have assumed that the duration of a source active period is exponentially distributed with parameter  $\mu_i$  (for source  $i$ ). During the active period the source emits bits at a constant rate of  $b_i$  bits/second. The data is bundled into packets with  $B_p$  bits/packet. The probability that there are  $j$  packets in a message is given by

$$D_i = \int_{(j-1)B_p/b_i}^{jB_p/b_i} \mu_i \exp(-\mu_i t) dt, \quad i = 1, 2, \dots, N$$

$$= \exp(-(j-1)B_p\mu_i/b_i)[1 - \exp(-B_p\mu_i/b_i)].$$

Let

$$A \triangleq \exp[-B_p\mu_i/b_i];$$

then

$$D_i = A^{i-1}(1 - A).$$

The mean number of packets per message is

$$1/M_i = \sum_{j=1}^{\infty} jD_j = \frac{1}{1 - \exp(-B_p \mu_i / b_i)}.$$

#### APPENDIX B

In an earlier paper Avi-Itzhak and Naor<sup>11</sup> found the average delay of a customer arriving at a server that is subject to random breakdown. Recently, using a similar line of reasoning, Avi-Itzhak<sup>14</sup> found the Laplace-Stieltjes transform of the density of this delay  $T'_i$  to be:

$$\mathcal{L}_{T'_i}(v) = (1 - U_i^* - \gamma\theta_i) \frac{[\Lambda_i^* \mathcal{L}_{L_i}(v) - \Lambda_i^* - v] \mathcal{L}_{S_i}(v + \Lambda_i^* - \Lambda_i^* \mathcal{L}_{L_i}(v))}{\lambda_i - v - \lambda_i \mathcal{L}_{S_i}(v + \Lambda_i^* - \Lambda_i^* \mathcal{L}_{L_i}(v))}, \quad (34)$$

where  $\mathcal{L}_{L_i}(v)$  and  $\mathcal{L}_{S_i}(v)$  are the Laplace-Stieltjes transforms of  $L_i$  and  $S_i$  respectively. (Recall that in the main body of the text  $L_i$  is defined as the duration of the line busy period at station  $i$  and  $S_i$  is defined as the time required to multiplex a message on a free line.) In this derivation it is assumed that the line idle periods are exponentially distributed with parameter  $\Lambda_i^*$ . It is also assumed that messages arrive at a Poisson rate  $\lambda_i$ .

In order for this result to be applicable to our problem, some modification of equation (34) is necessary. The expected value of  $T'_i$  yielded by (34) when the line is entirely free for a long period of time is  $E[S_i]$ . But this is a delay that is due to multiplexing alone and is not a function of line traffic. Since we are interested in delay that is dependent on line congestion we remove this multiplexing delay.

The delay described by equation (34) is the sum of two independent components, the waiting time and the residence time. The waiting time is the interval from when the message first arrives until it is first multiplexed on the line. The residence time is the interval in which the message is multiplexed on the line, including line busy periods during which the message is blocked. The L - S transform of the density of the residence time is given by

$$\begin{aligned} & \mathcal{L}_{S_i}(v + \Lambda_i^* - \Lambda_i^* \mathcal{L}_{L_i}(v)) \\ &= \int_0^{\infty} dt e^{-vt} \sum_{k=0}^{\infty} \int_0^t dx \frac{(\Lambda_i^* x)^k e^{-x\Lambda_i^*}}{k!} f_{L_i}^k(t-x) f_{S_i}(x), \quad (35) \end{aligned}$$

where  $f_{s_i}(x)$  is the density of the message multiplexing time and  $f_{L_i}^{*k}(x)$  is the  $k$ -fold convolution of the line busy period. This expression is obtained by adding the message multiplexing times and all of the intervening line busy periods. Now if we simply add together only the line busy periods, removing the line multiplexing time, we have

$$\mathcal{L}_{S_i}(\Lambda_i^* - \Lambda_i^* \mathcal{L}_{L_i}(v)) = \int_0^\infty dt e^{-\lambda_i t} \sum_{k=0}^\infty \int_0^\infty dx \frac{(\Lambda_i^* x)^k}{k!} e^{-x \Lambda_i^*} f_{L_i}^{*k}(t) f_{s_i}(x). \quad (36)$$

Equation (34) becomes

$$\mathcal{L}_{T_i}(v) = (1 - U_i^* - \gamma \theta_i) \frac{[\Lambda_i^* \mathcal{L}_{L_i}(v) - \Lambda_i^* - v] S_i(\Lambda_i^* - \Lambda_i^* \mathcal{L}_{L_i}(v))}{\lambda_i - v - \lambda_i \mathcal{L}_{S_i}(v) + \Lambda_i^* - \Lambda_i \mathcal{L}_{L_i}(v)}. \quad (37)$$

#### REFERENCES

1. Pierce, J. R., Coker, C. H., and Kropfl, W. J., "Network for Block Switching of Data," IEEE Conv. Rec., New York, March 1971.
2. Steward, E. H., "A Loop Transmission System," 1970 ICC, vol. 2, pp. 36-1, 36-9.
3. Farmer, W. D., and Newhall, E. E., "An Experimental Distributed Switching System to Handle Bursty Computer Traffic," Proc. ACM Conf., Pine Mountain, Georgia, October 1969.
4. Fraser, A. G., "The Coordination of Communicating Processes," unpublished work.
5. Kropfl, W. J., "An Experimental Data Block Switching System," unpublished work.
6. Jackson, P. E., and Stubbs, C. D., "A Study of Multi-access Computer Communications," AFIPS, Conf. Proc., vol. 34, p. 491.
7. Jackson, P. E., and Fuchs, E., "Estimates of Distributions of Random Variables for Certain Computer Communications Traffic Models," Proc. ACM Conf., Pine Mountain, Georgia, October 1969.
8. Pilc, R. J., unpublished work.
9. Chu, W. W., "An Analysis of Buffer Behavior for Batch Poisson Arrivals and Single Server with Constant Output Rate," IEEE Trans. Commun. Tech., COM-18, No. 5 (October 1970), pp. 613-619.
10. Kleinrock, L., *Communications Nets—Stochastic Message Flow and Delay*, New York: McGraw-Hill, 1964.
11. Avi-Itzhak, B., and Naor, P., "Some Queueing Problems with the Service Station Subject to Breakdown," Oper. Res., 11, No. 3, 1963, pp. 303-320.
12. Sherman, D. N., "Data Buffer Occupancy Statistics for Asynchronous Multiplexing of Data in Speech," Proc. ICC, San Francisco, California, June 1970.
13. Little, J. D. C., "A Proof of the Queueing Formula  $L = \lambda W$ ," Oper. Res., 9, 1961, pp. 383-387.
14. Avi-Itzhak, B., unpublished work.

# Analysis and Design of Elementary Blinders for Large Horn Reflector Antennas

By DAVID T. THOMAS

(Manuscript received May 28, 1971)

*An analysis of E-plane (transverse) radiation from horn reflector antennas for horizontal (transverse) polarization is presented. This analysis was based on Geometrical Theory of Diffraction with modifications to account for (i) finite edges, (ii) grazing incident wave, and (iii) aperture illumination. Once proven valid for our purposes, the analysis was extended to permit blinders to be added to the antenna.*

*Experimental and theoretical studies of single edge blinders have shown them to move the azimuth location of undesirable high sidelobes but not substantially reduce the sidelobe level. A half blinder, however, was shown to reduce the undesired 90-degree sidelobe to  $-62$  dB, an 8-dB reduction. Simultaneously, sidelobe levels are below  $-62$  dB for azimuths between 35 degrees and 180 degrees at both 3.74 and 6.325 GHz. Theoretical predictions indicate it is broadband at 4, 6, and 11 GHz. The half blinder also has excellent mechanical features.*

## I. INTRODUCTION

In recent years, demands have been made to improve the sidelobe performance of the Bell System horn reflector antenna. One demand is related to the Metropolitan Junction Concept\* for radio relay route planning. This concept was initiated in the mid 1960's and resulted in narrower angles between radio relay routes converging on a junction point. Generally, increased service demands also added to route congestion and placed more stringent requirements on the antenna performance. A combined experimental and theoretical program was begun with the expressed purpose of reducing certain high sidelobes.

\* In the Metropolitan Junction Concept, only radio relay routes terminating in a large city are brought into the city. All other routes bypass the city around a ring of stations about 20 miles out. This is contrary to the practice prior to the 1960's.

A previous paper<sup>1</sup> discussed improvements in the transverse-plane radiation levels for vertical (longitudinal) polarization (VP). This present paper is addressed to transverse-plane radiation for horizontal (transverse) polarization (HP).\*

The horn reflector antenna<sup>2</sup> is a combination of a square electromagnetic horn and a reflector which is a sector of a paraboloid of revolution. A side view and front plane view of the antenna are illustrated in Fig. 1. The results given in this paper refer to the Bell System horn reflector antenna which has the following aperture dimensions:

Flare half angle	$\alpha = 14.5$ degrees
Front tilt angle	$\beta = 14.5$ degrees
Aperture side edge length	2.59 meters
Average aperture width	2.59 meters.

The intended frequency bands of operation are 3.70–4.20 GHz, 5.925–6.325 GHz, and 10.7–11.7 GHz.

One very interesting aspect of this antenna is the low inherent sidelobes in the azimuth (transverse) plane. For horizontal polarization, the sidelobe levels beyond 30 degrees are 60 dB or more below the main beam for the Bell System antenna, except for a major high-sidelobe region near 90 degrees with levels of about  $-52$  dB at 3.74 GHz and  $-58$  dB at 6.325 GHz.

The elimination of this high sidelobe region was the major purpose of this work. One approach earlier tried by R. R. Grady<sup>1</sup> was to add "blinders," i.e., change the shape of the side edges of the aperture. Although the blinder shapes tried by Grady moved the location of the major high-sidelobe region of the antenna, the overall reduction in sidelobe levels was insufficient for our purposes.

In order to expedite development of the complex blinder shapes which we felt would be necessary, a theoretical model was first developed for the original antenna and is presented here. This same model has been extended to predict the radiation patterns of horn reflector antennas with multiple edge shaped blinders attached.

## II. GEOMETRICAL THEORY OF DIFFRACTION

The analytical method used for predicting the E-plane radiation was based on Geometrical Theory of Diffraction (GTD).<sup>3,4</sup> GTD has a long history of providing solutions to electromagnetics problems.

\* Longitudinal polarization and longitudinal plane are aligned with the pyramidal horn axis. Transverse polarization and transverse plane are perpendicular to the horn axis.

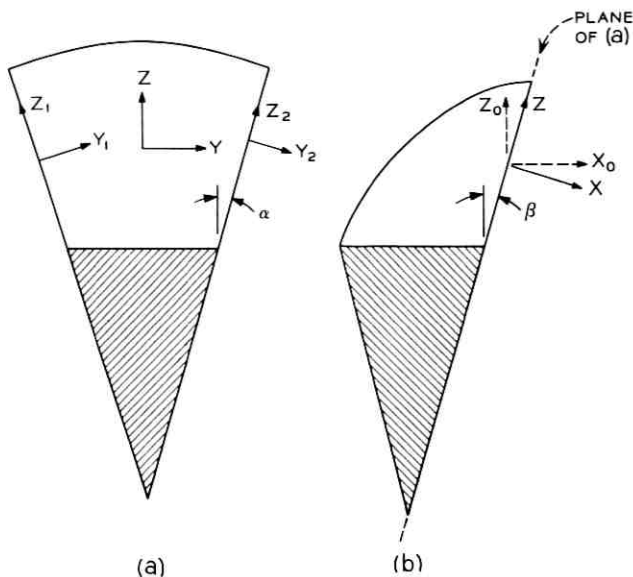


Fig. 1—Front and side views of a horn reflector antenna.

In situations similar to ours, GTD has successfully predicted the far sidelobe levels of pyramidal horn antennas<sup>5-7</sup> and other structures such as parallel plate waveguides.<sup>8,9</sup> In order to apply GTD to the problem at hand, it was necessary to account for (i) the *finite* length of each edge<sup>10</sup> and (ii) the incident wave direction *parallel* to the side walls of the antenna.<sup>11</sup> In addition, the illumination function with the  $TE_{10}$  incident mode in the horn was included. Also, as the azimuth angle passes 90 degrees, visually one edge disappears. To account for this phenomenon, the contribution of the disappearing edge was neglected when the azimuth angle exceeds 90 degrees, i.e., only singly diffracted rays were included. Two checks on the accuracy of our model were used: (i) the *measured* E-plane radiation pattern for HP at 3740 MHz, and (ii) radiation patterns computed by an approximate Kirchhoff *Aperture Integral* as described in a later section.

The incident wave in the pyramidal horn section is the  $TE_{10}$  mode with orientation depending on polarization. For horizontal polarization, the amplitude variation is sinusoidal from front to back and uniform from side to side. After reflection by the paraboloidal surface, the incident wave amplitude is tapered by the  $1/R$  spherical attenuation and slightly distorted but, to a good approximation, the vertical



for the tilted aperture and the fact that the incident wave direction is not perpendicular to the aperture.

For a grazing incident wave (direction of propagation parallel to the sides) such as we have,  $\gamma$  is zero and only the first term of the diffraction coefficient remains,<sup>11</sup>

$$D = -\frac{e^{i\pi/4}}{\sqrt{8\pi K} \cos \beta} \text{CSC} \left( \frac{\phi'}{2} \right). \quad (4)$$

The angle,  $\zeta$ , which relates  $\phi'$  and  $\phi_1$  as

$$\phi' = \phi_1 - \zeta \quad (5)$$

was found from the coordinate transformations in the Appendix to be defined by

$$\tan \zeta = \sin \alpha \tan \beta. \quad (6)$$

For the second edge, we found that

$$\phi' = \phi_2 + \zeta, \quad (7)$$

with  $\zeta$  as given above.

The *finite* length of the diffracting edges has been considered by C. E. Ryan.<sup>10</sup> The diffracted field sources can be viewed mathematically as magnetic line currents. Since GTD is a *local* phenomenon, the use of magnetic currents is valid for finite edges as well. Taking into consideration the radiation patterns of finite length line currents, the *far zone* diffracted fields of the side edges become

$$H_{\theta_1} = -\frac{j\omega\epsilon}{4} \frac{2H_0 b}{K} \frac{e^{+iKR_1}}{R_1} \text{CSC} \frac{\phi_1 - \zeta}{2} \sin \theta_1 \cdot \frac{\cos [Kb(\cos \theta_1 - \sin \beta \cos \alpha)]}{\frac{\pi^2}{4} - (Kb)^2(\cos \theta_1 - \sin \beta \cos \alpha)^2}, \quad (8)$$

$$H_{\theta_2} = +\frac{j\omega\epsilon}{4} \frac{2H_0 b}{K} \frac{e^{+iKR_2}}{R_2} \text{CSC} \frac{\phi_2 + \zeta}{2} \sin \theta_2 \cdot \frac{\cos [Kb(\cos \theta_2 - \sin \beta \cos \alpha)]}{\frac{\pi^2}{4} - (Kb)^2(\cos \theta_2 - \sin \beta \cos \alpha)^2}. \quad (9)$$

There remains only the superposition of  $H_{\theta_1}$  and  $H_{\theta_2}$  and the cal-

ulation of radiation patterns. In the azimuth plane,  $\phi_o$  will vary from 0 degrees to 180 degrees and  $\theta_o$  is 90 degrees. Only the horizontal polarized field component,  $E_{\phi_o}$ , contributes to the azimuth radiation pattern. Since  $H_{\theta_o}$  corresponds to  $E_{\phi_o}$ , the HP fields are

$$\vec{H}_{HP} = (\hat{\theta}_o \cdot \hat{\theta}_1)H_{\theta 1} + (\hat{\theta}_o \cdot \hat{\theta}_2)H_{\theta 2}. \quad (10)$$

The normalized *directivity* will be

$$G(\phi_o) = \frac{|\vec{H}_{HP}|_{\theta_o = \pi/2}^2}{|\vec{H}_{HP}|_{\theta_o = 0}^2}. \quad (11)$$

For azimuth angles 0 degrees to 90 degrees, equation (10) was used. Beyond 90 degrees, however, only one edge was assumed to be visible and the second edge contribution was neglected. The discontinuity at 90 degrees produced by this move is very small and the slightly improved accuracy which would result if doubly diffracted rays were used was not felt worth the additional work.

### III. KIRCHHOFF APERTURE THEORY

In order to provide an independent check on the accuracy of our previous model, the radiation pattern was computed using Kirchhoff Aperture Integrals.<sup>13,14</sup> Once the incident fields,  $\vec{E}^i(Y, Z)$ , are known in the actual antenna aperture, the *far zone* radiated fields,  $\vec{E}^s(R, \theta, \phi)$ , are given by

$$\vec{E}^s = \frac{jK}{4\pi R} [e^{iKR} [\mathbf{R} \times (\mathbf{n} \times \vec{N}) - \mathbf{R} \times (\mathbf{R} \times (\mathbf{n} \times (\mathbf{n}_i \times \vec{N})))] \quad (12)$$

where

$\mathbf{R}$  is the radial unit vector,

$\mathbf{n}$  is the outward unit normal to the aperture,

$\mathbf{n}_i$  is the unit vector in the direction of propagation of the incident wave,

and  $\vec{N}$  is given by

$$\vec{N} = \iint_{\text{Aperture}} \vec{E}^i(Y, Z) e^{-iK(Y \sin \theta \sin \phi + Z \cos \theta)} dy dz, \quad (13)$$

and the integral is over the actual aperture—not the projected aperture. The coordinates  $XYZ$  are as shown in Fig. 1, with  $R\theta\phi$  being the spherical coordinates associated with  $XYZ$ . For HP,  $N_z$  is neglected and  $N_r$  is found to be

$$N_Y = \frac{\pi ab}{-jKa \sin \theta \sin \phi} \cdot \left\{ e^{-jKa \sin \theta \sin \phi} \frac{\cos [Kb(\cos \theta - \sin \beta + \tan \alpha \sin \theta \sin \phi)]}{\frac{\pi^2}{4} - (Kb)^2(\cos \theta - \sin \beta + \tan \alpha \sin \theta \sin \phi)^2} - e^{+jKa \sin \theta \sin \phi} \frac{\cos [Kb(\cos \theta - \sin \beta - \tan \alpha \sin \theta \sin \phi)]}{\frac{\pi^2}{4} - (Kb)^2(\cos \theta - \sin \beta - \tan \alpha \sin \theta \sin \phi)^2} \right\}. \quad (14)$$

Coordinate transformations between  $\theta$ ,  $\phi$  and  $\theta_o$ ,  $\phi_o$  are given in the Appendix.

A computer program based on equations (8) to (11) was written to

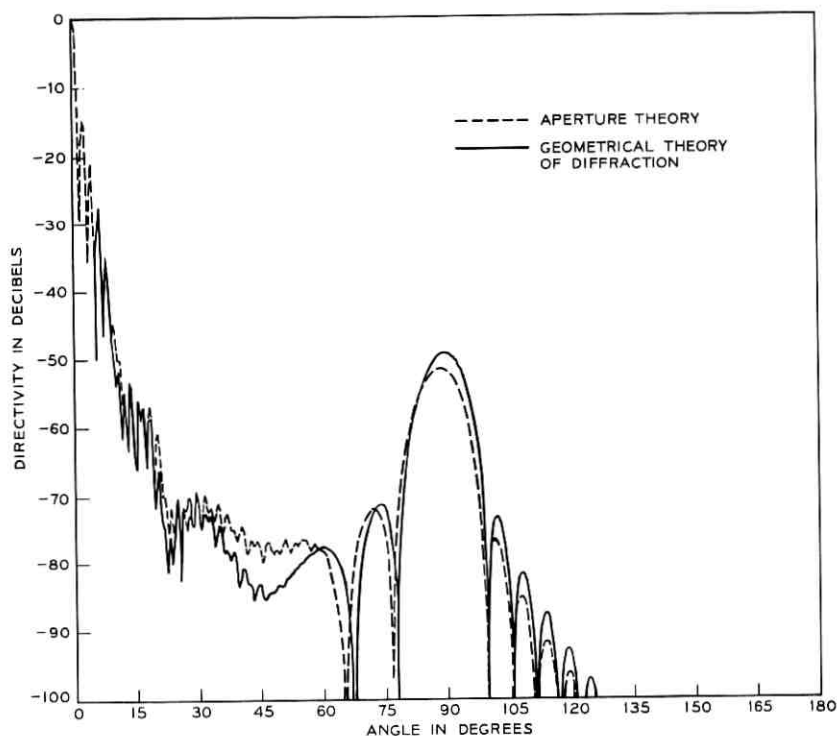


Fig. 3—Comparison of predicted transverse-plane ( $\phi_o$ ) radiation patterns of a horn reflector antenna using GTD and aperture theory (transverse polarization at 3740 MHz).

calculate and plot the *far zone* radiation pattern of the Bell System horn reflector antenna in the azimuth plane for horizontal polarization. Figure 3 compares the results with a similar radiation calculation using the approximate Kirchoff Aperture Integral of equations (12) to (14). The agreement is remarkably good, which is somewhat surprising in view of the limitations of aperture theory. In this case at least aperture theory appears to be accurate for azimuth angles,  $\phi_0$ , up to almost 90 degrees.

The necessity of using GTD instead of Aperture Integrals is twofold: (i) we are interested in far sidelobes beyond 90 degrees where Aperture Integrals are inappropriate, and (ii) the ultimate goal is a treatment of the antenna edges, multiple edge blinders, for example, which would require a degree of sophistication beyond the capacity of Aperture

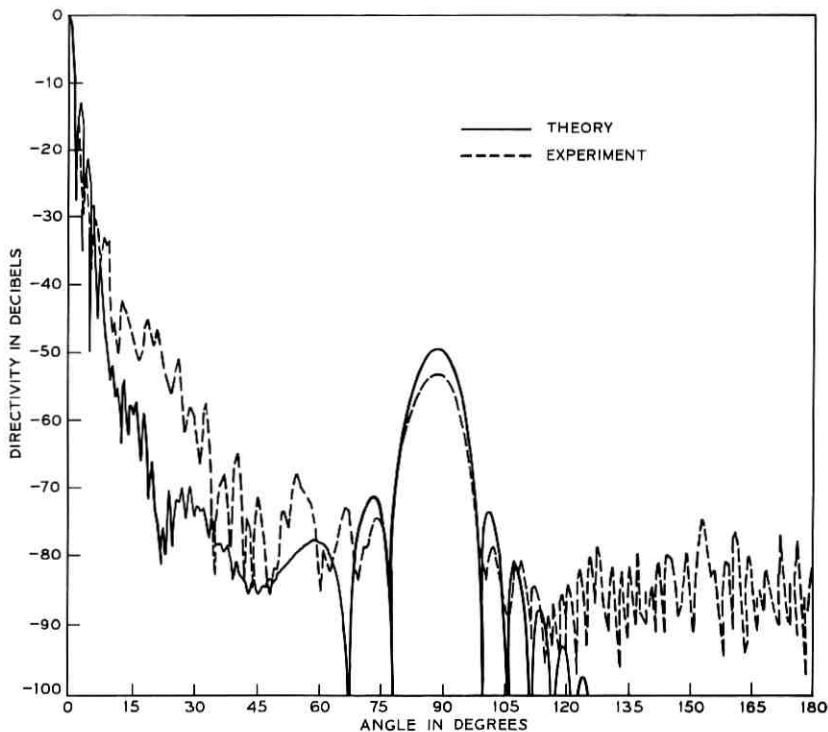


Fig. 4—Comparison of transverse-plane ( $\phi_0$ ) measured radiation and radiation predicted by GTD for the horn reflector antenna (transverse polarization at 3740 MHz).

Integrals but well within the capability of the GTD methods described here.

A comparison of GTD with a measured pattern appears in Fig. 4. The measured pattern was taken on a production model of the Bell System horn reflector antenna for HP and 3740 MHz. In the measurement it was necessary to tilt the antenna forward by 0.9 degree to aim it at the transmitting antenna. Taking this into account altered the theoretical GTD pattern of Fig. 4. The similarity of measured and theoretical patterns confirms the validity of the model. The early sidelobes ( $\phi_0 < 8$  degrees) agree precisely and our main concern, the high sidelobe near 90 degrees, is nicely predicted. Differences in sidelobe levels between GTD theoretical curves and experimental radiation patterns can probably be ascribed to inaccurate aperture illumination and minor structural differences between our model and the actual

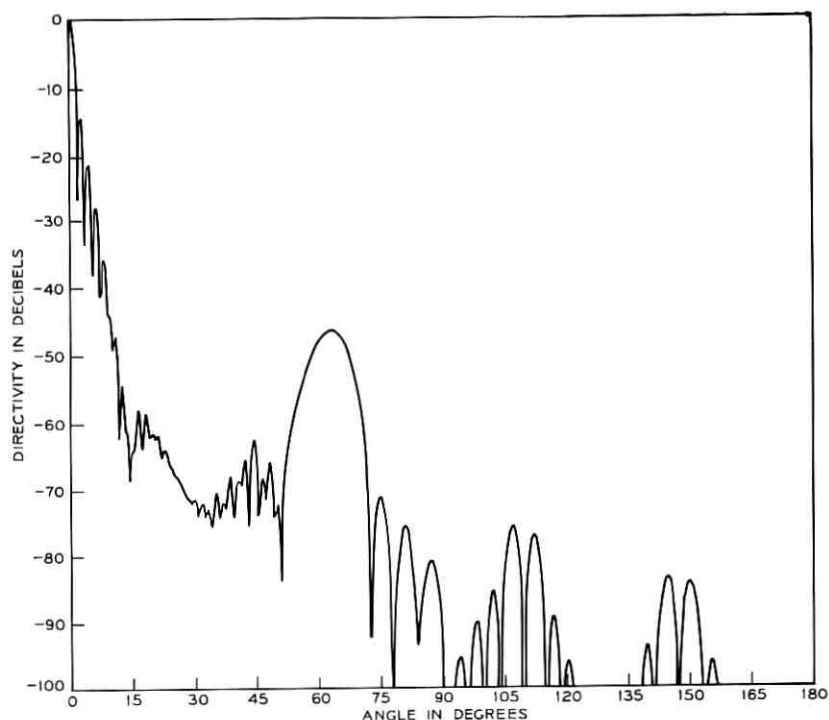


Fig. 5—Theoretical transverse (azimuth) plane radiation for horn reflector antenna with single edge blinder attached ( $\beta = 25$  degrees)—transverse polarization (HP) at 3.74 GHz.

antenna. However, as a blinder design aid, the GTD model is entirely adequate.

#### IV. SINGLE EDGE BLINDERS

Grady<sup>1</sup> has reported measurements of the azimuth pattern for HP of the horn reflector antenna with single edge blinders attached. These single edge blinders alter the front tilt angle,  $\beta$ , and move the azimuth location of the high sidelobe but do little to reduce it. The theory described above was tested for single edge blinders and concurred with Grady, as illustrated in Figs. 5 and 6 for front tilt angles of 5 degrees and 25 degrees. Notice the major high sidelobe is moved but the level is only slightly changed.

A third single edge blinder tested analytically had a front tilt angle,

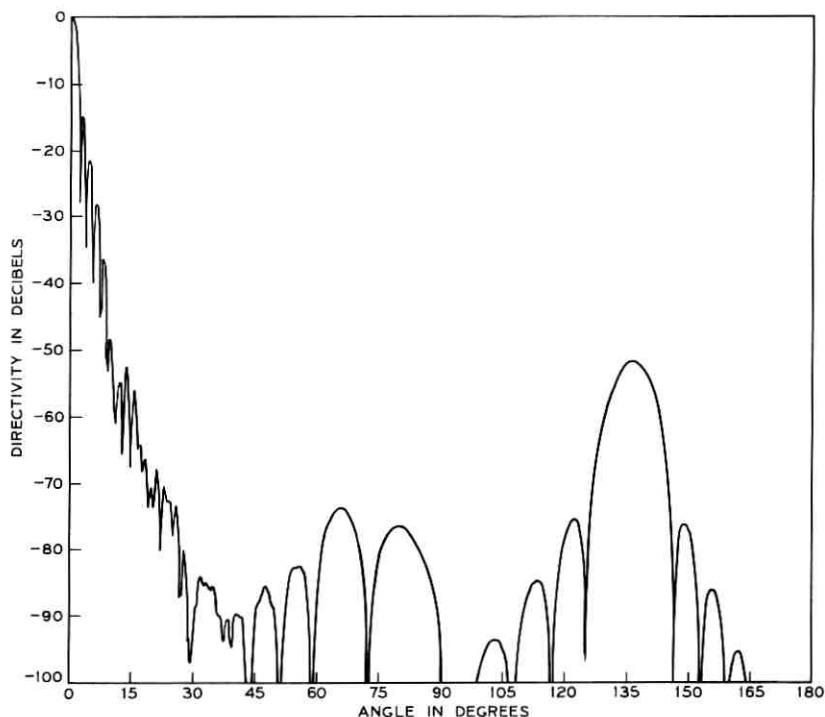


Fig. 6—Theoretical transverse (azimuth) plane radiation for horn reflector antenna with single edge blinder attached ( $\beta = 5$  degrees)—transverse polarization (HP) at 3.74 GHz.

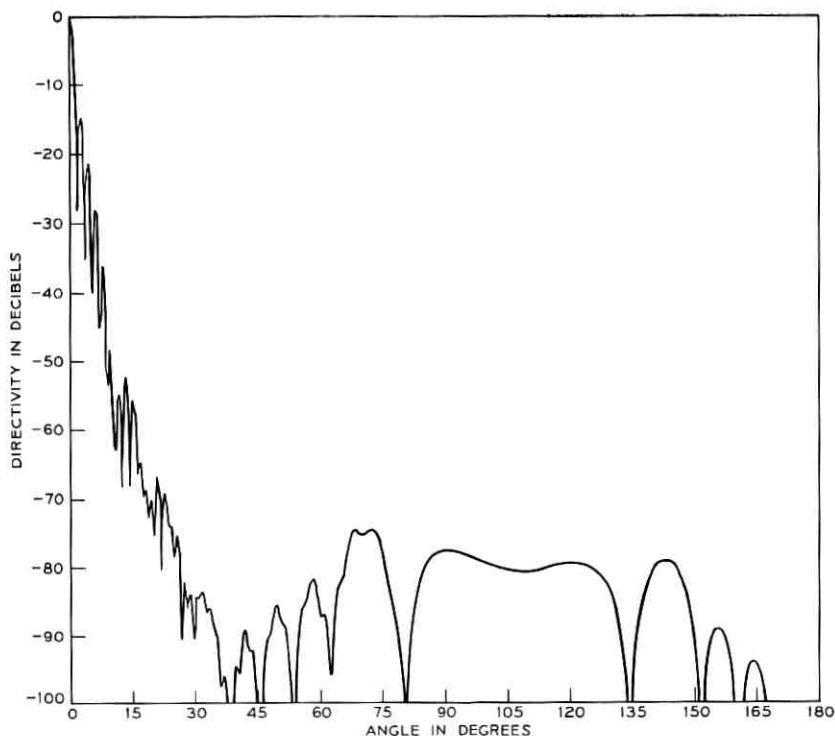


Fig. 7—Theoretical transverse (azimuth) plane radiation for horn reflector antenna with single edge blinder attached ( $\beta = -5$  degrees)—transverse polarization (HP) at 3.74 GHz.

$\beta$ , of  $-5$  degrees. Whenever  $\beta$  is negative ( $\beta < 0$  degrees), the major high sidelobe disappears completely in the azimuth plane, as is evident in Fig. 7. Apparently this blinder solves our problem but the large size of such a blinder creates difficult mechanical problems such as weight and windload. Making this blinder out of fine mesh wire might be an agreeable compromise but has not yet been tested.

A parametric study followed, leading to an equation which relates front tilt angle,  $\beta$ , to major sidelobe location,  $\phi_H$  (in the azimuth plane), as

$$\phi_H = 2 \tan^{-1} \left( \frac{\tan \alpha}{\sin \beta} \right). \quad (15)$$

As seen earlier, when  $\beta < 0$ , the major sidelobe disappears.

So it would appear that a single edge blinder is not a satisfactory

fix for reducing the unwanted high sidelobe. The best one can do without huge blinders is move the sidelobe to an unobtrusive location, a poor solution since special engineering would be required for each site and at some sites no amount of special engineering would produce good results.

#### V. A HALF BLINDER FOR SIDELOBE REDUCTION

Since a single edge blinder did not achieve the desired sidelobe reduction, two edge blinders were tried. We observed in the theoretical analysis [equation (8)] that the far zone field,  $\bar{H}$ , is proportional to edge length. Since each front tilt angle,  $\beta$ , produces a strong high sidelobe at a specific angle, a division of the blinder length into two edges at different front tilt angles  $\beta_1$ ,  $\beta_2$  would reduce the fields by half in the direction of each major sidelobe. Meanwhile, back at the main beam ( $\theta = 0$  degrees), the energy transmitted would *not* be altered, since blinder shape does not affect the main beam. As a result, a *two-edge blinder* should produce two high sidelobes, each 6 dB lower than the high sidelobe of a comparable single edge blinder.

The actual two-edge blinder tested was a half blinder, which retained the original front tilt angle ( $\beta_1 = 14.5$  degrees) for half the front edge. The other angle,  $\beta_2$ , was taken to be 4.5 degrees in order to widely separate the high sidelobes of the two edges. This half blinder con-

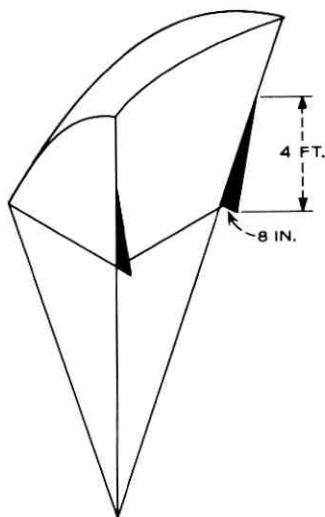


Fig. 8—Horn reflector antenna with half blinder attached.

figuration is shown in Fig. 8. Figure 9 compares the theoretical results for a horn reflector antenna with and without the half blinders attached. Notice the 6-dB reduction in sidelobe level of the 90-degree sidelobe, exactly as suggested above.

Based on the predicted sidelobe levels of the half blinder, a model was built for experimental tests. The dimensions of the half blinder built for testing were base 8 inches, height 4 feet, which provide an acute angle of about 10 degrees. A measured antenna pattern for HP at 3740 MHz is shown in Fig. 10 and compared with the theoretical curves for the same blinder. The comparison is quite good, with the two major sidelobe locations agreeing very well and the measured sidelobe levels 2 to 3 dB below predicted values. The 2- to 3-dB lower measured sidelobes occur quite consistently in all available comparisons of measured and predicted curves and are thought to be due to an

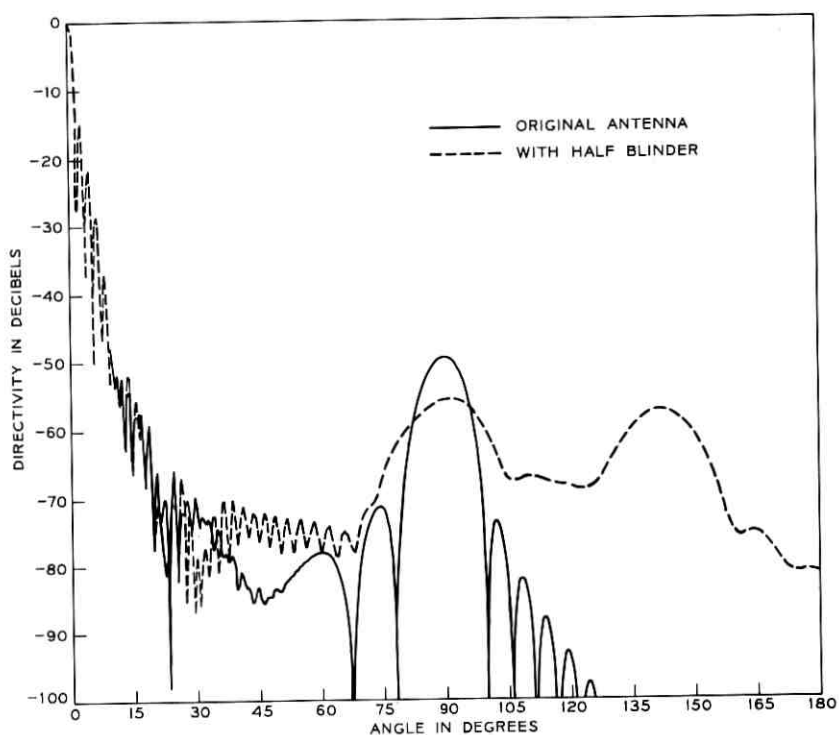


Fig. 9—Theoretical transverse (azimuth) plane radiation patterns for horn reflector antenna with and without half blinders attached—transverse polarization (HP) at 3.74 GHz.

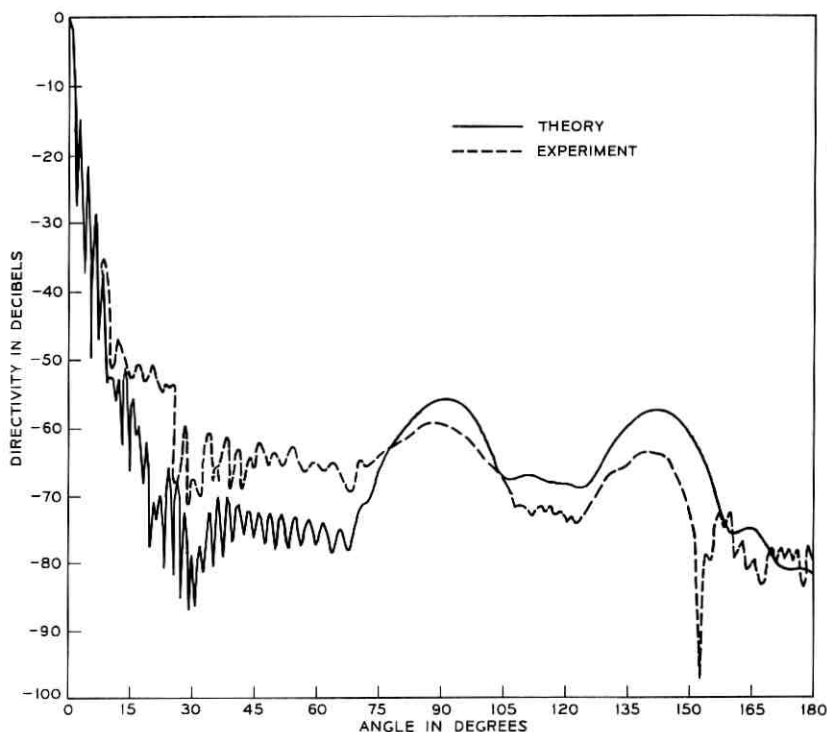


Fig. 10—Comparison of measured and GTD predicted transverse (azimuth) plane radiation of horn reflector antenna with half blinders attached—transverse polarization (HP) at 3.74 GHz.

unexpected amplitude taper near the edges of the antenna which was not used in the analytical model.

The sinusoidal distribution of incident energy in the aperture makes the fields strongest near the center (vertically) of the aperture. Hence, moving the half blinders up from the bottom should further reduce the high sidelobe near 90 degrees (now  $-59$  dB). This is because more of the power diffracted by the edges would be diverted to the second high sidelobe near 140 degrees (which was somewhat lower). Experimentally adjusting for optimum sidelobes, it was found that 9 inches up from the bottom was best. For the half blinders located 9 inches above the bottom of the aperture, the measured pattern (3740 MHz, HP) is shown in Fig. 11. This final adjustment gave sidelobe levels  $-62$  dB or below for azimuth angles from 35 degrees to 180 degrees, reducing the unwanted sidelobe to acceptable levels.

To verify the suitability of the half blinder for broadband operation,

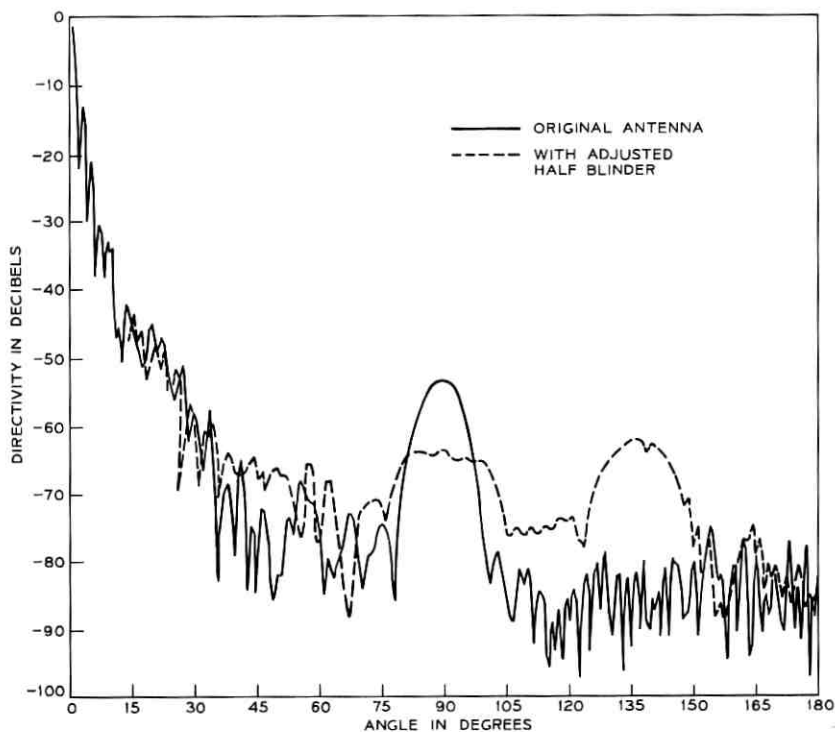


Fig. 11—Comparison of measured transverse (azimuth) plane radiation of horn reflector antenna with and without adjusted (up 9 inches) half blinders attached—transverse polarization (HP) at 3.74 GHz.

theoretical patterns were run for three frequencies (*high, middle, low*) in each of the 4, 6, and 11 GHz bands. These curves show that similar results are obtained in all three frequency bands and indicate better results should be obtained at 6 and 11 GHz. Of course, this is expected since 6 and 11 GHz patterns for the original antenna have lower sidelobes than for 4 GHz. Thus, we can expect good broadband performance of the half blinder in the three frequency bands.

Mechanically, the half blinder is ideal. Its small size (8 inches by 4 feet) makes it easy to fabricate and attach to existing antennas and the additional windload with it attached will be negligible.

## VI. CONCLUSIONS

This paper reports results of research still in progress aimed at reducing undesirable high sidelobe levels in the E-plane radiation for

HP. Tests (both experimental and theoretical) of single edge blinders have shown that altering the front tilt angle,  $\beta$ , of the horn reflector succeeds in moving the location of the undesirable sidelobe but does not substantially reduce the level.

A half blinder attached to the antenna, however, reduced the undesirable 90-degree sidelobe level to 62 dB below the main beam, an 8-dB reduction. Simultaneously, radiation levels were maintained at or below -62 dB for all azimuth angles from 35 degrees to 180 degrees. The antenna response with half blinder attached has been theoretically predicted to be broadband at 4, 6, and 11 GHz and the mechanical features are excellent. Unfortunately, the raised radiation levels from 100 degrees to 150 degrees (through below -62 dB) and the unacceptable levels near 30 degrees indicate the half blinder may not be suitable for general application. Future writings will describe the design of many edged blinders and the effect of curved blinders on radiation levels.

#### VII. ACKNOWLEDGMENTS

The measured patterns were taken by Jack E. Millwater of the Antenna Design Department, Bell Telephone Laboratories, Whippany, New Jersey. Suggestions regarding the interpretation of the angles  $\gamma$  and  $\zeta$  were made by T. S. Chu.

#### APPENDIX

It was helpful to describe the various coordinate systems to be used for the aperture and the edges. We needed various coordinate transformations in order to orient the edges correctly for the Geometrical Theory of Diffraction. Each side edge had its own coordinate, with origin at the center of the edge, and  $Z$ -axis directed along the edge. These are shown in Fig. 1. The appropriate coordinate transformations are:

$$\left. \begin{aligned} X_1 &= X \\ Y_1 &= (Y + a) \cos \alpha + Z \sin \alpha \\ Z_1 &= -(Y + a) \sin \alpha + Z \cos \alpha \\ X_2 &= X \\ Y_2 &= (Y - a) \cos \alpha - Z \sin \alpha \\ Z_2 &= (Y - a) \sin \alpha + Z \cos \alpha \end{aligned} \right\} \quad (16)$$

and, in addition,

$$\left. \begin{aligned} X &= X_o \cos \beta - Z_o \sin \beta \\ Y &= Y_o \\ Z &= X_o \sin \beta + Z_o \cos \beta \end{aligned} \right\} \quad (17)$$

where  $\alpha$ ,  $\beta$ ,  $a$ , and  $b$  are described in Section I. In addition, spherical coordinates will be employed so we have a need for transformation of  $R$ ,  $\theta$ ,  $\phi$  into  $R_1$ ,  $\theta_1$ ,  $\phi_1$  and  $R_2$ ,  $\theta_2$ ,  $\phi_2$ . However, they are obtainable from the above equations and are not given except for radii  $R_1$ ,  $R_2$  in the *far field*. They are

$$\begin{aligned} R_1, R_2 &= \sqrt{R^2 + a^2 \pm 2Ra \sin \theta \sin \phi} \\ R_1, R_2 &\approx R \pm a \sin \theta \sin \phi. \end{aligned} \quad (18)$$

These are needed for correct phase reference in superposing the two edge contributions.

#### REFERENCES

1. Grady, R. R., "Sidelobe Control in the Cornucopia or Horn Reflector Antenna," presented to National Electronics Conference, Chicago, Illinois, December 7-9, 1970.
2. Crawford, A. B., Hogg, D. C., and Hunt, L. E., "A Horn Reflector Antenna for Space Communication," *B.S.T.J.*, 40, No. 4 (July 1961), pp. 1095-1116.
3. Keller, J. B., "Geometrical Theory of Diffraction," *J. Opt. Soc.*, 52, (1962), pp. 116 ff..
4. Kouyoumjian, R. G., "Asymptotic High Frequency Methods," *IEEE Proc.*, 53, (1965), pp. 864 ff..
5. Rudduck, R. C., and Tsai, L. L., "Application of Wedge Diffraction and Wave Interaction Methods to Antenna Theory," from Application of Optical Methods to Microwave Problems, Ohio State University Short Course, 1969. [See also *IEEE Trans.*, *AP-16*, (1968) pp. 83 ff..]
6. Russo, P. M., Rudduck, R. C., and Peters, L., Jr., "A Method for Computing E-Plane Patterns of Horn Antennas," *IEEE Trans.*, *AP-13*, (1965), pp. 219 ff..
7. Yu, J. S., Rudduck, R. C., and Peters, L., Jr., "Comprehensive Analysis of Horn Antennas by Edge Diffraction Theory," *IEEE Trans.*, *AP-14*, (1966), pp. 138 ff..
8. Ryan, C. E., and Rudduck, R. C., "A Wedge Diffraction Analysis of the Radiation Patterns of Parallel-Plate Waveguides," *IEEE Trans.*, *AP-16*, (1968), pp. 490 ff..
9. Rudduck, R. C., and Wu, D. C. F., "Slope Diffraction Analysis of TEM Parallel-Plate Guide Patterns," *IEEE Trans.*, *AP-17*, (November 1969).
10. Ryan, C. E., "Equivalent Current Concepts and Three Dimensional Radiation Solution," from Application of Optical Methods to Microwave Problems, Ohio State University Short Course, 1969.
11. Kouyoumjian, R. G., "An Introduction to Geometrical Optics and Geometrical Theory of Diffraction," from Application of Optical Methods to Microwave Problems, Ohio State University Short Course, 1969. (See also Ref. 3.)
12. Sommerfeld, A., *Optics*, New York: Academic Press, 1954, p. 261.
13. Stratton, J. A., *Electromagnetics*, New York: McGraw-Hill, 1941, p. 424.
14. Silver, S., *Microwave Antenna Theory and Design*, New York: McGraw-Hill, 1948, p. 162.



# Transient Effects in Telephone Switching Circuits When Relay Windings are Disconnected

By H. N. WAGAR

(Manuscript received April 1, 1971)

*This paper presents an analytical review of the transient events relating to charge, current, voltage, and energy upon disconnection of inductive loads in switching circuits. Based on good agreement between theory and experiment, the analysis is found applicable to a number of long-standing relay and switching circuit problems involving radiation interference, voltage breakdowns in various elements of the contact circuit, and contact erosion.*

## I. INTRODUCTION

The disconnection of a relay in a switching circuit involves a number of time-variant design problems for which a quantitative treatment is needed. These mainly concern (i) the release time of the structure, or (ii) the transient current and voltage surges which are a potential cause of oscillations and breakdowns in the circuitry. The subject of release time is chiefly related to a change in the core's magnetization from its operated to its residual value, i.e., a very substantial change in core flux occurring over a comparatively long time, typically several milliseconds. The transient circuit surges tend to develop much earlier in the interval after disconnection, often in times from about  $10^{-6}$  to  $10^{-4}$  second during which the core's magnetization has not yet had time to change appreciably. Thus, while both phenomena are related to the core's demagnetization curve, their performance tends to be controlled by different features of this nonlinear characteristic. The subject of release time, including the design of slow release relays, has been on a firm quantitative basis for many years,<sup>1-4</sup> based on relationships involving the whole demagnetization curve. However, only qualitative or empirical treatments have so far been available to describe the transient surges of current and voltage. An analytical

description of these surges is indispensable to the understanding of voltage breakdowns or radiation interference in the contact wiring; and a renewed interest in these latter subjects has prompted their further study as outlined in this report.

The surges principally result from the tendency for the inductance to maintain current flow after the main current path has been opened; current is then diverted into the circuit capacitances, temporarily charging them to high voltages, even to several hundred times the original battery voltage (when the capacitance is very small). Previous analyses based on a conventional lumped-element  $L, R, C$  treatment have not agreed well with experiment, attributed mainly to difficulties in suitably defining the load's nonlinear inductance and to the neglect of eddy current losses in the core. In attempting to recognize these in the present analysis, some simplifications were possible by assuming an effective lumped-element value of inductance which corresponds to the differential permeance of the load's magnetic circuit in the operated region. This concept, and an allowance for eddy current losses, give results which agree well with experiment over several decades of variation in the basic parameters. Over the three decades of principal interest when studying breakdown voltage, this effective inductance is found to be essentially constant, being basically determined by the differential permeance of the core's demagnetization curve at the operated point. Beyond this region, where pulses are slower, the use of a progressively increasing permeance, which recognizes the wider range of the demagnetization curve that comes into play, helps improve the accuracy. The study covered in this report deals mainly with the region where the faster pulses predominate.

### 1.1 *Outline of Analysis Procedure*

Expressions are first obtained for the general case of a relay winding having both a short-circuited secondary and an  $RC$  network, as commonly used for contact protection, bridging the main winding. By assigning suitable values to each of these terms, the results can then be simplified to cover a range of practical situations such as the ordinary unprotected relay coil, the coil bridged by either capacitor or resistor alone, and the air core coil. Of these, the most common case, that of a relay coil shunted only by a capacitor (representing distributed capacitance, wiring capacitance, etc.), is selected for detailed study. Based on good experimental agreement for a wide range of test cases, the results are then applied to a number of special relay and switching circuit design problems.

The surges to be studied are illustrated by the curves in Fig. 1. This view shows a typical relay switching circuit in schematic form, and the transient current and voltage surges when contact X is opened. A major objective is to describe these surges analytically. The initial phase of the analysis is to derive expressions for current and voltage, as a function of time, when the load is disconnected by an "ideal" (i.e., nonbreakdown) contact. The smooth curves in Fig. 1 show typical results when a telephone relay is controlled by a (nonarcing) mercury contact. They have practical interest whenever the switching is done by a vacuum tube, a transistor, or a mercury contact which is well enough insulated to avoid breakdowns. Such curves also determine the conditions for breakdown when apparatus, wiring, or contacts of known dielectric strength are connected in the circuit. For example, the irregular curves in Fig. 1 show the multiple breakdowns that occur across a typical relay contact in air, as its surfaces separate. This result was obtained by replacing the previous mercury contact by an ordinary mechanical contact (on a wire-spring relay) and repeating the measurement as a double exposure on the same film. Such breakdowns, sometimes termed "B-type transients" or "showering arcs," represent successive charging of local capacitance to the dielectric breakdown of the contact's gap, its discharge through the local contact circuit, and a renewed charging cycle. They have been described qualitatively in considerable detail,<sup>5-8</sup> and there have also been some efforts at a quantitative treatment.<sup>9,10</sup> Each successive charging cycle is the beginning of a new "ideal" contact surge; hence the definition of this curve facilitates the study of such breakdowns.

A second phase of the analysis examines these surges from the stand-

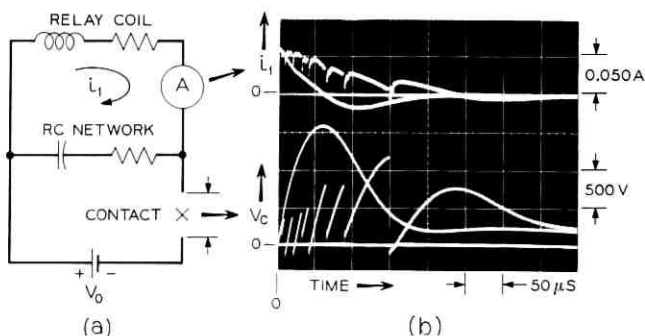


Fig. 1—Surges when contacts open an inductive load. (a) Test Circuit. (b) Current and voltage vs time after interruption for ideal contact (smooth curve) and typical mechanical contact (irregular curves).

point of the amount of inductive energy which is available to be dissipated into the arcing contact circuit, with attendant surges and contact erosion.

### 1.2 Objectives

This paper aims to present these relationships in general form, with enough experimental data to verify the analysis. Some specific fields of relay and circuit design where immediate applications are expected, and which were an incentive for this study, will now be summarized.

- (i) The general definition of the "ideal" contact surges. It is found that all variations are definable in terms of two dimensionless ratios:  $\beta = CR^2/\Phi N^2$ , the "load design factor," and  $G_2/G_1$  or the ratio of secondary to primary coil constants (summarized in Table I and further described below). The surge equations can then be used to predict such variations as peak voltage, amplitude and frequency of oscillations, rise time, or degree of damping. The analysis also shows that the response is oscillatory between two particular values of  $\beta$ , with overdamped behavior above or below these values.
- (ii) An understanding of how the coil's stored inductive energy is released. Relationships are found which determine that part consumed in internal and external dissipative losses, and that part which goes into capacitive energy storage from which it may be discharged into erosion-producing arcs.
- (iii) A fuller understanding of that portion of the coil's stored inductive energy that can be released during the transient period, the major features of which depend on (a) the incremental permeance of the static demagnetization curve at the releasing point, and (b) the energy replenishment from the battery during each arc breakdown interval. This is especially important in the study of contact erosion.
- (iv) An explanation of some hitherto "anomalous" results. Among these are: (a) A quantitative picture of releasable coil energy as influenced by "stop-pin" height; it is shown here to be related directly to the degree of coil saturation, in accord with experience, rather than to the total stored energy as had previously been suggested. (b) A quantitative picture of the oscillations which occur with "copper-sleeve" relays. This is found to be related to that portion of the main winding which is uncoupled to the secondary.

TABLE I—CIRCUIT CONSTANTS

- $V_o$  = Battery voltage.
- $V_c$  = Instantaneous voltage across contacts.
- $I_o$  = Steady state current =  $V_o/R_w$ .
- $i_1, i_2$  = Instantaneous current in primary or secondary circuits respectively.
- $q_1$  = Instantaneous charge on capacitor.
- $N_1, N_2$  = Turns in primary, or secondary, respectively.
- $R_w, R_2$  = Resistance of primary, or secondary, winding respectively.
- $R_n$  = Primary circuit resistance external to coil (i.e., resistance of RC network).
- $R_1$  = Total resistance of primary circuit =  $R_w + R_n$ .
- $G_1, G_2$  = Coil constant for primary or secondary circuit  
 $= \frac{N_1^2}{R_1} \frac{N_2^2}{R_2}$  respectively (mho).
- $G_c$  = Eddy current constant of core (for which  $N_2 = 1$ ).  
 [Note that  $\frac{1}{G_1} = \frac{R_w + R_n}{N_1^2} = \frac{1}{G_w} + \frac{1}{G_n}$ .]
- $L_1, L_2$  = Incremental inductance of primary or secondary  
 $N_1^2\Phi, N_2^2\Phi$  respectively.
- $\Phi$  = Incremental permeance of coil magnetic circuit at specified magnetization (i.e., corresponding to operated ampere-turns).
- $C$  = Capacitance across load coil.
- $\Phi$  = Magnetic flux.

	General Case	Case for $R_n = 0$	Case for $G_2 = 0$	Case for $G_2 = 0$ and $R_n = 0$
$R' =$ Effective Resistance	$R_1 + \frac{G_2\Phi}{C}$ or $R_1(1 + \frac{G_2/G_1}{\beta_1})$	$R_w + \frac{G_2\Phi}{C}$ or $R_w(1 + \frac{G_2/G_w}{\beta_w})$	$R_1$	$R_w$
$L' =$ Effective Inductance	$L_1(1 + G_2/G_1)$	$L_1(1 + G_2/G_w)$	$L_1$	$L_1$
$\beta =$ Load Design Factor	$\beta_1 = \frac{CR_1^2}{\Phi N_1^2}$	$\beta_w = \frac{CR_w^2}{\Phi N_1^2}$	$\beta_1$	$\beta_w$

(v) The ability to make design estimates for a number of applications. Examples are: (a) Number and frequency of breakdowns in a "B" type transient, and the energy available for causing erosion. (b) Peak value of the final surge, following a "B" type transient as for the tail of the irregular curve in Fig. 1. This is needed in verifying whether wiring insulation will be damaged when coils with large numbers of turns are disconnected. (c) Choice of proper test values for use in the production testing of relay coils to determine whether their internal insulation

- breakdown strength is satisfactory. (For this test, which has been in use on an empirical basis for many years, the energized coil circuit is interrupted by an "ideal" vacuum tube "switch"; if the coil's self-induced voltage causes an internal breakdown, the coil is rejected as an incipient service failure because of faulty insulation or lead configuration.) (d) The ability to reinterpret inconclusive data from past contact tests, or to better define tests made years ago so that their applicability to today's designs in today's circuits may be better understood.
- (vi) Assessment of the mutual impact of contact erosion and relay miniaturization. For example, a smaller relay coil usually means less energy for the contact to control and therefore a smaller contact volume for a given contact life. A smaller contact volume means less wear allowance in the relay's armature motion, and hence a lower mechanical work requirement, with a correspondingly smaller relay magnet. Thus a knowledge of the interaction between the relay's inductive energy and the resulting contact wear can be an important guide to design for minimal relay sizes for a switching system where all the relays are of the same basic structure (i.e., the contacts of one relay control the winding of another).

The paper is divided into three major sections: Analysis, Experiment, and Discussion. The circuit is first analyzed in general terms, giving results which for some cases are considered too complex for further treatment in this study. Substitutions are then made which considerably simplify the equations and lead to detailed answers for the important practical case of the unprotected relay coil. The major experimental results and discussion relate to this case.

## II. ANALYSIS

In this section, we shall (i) develop the circuit equations and apply them to the consideration of special situations such as (ii) critical damping, (iii) peak voltage, and (iv) energy relationships.

### 2.1 *Development of the Circuit Equations*

This section defines a circuit model, presents the loop equations, and gives the resulting solution for current in the main circuit. This value of current as a function of time is then used to derive the related values of charge, contact voltage, and rate of change of voltage.

## 2.1.1 Choice of Circuit Model

A simple relay winding shunted by an  $RC$  network, being connected or disconnected from a battery by means of an ideal contact, was chosen for the study. As only the surge on disconnection is studied, the influence of wiring can be included in the capacitive term, and so the results are generally applicable whether connections between contact and relay are very short, as on a printed wiring board, or quite long, as through a considerable loop of switchboard cabling. Reflections and surge impedance of the wiring are important in considering the individual showering arcs, as has been done for example in recent work of G. W. Mills<sup>10</sup> and J. R. Pharney;<sup>11</sup> but these features are outside the scope of the present study.

After some initial experiments, it was found that an adequate representation of an actual relay control circuit required the recognition of: (i) the distributed capacitance of the coil; (ii) a coupled secondary winding to represent core losses, copper sleeves, etc.; (iii) an effective lumped inductance representing the region of the demagnetization curve that is active during the initial surge; and (iv) (under certain conditions) a portion of the main winding which is not coupled with the core or secondary winding. The resulting study circuit is seen in Fig. 2a. For example, (i) it was found that distributed capacitance of typical relay coils is in the vicinity of 100–200 pF, which is too large

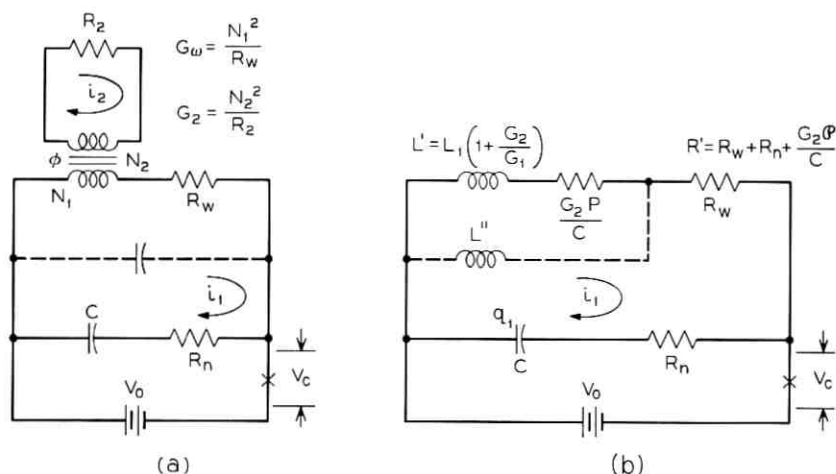


Fig. 2—Circuits for fully representing a relay as a contact load. (a) Circuit chosen for analysis. (b) Transformed circuit.

to ignore. Likewise, (ii) it was found that the discharges of typical relay structures can be so fast that the core losses (i.e., dissipation in an effective secondary winding) must be recognized. The additional influence of that portion of the coil winding which is not coupled to the "secondary" plays a significant role only when dealing with coils having a secondary consisting of a copper sleeve or short-circuited turns; it will be examined as a special case of the above circuit in Section 2.2. Following this general solution, the simpler cases are readily found as special cases; e.g., setting the protection network resistance  $R_n = 0$  gives the case of an ordinary relay coil with distributed or direct shunt capacitance, setting the eddy current coil constant  $G_2 = 0$  gives the case of an air core coil, or setting  $C = \infty$  represents a pure resistive shunt.

The first objective is therefore to evaluate the current, charge, and contact voltage in the primary circuit for the period immediately after interrupting the circuit shown in Fig. 2a. The following considerations will be used in the initial analysis:

- (i) The contact is "ideal," i.e., no gaseous or metal vapor breakdowns occur. This is in fact closely simulated by a mercury contact, and even more completely by certain vacuum tubes and transistors.
- (ii) Perfect coupling is assumed between primary and secondary.
- (iii) The initial conditions (just prior to  $t = 0$ ) are that the steady current is  $I_o = (V_o/R_w)$ ,\* and the capacitor is charged to the value  $-V_o$ .
- (iv) The flux  $\Phi$  which is linked to both primary and secondary windings is proportional to the algebraic sum of the instantaneous ampere turns of primary and secondary, in accordance with the usual magnetic circuit concepts.
- (v) The inductance of the load can be represented by a lumped value which effectively simulates the flux-current relation in the coil's working region. Use of a lumped-constant term simplifies the circuit equations, which otherwise become very difficult to solve in simple forms. The meaning of a lumped-constant inductance is better understood with the help of Fig. 3, which shows the static flux-ampere turn characteristic of a typical relay magnet for operating and releasing cycles. For the present case, the releasing cycle, or demagnetization curve, applies. The instantaneous inductance is the slope of

---

\* For definitions of terms, see Tables I, II, and III.

TABLE II—CONSTANTS APPEARING IN EQUATIONS

CONST.	GENERAL EXPRESSION	VALUE WHEN $R_n = 0$	VALUE WHEN $G_2 = 0$	VALUE WHEN $\begin{cases} R_n = 0 \\ G_2 = 0 \end{cases}$
$K =$	$\frac{1+G_2/G_w}{1+G_2/G_1}$	$= 1$	$= 1$	$= 1$
$a =$	$\frac{R_w}{L_1(1+G_2/G_w)} = \frac{R_w}{KL'}$	$= \frac{R_w}{L_1(1+G_2/G_w)} = \frac{R_w}{L'}$	$= \frac{R_w}{L_1} = \frac{R_w}{N_1^2 \theta} = \frac{1}{G_w \theta}$	$= \frac{R_w}{L_1} = \frac{R_w}{N_1^2 \theta} = \frac{1}{G_w \theta} = 2b$
$b =$	$\frac{R_1 + \frac{G_2 \theta}{C}}{2L'(1+G_2/G_1)} = \frac{1 + \frac{G_2/G_w}{\beta_1}}{2G_1 \theta (1+G_2/G_1)}$	$= \frac{R_w + \frac{G_2 \theta}{C}}{2L_1(1+G_2/G_w)} = \frac{1 + \frac{G_2/G_w}{\beta_1}}{2G_w \theta (1+G_2/G_w)}$	$= \frac{R_1}{2L'} = \frac{R_1}{2N_1^2 \theta} = \frac{1}{2G_1 \theta}$	$= \frac{R_w}{2L_1} = \frac{R_w}{2N_1^2 \theta} = \frac{1}{2G_w \theta}$
$(a-b) =$	$\frac{1}{2L'} \left[ R_w - \frac{G_2 \theta}{C} - R_n \frac{1-G_2/G_w}{1+G_2/G_1} \right]$ $\frac{R_w - \frac{G_2}{\beta_1} / G_1}{R_1} - \frac{R_n(1-G_2/G_w)}{R_1(1+G_2/G_w)}$ $= \frac{1 - \frac{G_2/G_w}{\beta_1}}{2G_w \theta (1+G_2/G_w)}$	$= \frac{1}{2L'} \left[ R_w - \frac{G_2 \theta}{C} \right]$ $= \frac{1 - \frac{G_2/G_w}{\beta_1}}{2G_w \theta (1+G_2/G_w)}$	$= \frac{R_w - R_n}{2L_1}$ $= \frac{R_w - R_n}{2N_1^2 \theta}$	$= \frac{R_w - R_n}{2L_1} = b$
$\omega_0 =$	$\frac{1}{\sqrt{L' C}} = \frac{1}{G_1 \theta \sqrt{\beta_1 (1+G_2/G_1)}}$	$= \frac{1}{\sqrt{L' C}} = \frac{1}{G_w \theta \sqrt{\beta_w (1+G_2/G_w)}}$	$= \frac{1}{\sqrt{L C}} = \frac{1}{N_1 \sqrt{\theta C}}$	$= \frac{1}{\sqrt{L C}} = \frac{1}{N_1 \sqrt{\theta C}}$
$\omega =$	$\sqrt{\omega_0^2 - b^2} = \frac{\sqrt{4L' C - C^2 \left( R_1 + \frac{G_2 \theta^2}{G} \right)^2}}{2L' C} = \frac{\sqrt{\frac{4}{\beta_1} - \left( 1 - \frac{G_2/G_1}{\beta_1} \right)^2}}{2G_1 \theta (1+G_2/G_1)}$	$= \frac{\sqrt{4L^2 C - C^2 \left( R_w + \frac{G_2 \theta^2}{C} \right)^2}}{2L C} = \frac{\sqrt{\frac{4}{\beta_w} - \left( 1 - \frac{G_2/G_w}{\beta_w} \right)^2}}{2G_w \theta (1+G_2/G_w)}$	$= \frac{\sqrt{4L_1^2 C - C^2 R_1^2}}{2L_1 C} = \frac{\sqrt{\frac{4}{\beta_1} - 1}}{2G_1 \theta}$	$= \frac{\sqrt{4L_1^2 C - C^2 R_w^2}}{2L_1 C} = \frac{\sqrt{\frac{4}{\beta_w} - 1}}{2G_w \theta}$
$m =$	$\frac{\omega_0}{1+G_2/G_w} \sqrt{1+G_2/G_w - \frac{CR_n}{G_w \theta}}$	$= \frac{\omega_0}{\sqrt{1+G_2/G_w}}$	$= \frac{\omega_0 \sqrt{1 - \frac{CR_n}{G_w \theta}}}{\sqrt{1+G_2/G_w}}$	$= \omega_0$

TABLE III—EXPRESSIONS INVOLVING PHASE ANGLE

VARIABLE	GENERAL EXPRESSION	VALUE WHEN $R_n = 0$	VALUE WHEN $G_2 = 0$	VALUE $\left\{ \begin{array}{l} R_n = 0 \\ G_2 = 0 \end{array} \right.$	VALUES OF $\theta$ & $\phi$
$\sin \theta = \frac{\omega}{\omega_0}$	$\frac{\omega}{\omega_0} = \sqrt{1 - \frac{b^2}{\omega_0^2}} = \sqrt{\frac{4 - \beta_1 \left(1 - \frac{G_2/G_1}{\beta_1}\right)^2}{4(1 + G_2/G_1)}}$	$\frac{4 - \left(1 - \frac{G_2/G_1}{\beta_1}\right)^2}{4(1 + G_2/G_1)}$	$\sqrt{1 - \frac{\beta_1}{4}}$	$\sqrt{1 - \frac{\beta_w}{4}}$	$\theta = \tan^{-1} \frac{\omega}{b}$
$\cos \theta = \frac{b}{\omega_0}$	$\frac{b}{\omega_0} = \frac{CR_1 + G_2\phi}{2\sqrt{CN^2\phi(1 + G_2/G_1)}} = \frac{\sqrt{\beta_1 \left(1 + \frac{G_2/G_1}{\beta_1}\right)}}{2\sqrt{1 + G_2/G_1}}$	$\frac{CR_w + G_2\phi}{2\sqrt{CN^2\phi(1 + G_2/G_1)}}$	$\frac{\sqrt{\beta_1}}{2} \frac{R_1}{N_1} \sqrt{\frac{C}{\phi}}$	$\frac{1}{2} \frac{R_w}{N_1} \sqrt{\frac{C}{\phi}}$	$\theta \leq \frac{\pi}{2}$
$\tan \theta = \frac{\omega}{b}$	$\frac{\omega}{b} = \frac{\sqrt{\frac{4}{\beta_1} \left(1 - \frac{G_2/G_1}{\beta_1}\right)^2}}{1 + \frac{G_2/G_1}{\beta_1}}$	$\frac{4 - \left(1 - \frac{G_2/G_1}{\beta_1}\right)^2}{1 + \frac{G_2/G_1}{\beta_1}}$	$\sqrt{\frac{4 - \beta_1}{\beta_1}}$	$\sqrt{\frac{4 - \beta_w}{\beta_w}}$	
$\sin \phi = \frac{\omega}{m}$	$\frac{\omega}{m} = \sqrt{\frac{4 - \beta_1 \left(1 - \frac{G_2/G_1}{\beta_1}\right)^2}{4(1 + G_2/G_1)}} \frac{(1 + G_2/G_w)}{\sqrt{1 + G_2/G_w - \frac{CR_n}{G_w\phi}}}$	$\sqrt{1 + G_2/G_w} \sin \theta$	$\frac{\sin \theta}{\sqrt{1 - \frac{CR_n}{G_w\phi}}}$	$\sin \theta$	$\phi = \tan^{-1} \frac{\omega}{a-b}$
$\cos \phi = \frac{a-b}{m}$	$\frac{a-b}{m} = \frac{\sqrt{\beta_1 \left(1 + \frac{G_2/G_1}{\beta_1}\right)^2} \left[ \frac{R_w}{R_1} - \frac{G_2/G_1}{\beta_1} - \frac{R_n(1 - G_2/G_w)}{R_1(1 + G_2/G_w)} \right]}{2\sqrt{1 + G_2/G_w} \left(1 + \frac{G_2/G_w}{G_w\phi}\right) \left(1 + \frac{G_2/G_1}{\beta_1}\right)}$	$\frac{G_2/G_w}{1 + \frac{G_2/G_w}{G_w\phi}} \cos \theta$	$\frac{R_w - R_n}{R_1} \frac{CR_n}{G_w\phi} \cos \theta$	$\cos \theta$	WHEN $a \geq b$ , $0 < \phi \leq \frac{\pi}{2}$ $b > b$ , $\frac{\pi}{2} < \phi \leq \pi$
$\tan \phi = \frac{\omega}{a-b}$	$\frac{\omega}{a-b} = \frac{\sqrt{\frac{4}{\beta_1} \left(1 - \frac{G_2/G_1}{\beta_1}\right)^2} \left[ \frac{R_w}{R_1} - \frac{G_2/G_1}{\beta_1} - \frac{R_n(1 - G_2/G_w)}{R_1(1 + G_2/G_w)} \right]}{\sqrt{1 + G_2/G_w - \frac{CR_n}{G_w\phi}} \left(1 + \frac{G_2/G_1}{\beta_1}\right) \tan \theta}$	$\frac{\left(1 + \frac{G_2/G_w}{\beta_w}\right) \tan \theta}{\left(1 - \frac{G_2/G_w}{\beta_w}\right)}$	$\frac{R_1}{R_w - R_n} \tan \theta$	$\tan \theta$	NOTE: VALUES IN THIS TABLE ARE FOR $\omega_0^2 > b^2$ ; WHEN $b^2 > \omega_0^2$ , SUBSTITUTE $\sin \theta$ , $\cos \theta$ , $\tan \theta$ FOR $\sin \theta$ , $\cos \theta$ , $\tan \theta$ RESPECTIVELY. WHEN $\omega_0 = b$ , SEE TABLE XI.

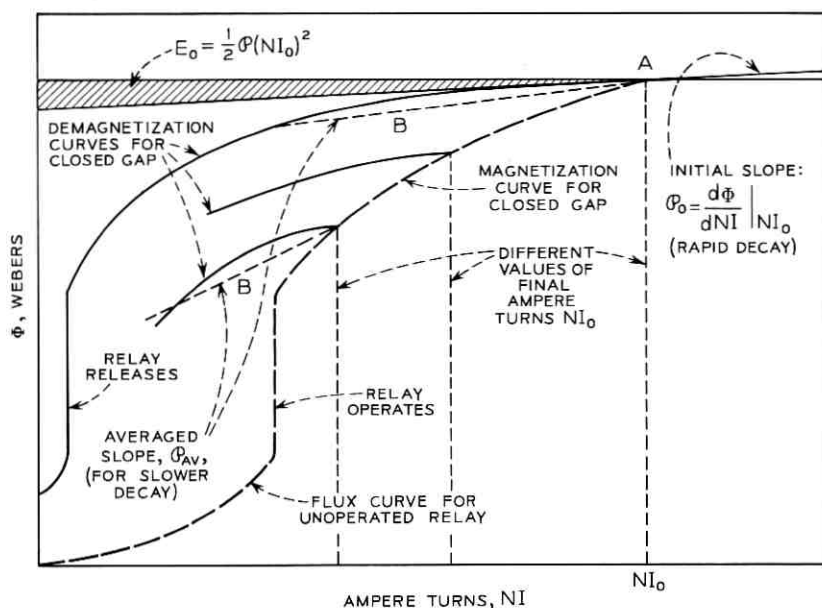


Fig. 3—Representation of inductance,  $L = \Phi N^2$ , when contact opens a relay coil circuit.

this demagnetization curve in the applicable working range, and may be expressed as

$$L = \Phi N^2$$

where  $\Phi = (d\Phi/dNI) |_{NI_0}$ ,  $N$  = number of turns in the coil, and  $NI_0$  = ampere turns at the operated point (i.e., starting point of the demagnetization curve on disconnection).  $\Phi$  is the differential permeance, or slope of the demagnetization curve, over the region where flux is changing during the surge. In the case of very fast surges, the flux is substantially unchanged during the surge, and the value of  $\Phi$  at  $NI_0$  applies, as shown at A in Fig. 3. For slower surges, a larger value of  $\Phi$  representing an average slope over the working range, as indicated by the dotted lines B in the figure, is presumed to apply. Values of  $\Phi$  are further discussed in Section 3.1.2.

The analysis has been developed around this general circuit. The resulting general solution, which involves an appreciable number of variables, is relatively complex and its detailed examination is reserved for later computer-assisted studies. For the present study, special

attention is aimed only at the simpler but important practical case of the ordinary unprotected relay, which involves only a simple capacitive shunt, a term which is always needed if only to cover the inevitable distributed capacitance of the coil itself. In addition, the manner in which the general expressions reduce to simpler forms, by neglecting appropriate terms, will be noted; conformity to previously known solutions for the conventional  $L, R, C$  circuit affords at least partial confirmation of the general analysis. The special cases chosen for detailed consideration are:

$$R_n = 0, G_2 \text{ finite (relay coil with capacitive shunt),}$$

$$R_n \text{ finite, } G_2 = 0 \text{ (air core coil with } RC \text{ shunt), and}$$

$$R_n = 0, G_2 = 0 \text{ (air core coil with capacitive shunt).}$$

The appropriate expressions for each of these cases are tabulated in the accompanying tables.

The symbols applicable to this model circuit are summarized in Table I. The notation using terms  $G = N^2/R$  for coil constant, and expressing inductance in terms of turns and permeance  $\mathcal{O}$  ( $L = \mathcal{O}N^2$ ), has been used because of its convenience and common use in relay design. The resulting equations are also considerably simplified by their use.

### 2.1.2 Equations for Current in Primary

The equations for the model circuit, Fig. 2a, are derived in Appendix A. The procedure was to sum the voltages around primary and secondary circuits, respectively, using the flux common to both windings to determine the inductive terms,  $N_1(d\Phi/dt)$  and  $N_2(d\Phi/dt)$ . LaPlace Transform techniques were used to represent the initial conditions and obtain the solution for current  $i_1$  in the primary circuit. The three possible solutions, oscillatory, critically damped, or overdamped [i.e.,  $\omega_o^2$  greater than, equal to, or less than  $b^2$ ] are:

$$\text{Case I:} \quad i_1 = \frac{Ki_o e^{-bt} \sin(\omega t + \varphi)}{\sin \varphi} \quad (\omega_o^2 < b^2)$$

Oscillatory

$$\text{Case II:} \quad i_1 = Ki_o e^{-bt} [1 + (a - b)t] \quad (\omega_o^2 = b^2) \quad (1)$$

Critically Damped

$$\text{Case III:} \quad i_1 = \frac{Ki_o e^{-bt} \sinh(\omega t + \varphi)}{\sinh \varphi} \quad (\omega_o^2 > b^2).$$

Overdamped

The values of the constants, of the phase angles, and of related terms, are summarized in Tables II and III respectively. The circuit equations

also showed that the transformed circuit of Fig. 2b could be used to represent all the variations in the primary circuit, where the primed values of  $L$  and  $R$  represent the effective values of primary circuit inductance and resistance respectively. This simplification results from the term  $G_2\phi/C$ , which is found to represent the dissipative losses due to the secondary. (The term  $L''$  will be discussed in Section 2.2.2.)

### 2.1.3 Equations for Charge, Current, and Contact Voltage

The expression for current, equation (1), may be used to derive equations for charge and contact voltage as a function of time. The charge  $q_1$  is given by

$$q_1 = \int i_1 dt \quad (2)$$

and contact voltage by

$$V_c = V_o + \frac{q_1}{C} + i_1 R_n. \quad (3)$$

The resulting general expressions for all these variables are summarized in Table IV for the cases: oscillatory, critically damped, and overdamped. Equations are also given for two important special cases:  $R_n = 0$ , and both  $R_n$  and  $G_2 = 0$  (i.e., capacitive shunt only, or air core coil, respectively.) Of course, other special cases can be derived by making appropriate substitutions into the general equations. Table V similarly summarizes these results for the instant of contact opening, i.e., for conditions at  $t = 0$ . It is found that, at  $t = 0$ , Cases I, II, or III all give equal values for each variable, as one would expect.

The equations in Table IV express the variations in charge, current, and contact voltage as a function of time. Of these, it is often of greatest interest to consider the contact voltage; a normalized version is plotted in Fig. 8 based on the discussion of peak voltages in Section 2.3.

### 2.2 Discussion of Conditions at Critical Damping

The boundary condition for critical damping, now to be considered, helps to explain the way in which the various kinds of surges are influenced by the circuit parameters. Comparison of experimentally observed conditions at the critical damping point with this analysis also provides confirmation for much of the analysis; these measurements also provide means for determining effective values for the core loss

TABLE IV—BASIC CIRCUIT EQUATIONS

VARIABLE		COLUMN 1	COLUMN 2	COLUMN 3
		GENERAL CASE	WHEN $R_n = 0$	WHEN $\begin{cases} R_n = 0 \\ G_2 = 0 \end{cases}$
<u>CASE I</u>				<u>CASE I</u>
(a)	$q_1 =$	$-\frac{KI_0 e^{-bt}}{\omega_0 \sin \phi} \sin(\omega t + \phi + \theta)$	$= -\frac{CV_0 \beta \omega^{-1/2} e^{-bt}}{\sin \theta} \sin(\omega t + \phi + \theta)$	$= -\frac{CV_0 \beta \omega^{-1/2} e^{-bt}}{\sin \theta} \sin(\omega t + 2\theta)$
(b)	$i_1 =$	$\frac{KI_0 e^{-bt}}{\sin \phi} \sin(\omega t + \phi)$	$= \frac{I_0 e^{-bt}}{\sin \phi} \sin(\omega t + \phi)$	$= \frac{I_0 e^{-bt}}{\sin \theta} \sin(\omega t + \theta)$
(c)	$V_c - V_0 =$	$\frac{KI_0 e^{-bt}}{\sin \phi} \left[ R_n \sin(\omega t + \phi) - \frac{1}{\omega_0 C} \sin(\omega t + \phi + \theta) \right]$	$= -\frac{V_0 \beta \omega^{-1/2} e^{-bt}}{\sin \theta} \sin(\omega t + \phi + \theta)$	$= -\frac{V_0 \beta \omega^{-1/2} e^{-bt}}{\sin \theta} \sin(\omega t + 2\theta)$
(d)	$\dot{V}_c =$	$\frac{KI_0 e^{-bt}}{\sin \phi} \left[ \frac{1}{C} \sin(\omega t + \phi) - \omega_0 R_n \sin(\omega t + \phi - \theta) \right]$	$= \frac{I_0 e^{-bt}}{C \sin \phi} \sin(\omega t + \phi)$	$= \frac{I_0 e^{-bt}}{C \sin \theta} \sin(\omega t + \theta)$
<u>CASE II</u>				<u>CASE II</u>
(a)	$q_1 =$	$-CV_0 e^{-bt} \left[ 1 + \frac{b(a-b)}{a} t \right]$	$= -CV_0 e^{-bt} \left[ 1 + \frac{b(a-b)}{a} t \right]$	$= -CV_0 e^{-bt} \left( 1 + \frac{bt}{a} \right)$
(b)	$i_1 =$	$KI_0 e^{-bt} [1 + (a-b)t]$	$= I_0 e^{-bt} [1 + (a-b)t]$	$= I_0 e^{-bt} (1 + bt)$
(c)	$V_c - V_0 =$	$-V_0 e^{-bt} \left[ 1 - \frac{KR_n}{R_w} + (a-b) \left( \frac{b}{a} - \frac{KR_n}{R_w} \right) t \right]$	$= -V_0 e^{-bt} \left[ 1 + \frac{b(a-b)}{a} t \right]$	$= -V_0 e^{-bt} \left( 1 + \frac{bt}{a} \right)$
(d)	$\dot{V}_c =$	$\frac{KI_0 e^{-bt}}{C} [1 - CR_n(2b-a) + (a-b)(1 - bCR_n)t]$	$= \frac{I_0 e^{-bt}}{C} [1 + (a-b)t]$	$= \frac{I_0 e^{-bt}}{C} (1 + bt)$
<u>CASE III</u>				<u>CASE III</u>
(a)	$q_1 =$	$-\frac{KI_0 e^{-bt}}{\omega_0 \sin \theta \phi} \sin(\omega t + \phi + \theta)$	$= -\frac{CV_0 \beta \omega^{-1/2} e^{-bt}}{\sin \theta \phi} \sin(\omega t + \phi + \theta)$	$= -\frac{CV_0 \beta \omega^{-1/2} e^{-bt}}{\sin \theta \phi} \sin(\omega t + 2\theta)$
(b)	$i_1 =$	$\frac{KI_0 e^{-bt}}{\sin \theta \phi} \sin(\omega t + \phi)$	$= \frac{I_0 e^{-bt}}{\sin \theta \phi} \sin(\omega t + \phi)$	$= \frac{I_0 e^{-bt}}{\sin \theta \phi} \sin(\omega t + \theta)$
(c)	$V_c - V_0 =$	$\frac{KI_0 e^{-bt}}{\sin \theta \phi} \left[ R_n \sin(\omega t + \phi) - \frac{1}{\omega_0 C} \sin(\omega t + \phi + \theta) \right]$	$= -\frac{V_0 \beta \omega^{-1/2} e^{-bt}}{\sin \theta \phi} \sin(\omega t + \phi + \theta)$	$= -\frac{V_0 \beta \omega^{-1/2} e^{-bt}}{\sin \theta \phi} \sin(\omega t + 2\theta)$
(d)	$\dot{V}_c =$	$\frac{KI_0 e^{-bt}}{\sin \theta \phi} \left[ \frac{1}{C} \sin(\omega t + \phi) - \omega_0 R_n \sin(\omega t + \phi - \theta) \right]$	$= \frac{I_0 e^{-bt}}{C \sin \theta \phi} \sin(\omega t + \phi)$	$= \frac{I_0 e^{-bt}}{C \sin \theta \phi} \sin(\omega t + \theta)$

TABLE V—BASIC CIRCUIT EQUATIONS WHEN  $t = 0^+$ 

Variable	General Case	Case when $R_n = 0$
(a) $q_1 =$	$-CV_o$	$= -CV_o$
(b) $i_1 =$	$KI_o$	$= I_o$
(c) $V_c =$	$KI_oR_n$	$= 0$
(d) $\dot{V}_c =$	$\frac{K^2I_o}{C} \left[ 1 - \frac{CR_n^2}{L_1(1 + G_2/G_w)_2} \right]$	$= \frac{I_o}{C}$

term,  $G_2$ , and the effective permeance,  $\mathcal{P}$ , of the core, as will be seen in Section 3.2.

### 2.2.1 General Expressions

The critically damped condition is  $\omega_0^2 = b^2$ , or alternatively:

$$\frac{CR'^2}{4L'} = 1. \quad (4)$$

Substituting values for  $R'$  and  $L'$  from Table I,

$$C \left( \frac{G_2 \mathcal{P}}{C} + R_1 \right)^2 = 4N_1^2 \mathcal{P} (1 + G_2/G_1).$$

This expression is simplified by making the substitution

$$\beta_1 = \frac{CR_1^2}{\mathcal{P}N_1^2},$$

yielding a quadratic equation which can be expressed in terms of only two variables,  $\beta_1$  and  $G_2/G_1$ . The solution is given by either of the two equivalent expressions, equations (5a) and (5b), of which the former is usually more convenient:

$$G_2/G_1 = \beta_1^{\frac{1}{2}} (\beta_1^{\frac{1}{2}} \pm 2) \quad (5a)$$

or

$$\beta_1 = 2 \left[ 1 + \frac{G_2}{2G_1} \pm \left( 1 + \frac{G_2}{G_1} \right)^{\frac{1}{2}} \right]. \quad (5b)$$

These equations have two solutions, which depend on whether  $G_2/G_1 > \beta_1$ , or  $G_2/G_1 < \beta_1$ . The two solutions are plotted in Fig. 4, for the range of these values likely to be encountered in relay switching

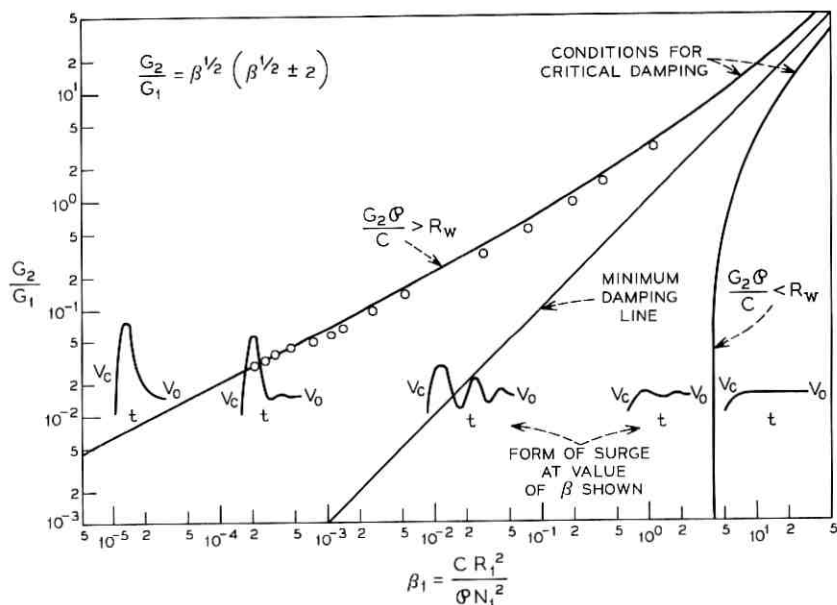


Fig. 4—Conditions for critical damping— $G_2/G_1$  vs  $\beta_1$ .\*

practice. Thus, the boundary between oscillatory and overdamped conditions is determined by either of two circumstances:

- (i) Losses in *secondary* circuit are dominant [use + sign in equation (5a) or - sign in equation (5b)], for which

$$\frac{G_2}{G_1} > \beta_1, \quad \text{or} \quad \frac{G_2 \Phi}{C} > R_1.$$

Here,

$$\frac{G_2}{G_1} = \beta_1^2 (\beta_1^2 + 2) \quad (6a)$$

or

$$\beta_1 = 2 \left[ \left( 1 + \frac{G_2}{2G_1} \right) - \left( 1 + \frac{G_2}{G_1} \right)^{1/2} \right] \quad (6b)$$

and there are positive values of  $G_2/G_1$  for all positive values of  $\beta_1$ .

\* The subscripts "1" or "w", applied to  $G$  and  $\beta$  in various figures, are used to call attention to the applicability of the information; e.g.,  $\beta_1$  indicates that the general analysis (including  $RC$  network) applies;  $\beta_w$  indicates the analysis specifically applied to the unprotected case, where  $R_n = 0$ .

(ii) Losses in *primary* circuit are dominant [use - sign in equation (5a) or + sign in equation (5b)], for which

$$\frac{G_2}{G_1} < \beta_1, \quad \text{or} \quad R_1 > \frac{G_2 \phi}{C}.$$

Here,

$$\frac{G_2}{G_1} = \beta_1^{\frac{1}{2}}(\beta_1^{\frac{1}{2}} - 2) \quad (7a)$$

or

$$\beta_1 = \left[ 1 + \frac{G_2}{2G_1} + \left( 1 + \frac{G_2}{G_1} \right)^{\frac{1}{2}} \right] \quad (7b)$$

and meaningful (i.e., positive) values of  $G_2/G_1$  only exist when  $\beta_1 > 4$ .

Note that, when  $G_2 = 0$ , i.e., there are no eddy current losses, then from equation (5b),

$$\beta_1 = 4$$

as is well known for the conventional  $L, R, C$  circuit.

The condition

$$\frac{G_2}{G_1} = \beta_1 \left( \text{or } \frac{G_2 \phi}{C} = R_1 \right)$$

is seen to be incompatible with critical damping. It is indicated by the 45-degree line in Fig. 4 which in fact corresponds to the point of minimum damping. The character of the contact voltage surges in the various regions is sketched on the figure, summarized as follows. For a given value of  $G_2/G_1$ , the response will be oscillatory for values of  $\beta_1$  lying between the two curves, with minimum damping when  $\beta_1 = G_2/G_1$ . When  $\beta_1$  equals or exceeds the value delineated by the right-hand curve, the response will be critically damped or overdamped with a gradual asymptotic rise to  $V_o$ . When  $\beta_1$  equals or is less than the value delineated by the left-hand curve, the response will be critically damped or overdamped with a single overshoot followed by an asymptotic decay to  $V_o$ .

Since the principal variation in  $\beta_1$  is usually the result of variations in  $C$ , it is also useful to replot Fig. 4 in the form  $G_2/G_1$  vs  $C$ , for a range of values of  $(N_1/R_1)^2 \phi$ . Such a family of curves is given in Fig. 5. It is sometimes helpful to analyze experimental data by plotting the points on such a graph.

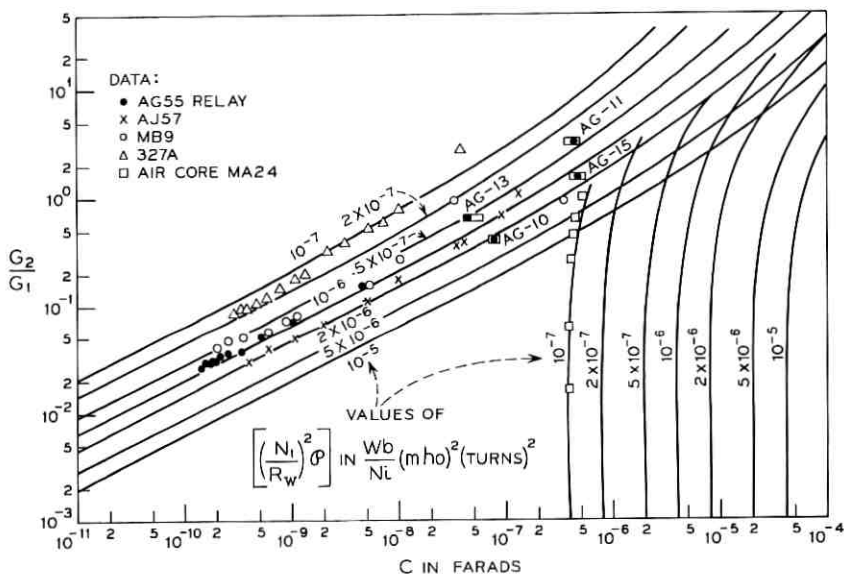


Fig. 5—Conditions for critical damping— $G_2/G_1$  vs  $C$ .

The data points seen in Figs. 4 and 5 will be explained in the later discussion of experimental results, Section 3.2.

The critically damped circuit equations, Case II in Table IV, may now be extended to include expressions for the two-valued equalities of equation (5), which were not previously obvious. For this purpose it is convenient to make available the related values of some of the terms appearing in these equations. In the present study we consider only the simpler cases for  $R_n = 0$ , or both  $R_n$  and  $G_2 = 0$ , which are summarized in Table VI. Using these equalities, the critically damped circuit equations of Table IV can be simplified for easier handling, as given for reference purposes in Table VII.

The predicted boundaries between overdamped and oscillatory conditions shown in Figs. 4 and 5 afford a convenient means for experimentally verifying the foregoing circuit analysis. A test relay is selected which has parallel-wound primary and secondary coils. The primary is bridged by a variable capacitor,  $C$ , while the secondary is bridged by a variable resistor,  $R'_2$ . For a chosen setting of  $C$ , the contact voltage surge  $V_c$  is observed by oscilloscope, and  $R'_2$  is varied until the surge appears to be critically damped. This process may be repeated for any desired number of settings for  $C$ , which must include corrections to include any distributed capacitance in the winding and wiring,

Constant	Core Losses Dominant	Coil Losses Dominant
	i. e. $\frac{G_2 \Phi}{C} > R_w$ , or $G_2/G_w > \beta_w$	i. e. $\frac{G_2 \Phi}{C} < R_w$ , or $G_2/G_w < \beta_w$
$G_2/G_w =$	(holds for all values of $\beta_w > 0$ ) $\beta_w^{\frac{1}{2}}(\beta_w^{\frac{1}{2}} + 2)$	(holds only for values of $\beta_w \geq 4$ ) $\beta_w^{\frac{1}{2}}(\beta_w^{\frac{1}{2}} - 2)$
$1 + G_2/G_w =$	$(\beta_w^{\frac{1}{2}} + 1)^2$	$(\beta_w^{\frac{1}{2}} - 1)^2$
$\frac{G_2/G_w}{\beta_w} =$	$1 + 2\beta_w^{-\frac{1}{2}}$	$1 - 2\beta_w^{-\frac{1}{2}}$
$a =$	$\frac{1}{G_w \Phi (\beta_w^{\frac{1}{2}} + 1)^2}$	$\frac{1}{G_w \Phi (\beta_w^{\frac{1}{2}} - 1)^2}$
$b =$	$\frac{1}{G_w \Phi \beta_w^{\frac{1}{2}} (\beta_w^{\frac{1}{2}} + 1)}$	$\frac{1}{G_w \Phi \beta_w^{\frac{1}{2}} (\beta_w^{\frac{1}{2}} - 1)}$
$a - b =$	$-\frac{1}{G_w \Phi \beta_w^{\frac{1}{2}} (\beta_w^{\frac{1}{2}} + 1)^2}$	$\frac{1}{G_w \Phi \beta_w^{\frac{1}{2}} (\beta_w^{\frac{1}{2}} - 1)^2}$
$b/a =$	$\frac{\beta_w^{\frac{1}{2}} + 1}{\beta_w^{\frac{1}{2}}}$	$\frac{\beta_w^{\frac{1}{2}} - 1}{\beta_w^{\frac{1}{2}}}$
$\frac{b}{a}(a - b) =$	$-\frac{1}{G_w \Phi \beta_w (\beta_w^{\frac{1}{2}} + 1)}$	$\frac{1}{G_w \Phi \beta_w (\beta_w^{\frac{1}{2}} - 1)}$

TABLE VII—CIRCUIT EQUATIONS AT CRITICAL DAMPING (FOR THE CASE WHEN  $R_n = 0$ )

Variable	Core Losses Dominant	Coil Losses Dominant
	$\frac{G_2 \Phi}{C} > R_w$ , or $G_2/G_w > \beta_w$	$\frac{G_2 \Phi}{C} < R_w$ , or $G_2/G_w < \beta_w$
	(holds for all values of $\beta_w > 0$ )	(holds only for values of $\beta_w \cong 4$ )
$q_1 =$	$-CV_e e^{-bt} \left[ 1 - \frac{t}{G_w \Phi \beta_w^{\frac{1}{2}} (\beta_w^{\frac{1}{2}} + 1)} \right]$	$-CV_e e^{-bt} \left[ 1 + \frac{t}{G_w \Phi \beta_w^{\frac{1}{2}} (\beta_w^{\frac{1}{2}} - 1)} \right]$
$i_1 =$	$I_e e^{-bt} \left[ 1 - \frac{t}{G_w \Phi \beta_w^{\frac{1}{2}} (\beta_w^{\frac{1}{2}} + 1)} \right]$	$I_e e^{-bt} \left[ 1 + \frac{t}{G_w \Phi \beta_w^{\frac{1}{2}} (\beta_w^{\frac{1}{2}} - 1)} \right]$
$V_c - V_o =$	$-V_e e^{-bt} \left[ 1 - \frac{t}{G_w \Phi \beta_w^{\frac{1}{2}} (\beta_w^{\frac{1}{2}} + 1)} \right]$	$-V_e e^{-bt} \left[ 1 + \frac{t}{G_w \Phi \beta_w^{\frac{1}{2}} (\beta_w^{\frac{1}{2}} - 1)} \right]$
$\dot{V}_c =$	$\frac{I_e}{C} e^{-bt} \left[ 1 - \frac{t}{G_w \Phi \beta_w^{\frac{1}{2}} (\beta_w^{\frac{1}{2}} + 1)} \right]$	$\frac{I_e}{C} e^{-bt} \left[ 1 + \frac{t}{G_w \Phi \beta_w^{\frac{1}{2}} (\beta_w^{\frac{1}{2}} - 1)} \right]$
where	$\frac{1}{G_w \Phi \beta_w^{\frac{1}{2}} (\beta_w^{\frac{1}{2}} + 1)}$	$\frac{1}{G_w \Phi \beta_w^{\frac{1}{2}} (\beta_w^{\frac{1}{2}} - 1)}$
$b =$		

as is discussed in Section 3.1. These data may then be analyzed to give estimates for  $G_e$  and  $\mathcal{O}$  for the particular structure being studied; and also to compare the measured variation of  $G_2/G_1$  vs  $\beta$  against the predicted values, as is discussed in Sections 3.1.3 and 3.2.

In accord with relay design practice, assume that the effective secondary coil constant,  $G_2$ , is the sum of two separate terms,

$$G_s = \frac{N_2^2}{R_2 + R_2'}$$

and  $G_e$ , representing the actual secondary winding, and the single-turn eddy current coupling term for the core, respectively. An approximate estimate of  $G_e$  may then be obtained from an examination of those data points for which  $G_s$  has quite small values. This procedure is helped by the fact that, at small values of  $G_2/G_1$  and  $\beta$ , the critical damping equations (6) may be further simplified. By series expansion of equation (6b), neglecting terms of higher than second order, it reduces to

$$\beta_1 = \frac{1}{4} \left( \frac{G_2}{G_1} \right)^2 \quad (8)$$

or, from Table I,

$$G_2 = G_s + G_e = 2N_1 \sqrt{C/\mathcal{O}}. \quad (9)$$

Thus, a plot of  $G_2$  vs  $C^{\frac{1}{2}}$ , for small values of  $G_2$ , should yield a straight line with a negative intercept equal to  $G_e$  and a slope of  $2N_1\mathcal{O}^{-\frac{1}{2}}$ , from which  $\mathcal{O}$  may also be determined. This procedure is indicated in the experiment summarized in Table VIII, and further discussed in Section 3.1, with determination of  $G_e$  shown in Fig. 17. In this example,  $G_e$  was found to equal about 220 mho. Using this figure to obtain an approximate value for  $G_2$ , the effective value of permeance  $\mathcal{O}$  (at least for small values of  $G_2$ ) may then be determined using equation (9), as is also shown in Fig. 17.

### 2.2.2 Peak Voltages and Oscillations due to Imperfect Coupling Between Primary and Secondary

The foregoing analysis is found to afford an accurate picture of the transients upon disconnection, so long as the windings are well coupled, as is shown in Section III. Such coupling is best obtained by the use of parallel windings, wherein each turn of one coil is coupled to the same flux as the corresponding turn of the other coil. However, when the coils are wound concentrically, there is a departure from this ideal

TABLE VIII—CRITICAL-DAMPING MEASUREMENTS ON A WIRE SPRING (AG-55) RELAY

Observed Parameters at Critical Damping		Calculations							$\beta_w$	
$C(f)$	$R_2'$	$C_{eff} = C + C_d$	$(C_{eff})^{1/2}$	$R_e + R_2'$	$G_s$	$G_s + G_e$	$G_2/G_w$	Experimental†	Theoretical (Fig. 4)	
$0.24 \times 10^{-6}$	0	$0.24 \times 10^{-6}$		44.5	114,700	114,900	3.03	1.10	1.0	
0.14	50	0.14		94.5	53,900	54,100	1.43	0.389	0.3	
0.09	100	0.09		144.5	35,200	35,420	0.935	0.20	0.15	
0.05	200	0.05		244.5	20,800	21,020	0.514	$8.65 \times 10^{-2}$	$5.5 \times 10^{-2}$	
0.02	400	0.02		445	11,450	11,670	0.308	2.99	2.28	
$0.4 \times 10^{-8}$	1000	$0.41 \times 10^{-8}$		1045	4,850	5,090	0.134	0.539	0.45	
0.2	1500	0.217		1545	3,290	3,510	0.0925	0.27	0.22	
0.103	2300	0.120		2345	2,170	2,390	0.0631	0.146	0.137	
$7.65 \times 10^{-10}$	2700	$9.35 \times 10^{-10}$		2745	1,850	2,070	0.0546	0.112	0.106	
4.55	3000	6.25		3045	1,670	1,890	0.0499	$7.46 \times 10^{-4}$	$6.2 \times 10^{-4}$	
2.15	3600	3.85	$1.96 \times 10^{-5}$	3645	1,392	1,612	0.0425	4.57	4.5	
1.1	4400	2.8	1.68	4445	1,143	1,363	0.0360	3.2	3.3	
0.52	5100	2.22	1.49	5145	988	1,208	0.0318	2.61	2.5	
0.10	5800	1.80	1.34	5845	871	1,091	0.0288	2.11	2.0	

Initial Data:  $N_1 = 6525$   $R_w = 1125$   $G_w = N_1^2/R_w = 37,900$

$N_2 = 2260$   $R_s = 44.5$   $G_{max}^2 = N_2^2/R_s = 114,700$

Measured Value of  $C_d = 170 \times 10^{-12}f$

\* From these data, see Fig. 17, and infer that  $G_e = 220$  mho,  $\phi = 2.6 \times 10^{-8}$  Wb/NI.  
 †  $\beta_w = (CR_w^2/\phi N_1^2)(1 + G_2/G_w) = 1.14 \times 10^8 (1 + G_2/G_w)C$ .

situation due to independent transient currents which arise within the uncoupled portion of the main winding. An additional oscillatory condition develops in such cases, which is particularly noticeable for relays with copper sleeves, whose core losses tend to be very high; this condition becomes more and more noticeable when the circuit approaches critical damping or is well into the overdamped core-loss region. This behavior may be explained by recognizing the role of the uncoupled part of the primary winding, now to be discussed.

Recall that the core loss is governed by a term  $G_2\mathcal{P}/C$  representing the resistive losses in the secondary, and note that this term grows very large as  $C$  becomes small. Thus, in the critical damping region, this large term tends to block all flow of current in the primary inductance. However, that portion of the primary inductance which is not coupled to the secondary, i.e., which does not share the same common flux, will not experience opposition to current flow from the term  $G_2\mathcal{P}/C$  (because, for it,  $G_2 = 0$ ). The uncoupled part of the winding provides a parallel path tending to bypass the main winding in series with its core-loss term, as shown by the dotted lines in Fig. 2b. Its inductance may be much less than that of the coupled part of the winding, but still capable of generating appreciable superimposed surges into the rest of the circuit. The equivalent circuit for this condition reverts to the simple case for which only coil losses apply (i.e., no secondary winding) but for which the inductance is represented by a new term

$$L'' = \mathcal{P}''N_1^2 \quad (10)$$

where  $\mathcal{P}''$  represents the effective differential permeance of that part of the coil which does not couple to the secondary. It may be found experimentally, or be approximated by rule of thumb, as discussed in Section III. The resulting oscillations, as to frequency, peak voltage, etc., may be predicted through the use of the equations in Table II, for the case that  $G_2 = 0$ , and using  $L''$  to represent the inductance. Peak voltage effects for this case may be read from Fig. 8, where  $\beta$  is estimated by using  $\mathcal{P}''$  for permeance. The oscillation frequency is approximated from the value of  $\omega_o$  given in Table II:

$$f_o = \frac{\omega_o}{2\pi} = \frac{1}{2\pi N_1 \sqrt{\mathcal{P}''C}} \quad (11)$$

Conversely, when the oscillation frequency is measured, corresponding to a given set of circuit conditions (i.e.,  $\beta$ ,  $G$ , etc.), the value of  $\mathcal{P}''$  can be evaluated. Measurements on various relays are shown in Section

III to correlate well with this relation, where  $\mathcal{O}''$  is found to have a value of about  $0.6 \times 10^{-8}$  Wb/NI for various structural types typical of telephone switching.

### 2.3 Determination of Peak Values of Contact Voltage, and Related Values of Charge and Current

The peak values of the time-dependent variables  $q_1$ ,  $i_1$ , and  $V_c$  may be determined by differentiating the corresponding equations as given in Table IV with respect to  $t$ , setting the result equal to 0, solving for  $t$  under these conditions (designated  $t'$ ), and then evaluating each of the original equations when  $t$  is replaced by  $t'$ . These steps together with the resulting expressions for  $t'$  and for  $q_1$ ,  $i_1$ , or  $V_c$  are briefly outlined in Appendix B. The derivations apply to the previously noted general case which includes an RC network shunted across the load, but the resulting general expressions are too involved for a full treatment in the present report. When the network resistance  $R_n$  is set equal to zero, however, representing the simpler unprotected case, the resulting expressions are relatively convenient to work with. These expressions, which are also developed in Appendix B, are summarized in Table IX. The peak voltage relations hold greatest interest, and will now be considered in more detail.

As seen in Appendix B, and Table IX, the peak voltage expressions for an unprotected load ( $R_n = 0$ ) are:

Condition	Time to Peak, $t'$	Contact Peak Voltage, $V_p$
I	$t' = \frac{\pi - \varphi}{\omega}$	$V_p = V_o \left[ 1 + \beta_w^{-1} \exp \left( -\frac{\pi - \varphi}{\tan \theta} \right) \right]$ . (12)
II	$= G_w \mathcal{O} \beta_w^{\frac{1}{2}} (1 + \beta_w^{\frac{1}{2}})^2$	$= V_o [1 + \beta_w^{-\frac{1}{2}} e^{-(1 + \beta_w^{\frac{1}{2}})}]$ . (13)
III	$= -\frac{\varphi}{\omega}$	$= V_o \left[ 1 + \beta_w^{-1} \exp \left( -\frac{\varphi}{\tanh \theta} \right) \right]$ . (14)

These equations express the peak voltage in terms of the variables  $\beta_w$ ,  $\theta$ , and  $\varphi$ . Actually, both  $\theta$  and  $\varphi$  may also be expressed in terms of  $\beta_w$  and  $G_2/G_w$  (see Table III). The equations are given in the form shown for the sake of compactness. However, when computations are made, the more detailed values for these terms can be substituted from Table III. (The subscript  $w$  is used to indicate that the value of  $R$  in this case is only the winding resistance, i.e.,  $R_n = 0$ ).

For this case of unprotected load, equations (12), (13), and (14) may be used to plot the time-to-peak, and the peak voltage. It is



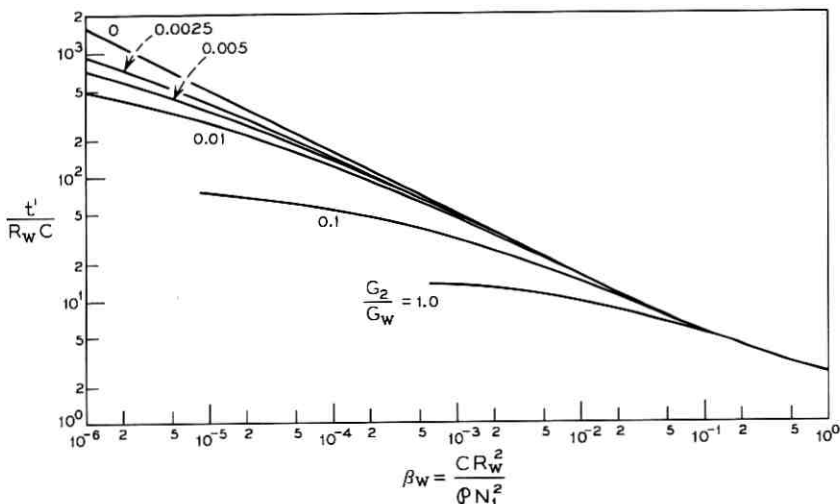


Fig. 6—Time,  $t'$ , to reach peak voltage vs load design factor,  $\beta$ .

convenient to plot these in ratio form, using the ratio of peak time to capacitive time constant,  $t'/R_w C$ , and the ratio of peak voltage to battery voltage,  $V_p/V_o$ , respectively. These results are given in Figs. 6 and 7, as a function of  $\beta_w$ , for various values of  $G_2/G_w$ . They are found to be in good agreement with actual experience, as will be shown in Section 3.3, where measurements and theory are compared for both  $t'$  and  $V_p$ . It is seen that the ratio  $G_2/G_w$  has a pronounced influence

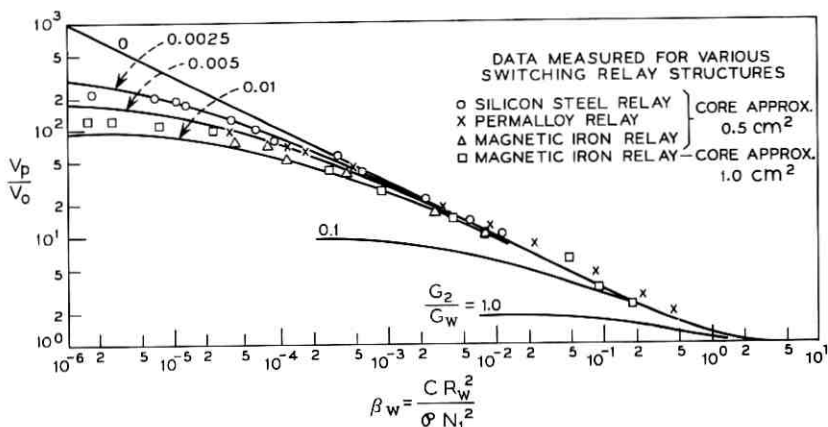


Fig. 7—Peak voltage,  $V_p$ , as a function of load design factor,  $\beta$ .

on the peak voltage across the opening contacts, and that even very small values of this ratio can lower the peak voltage and pulse time by several fold compared to the air core (i.e., nondissipative) case. This is particularly noticeable when small values of  $\beta_w$  (usually corresponding to small values of shunt capacitance) are involved.

A summary of the equations for the peak-related values of  $q_1$ ,  $i_1$ , and  $V_c$  is also given in Table IX.

The relations determining these peak values may be used to restate the circuit equations in ratio form, if desired. As the contact voltage expressed in this form is of particular interest in later discussions, its value (when  $R_n = 0$ ) is given below as

$$\frac{V_c - V_o}{V_p - V_o} = - \frac{\exp\left(-\frac{\pi - \varphi}{\tan \theta} (1 - \tau)\right) \sin\{(\pi - \varphi)\tau + \varphi + \theta\}}{\sin \theta}. \quad (15)$$

Equation (15) expresses the ratio of instantaneous to peak coil voltage as a function of the ratio of instantaneous to peak time,  $\tau$ , following disconnection. A plot of this expression for two values of  $\beta_w$  is given in Fig. 8.

#### 2.4. Energy Losses During the Surge

The surges just discussed can lead to breakdowns in wiring, in apparatus, or between the opening contacts. The breakdown itself is usually a very rapid event resulting from the discharge of the circuit capacitance through the low-impedance breakdown path of electrodes

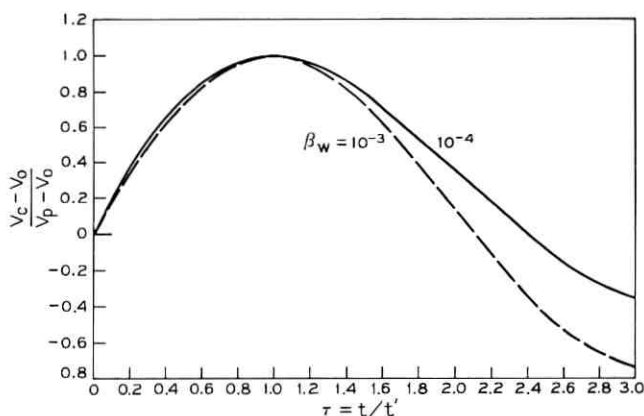


Fig. 8—Normalized plot of coil surge voltage ( $V_c - V_o$ ) vs time.

and battery. The energy transferred from inductance to capacitance is thus the preponderant source of breakdown damage, and expressions are therefore needed to describe the manner in which the inductive energy is dissipated or transferred to the capacitor. In this section, a brief discussion is given of the breakdown process, followed by the derivation of energy expressions based on the foregoing circuit equations.

#### 2.4.1 Breakdowns

The earlier expressions for contact voltage are of particular interest when breakdowns occur, because it is the value of voltage—matched against the dielectric strength of the wiring, of the connected apparatus, or of the contact itself—which determines when and how often breakdowns will occur. These breakdown possibilities are indicated in the simplified view of Fig. 9, which shows a typical voltage surge vs time after disconnection, and also two forms of dielectric characteristics representing the breakdown strength of portions of the circuit. The horizontal line, designated A, represents, for example, the breakdown characteristic of a pair of wires or apparatus terminals with constant spacing. The line of rising slope, designated B, represents the break-

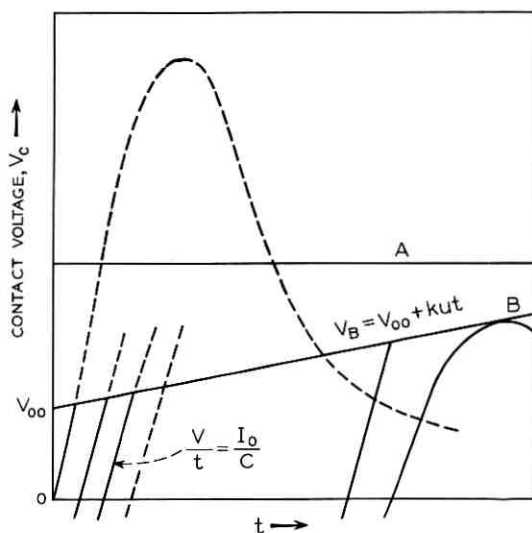


Fig. 9—Interaction between inductive surge and contact's dielectric characteristic (simplified view).

down characteristic of separating contacts. Its characteristic is well approximated by the equation

$$V_B = V_{oo} + kut \quad (16)$$

(see for example Ref. 9)

where  $V_{oo}$  = minimum gas breakdown (usually the Paschen breakdown point which for air is about 320 volts),

$k$  = slope constant (for air it is approximately  $7 \times 10^6$  V/m),  
and

$u$  = contact separation velocity.

There will be a gas breakdown whenever the coil's voltage characteristic, plus the battery voltage, exceeds the electrode separation characteristic, as is shown in the figure for the case of separating contacts. Each breakdown is commonly followed by an arc resulting from the discharge of the local capacitance, which was charged to a voltage ( $V_B - V_o$ ), through the low-impedance local wiring, usually causing a partial capacitive discharge and an extinction of the arc due to reverse oscillations. Following this, a new charging cycle begins which is similar to the earlier surge except rising toward a somewhat lower peak voltage representing the energy remaining in the load after the first breakdown. This procedure will continue repetitively until the residual load energy is insufficient to develop a surge whose peak value can reach the electrodes' dielectric breakdown.

For the constantly-spaced electrodes, each disconnection will lead to a group of multiple breakdowns which induce radiation in the wiring and a slow erosion of their surfaces. For example, fine-wire coils with too-close leadouts can eventually develop open-circuits as a result of this slow attrition.

Similarly, separating contacts experience an erosion of their surfaces. In the case of relay contacts, it is desirable to correlate the amount of erosion with the circuit parameters in order to determine either (i) the required contact volume to permit a given number of operations before failure, or (ii) the number of operations for a given contact volume. The remainder of this section will indicate one approach toward the correlation of contact erosion with the conditions of circuit and contact.

Many contact erosion studies have shown that the amount of metal lost is proportional to the energy dissipated between the electrodes during the discharge.<sup>7,9</sup> For the present case, a method of estimating this energy for the multiple breakdowns of the "B" type transient is therefore needed, and two alternate procedures are conceptually possible. The two approaches may be more clearly understood by a

reexamination of the oscilloscopic traces of coil current and contact voltage immediately following the contact opening, in Fig. 1. Each of the multiple surges for the mechanical contact is seen to be the early stage of an ideal contact surge which is interrupted when it reaches the breakdown characteristic of the contact gap, as is also indicated in Fig. 9. The breakdown is due to the voltage to which the capacitor is charged, plus the battery voltage, and when the breakdown does occur, it represents the discharge of this capacitance through the circuit comprising capacitance, contact, battery, and the low impedance of their wiring. This is a very rapid discharge, occurring in times that are negligible compared to the time required for the original surge to reach its breakdown value. The discharge is extinguished either by exhausting the capacitive stored energy  $\frac{1}{2}C(V_B - V_o)^2$ , or by reversals in voltage and current during the very high frequency breakdown discharge. Following extinction, a new surge develops as before. The energy dissipated in these multiple arcs may be approached in two ways: (i) by summing the individual energy terms (each of the form  $\Delta E = \int_0^t V_A I_A dt$ ), where  $V_A$  is the characteristic voltage across the arc for the particular contact metal (typically about 14 volts) and  $I_A$  is the current through the arc, or (ii) by the total of the energy increments which are transferred from the coil to the capacitor to the arc (which should be related to the total initial inductive energy). Though the determination of  $V_A$ ,  $I_A$  and  $t$  are subject to many difficulties of estimation, efforts to treat this problem with computer techniques have shown much promise.<sup>10</sup> The alternative procedure, namely to find the inductive energy which can be released into the arc, via the capacitor, will be considered here. Contact erosion should be strongly related to this energy, which will be discussed for the ideal inductive case in Section 2.4.2, and for the usual showering case in Section 2.4.3.

A more rigorous treatment must include the additional energy supplied from the battery during each breakdown arc, and an introductory discussion is given in Section 2.4.4.

#### 2.4.2 Energy Dissipation Following Disconnection—Ideal Contact

First, let us find the energy consumed during the inductive surge, as a function of time. For simplicity, the analysis given here will consider the case that  $R_n = 0$ , i.e., the unprotected load. Based on the equivalent circuit of Fig. 2b, and equation (Ib) Col. 2 of Table IV, the energy dissipated in the circuit resistance is seen to be

$$E_{\text{res}} = \int_0^t i_1^2 R' dt = \frac{I_0^2 R'}{\sin^2 \varphi} \int_0^t e^{-2bt} \sin^2 (\omega t + \varphi) dt. \quad (17)$$

Upon integrating between the limits indicated, this internally dissipated energy is found to be

$$E_{\text{res}} = \frac{L'I_0^2}{2 \sin^2 \varphi} \{ [1 - \cos \theta \cos (2\varphi + \theta)] - e^{-2bt} [1 - \cos \theta \cos [2(\omega t + \varphi) + \theta]] \}. \quad (18)$$

A closer inspection of equation (18), and further rearrangement of terms based on the relations of Tables II and IV, gives the alternative expression

$$E_{\text{res}} = \frac{L_1 I_0^2}{2} (1 + G_2/G_w + \beta_w) - e^{-2bt} \left[ \frac{\sin^2 (\omega t + \varphi) + \sin^2 (\omega t + \varphi + \theta)}{\sin^2 \theta} \right] \quad (19)$$

$$= E_o - E_u \quad (20)$$

where  $E_o$  = initially available energy in coil and capacitance

$$= \frac{1}{2} L'I_0^2 + \frac{1}{2} CV_o^2, \quad (21)$$

$E_u$  = undissipated energy, i.e., that portion of initially stored energy, which, at time  $t$ , has not yet been dissipated

=  $E_{\text{ind}}$ , energy still stored in inductance,  $L'$ ,

+  $E_{\text{cap}}$ , energy so far transferred to capacitor,  $C$ .

These expressions thus offer the means for quantitatively estimating the way in which the initially stored energy is either internally dissipated (in the resistive term  $R'$ ) or made available for release outside the system (i.e., stored in the capacitor).

The extent to which energy may be released outside the coil system, as for example into a contact arc, is perhaps more easily pictured by further reference to Fig. 2, recalling that, for the present discussion,  $R_n = 0$ . At the time when the capacitor  $C$  is charged to a value capable of producing a dielectric breakdown at a contact voltage,  $V_B$ , it possesses an energy content  $\frac{1}{2}C(V_B - V_o)^2$  which can be rapidly dissipated in the low-impedance contact circuit during a breakdown. The maximum capacitive energy which can be so discharged occurs at the time  $t'$  and at the voltage  $V_p$ .  $t'$  is the time when the main circuit current

equals zero; at this instant all the undissipated inductive energy has been transferred into the capacitor. The energy in the system at this point,  $E'_u = E_{\text{cap}}$ , is therefore a useful measure of the maximum portion of the coil energy which can be released to do external damage. By substituting the value of  $t'$  from equation (12) into the second right-hand term of equation (19), this is seen to give

$$\left. \frac{E_{\text{cap}}}{E_o} \right|_{\text{max}} = \frac{E'_u}{E_o} = \frac{\exp\left(-\frac{2(\pi - \varphi)}{\tan \theta}\right)}{1 + G_2/G_w + \beta_w} \quad (22)$$

Equation (22) states the maximum fraction of the initial releasable inductive energy that would be capable of doing external damage. Since  $\varphi$  and  $\theta$  are themselves (from Table III) expressible solely in terms of the circuit and relay design parameters  $\beta_w$  and  $G_2/G_w$ , this energy factor is similarly dependent on only these two variables. The result for a wide practical range of relay and circuit variables is given by the family of curves plotted in Fig. 10. It is interesting that these curves indicate a central range of values for  $\beta_w$  where the energy that can be externally released is a maximum, with lesser energy values for larger or smaller values of  $\beta_w$ . This seems physically reasonable because small values of  $\beta_w$  correspond to small values of  $C$  and rapid pulses, while large values of  $\beta_w$  correspond to slow pulses. Thus, for the short pulses, more energy is forced into eddy-current dissipation, while for the slow pulses there is ample time to dissipate energy in

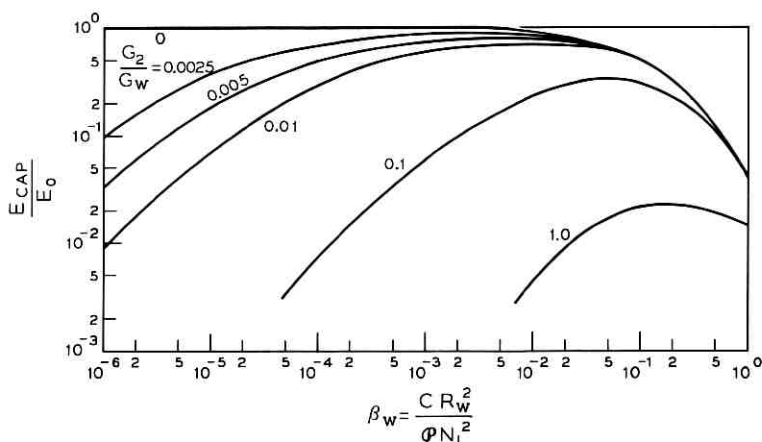


Fig. 10—Fraction of releasable energy,  $E_{\text{cap}}/E_o$ , available as potential source of arcing damage vs  $\beta$ .

the coil resistance before the capacitance is charged; for intermediate values of  $\beta_w$ , both dissipation terms are relatively small.

To summarize this concept of maximum releasable energy, consider an illustrative case for which the following circuit and relay design conditions are given:

Circuit:  $V_o = 50$  volts,  $C = 10^{-9}$  F,  $I_o = 0.100$  ampere.

Relay Coil:  $N_1 = 3100$  turns,  $R_w = 500$  ohms,

$\Phi = 2.5 \times 10^{-8}$  Wb/Nl,  $G_2 = 100$  mho.

Determination of parameters and associated energy:

$$\beta_w = \frac{10^{-10} \times 250,000}{2.5 \times 10^{-8} \times 10^6} = 10^{-3}.$$

$$G_w = \frac{10^6}{500} = 20,000 \text{ mho}; \quad G_2/G_w = 0.005.$$

$$E_o = \frac{2.5 \times 10^{-8}}{2} (3100 \times 0.1)^2 \\ = 1.25 \times 10^{-3} \text{ J, initially available.}$$

From the chart:  $E_{\text{cap}}/E_o = 0.74$ , or maximum releasable energy =  $0.92 \times 10^{-3}$  joule. Since contact erosion is believed proportional to the energy delivered to the arc, this number is a useful starting point in establishing the system's erosion-inducing energy. For arcing contacts, it may be materially improved, it is believed, by an upward correction to the initial energy  $E_o$  as will be discussed in Section 2.4.4.

#### 2.4.3 Energy Dissipation During "B" Type Transient

The preceding results are directly applicable to the repetitive breakdowns that occur between ordinary relay contacts that are separating in an air environment. The breakdowns occur when the surge voltage transient exceeds the dielectric breakdown characteristic of the contact gap, as previously discussed in Section 2.4.1 and illustrated in Fig. 9. Each breakdown occurs during a surge of the form of equation (15), which rises to intersect the contact characteristic given by equation (16) as illustrated in the figure.

2.4.3.1 *Steps During the Breakdown Process.* The energy losses during this series of breakdowns will thus be somewhat different from those in the idealized case discussed in Section 2.4.2 because they occur at an earlier stage of the surge. This effect may be visualized by considering the following simplified statement of representative sequential steps in the total breakdown process:

- (i) The surge rises to a value of  $V_B$  given by equation (16). An amount of energy  $\frac{1}{2}C(V_B - V_o)^2$  is released into the arc circuit while concurrently an amount of energy given by equation (19) is dissipated internally. The energy still remaining in the inductance to serve as a source for the next surge is  $E_{ind}$  and it comprises the initial energy of the previous surge minus the capacitive and resistive terms just mentioned. (A later and more rigorous study must also include the capacitive energy that is not dissipated during the surge, and so temporarily returned to the system, and also the energy replenishment from the battery.)
- (ii) A new surge now develops which will rise toward a lower peak value defined by the inductive energy content after the previous surge, and a new breakdown occurs when a higher value of  $V_B$  is reached, as determined by the intersection of the coil surge with the contact's dielectric characteristic, equation (16). From the earlier work,<sup>9</sup> or from an inspection of Fig. 9, each new breakdown voltage is approximated by

$$V_{B_n} = V_{B_{n-1}} \left( 1 + \frac{2kuC/I_o}{1 - 2kuc/I_o} \right) = V_{B_{n-1}} \left( \frac{1}{1 - 2kuC/I_o} \right) \quad (23)$$

These approximate expressions result from assuming (a) that the relevant part of the surge is closely represented by using its initial slope, i.e.,  $V/t = I_o/C$  when  $t = 0$  (from Table V, Case I(d)), and (b) that the average initial current from the first to the last of the series of surges is given by  $I_o/2$ .

- (iii) Similar steps continue until the amount of energy that must be imparted to the capacitor in order to produce a breakdown exceeds the energy remaining in the inductor. Further breakdowns cannot occur, and any remaining energy is dissipated in the coil's internal resistances.

**2.4.3.2 Energy Relations During the Surge.** An approximate method of estimating the energy that will be available as a driving source for arc damage will now be given. (One method would be to use a series of linear approximations for energy similar to that for  $V/t$  in item *ii* of Section 2.4.3.1. However, the procedure now to be given offers some simplicity, more rigor, and more insight into the mechanism of energy loss.) The method chosen requires a more detailed picture of the energy dissipation during the first stages of the surge, and a statement of the necessary energy content at each successively increasing breakdown voltage, now to be examined.

Equation (19) makes it possible to compare the energy lost in resistive elements, the energy still remaining in the inductor, and that stored in the capacitor, as a function of time. Thus, from equation (19),

$$\frac{E_{res}}{E_o} = 1 - \frac{E_{ind}}{E_o} - \frac{E_{cap}}{E_o}. \quad (24)$$

It is readily verified that the first and second  $(\sin)^2$  terms in equation (19) define the inductive and capacitive energies, respectively. Normalizing these expressions, as was done for  $V_c$  in Section 2.3, we then write

$$\frac{E_{ind}}{E_o} = \frac{\exp\left(-\frac{2(\pi - \varphi)}{\tan \theta} \tau\right) \sin^2\{(\pi - \varphi)\tau + \varphi\}}{(1 + G_2/G_w + \beta_w) \sin^2 \theta} \quad (25)$$

$$\frac{E_{cap}}{E_o} = \frac{\exp\left(-\frac{2(\pi - \varphi)}{\tan \theta} \tau\right) \sin^2\{(\pi - \varphi)\tau + \varphi + \theta\}}{(1 + G_2/G_w + \beta_w) \sin^2 \theta}. \quad (26)$$

Equations (24), (25), and (26) are plotted in Fig. 11 for the case that  $G_2/G_w = 0.005$ , and two different values of  $\beta_w$  ( $= 10^{-4}$  and  $10^{-3}$ ). These curves show that the total losses during a discharge series may be divided between resistive and capacitive losses in quite different ratios, depending on the time at which the breakdown occurs, and also on the values of  $\beta_w$  and  $G_2/G_w$ . Thus, arc damage at the contacts, which comes only from the capacitive energy term,  $E_{cap}$ , will be a larger or a lesser fraction of the total initial inductive energy, depending

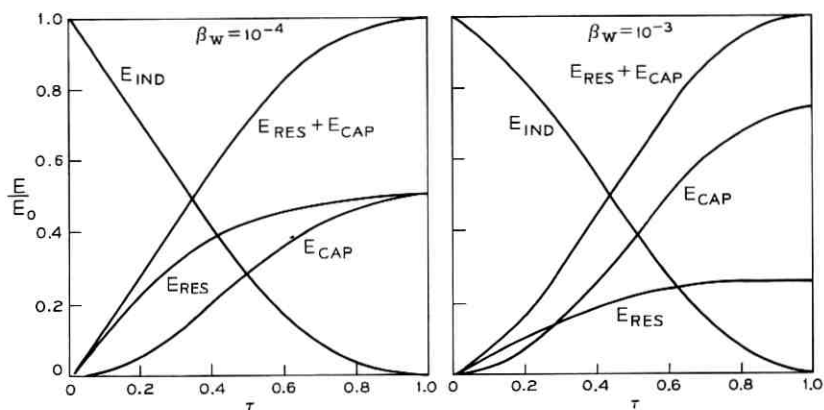


Fig. 11—Dynamic energy relationships during inductive surge. ( $G_2/G_w = 0.005$ ).

on its ratio to the energy which is concurrently dissipated resistively,  $E_{res}$ . By means of the relations given here, these various forms of energy loss can now be calculated, based on the known properties of the control contact, the relay load, and the circuit between them. In illustration, it is evident from Fig. 11 that the resistive losses comprise a much higher fraction of the total initial energy for the lower value of  $\beta_w (10^{-4})$ . Accordingly, contact wear should be less for this case than for the case when  $\beta_w = 10^{-3}$ .

2.4.3.3 *Illustration.* The following example illustrates the steps for making a simple estimate of energy into the arc for a particular case. The needed starting data are as follows:

Given:  $\left\{ \begin{array}{l} \text{Control contact: separation velocity, } u; V_B \text{ vs gap as given} \\ \text{by equation (16).} \\ \text{Circuit and load: } R_w, N_1, C, G_2, V_o, NI_o, \mathcal{P}, (R_n = 0). \end{array} \right.$

Estimation of Energy:

- (i) From above data, find  $G_w = (N_1^2/R_w)$ ,  $G_2/G_w$ , and  $\beta_w$ .
- (ii) Based on  $\beta_w$  and  $G_2/G_w$ , find  $V_p/V_o$  from Fig. 7, which in turn determines  $V_p$ .
- (iii) The values of  $u$ ,  $k$ ,  $I$ , and  $C$  give a ratio which determines each successive new breakdown voltage according to equation (23). This in turn determines the capacitive energy which must be drawn from the inductive source, for each successive breakdown.
- (iv) Reference to the normalized surge curves (Fig. 8) gives the normalized time for successive surge breakdowns, from which the values of  $E_{cap}$ ,  $E_{res}$ ,  $E_{ind}$ , and residual  $E_{ind}$  can be found (Fig. 11).
- (v) This procedure is continued iteratively until the residual inductive energy is less than the required capacitive energy for the next sequential breakdown. At this point, no further breakdowns can occur. The cumulative capacitive energy ratio for all the breakdowns to this point then determines that portion of the initial energy which can produce contact arc damage.

These steps are of course conveniently performed by computer, but are not too complex for approximation using a slide rule. In one trial example: a relay with values of  $G_2/G_w = 0.005$  and  $\beta_w = 10^{-3}$ , and other constants as in the example of Section 2.4.2, a slide-rule calculation indicated a series of 10 breakdowns, which checked with experiment, and gave at the time of the last breakdown:

$$\text{Cumulative } \frac{E_{cap}}{E_o} = 0.34,$$

$$\text{Residual } \frac{E_{\text{ind}}}{E_o} = 0.11,$$

$$\text{Cumulative } \frac{E_{\text{res}}}{E_o} = 0.55.$$

Thus, the indicated energy which is capable of producing contact damage in this case was estimated to be

$$\begin{aligned} E_{\text{cap}} &= 0.34 \times E_o \\ &= 0.34 \times 1.25 \times 10^{-3} \\ &= 0.425 \times 10^{-3} \text{ joule.} \end{aligned}$$

In the specific example in Section 2.4.2, it had been estimated that the *maximum* releasable energy that could be expended in arcing was  $0.74 E_o$ . However, in this extension of that case, where multiple breakdowns occur, with attendant changes in the ratio of resistive to capacitive losses, and with some energy still remaining in the system after the last breakdown, the energy releasable into the arc circuit is found to be only  $0.34 E_o$ , i.e. about 46 percent of the hypothetical maximum. In general, it is expected that the energy releasable to cause arcing erosion will be considerably less than the maximum energy as given by Fig. 10, though roughly proportional to it.

As already discussed in Section 2.4.2, the above procedure ignores a replenishment of energy into the system, during each brief arcing interval, due to the closed-circuit paths for battery current into the capacitor and into the inductor. Correction for these effects, discussed in the next section, will modify the results just obtained; it is expected that an upward revision in  $E_o$ , which recognizes the circuit current as well as the initial inductive energy, will result. The stepwise analysis just given is therefore an approximate treatment. Its special value is the insight it offers into the apportionment of energy available at the onset of each surge between internal dissipative losses, and between capacitive and inductive portions, which are the potential sources for arcing and associated contact erosion.

#### 2.4.4 Modifications in Energy Term, $E_o$ , Due to Replenishment of Inductive Energy During Showering Arcs

When the capacitive energy is released into the arc, at breakdown, oscillations in the arc circuit tend to extinguish it before the full energy is released—either because contact voltage drops below the arc voltage or current falls below the minimum arc sustaining current. The unreleased energy remains in the system; some will be dissipated in the circuit resistance and some will be transferred to inductance and back

to capacitor, and so will contribute to later breakdowns. The total of such available energy has an upper limit already given by  $E'_u$  in equation (22), of the form

$$E'_u = E_o f(t)$$

where  $E_o = \mathcal{O}(NI_o)^2/2$  and  $\mathcal{O}$  represents the differential permeance at  $NI_o$ . But when additional energy is pumped back into the system, from the battery, during each arc, the term  $E_o$  must be replaced by  $(E_o + E_i)$  where  $E_i$  is this incremental battery energy. Information about the term  $E_i$  is therefore essential to a full understanding of energy entering into the arcing and eroding process.

A first indication of the approximate values for  $E_i$  comes from empirical erosion studies such as those discussed in Ref. 9. In this work it was found that  $E_i = kI_o$  where  $I_o$  is the steady state circuit current and  $k$  is a term related to (i) arc voltage (ii) total time of all the arcs, (iii) magnetic constants of the circuit, etc. For a particular group of telephone relays it has the approximate value  $k = 0.1$  (in volt-seconds).

Further treatment of this correction term, which can be a major factor in some cases, is beyond the scope of the present paper. But because of its probable significance in many practical cases, its existence should be recognized. An extensive study of the importance of this battery-contributed energy replenishment, now nearly complete, by Pharney<sup>11</sup>, confirms the importance of a corrective current term as indicated above.

### III. EXPERIMENT

The foregoing analysis has been found to agree well with experiment for a variety of applications problems. Some of these experiments will now be summarized, indicating (i) experimental determinations for some of the important circuit constants, (ii) confirmation of various critical damping relations, and (iii) verification of the peak time and voltage relations. While the data apply specifically to the case of an unprotected load ( $R_n = 0$ ), the methods seem equally applicable to future studies of the more complicated general case.

#### 3.1 Evaluation of Circuit Parameters Which Describe the Relay Structure

The principal variables to be considered are the effective distributed capacitance of the coil, its effective inductance, and the core-loss term.

### 3.1.1 Distributed Capacitance, $C_d$

When one measures the voltage surges which develop upon disconnecting a coil in a circuit with very short wiring and no other apparent capacitance, it is found that the circuit behavior is as though a capacitance of the order of 50 to 200 pF were bridged across the coil. This is called the coil's effective distributed capacitance,  $C_d$ ; usually its value is fairly constant, for a particular basic structure and form of winding, regardless of number of turns, size wire, etc. This value should be known with fair accuracy in order to predict the relay's surge behavior in an actual circuit.

The initial slope of the surge voltage curve may be used to find this value of apparent capacitance for any particular coil structure. Note in Table V that, for the case that  $R_n = 0$ , the value of  $\dot{V}_c$  at time  $t = 0$ , is

$$\left. \frac{dV_c}{dt} \right|_0 = \frac{I_o}{C}.$$

Thus, to estimate the value of  $C$ , one may open the coil circuit, preferably by means of an ideal contact, and note the initial slope of the voltage surge, which can be quite easily measured with an oscilloscope. Then the indicated value of shunt capacitance is

$$C = \left. \frac{I_o}{\dot{V}_c} \right|_{t=0}. \quad (27)$$

This technique can be used to measure any given structure, when all external capacitance is carefully minimized. To avoid possible errors from use of a single measurement, it is sometimes worthwhile to repeat the above measurement after adding several different values of external shunt capacitance. Figure 12 demonstrates this procedure in a typical measurement made on a particular form of relay structure. The seven approximately straight lines on the oscillogram (Fig. 12a) are the initial slopes when the bridged capacitance was successively changed from 0 to 50, 100, 200, 400, 750, and 1000 pF. The upper trace is a measurement of current taken simultaneously, to give the proper value of  $I_o$  for substitution in equation (27). After making appropriate corrections for capacitance of the measuring leads, the apparent capacitance was calculated and plotted against the actual values used in the experiment. This plot is seen in Fig. 12b. The intercept on the apparent-capacitance scale corresponding to  $C_{\text{external}} = 0$  is seen to be 140 pF, which is taken as the effective value of  $C_d$  for this particular test coil.

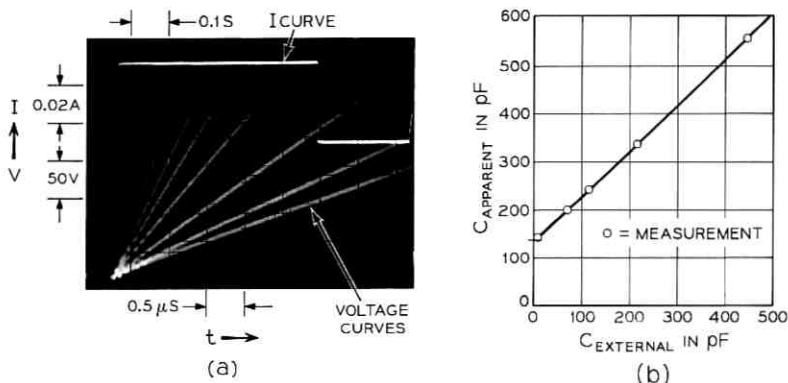


Fig. 12—Experimental determination of distributed capacitance,  $C_d$ . (a) Measurement of  $V_c$  and  $I_o$ . (b) Plot of  $C_{\text{apparent}}$  vs  $C_{\text{external}}$ .

Values for  $C_d$  which were measured for a number of different structural forms of relays are summarized below, together with brief data on relay construction.

#### Measured Values of $C_d$ for Certain Relay Coils

Code Designation	Coil Description					
	$N_1$	$R_w$	Relative Volume	Shape	Form of Structure	$C_d$
286	2,740	288	large	1/2 full	wire spring	120
280	26,550	12,450	large	full	polarized	125
AF33	11,850	950	medium	full	wire spring	140
AJ5	19,400	2,500	medium	full	wire spring	125
AJ7	34,900	9,100	medium	full	wire spring	110
AJ12	5,150	700	medium	short	wire spring	110
AJ57	P 3,235	200	medium	concentric	wire spring	140
	S 3,235	200	—	—	—	—
AJ503	2,110	270	medium	hollow	wire spring	200
AG55	P 6,525	1,000	medium	concentric	wire spring	180
	S 2,260	42	—	—	—	—
MA24	P 2,400	200	small	full	flat spring	115
	S 2,400	200	—	—	—	—
MB9	P 4,200	440	small	full	flat spring	170
	S 3,500	350	—	—	—	—
295A	5,180	525	medium	full	6 large mag. reed contacts	195
311A	3,950	550	small	full	3 small mag. reed contacts	210
327B	7,740	950	small	full	1 small mag. reed contact	140
327D	16,550	2,000	small	full	1 small mag. reed contact	150
Miniature Structure	4,300	1,560	very small	full	armature	80

### 3.1.2 *Effective Inductance*

The present study has postulated a circuit model which comprises lumped parameters, including the inductance. The inductance of an air core coil should rigorously satisfy this assumption. However, for coils using ferromagnetic materials, the flux linkages are a nonlinear function of the coil current. It is therefore necessary to consider the magnetization curve of the load circuit and to determine the effective working region for the particular load structure and circuit condition. This may be clarified by further considering the magnetization characteristic for a typical load structure shown in Fig. 3. The dotted curve shows a representative path that may have been followed by the prior operation of the unit, and point A indicates the starting condition of the inductive load at the time it is disconnected. The heavy curve is the demagnetization characteristic of the structure, which is the region of interest for the present discussion. Now, if the load is connected in a fast circuit (as for example with only a small capacitance) the circuit equations determine that the transient responses will be so fast that the core flux cannot change appreciably (being retarded by the core's eddy currents) in the time available during the early stages of the transient. In this case, the initial slope of the demagnetization curve (i.e., slope at Point A) should define the inductance quite accurately, and one may represent it as  $L = \Phi N^2$  where  $\Phi$  represents the differential permeance or slope of the demagnetization curve at the operated point, i.e.,

$$\Phi_o = \left. \frac{d\Phi}{dNI} \right|_{I_o}$$

However, if the load is in a slow circuit (for example with a large capacitance), there can be time for an appreciable amount of demagnetization. The inductance then grows larger as the transient progresses (i.e.,  $\Phi$  increases as the  $\Phi$ - $NI$  characteristic is traversed downward). The assumed lumped inductance no longer rigorously applies.

In the present study, for the sake of analytical simplicity, this variation will be either ignored, or be treated by assuming a progressively larger value of  $\Phi$  as conditions combine to give slower transients. Based on the lumped-constant approach,  $\Phi$  would be estimated by an averaging procedure over the portion of the demagnetization curve which is traversed during the transient. While it is believed that  $\Phi_{av}$  will largely depend on the ratio of the peak transient time  $t'/RC$  to the core-loss transient time-constant,  $G_2\Phi$ , the subject is not treated

further here except as an averaged value of  $\mathcal{O}$  is determined empirically. An averaged value of  $\mathcal{O}$  is indicated in concept by the slope of dotted lines such as B in Fig. 3. Use of  $\mathcal{O}_0$  usually gives good agreement with the analysis over several decades of variation in  $\beta$ .

$\mathcal{O}_0$  may be determined by magnetization data on the particular structure, or by various interpretations of actual surge measurements. While dynamic magnetization measurements are to be preferred, nevertheless static flux data have proven very useful. Determination using such a magnetic circuit approach is illustrated in Fig. 13. The two curves are actual demagnetization curves (taken statically) for two typical telephone relay structures: a standard wire-spring relay, and a flat-spring miniature relay. For the particular operated conditions shown, the resulting values of  $\mathcal{O}_0$  are seen to be  $1.8 \times 10^{-8}$  Wb per ampere-turn in both cases. While these curves were obtained by measurements with a search coil, they could also have been estimated by well-known techniques of magnetic circuit analysis.

The effective inductance may be inferred based on measurements, in a known circuit, of the transient behavior of such properties as frequency, critical damping, peak voltage, initial slope, etc. A few of these are noted below.

3.1.2.1 *Frequency Method.* When circuit conditions are appropriate for an oscillatory response, as when  $G_2\mathcal{O}/C$  and  $R_1$  are approximately equal (discussed in Section 2.2), the frequency may be related to the circuit parameters based on relations given in Table II. Thus,

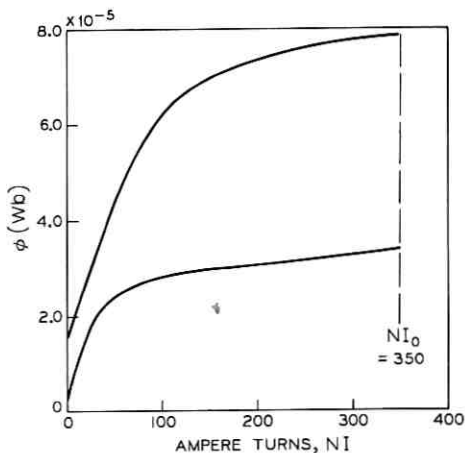


Fig. 13—Demagnetization curves of typical relays. Upper: AF relay. Lower: MA relay.

$$f = \frac{\omega_o}{2\pi} = \frac{1}{2\pi G_1 \mathcal{P} \sqrt{\beta_1(1 + G_2/G_1)}} \\ = \frac{1}{2\pi N_1 \sqrt{C \mathcal{P}(1 + G_2/G_1)}}$$

or

$$\mathcal{P} = \frac{1}{4\pi^2 N_1^2 C f^2 (1 + G_2/G_1)}. \quad (28)$$

Measured values of  $f$ , together with known values of  $N_1$ ,  $G_1$ , and  $G_2$  are substituted in equation (28) to find the effective value of  $\mathcal{P}$ .

3.1.2.2 *Method Based on Initial Slope of  $\dot{V}_c$* . From Table V, note that when  $t = 0$ ,  $\dot{V}_c = 0$ , for a load shunted by an  $RC$  network, when

$$CR_n^2 = L_1(1 + G_2/G_w)^2$$

or

$$\mathcal{P} = \frac{CR_n^2}{N_1^2(1 + G_2/G_w)^2} \quad (29)$$

Ordinarily,  $G_2/G_w$  is less than 0.01 and is neglected. Thus, in a circuit like Fig. 2a, one may vary  $R_n$  and  $C$  in various ways until oscillographic measurement of the contact voltage surge gives a zero initial slope. Because of its convenience, this method has been used extensively in the present study. It also provides some picture of how the inductance varies with the shunt capacitance which is a rough measure of the speed of the transient. The method is illustrated in Fig. 14. Figure 14a shows a family of surges for different values of  $R_n$ , with  $C$  fixed, and Fig. 14b shows a group of curves for which  $C$  and  $R_n$  have been adjusted to give  $\dot{V}_c = 0$  at  $t = 0$ . The above procedure finds the combination of  $R_n$  and  $C$  for zero initial slope, and substitutes these values, together with  $N_1$ , into equation (29). The results for a variety of representative armature-type relay structures are summarized in Fig. 15. It is seen that varying the direct shunt capacitance  $C_s$  has a much larger influence on the variation of  $\mathcal{P}$ , than does varying  $C$  in the  $RC$  network, presumably because the pulse transient is so slowed that it encompasses a larger range of the demagnetization curve. The spread in the data for various structures is thought to be explained by the range of conditions for magnetic structure, stop disc height, operated ampere-turns, etc. Figure 16 gives a summary of the effective permeance for a wide range of sealed magnetic contact relays; the value of  $\mathcal{P}$  is seen to be proportional to the number of contact units, as expected from magnetic

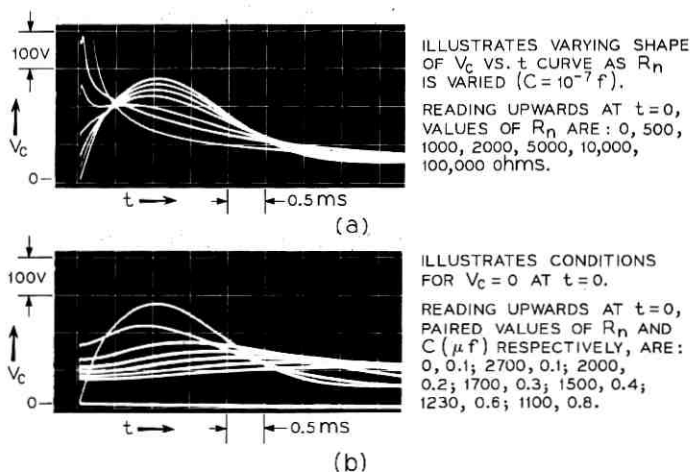


Fig. 14—Illustration of method of measuring effective inductance, based on  $\dot{V}_c = 0$  at  $t = 0$ . [AJ12 Relay;  $N_1 = 5150$ ;  $R_w$  (hot) = 877 ohms.]

circuit analysis. Each contact adds a permeance of about  $0.12 \times 10^{-8}$  Wb/ $NI$  per unit. Departures from complete proportionality are attributed to different amounts of magnetic material in the return paths for various of these structures.

The above values are found to check well with values for  $\mathcal{O}$  which are found as a by-product of other tests, as will be seen below.

One may estimate the initial effective stored inductive energy, which will be released into the system upon disconnection, by means of the relation

$$E_o = \frac{1}{2} \mathcal{O} (1 + G_2/G_w) (NI_o)^2 \quad (30)$$

where  $NI_o$  is the value of ampere-turns at the point of release.

### 3.1.3 Method of Determining Effective Eddy Current Conductance, $G_e$ , of Relay Core

The properties of a coupled secondary winding may be calculated directly from the relation  $G_2 = N_2^2/R_2$  or from standard conductance formulas for copper sleeves.<sup>4</sup> When sleeves are used, their conductance values ordinarily outweigh the core's eddy current conductance to the point that it can be ignored. However, especially for unprotected applications, an estimate of the core's effective eddy current value is needed; and at the present time only experimental procedures seem suitable. Two such methods will now be discussed, one based on readings

of current or surge voltage at  $t = 0$ , and the other based on measurements of critical damping involving the use of a supplementary secondary winding.

3.1.3.1 *Method Based on Value of  $i_1$  or  $V_c$  at  $t = 0$ .* An examination of the circuit variables indicates several equations where the term  $G_2/G_1$  appears. For example, in Table V, the initial values of  $i_1$  or  $V_c$  involve the term

$$K = \frac{1 + G_2/G_w}{1 + G_2/G_1} = \frac{i_1 \text{ at } t = 0^+}{I_o} = \frac{V_c \text{ at } t = 0^+}{I_o R_n}$$

Thus it is conceptually possible to measure  $G_2$  by observing the value of  $K$ , experimentally, as by oscilloscope, for particular values of  $R_n$  and  $R_w$ . Rearrangement of the above expression then gives

$$G_2/G_w = \frac{1}{\frac{K R_n}{1 - K R_w} - 1} \tag{31}$$

However, for small values of  $G_2$ , the value of  $K$  will evidently be close

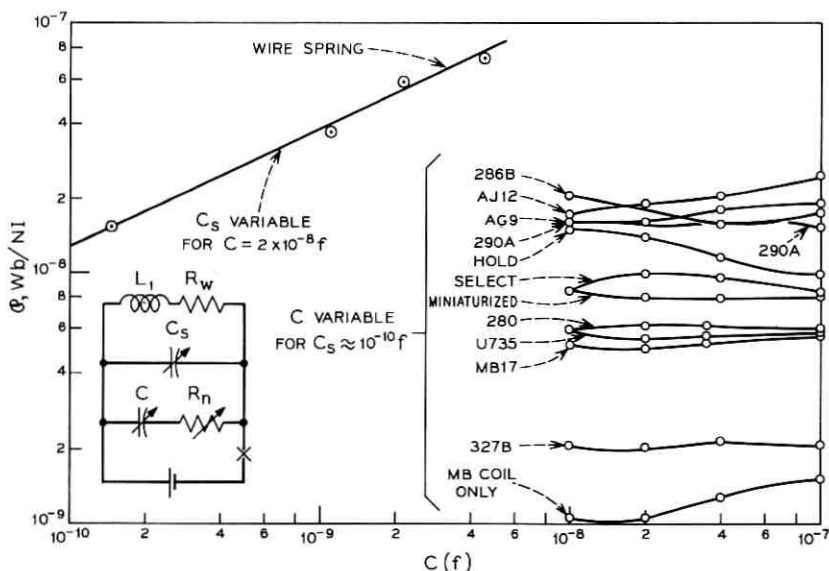


Fig. 15—Values of  $\phi$  determined by  $\dot{V}_c = 0$  at  $t = 0$  method (conventional relays).

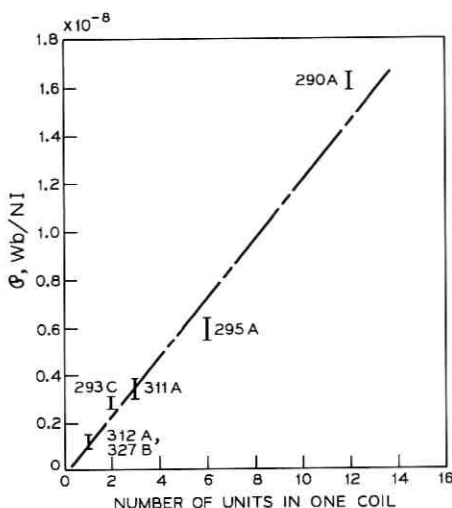


Fig. 16—Values of  $\Phi$  determined by  $\dot{V}_c = 0$  at  $t = 0$  method (magnetic reed relays).

to unity, requiring experimental accuracies that seem quite difficult; therefore this method seems of doubtful value for measuring small values of  $G_2$ , though probably useful when  $G_2/G_w$  exceeds about 0.1 as for copper sleeves, etc.

3.1.3.2 *Two-winding Method.* Instead, the method using two windings as already derived in Section 2.2.1 seems more useful. The procedure is to vary the shunt capacitance across the primary winding (with  $R_s = 0$ ) and observe the value of series resistance across the secondary (or vice versa) for which critical damping is recognized on an oscilloscope. These steps are repeated over a range of values for  $C$  in the region of  $10^{-10}$  to  $10^{-9}$  F. After correcting  $C$  for the distributed capacitance of the primary winding, the resulting values of

$$G_s = \frac{N_2^2}{R_2 + R_2'}$$

are plotted against  $C^{\frac{1}{2}}$ . In accordance with equation (9), the data tend to fall on a straight line whose zero intercept represents  $G_e$ . The effective permeance is then determined from the slope as

$$\Phi = \frac{4N_1^2}{(\text{Slope})^2}. \quad (32)$$

Figure 17 illustrates this procedure for a typical wire spring relay.

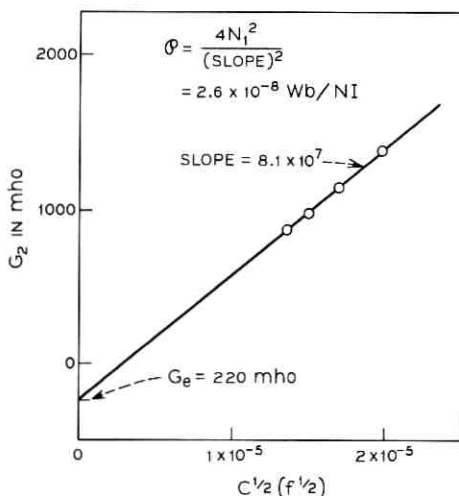


Fig. 17—Experimental determination of eddy current conductance,  $G_e$ .

The data are from the small values for  $C$  and  $G_2$ , in Table VIII, which will be discussed in connection with more extended experiments on critical damping (Section 3.2). In the present experiment, the inferred value of  $G_e$ , which is the negative intercept on the  $G_2$  axis of Fig. 17, is found to be 220 mho, and the slope is  $0.81 \times 10^8$  mho  $f^{-1/2}$ , which from equation (32) gives  $\phi = 2.6 \times 10^{-8}$  Wb/Nl.

### 3.2 Critical Damping Measurements

This section will describe measurements to verify the occurrence of critically damped relationships derived in Section 2.2, and to confirm the analysis for windings which are imperfectly coupled.

#### 3.2.1 Critical-damping Boundaries

Determination of the effective eddy current term  $G_e$  described in the previous section is a by-product of an experiment to verify the analysis of Section 2.2 which derived relations for the boundaries between oscillatory and damped conditions. It was particularly interesting to verify the case for core losses dominant, as this relation had not previously been recognized. The procedure, as previously noted, was to interrupt the primary winding of a two-winding test coil with a mercury contact (to minimize arcing) and to observe the character of the interrupted surge as the values of  $G_2$  and of the capacitance  $C$  across the primary were varied. ( $G_2$  is varied by varying

the value of  $R'_2$  across its terminals). The value of the variable term for which the pulse changes from damped to oscillatory is fairly easy to recognize, using an oscilloscope. A set of such measurements is given in Table VIII together with calculations for plotting the data to check the validity of equation (5). The procedure was to (i) determine the corrected value of  $G_2$  from equation (9), using the steps noted in the previous section and Fig. 17, (ii) tabulate  $G_2/G_w$ , and (iii) estimate the corresponding value of  $\beta_w$ .

A special consideration applies to this calculation of  $\beta_w$ . The analysis in Section II has shown that the effective inductance increases with  $G_2/G_w$  (see Table I) as follows:

$$L' = \mathcal{O}'(1 + G_2/G_w).$$

Here a prime has been added to the permeance term to indicate that  $\mathcal{O}'$  represents the actual state of magnetization of the coil's magnetic circuit. The value of  $\mathcal{O}$  in the formula  $\beta_w = CR_w^2/\mathcal{O}N_1^2$  must be related to this experimental value as follows

$$\mathcal{O} = \mathcal{O}'/(1 + G_2/G_w).$$

Thus, for the present measurements, a correction has been applied so that  $\beta_w$  can be evaluated using the experimental value,  $\mathcal{O}'$ . The corrected value is

$$\beta_w = (CR_w^2/\mathcal{O}'N_1^2)(1 + G_2/G_w). \quad (33)$$

The values of  $\beta_w$  as estimated in this way, and as read from the curve, of Fig. 4, are listed in adjacent columns of Table VIII, and the experimental points are plotted as circles in Fig. 4. Agreement between experiment and analysis is seen to be good, especially considering that a constant value of  $\mathcal{O}'$  has been assumed to apply over the whole range of the experiment.

The family of curves in Fig. 5 provides a convenient method for analyzing the data for a particular structure. In this case one plots the value of  $G_2/G_w$  vs the corrected shunt capacitance at critical damping. Then, based on the known values for  $N_1$  and  $R_w$  for the given structure, one infers the effective value for  $\mathcal{O}'$  from the numerical value for the appropriate curve, using the correction technique of the preceding paragraph. Data for several different structures with secondary windings are plotted, and also for several relays with copper sleeves. The copper sleeve cases are identified by a dot (measured value) surrounded by a rectangle representing the possible spread in the various parameters for a sample relay drawn from stock. The

copper sleeve relays represent the four standard sizes used in slow release relays for telephone switching. Agreement is again seen to be good.

### 3.2.2 *Oscillations in Imperfectly Coupled Circuits*

Measurements using secondary windings give somewhat different results depending on the form of winding used. When the primary and secondary are perfectly coupled, as with parallel-wound coils, the boundary between oscillatory and damped regions accords with the analysis given above. However, when primary and secondary are not perfectly coupled, as in the case of concentric windings, or of copper sleeves, a new and at first unexpected result is noted. In this case, there is a new form of oscillation which becomes noticeable as one operates near or beyond the region of critical damping—this is the discharge of the uncoupled portion of the inductance which is not attenuated by the core-loss term. The analytical basis was discussed in Section 2.2.2 and some data on numerical values will now be given.

The presence of shorted secondary windings which are not perfectly coupled to the primary winding was seen to lead to two superimposed transient patterns: (i) that due to the coupled portion of the winding which experiences critical damping below values of  $\beta$  determined by the coil losses, and (ii) that due to the uncoupled portion of the winding. For this group of windings, operating in the overdamped region, one observes oscillations in the circuit which are produced by the parallel inductive path of the uncoupled part of the main winding. Such oscillations are particularly noticeable with relays using copper sleeves. In fact the experimental observation of such oscillations is often helpful in the experimental determination of the critically-damped condition for the coupled portion of the winding. The following results are given as guides for dealing with these effects, which often need to be considered in the course of relay application studies. They are taken from extensive measurements on copper sleeve relays.

Among the general results were (i) the consistent observation that, when the coupled portion of the main winding was operating in the core-loss overdamped region, the amplitude and frequency of the oscillations for the uncoupled portion of the coil were independent of the value of  $G_2$ , and (ii) the frequency was proportional to  $C^{-1}$ , as predicted by equation (11). In addition, the critical damping boundary for four sizes of sleeve (covering a range of  $G_2$  between about 40,000 and 200,000 mho) was measured. The data were then analyzed

to give the corrected value of effective core permeance for different values of  $G_2/G_1$ , in the same manner discussed in Section 3.2.1. This value of permeance  $\mathcal{O}'$  is determined by using the value of  $\beta_w$  for a given value of  $G_2/G_w$  from the curves, Fig. 4, and substituting in equation (33), as is shown in the left-hand side of Table X. The spread in the indicated value of  $\mathcal{O}'$  seems reasonable for a group of randomly selected stock relays.

The right-hand portion of the table shows measured values of frequency when the primary was shunted by a capacitor,  $C = 10^{-8}$  F. Now, calling the effective value for this uncoupled inductance  $L'' = \mathcal{O}''N_1^2$ , all the test samples are seen to show values for  $\mathcal{O}''$  of about  $0.6 \times 10^{-8}$  Wb/NI. This value can be used to estimate  $\beta$ ,  $V_p$ ,  $f$ , etc., for the uncoupled portion of the winding, for which  $G_2 = 0$ .

These data indicate that the uncoupled portion of the main winding can contain an appreciable energy which is externally releasable, even though the core-loss term due to the copper sleeve is very large. For example, for the relays studied in Table X, the initial releasable energy is about  $E = 0.6 \times 10^{-8}(NI_o)^2$  joule.

The above concepts explain the general transient behavior of copper sleeve relays. The numerical values which are given for  $\mathcal{O}$  only apply to the particular structural group of relays studied here (the slow-releasing class of the wire spring family).

### 3.3 Time-to-Peak, $t'$ , and Peak Voltage, $V_p$

Peak voltage measurements, i.e., measurement of the time-to-peak and the value of the peak voltage, offer further opportunities to check the analysis. The following discussion examines the measurements for both peak time and peak voltage on a single experimental unit, and also reconsiders a large series of peak voltage measurements which were made about 1953 based on then-current empirical practices.

#### 3.3.1 Measurements of $t'$ and $V_p$ on a Sample Wire Spring Relay

The values of  $t'$  and  $V_p$  were measured on a test relay over a range of shunt capacitances,  $C$ , representing a large spread of the variable  $\beta_w$ . Based on the known constants of the structure, the formula for  $t'/R_wC$ , equation (12) as plotted on Fig. 7, and discussed in Section 2.3, was used to infer the associated value of  $\beta_w$ . This value of  $\beta_w$  was then used to predict the expected value of  $V_p/V_o$ , from Fig. 7. These results are summarized in Table XI, together with the measured values of  $V_p/V_o$ . The measured and predicted values for  $V_p/V_o$  are seen to agree very closely, and are taken to support the analysis.

TABLE X—COPPER SLEEVE RELAYS—MEASUREMENTS ON CRITICAL DAMPING AND UNCOUPLED INDUCTANCE

Code	Properties of Test Relay					Critical Damping Data		Uncoupled Inductance Data		
	Primary Coil			Secondary		$\beta_w$ (from Fig. 4)	$C_{\text{meas}}$ for Crit. Damp- ing (F)	$\phi'$ [From Eq. (32)] (Wb/NI)	$f_{\text{meas}}$ for $C=10^{-8}$ F (Hz)	$\phi''$ [From Eq. (11)] (Wb/NI)
	$N_1$	$R_w$ (ohms)	$G_w$ (mho)	$[R_w/N_1]^2$	Sleeve*					
AG 10	10,050	996	100,000	0.00985	0.046" Al	0.036	$8 \times 10^{-8}$	$3.1 \times 10^{-8}$	2040	$0.61 \times 10^{-8}$
AG 13	16,050	2450	104,800	0.0231	0.046" Cu	0.082	$4.5 \times 10^{-8}$	$2.1 \times 10^{-8}$	1330	$0.56 \times 10^{-8}$
AG 15	7,800	702	86,700	0.0081	0.091" Cu	0.33	$4.8 \times 10^{-7}$	$3.0 \times 10^{-8}$	2605	$0.62 \times 10^{-8}$
AG 11	8,250	1180	57,700	0.0204	0.147" Cu	1.15	$4.5 \times 10^{-7}$	$3.5 \times 10^{-8}$	2470	$0.61 \times 10^{-8}$

\* Wall Thickness, Material.

The final column in Table XI indicates the effective value of  $\mathcal{P}$  for this same series of measurements. It is seen to have a fairly constant value for values of  $\beta_w$  greater than about  $10^{-7}$ , and to gradually increase above this point. In line with earlier discussions, this increasing trend accords with the view that slower surges involve larger changes in the demagnetization curve and correspondingly larger values of  $\mathcal{P}$ . In keeping with this picture, it appears that the values of  $\mathcal{P}$  as determined at the initial stages of the pulse (from  $\dot{V}_c = 0$  at  $t = 0$  in Section 3.1.2) should be increased by a factor of 2-3 when working with events at the peak of the pulse, where the flux curve has had more time to change.

### 3.3.2 Use of 1952 Data to Further Confirm Peak Voltage Relation

During a two-year period starting in about 1952, an extensive study was originated by M. M. Atalla, and later extended by many others, into the values for peak voltages when contacts open relay loads. The data were found to fit a formula relating  $V_p/V_o$  to a variable similar to the  $\beta_w$  term used in the present study, modified by an exponential term that was determined empirically. These very extensive data are available for comparison with the present analysis; their sources are unpublished Bell Laboratories memoranda. This earlier study used the following notation for the term designated  $\beta_w$  in the present work:

$$\beta_w = \mathcal{R}_o C \left( \frac{R}{N} \right)^2$$

where  $\mathcal{R}_o$  represented the reluctance of the relay's magnetic circuit, and is the reciprocal of  $\mathcal{P}$ , the permeance as used in this report. This reluctance value, technically described as the "closed-gap reluctance," is a design constant which is tabulated for all telephone type relays. In the light of the present analysis, this value of reluctance, which represents the steepest slope of the *magnetization* curve, should be replaced by the uppermost slope of the *demagnetization* curve, representing a much higher reluctance (or lower permeance). Thus, all the earlier data can be used as a check on the present analysis if a relationship between these two figures is known. Data are not available for all the specific cases involved; however, it was determined from a review of magnetic data for many of these structures that a correction from the  $\mathcal{R}_o$  values mentioned above to values for  $\mathcal{R}$  which are related to the demagnetization curve could be approximated by increasing  $\mathcal{R}_o$  by the factor 7.5. When this is done, when units are changed from

TABLE XI—MEASUREMENTS OF  $t'$  AND  $V_p$ 

$C$ (F)	$C + C_d$ (F)	Meas. $t'$ (s)	$R_w C$	$t'/R_w C$	$\beta_w$ (from Fig. 6)	$V_p/V_o$ (from Fig. 7)	Meas. $V_p/V_o$	$C \left[ \frac{R}{N} \right]^2$	Inferred $\Phi$ ( $W_b/NI$ )
$0.825 \times 10^{-9}$	$0.965 \times 10^{-9}$	$34 \times 10^{-6}$	$295 \times 10^{-9}$	115	$1.5 \times 10^{-4}$	61	62	$8.66 \times 10^{-12}$	$5.77 \times 10^{-8}$
1.0	1.14	37	350	105	1.7	58	58	10.2	6.0
4.0	4.14	77.5	$1.27 \times 10^{-6}$	61	6.0	36	37	37.0	6.16
$0.01 \times 10^{-6}$	$0.01 \times 10^{-6}$	128	306	41.9	$1.3 \times 10^{-3}$	26	25	89.4	6.87
0.05	0.05	338	15.3	22.1	5.0	14	13	447	8.95
0.1	0.1	510	30.6	16.3	$1 \times 10^{-2}$	10	10	894	8.94
0.5	0.5	1500	153	9.8	2.6	6.2	5.5	4470	17.2

Initial Data:  $N_1 = 3235$   $R_w = 306$  (hot)  $G_w = 34,200$  mho  $(R/N)^2 = 0.00894$

$G_2 = 200$  mho (est.)  $G_2/G_w = 0.0066$

Measured Value of  $C_d = 140 \times 10^{-12}$ F

egs to SI, and the new values of  $\beta_w$  are calculated, and  $\mathcal{R}$  is converted to  $\mathcal{P}$  (its reciprocal), a large number of data points for different structures becomes available for use here. The revised data points, taken from the unpublished memoranda, are plotted for various structures on Fig. 7. They are seen to show very good agreement between analysis and experiment for a wide range of telephone relays. The agreement could be further improved at the longer transient times (larger values of  $C$  or  $\beta_w$ ) if an added correction for increasing differential permeance were made, along the lines indicated in Table XI (column showing "Inferred  $\mathcal{P}$ .")

Although the core-loss terms for these particular structures have not been measured by the methods outlined in this paper, the data points as plotted for the various structures in Fig. 7 are consistent with the expectation that large cores, or low-resistivity cores, should have larger values of  $G_2/G_w$  than small or high resistivity cores. These results therefore offer additional confirmation for the analysis of Section II.

#### SECTION IV. DISCUSSION

Based on the close agreement between analysis and experiment, the formulas given here appear well suited for use in analyzing the various transient effects associated with a contact opening an inductive load. Because of satisfactory prediction of pulse times, peak voltages, frequencies, and regions of damping or oscillation, it also seems reasonable to extend the use of these relations to the approximate estimation of energy dissipated in the contact arc, according to the analysis of Section 2.4.

Returning to the list of various problems discussed in Section I, the present study should therefore find application in the following areas.

- (i) Prediction of surges from relay windings as a function of time, including breakdown values, times, oscillations, etc. The results apply equally to loads controlled by transistors, vacuum tubes, or relay contacts. While the examples are mainly given for the "unprotected" load, the basic formulas are available for the study of other cases.
- (ii) Extension of the above work to predict the energy which will be internally dissipated or be made available via the capacitor to do damage in arcing, as in contact erosion. Extension of the present work is still needed to more fully evaluate the energy

replenished into the system from the battery during arcing. It is expected that continuing work<sup>11</sup> will improve understanding of the present empirical technique which relates contact erosion to the sum of an energy term and a current term.

- (iii) Reasonable explanations now are available for earlier uncertain points.
- (a) Relays with higher stop discs (i.e., larger operated air gaps) will ordinarily be less close to saturation. Therefore, their differential permeance will be larger than otherwise, which predicts a larger releasable stored energy. Although this configuration does not represent the condition for maximum total stored energy, (which must be at the smallest air gap), it does represent the condition for large *initial release* of magnetic energy, i.e., the value of  $\mathcal{O}$  is larger.
  - (b) The oscillations which occur with copper sleeve relays are found to result from the uncoupled portion of the main winding. Relations are given for predicting their values.
- (iv) Methods for predicting various behavior patterns are demonstrated.
- (a) An example of a "B" type transient energy calculation is given.
  - (b) An extension of (a) above can be used to predict the final peak surge, following the last breakdown of a "B" type transient. Particularly with coils having a large number of turns, and a slowly rising surge, the number of breakdowns in a "B" type transient is relatively few. In such a case, a considerable residual inductive energy may remain following the last arc breakdown. The associated final surge tends toward higher than ordinary peak surges which need to be evaluated in order to insure adequate protection against breakdowns in the associated wiring.
  - (c) An analytical basis is available for determining the proper test conditions for coils being production-tested to withstand their own self-induced surge voltages.
  - (d) Many past evaluations of contact wear, and comparisons of various alloys and environments, are hard to compare with metals being studied today because the test conditions (magnetic structure of the load, circuit voltage, etc.) were so different from today's conditions. The relationships in this report are expected to permit the re-evaluation of some of this older data in a form that will permit comparisons on

a more universal basis. In one such test (1923), more than 250 metals and alloys in various gaseous environments were tested and compared. The review of this information in the context of today's applications problems should help to guide current design activities, as for example, those on sealed contacts.

- (v) Future design for relay miniaturization can be better evaluated based on fuller understanding of the influence of the inductive load on the wear (and hence the necessary volume, travel allowance, and required work) of the contacts which control it. For example, the basic element determining contact wear is the effective *releasable* stored magnetic energy. The principal factor in this quantity is the initially stored effective energy term  $\frac{1}{2}\mathcal{P}(NI_o)^2$ , and often an additional term proportional to current  $I_o$  due to energy replenishment into the system by the battery, during arcing. Thus, contact erosion is related to the square of the operated ampere-turns and the differential permeance of the magnetic circuit's demagnetization curve, together with a term of approximate value  $0.1 I_o$ . The most favorable condition is therefore that where the desired work output and operating time for the relay lead to a low value for  $NI_o$  (and also of current). The low value of  $NI_o$  is generally associated with a high-permeance magnetic circuit at the unoperated or critical gap condition. A high permeance at the closed-gap releasing current, however, is not compatible with low releasable energy. The present study suggests that contact life can be further improved if this sensitive unoperated structure were designed so that it is highly saturated (i.e., low  $\mathcal{P}$ ) once it is in the operated position.

This releasable energy may be further reduced through the conscious use of a secondary winding whose value of  $G_2$  is large enough to decrease the energy available for arcing by several fold while not being large enough to seriously influence release time. Typically, this means that one might profitably use a small closed secondary winding or copper sleeve having a value of  $G_2$  equal to about 1000 to 5000 mho. If desired, the effect on operate time could be minimized by completing the secondary winding circuit through a diode which is poled to make the secondary effective only on release.

If, in this way, the load magnet can be made to cause less contact wear, the smaller contact wear allowance can result in a lowered mechanical work requirement. This in turn leads to a

smaller magnet structure, and so on. The concept should thus prove useful in design steps aiming to optimize a miniature relay structure, including the sealed magnetic reed types with their thin electroplated contact regions.

## V. SUMMARY

This study has presented a group of analytical relations which describe the electrical transients when a contact opens an inductive load. In the past, relations based on a simple *LRC* analysis were found to be quite inaccurate. The present method expands the earlier approach to account for core losses, and is found to reduce to *LRC*-type relationships provided the lumped-constant terms have effective values as defined in Section II, and provided the value used for inductance recognizes the actual differential flux-ampere-turn characteristic for the particular load's magnetic circuit.

The analysis then leads to a group of useful relations for predicting surge times, peak voltages, or energies either consumed internally or available for external damage as in contact arcing. The analysis also predicts the conditions under which the surges are either oscillatory or damped. Experiments have confirmed these results, including the presence of two critically damped regions whenever the load possesses a finite secondary loss term. They have also explained the presence of an "anomalous" oscillatory condition for two-winding structures resulting from the uncoupled portion of the primary inductance.

Illustrations of how these results may be applied in circuit and relay design are given, as for example: the prediction of peak voltages, or of the chain of breakdowns in a "B" type transient; the estimation of energy available to produce contact erosion; and the determination of the oscillation frequencies in a given circuit. Experimental techniques were also described for determining the effective values of the various circuit constants, and typical values for a wide range of structures are given. The implications in relay design, as for miniaturization, are also discussed.

## APPENDIX A

### *Derivation of Basic Circuit Equations for Current*

#### *The Disconnection of a Relay Winding-General Case (Assuming Ideal Break Contact, an RC Shunt Network, and a Secondary Winding)*

Upon disconnection, transient currents will flow in the two meshes as shown in Fig. 2a. Using the notation of that figure, and of Table I,

the equations are

$$\left. \begin{aligned} N_1 \frac{d\Phi}{dt} + i_1 R_1 + \frac{\int i_1 dt}{C} &= 0 \\ N_2 \frac{d\Phi}{dt} + i_2 R_2 &= 0 \end{aligned} \right\} \quad (34)$$

These are interrelated through the magnetic circuit, for which we assume  $\Phi = \Phi_1 + \Phi_2$ , where  $\Phi_1$  and  $\Phi_2$  are proportional to the primary and secondary magnetizing forces,  $N_1 i_1$  and  $N_2 i_2$ , respectively. Now designating  $\mathcal{P}$  as the incremental permeance of the relay's magnetic circuit, i.e.,  $\mathcal{P} = d\phi/dNi$ , at the point in question, we write

$$\frac{d\Phi}{dt} = \mathcal{P} \left( \frac{dN_1 i_1}{dt} + \frac{dN_2 i_2}{dt} \right). \quad (35)$$

Making this substitution, the loop equations become

$$\left. \begin{aligned} N_1 \mathcal{P} \left( \frac{dN_1 i_1}{dt} + \frac{dN_2 i_2}{dt} \right) + i_1 R_1 + \frac{\int i_1 dt}{C} &= 0 \\ N_2 \mathcal{P} \left( \frac{dN_1 i_1}{dt} + \frac{dN_2 i_2}{dt} \right) + i_2 R_2 &= 0 \end{aligned} \right\} \quad (36)$$

We now adopt LaPlace Transform notation, and combine with initial conditions, which are that at  $t = 0$ , the charge on  $C$  is  $(-V_o)$ , and the core flux is  $\Phi_o = \mathcal{P} N_1 I_o$ . Equation (36) may then be rewritten:

$$\left. \begin{aligned} N_1 \mathcal{P} s (N_1 i_1 + N_2 i_2) + i_1 R_1 + \frac{i_1}{sC} &= N_1 \mathcal{P} N_1 I_o + \frac{V_o}{s} \\ N_2 \mathcal{P} s (N_1 i_1 + N_2 i_2) + i_2 R_2 &= N_2 \mathcal{P} N_1 I_o \end{aligned} \right\} \quad (37)$$

Using the second of these equations to find  $i_2$ , substituting into the first, and collecting terms:

$$i_1 = I_o \frac{N_1^2 \mathcal{P} (1 + G_2/G_w) s + R_w}{N_1^2 \mathcal{P} (1 + G_2/G_1) s^2 + \left( R_1 + \frac{G_2 \mathcal{P}}{C} \right) s + \frac{1}{C}} \quad (38)$$

This is recognized as the expression for a simple  $R, L, C$  circuit, as shown in Fig. 2b, for which the inductance and resistance have *effective* values:

$$L' = L_1(1 + G_2/G_1) = N_1^2 \Phi(1 + G_2/G_1)$$

$$R' = R_1 + G_2 \Phi/C.$$

Using these values, equation (38) becomes

$$i_1 = KI_o \frac{(s + a)}{(s + b)^2 + \omega^2} \quad (39)$$

where values of  $a$ ,  $b$ , and  $\omega$  are as given in Table II. Equation (39) is immediately solved by reference to tables of LaPlace Transforms. There are three cases:

- I. Oscillatory:  $\omega_o^2 > b^2$
- II. Critically Damped:  $\omega_o^2 = b^2$
- III. Overdamped:  $\omega_o^2 < b^2$

The solutions are found to be:

Case I.

$$i_1 = \frac{KI_o e^{-bt} \sin(\omega t + \varphi)}{\sin \varphi}$$

$$\text{where } \varphi = \tan^{-1} \frac{\omega}{a - b}$$

Case II.

$$i_1 = KI_o e^{-bt} [1 + (a - b)t]$$

Case III.

$$i_1 = \frac{KI_o e^{-bt} \sinh(\omega t + \varphi)}{\sinh \varphi}$$

$$\text{where } \varphi = \tanh^{-1} \frac{\omega}{a - b}$$

(40)

(See Table III for more detailed summary of values for  $\varphi$  and related terms.)

#### APPENDIX B

*Evaluation of Maximum or Minimum Values of  $q_1$ ,  $i_1$ , and  $V_c$ .*

The procedure for these determinations is to differentiate the corresponding expression for  $q_1$ ,  $i_1$  or  $V_c$  given in Table IV, with respect

to  $t$ , and set the result equal to zero. This result, which defines the times at which the slope of the transient = 0, then determines either a maximum or a minimum condition, as will be shown. The first maximum or minimum will be designated  $t'$ , i.e., "time-to-peak". The value for  $t'$  is then substituted into the original expression to give the "peak" value for  $q_1$ ,  $i_1$ , or  $V_c$  (using the subscript  $p$  to designate it). While the analysis shows the steps taken for the general case of a shunt  $RC$  network, the resulting equations are often fairly cumbersome. Thus, after indicating the direction of these general results, they are fully expressed for the case of shunt capacitance alone ( $R_n = 0$ ) which is the major subject of the present study. The steps are briefly outlined below:

*Case I—Oscillatory* (i.e.,  $\omega_o^2 > b^2$ )

#### *Charge*

From Table IV, the time derivative of charge is

$$\begin{aligned} \frac{dq_1}{dt} &= -\frac{Ki_o}{\omega_o \sin \varphi} \frac{d}{dt} [e^{-bt} \sin(\omega t + \theta + \varphi)] \\ &= -\frac{Ki_o}{\omega_o \sin \varphi} e^{-bt} [\omega \cos(\omega t + \theta + \varphi) - b \sin(\omega t + \theta + \varphi)] = 0. \end{aligned}$$

The derivative thus has a zero value when  $t' = \infty$  or, based on phase angle relations indicated in Table III, when

$$\tan(\omega t' + \theta + \varphi) = \tan \theta,$$

which is only satisfied at values of  $t'$ :

$$\begin{aligned} t'_q &= \frac{\pi - \varphi}{\omega}, \quad \frac{2\pi - \varphi}{\omega}, \quad \text{etc.} \\ &(\text{max}) \quad (\text{min}) \quad \text{etc.} \end{aligned} \quad (41)$$

Substituting equation (41) into the original expression for  $q_1$ :

$$q_{1p} = +\frac{Ki_o}{\omega_o \sin \varphi} \sin \theta \exp\left(-\frac{\pi - \varphi}{\tan \theta}\right). \quad (42)$$

For the case when  $R_n = 0$ , from the relations in Tables II and III, this reduces to

$$q_{1p} = CV_o \beta_w^{-1} \exp\left(-\frac{\pi - \varphi}{\tan \theta}\right). \quad (43)$$

#### *Current*

From Table IV, the time derivative of current is

$$\begin{aligned} \frac{di_1}{dt} &= \frac{Ki_o}{\sin \varphi} \frac{d}{dt} [e^{-bt} \sin (\omega t + \varphi)] \\ &= \frac{Ki_o}{\sin \varphi} e^{-bt} [\omega \cos (\omega t + \varphi) - b \sin (\omega t + \varphi)]. \end{aligned}$$

The derivative thus has a zero value when  $t' = \infty$  or, based on phase angle relations of Table III, when

$$\tan (\omega t' + \varphi) = \tan \theta,$$

which is only satisfied for values of  $t'$ :

$$\begin{aligned} t'_i &= \frac{\pi + \theta - \varphi}{\omega}, \quad \frac{2\pi + \theta - \varphi}{\omega}, \quad \text{etc.} \\ &\quad \text{min}^* \quad , \quad \text{max}^* \quad , \quad \text{etc.} \end{aligned} \quad (44)$$

Substituting equation (44) in the original expression for  $i_1$ :

$$i_{1,p} = \frac{Ki_o \sin \theta}{\sin \varphi} \exp \left( -\frac{(\pi + \theta - \varphi)}{\tan \theta} \right). \quad (45)$$

For the case when  $R_n = 0$ , from the relations in Fig. 4,

$$i_{1,p} = \frac{i_o}{\sqrt{1 + G_2/G_w}} \exp \left( -\frac{(\pi + \theta - \varphi)}{\tan \theta} \right). \quad (46)$$

### Contact Voltage

From Table IV, the time derivative of contact voltage is

$$\begin{aligned} \frac{dV_c}{dt} &= \frac{Ki_o}{\sin \varphi} \frac{d}{dt} \left[ e^{-bt} \left\{ R_p \sin (\omega t + \varphi) - \frac{1}{\omega_o C} \sin (\omega t + \varphi - \theta) \right\} \right] \\ &= \frac{Ki_o}{\sin \varphi} e^{-bt} \left[ \frac{1}{C} \sin (\omega t + \varphi) - \omega_o R_p \sin (\omega t + \varphi - \theta) \right]. \end{aligned}$$

The derivative has a zero value when  $t' = \infty$  or, based on phase angle relations of Table III, when

$$\tan (\omega t' + \varphi) = \frac{\tan \theta}{1 - \frac{1}{C\omega_o R_p \cos \theta}},$$

which is satisfied for values of  $t'$ :

$$t'_v = \frac{1}{\omega} \left[ \tan^{-1} \left\{ \frac{\tan \theta}{1 - \frac{1}{C\omega_o R_p \cos \theta}} \right\} - \varphi \right]. \quad (47)$$

\* (usually, however, there will be an initial maximum preceding min\*, at  $(\pi/2 - \varphi)$ , when  $\varphi < \pi/2$ ).

The general expression for peak voltage is then given by substituting equation (47) into the original voltage expression. The resulting rather complicated formula may be used to estimate peak voltages for the general case which includes an  $RC$  protection network, a procedure which is beyond the scope of the present report. For the case when  $R_n = 0$ , substituting values of the various terms from Tables II, III, and IV:

$$t' = \frac{\pi - \varphi}{\omega}, \quad \frac{2\pi - \varphi}{\omega}, \quad \text{etc.}$$

$$\max, \quad \min, \quad \text{etc.}$$

$$V_{c,p} = V_o \left[ 1 + \beta_w^{-1} \exp \left( -\frac{\pi - \varphi}{\tan \theta} \right) \right]. \quad (48)$$

*Case II—Critically Damped* (i.e.,  $\omega_0^2 = b^2$ )

For the critically damped case, as for Case I, the procedure is to find the time,  $t'$ , at which zero slope of the time derivative of each variable occurs, and the corresponding "peak" value, for the general case which includes the  $RC$  network. Following this, the results are given for the specific case for  $R_n = 0$ , with individual consideration of the two critically-damped conditions: core losses dominant, and coil losses dominant.

#### Charge

From Table IV, the time derivative of charge is

$$\frac{dq_1}{dt} = -\frac{Ki_o}{b^2} \frac{d}{dt} [e^{-bt} \{a + b(a - b)t\}]$$

$$= -Ki_o e^{-bt} [(b - a)t - 1].$$

The derivative has a zero value when  $t' = \infty$  or when

$$t'_q = \frac{1}{b - a}. \quad (49)$$

Substituting equation (49) into the original expression for  $q$ :

$$q_{1,p} = \frac{CV_o}{2} \left[ \frac{KR'}{R_w} - 2 \right] \exp \left( -\frac{b}{b - a} \right) \quad (50)$$

or

$$= 0.$$

*Current*

From Table IV, the time derivative of current is

$$\begin{aligned}\frac{di_1}{dt} &= Ki_o \frac{d}{dt} [e^{-bt} \{1 + (a - b)t\}] \\ &= -Ki_o e^{-bt} [b(b - a) - 2b + a].\end{aligned}$$

The derivative has a zero value when  $t'_i = \infty$ , or when

$$t'_i = \frac{2b - a}{d(d - a)}. \quad (51)$$

Substituting equation (51) into the original expression for  $i_1$ :

$$i_{1,p} = -Ki_o \frac{(b - a)}{b} \exp\left(-\frac{2b - a}{b - a}t\right) \quad (52)$$

or

$$= 0.$$

*Contact Voltage*

From Table IV, the time derivative of the contact voltage is

$$\begin{aligned}\frac{dV_o}{dt} &= -V_o \frac{d}{dt} \left[ e^{-bt} \left\{ 1 - \frac{KR_n}{R_w} + (a - b) \left( \frac{b}{a} - \frac{KR_n}{R_w} \right) t \right\} \right] \\ &= \frac{Ki_o}{C} e^{-bt} [1 - CR_n(2b - a) + (a - b)(1 - bCR_n)t].\end{aligned}$$

The derivative has a zero value when  $t'_v = \infty$ , or when

$$t'_v = \frac{1 - CR_n(2b - a)}{(b - a)(1 - bCR_n)}. \quad (53)$$

and its value may be found by substituting equation (53) into the original voltage expression.

*Cases Where  $R_n = 0$* 

A more detailed treatment for the case where  $R_n = 0$  will now be given, to indicate behavior under the two conditions for critical damping:

(i) Core losses dominant: i.e.,

$$\frac{G_2 \Phi}{C} > R_w, \quad \text{or} \quad \frac{G_2}{G_1} < \beta_w, \quad \text{or} \quad b > a \quad (\beta_w > 0)$$

(ii) Coil losses dominant: i.e.,

$$R_w > \frac{G_2 \Phi}{C}, \quad \text{or} \quad \beta_w < \frac{G_2}{G_1}, \quad \text{or} \quad a > b \quad (\beta_w \geq 4)$$

Then, the values of minimum or maximum circuit variable, and of corresponding times, are summarized below:

(i) *Core Losses Dominant*

*Charge*

$$t'_q = \frac{1}{b-a}$$

$$= G_w \mathcal{P} \beta_w^{\frac{1}{2}} (1 + \beta_w^{\frac{1}{2}})^2$$

$$q_{1,p} = CV_a \beta_w^{-\frac{1}{2}} e^{-(1+\beta_w^{\frac{1}{2}})}$$

*Current*

$$t'_i = \frac{2b-a}{b(b-a)}$$

$$= G_w \mathcal{P} \beta_w^{\frac{1}{2}} (\beta_w^{\frac{1}{2}} + 2)(\beta_w^{\frac{1}{2}} + 1)$$

$$i_{1,p} = -\frac{i_o}{(1 + \beta_w^{\frac{1}{2}})} e^{-(2+\beta_w^{\frac{1}{2}})}$$

*Contact Voltage*

$$t'_v = \frac{1}{b-a}$$

$$= G_w \mathcal{P} \beta_w^{\frac{1}{2}} (1 + \beta_w^{\frac{1}{2}})^2$$

$$V_{c,p} = V_o [1 + \beta_w^{-\frac{1}{2}} e^{-(1+\beta_w^{\frac{1}{2}})}]$$

(ii) *Coil Losses Dominant*

$$t'_q = -\frac{1}{a-b}$$

As  $a > b$ , a negative, i.e., impossible, value of  $t'$  is indicated. Thus,  $t'_q = \infty$  applies, and there is no peak value of  $q$ , which gradually decays to 0.

$$t'_i = -\frac{2b-a}{b(a-b)}$$

As just above, this expression is always negative, and  $t'_i = \infty$  applies, indicating no minimum, but a gradual decay to 0.

$$t'_v = -\frac{1}{a-b}$$

As above, this expression is always negative, and  $t'_v = \infty$  applies, indicating no maximum, but a gradual rise in contact voltage from 0 to  $V_o$ .

*Case III—Overdamped (i.e.,  $b^2 > \omega_o^2$ )*

By following steps similar to those for Case I, except noting that the equations are in hyperbolic rather than trigonometric form, the conditions for maxima or minima are found to be as follows:

*Charge*

The condition for a maximum is that  $t' = \infty$ , or

$$\tanh(\omega t' + \theta + \varphi) = \tanh \theta.$$

The latter case is seen to be satisfied when

$$t'_q = -\frac{\varphi}{\omega}. \quad (54)$$

Now, recalling that  $\varphi = \tanh^{-1} \omega/(a - b)$ , it is seen that a positive (i.e., realistic) value of  $t'$  only occurs when  $b > a$ , which is the case where core losses are dominant. Therefore when coil losses are dominant, the charge gradually decays to zero.

The resulting peak value of charge, when  $b > a$ , is

$$q_{1p} = \frac{K i_o \sinh \theta}{\omega_o \sinh \varphi} \exp\left(-\frac{\varphi}{\tanh \theta}\right) \quad (55)$$

where  $\varphi = \tanh^{-1} \omega/(b - a)$ .

For the case where  $R_n = 0$ , this reduces to

$$q_{1p} = C V_o \beta_w^{-\frac{1}{2}} \exp\left(-\frac{\varphi}{\tanh \theta}\right). \quad (56)$$

### Current

The condition for a minimum is

$$\tanh(\omega t' + \varphi) = \tanh \theta$$

which is seen to be satisfied when  $t' = \infty$ , or when

$$t' = \frac{\theta - \varphi}{\omega}.$$

As  $\varphi$  is always greater than  $\theta$  (see Table III),  $t'$  can only have a positive value when  $b > a$ , for which case

$$t' = \frac{\theta + \tanh^{-1} \frac{\omega}{b - a}}{\omega}. \quad (57)$$

There is no minimum for the case that  $a > b$ , except as the current gradually decays to zero.

The resulting peak value of current, when  $b > a$ , is

$$i_{1p} = \frac{K I_o \sinh \theta}{\sinh \varphi} \exp\left(-\frac{\theta - \varphi}{\tanh \theta}\right). \quad (58)$$

For the case where  $R_n = 0$ , this reduces to

$$i_{1p} = \frac{I_o}{\sqrt{1 + G_2/G_w}} \exp\left(-\frac{\theta - \varphi}{\tanh \theta}\right). \quad (59)$$

*Contact Voltage*

The condition for a maximum is that  $t' = \infty$ , or that

$$\tanh(\omega t' + \varphi) = \frac{\tanh \theta}{1 - \frac{1}{C\omega_o R_n \cosh \theta}}. \quad (60)$$

This expression may be used to give the peak voltage, when  $b > a$ , for the general case, as was indicated above for the oscillatory case.

For the case  $R_n = 0$ , the primary subject of the present paper, this becomes

$$\tanh(\omega t' + \varphi) = 0$$

or

$$t' = \frac{-\varphi}{\omega}. \quad (61)$$

As in the case of equation (54), this indicates a peak value of voltage only for the case where core loss dominates, for which

$$V_{cp} = V_o \left[ 1 + \beta_w^{-1} \exp\left(-\frac{\varphi}{\tanh \theta}\right) \right]. \quad (62)$$

When  $a > b$ , the voltage gradually rises to the asymptotic value  $V_c = V_o$ .

*Summary*

The foregoing expressions are summarized in Table VIII.

## REFERENCES

1. Turney, T. H., "The Principles of Relay Timing in Connection With Automatic Telephone Circuits," *J. IEE*, 66, No. 376 (April 1928), pp. 341-384.
2. Smith, Wagar, Vincent, and George, "Slow-Acting Relays," *Electrical Engineering*, 65, December 1946, pp. 557-63.
3. Peek, R. L., Jr., "Principles of Slow Release Relay Design," *B.S.T.J.*, 33, No. 1 (January 1954), pp. 187-217.
4. Peek, R. L., Jr., and Wagar, H. N., *Switching Relay Design*, New York: Van Nostrand, 1955, Chapters 4 and 11.
5. Curtis, A. M., "Contact Phenomena in Telephone Switching Circuits," *B.S.T.J.*, 19, No. 1 (January 1940), pp. 40-62.
6. Atalla, M. M., "Discharge Phenomena on Break of Inductive Circuits," *B.S.T.J.*, 33, No. 3 (May 1954), pp. 535-558.
7. Germer, L. H., "Physical Processes in Contact Erosion," *J. Appl., Phys.* 29, July 1958, pp. 1067-82.
8. Holm, R., *Electric Contacts*, Springer-Verlag, 1967, p. 313.
9. Wagar, H. N., "Predicting the Erosion of Switching Contacts That Break Inductive Loads," *IEEE Trans. PMP*, March 1969, pp. 16-24.
10. Mills, G. W., "The Mechanisms of the Showering Arc," *IEEE Trans. PMP*, March 1969, pp. 47-55.
11. Pharney, J. R., "A Closed Form Solution of the Arc Energy in a 'B' Type Transient Leading to a Simplified Prediction of Contact Life," to be published in *Trans. Sixth Int. Conf. Electric Contact Phenomena*, Chicago, Ill., June 5-8, 1972.

# Restoring the Orthogonality of Two Polarizations in Radio Communication Systems, I

By T. S. CHU

(Manuscript received March 5, 1971)

*The transmission medium or the radiating system often fails to maintain the orthogonality between two polarizations. Using a differential phase shifter and a differential attenuator, the orthogonality can be recovered by the transformation of two nonorthogonal elliptically polarized waves into two orthogonal polarizations.*

## I. INTRODUCTION

Making use of two orthogonal polarizations simultaneously can double the capacity of a radio communication system.<sup>1</sup> The requirement of maintaining orthogonality is easily fulfilled when the transmitting and receiving antennas are aligned in the beam maximum of each other. Sometimes this alignment is not possible; for example, in some satellite communication systems the ground stations are distributed across the beamwidth of the satellite antenna. Then any polarization variation within the antenna beamwidth will give rise to cross-polarization coupling. Rain attenuation may also introduce significant depolarization at the higher microwave frequencies.<sup>2</sup>

In practice the two orthogonal polarizations leaving the transmitter are either two orthogonal linearly polarized waves or two opposite circularly polarized waves. Whatever be the cause of polarization distortion, the failure to maintain orthogonality will produce two non-orthogonal elliptically polarized waves at the receiving terminal. The purpose of this paper is to present a method of recovering orthogonality by transforming the two nonorthogonal elliptically polarized waves into two orthogonal linear polarizations. The transformation employs a differential phase shifter and a differential attenuator.

## II. ANALYSIS

Two nonorthogonal elliptically polarized waves, I and II, can be represented by two polarization ellipses with their major axes oriented at an arbitrary angle  $\theta$  with respect to each other as shown in Fig. 1. The axial ratios  $A_1$  and  $A_2$  can be of the same or opposite sign depending on whether the polarization ellipses are rotating in the same or opposite directions. Let us find the representations of these two elliptically polarized waves in the X-Y coordinates where the  $X_1$ - and  $X_2$ -axes are counterclockwise rotations of  $\beta_1$  and  $\beta_2$  respectively from the X-axis. ( $\beta_2$  in the configuration of Fig. 1 is a negative value.) The ratio of clockwise to counterclockwise circularly polarized components for the polarization ellipse I (wave approaching) is

$$q_1 = \frac{1 + A_1}{1 - A_1} \quad (1)$$

where  $A_1$  is positive if the elliptic polarization is rotating clockwise and negative if the elliptic polarization is rotating counterclockwise. When the X-axis is used as phase reference for the two circularly polarized components, this ratio becomes

$$q_1' = \frac{1 + A_1}{1 - A_1} e^{-j2\beta_1}. \quad (2)$$

The ratio of the Y component to X component for the polarization

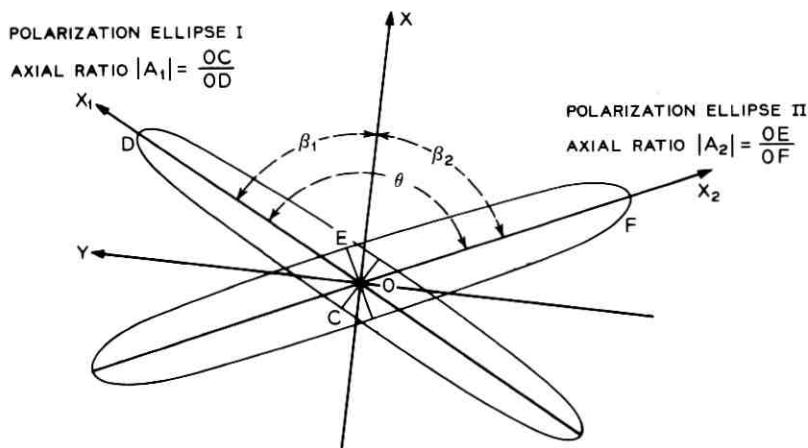


Fig. 1—Two nonorthogonal elliptically polarized waves.

ellipse I is<sup>3</sup>

$$P_1 = p_1 e^{-i(\pi/2)} = \frac{1 - q_1'}{1 + q_1'} e^{-i(\pi/2)}. \quad (3)$$

Substituting equation (2) into equation (3) yields an expression for  $P_1$ ; similarly we can find  $P_2$  for the polarization ellipse II.

$$P_i = \sqrt{\frac{(1 + A_i^2) - (1 - A_i^2) \cos 2\beta_i}{(1 + A_i^2) + (1 - A_i^2) \cos 2\beta_i}} \cdot \exp \left\{ j \tan^{-1} \left[ \frac{2A_i}{(1 - A_i^2) \sin 2\beta_i} \right] \right\}, \quad i = 1, 2 \quad (4)$$

$0 < \angle P_i < \pi$  when  $A_i > 0$ ;  $-(\pi/2) < \angle P_i < \pi/2$  when  $\sin 2\beta_i > 0$ .

In order to convert an elliptic polarization into a linear polarization, the phase difference between the X and Y components must be eliminated by a proper differential phase shifter. The condition for simultaneous transformations of two elliptic polarizations into two linear polarizations is

$$\angle P_1 = \angle P_2 \quad \text{or} \quad \angle P_1 + \pi = \angle P_2. \quad (5)$$

The above equations are equivalent to

$$\tan \angle P_1 = \tan \angle P_2. \quad (6)$$

Substituting equations (4) into equation (6), and using the relation  $\beta_2 = \beta_1 - \theta$ , the solution for  $\beta_1$  is

$$\beta_1 = \frac{1}{2} \cot^{-1} \left[ \frac{\cos 2\theta - \frac{A_2(1 - A_1^2)}{A_1(1 - A_2^2)}}{\sin 2\theta} \right], \quad 0 < \beta_1 < \frac{\pi}{2}. \quad (7)$$

The above expression fixes the orientation of the X - Y coordinates. By applying a phase delay  $\angle P_1$  to the components in the Y direction, the two elliptically polarized waves I and II are transformed into two linearly polarized waves L1 and L2 as illustrated in Fig. 2\* for the case of  $\angle P_1 + \pi = \angle P_2$ .

The angle between the two linear polarizations is

$$\psi = \tan^{-1} |P_1| \pm \tan^{-1} |P_2| \quad \text{when} \quad \begin{cases} \angle P_1 + \pi = \angle P_2 \\ \angle P_1 = \angle P_2 \end{cases} \quad (8)$$

\* When  $\angle P_1 < 0$ , the transformation into two linear polarizations can be also obtained by a phase delay  $|\angle P_1|$  in the X direction.

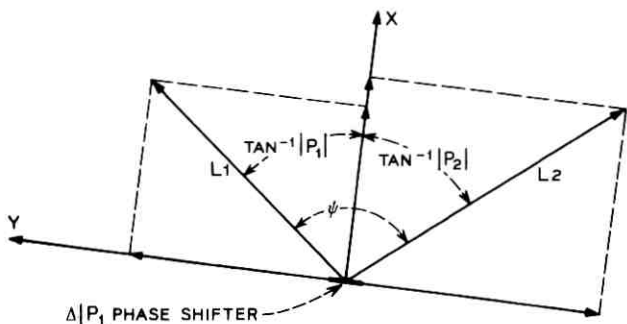


Fig. 2—Transformation into two linear polarizations.

where  $|P_1|$  and  $|P_2|$  are given by equations (4). Note that  $\psi$  is not necessarily a right angle. However, this angle can be changed to a right angle in the following manner. If  $\psi < \pi/2$ , an attenuation of  $\tan(\psi/2)$  can be imposed on the components of L1 and L2 in the direction B (which bisects the angle  $\psi$ ) as shown in Fig. 3a; i.e., at an angle

$$\chi = \frac{1}{2}[\tan^{-1} |P_1| \mp \tan^{-1} |P_2|] \quad \text{when} \quad \begin{cases} \angle P_1 + \pi = \angle P_2 \\ \angle P_1 = \angle P_2 \end{cases} \quad (9)$$

with respect to the X direction. If  $\psi > \pi/2$ , an attenuation of  $\cot \psi/2$  can be imposed on the components in the direction perpendicular to B as shown in Fig. 3b. The above orthogonalization by differential attenuation is the inverse of depolarization by attenuation due to oblate raindrops.<sup>2</sup> Obviously differential gain may also provide orthogonalization or depolarization.

The two orthogonal linear polarizations obtained by the above scheme may not be aligned with the polarization axes of the receiver.

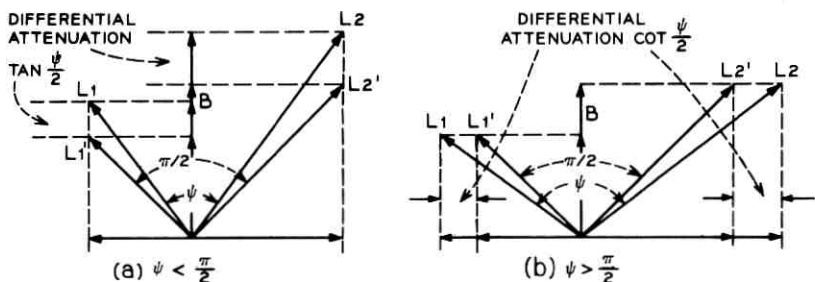


Fig. 3—Orthogonalization by differential attenuation.

In order to accomplish the alignment, one can use a  $\Delta\pi$  phase shifter properly oriented as shown in Fig. 4 where  $L1'$  and  $L2'$  are rotated into  $L1''$  and  $L2''$ .<sup>4</sup> This  $\Delta\pi$  phase shifter can be also placed in front of or immediately after the  $\Delta\perp P_1$  phase shifter. Then the orientations of the differential phase shifters and the differential attenuator must be changed accordingly.

### III. DISCUSSION

The above analysis suggests a method for restoring the orthogonality of two polarizations at the receiving end of the system. This method can be used when the two transmitted polarizations are either linear or circular. The differential phase shifter and the differential attenuator can be installed in a circular waveguide feeding the antenna. It follows from the reciprocity principle that the orthogonality of two polarizations will be also preserved if the direction of transmission is reversed.

If the polarization distortions are time-varying, the practical implementation of the above scheme appears to require two beacon signals, each of which would occupy a separate narrow frequency band and would be transmitted on one of the two orthogonal polarizations. The components of each signal in the two orthogonal polarizations of the receiver can be measured. The amplitude ratio and phase difference of these two components completely specify an elliptically polarized wave for each signal.

Now let us obtain some feeling for the required differential attenuation. In the absence of differential attenuation, each of the two linear polarizations separated by an angle  $\psi$  will have a cross polarization of  $|\tan \frac{1}{2}(\psi - \pi/2)|$  if their misalignment with respect to the two orthogonal linear polarizations of the receiver has been minimized. The

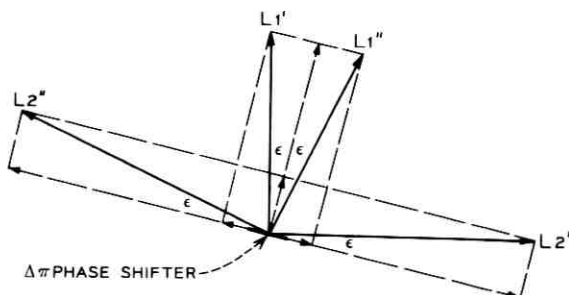


Fig. 4—Rotation by  $\Delta\pi$  section.

complete elimination of cross-polarization coupling will need a differential attenuator of  $\tan(\psi/2)$ . However, it is often only necessary to reduce the cross polarization to a certain system specification, such as  $-30$  dB. Then the required differential attenuation will be  $\tan(\psi/2)/\tan(\psi_0/2)$  or its reciprocal where  $|\tan \frac{1}{2}(\psi_0 - \pi/2)|$  is the tolerable cross polarization. For various system specifications of tolerable cross polarization, Fig. 5 shows the required differential attenuation versus the original cross polarization. Furthermore, one notes that the differential attenuation only affects one component of each signal. The attenuation of each total signal is  $\sin(\psi/2)/\sin(\psi_0/2)$  or  $\cos(\psi/2)/\cos(\psi_0/2)$  when  $\psi$  is less or greater than  $\pi/2$ . In the case of weak non-orthogonality the attenuation of the total signal is approximately half of the differential attenuation.

A reviewer has called the author's attention to the practice of using adjustable squeeze sections<sup>5</sup> for the reduction of crosstalk in the horn-reflector-antenna system. A differential phase shifter alone may reduce the cross-polarization coupling; however, the complete elimination of cross polarization in general requires the proper combination of a differential phase shifter and a differential attenuator as described in this paper.

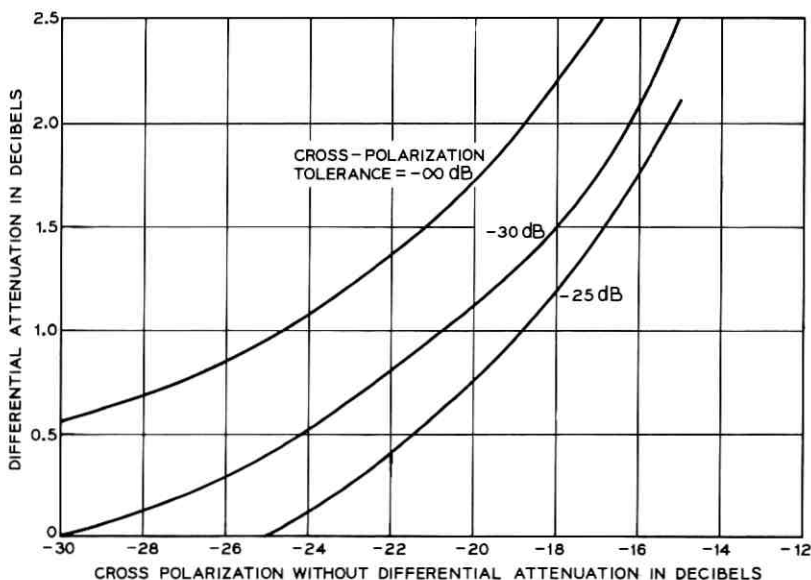


Fig. 5—Required differential attenuation for attaining a system specification of tolerable cross-polarization coupling.

## IV. ACKNOWLEDGMENT

The author wishes to thank A. B. Crawford and E. A. Ohm for stimulating discussions.

## REFERENCES

1. AT & T Co. Application for a Domestic Communication Satellite System (Filed with FCC October 19, 1970).
2. Saunders, M. J., "Cross Polarization at 18 and 30 GHz Due to Rain," IEEE Trans., *AP-19*, March 1971, pp. 273-277.
3. Rumsey V. H., "Transmission Between Elliptically Polarized Antennas," Proc. IRE, *39*, May 1951, pp. 535-540.
4. Fox, A. G., "An Adjustable Waveguide Phase Changer," Proc. IRE, *35*, December 1947, pp. 1489-1498.
5. Sandsmark, P. I., "Effect of Ellipticity on Dominant-Mode Axial Ratio in Nominally Circular Waveguides," IRE Trans., *MTT-3*, October 1955, pp. 15-20.



## Contributors to This Issue

TA-SHING CHU, B.S., 1955, The National Taiwan University; M.S., 1957, and Ph.D., 1960, Ohio State University; Bell Telephone Laboratories, 1963—. Mr. Chu has been concerned with problems involving electromagnetic wave propagation and microwave antennas. Member, IEEE, Commission 2 of URSI, Sigma Xi, Pi Mu Epsilon.

WARREN J. CLEMETSON, Bell Telephone Laboratories, 1960—. Mr. Clemetson has been concerned with the design of wideband FM deviators and self-scanning image sensors. Currently he is engaged in the development of the digital circuitry to drive the mm-wave path length modulator. Member, IEEE.

BERNARD GLANCE, Dipl. Ing., 1958, Ecole Spéciale de Mécanique et Electricité; Dipl. Ing., 1960, Ecole Supérieure d'Electricité, Paris, France; C.S.F., Research Center of Corbeville, Orsay, France, 1960-1966; Dipl. Docteur (Ing.), 1964, Sorbonne, Paris; Bell Telephone Laboratories, 1968—. At C.S.F., Mr. Glance had been engaged in research on microwave tubes. At S.F.D. Laboratories, he had worked on high-power microwave amplifiers. Mr. Glance is presently working on microwave solid-state integrated circuits.

JEREMIAH F. HAYES, B.E.E., 1956, Manhattan College; M.S., 1961, New York University; Ph.D., 1966, University of California, Berkeley; Faculty, Purdue University, 1966-1969; Bell Telephone Laboratories, 1969—. Mr. Hayes is currently engaged in a study of computer communications networks. Member, IEEE, AAAS, Sigma Xi, Eta Kappa Nu.

NORMAN D. KENYON, B.A., 1963, M.A., 1966, and Ph.D., 1967, Cambridge University, England; Bell Telephone Laboratories, 1968—. Mr. Kenyon is currently working on circuit structures for mm-wave IMPATT diodes. Member, IEEE.

KANEYUKI KUROKAWA, B.S., 1951, and Dr. of Eng., 1958, University of Tokyo; Assistant Professor, University of Tokyo, 1957-1963; Bell Telephone Laboratories, 1959-1961, 1963—. Mr. Kurokawa has worked on parametric amplifiers, microwave transistor amplifiers, Gunn and IMPATT oscillators, and PIN diode switches. He is currently supervisor of the mm-wave subsystems group in the Electron Device Laboratory. Mr. Kurokawa is the author of *An Introduction to the Theory of Microwave Circuits* (Academic Press, 1969). Member, IEEE, IECE of Japan.

B. OWEN, B. Tech. (E.E.), 1963, Welsh College of Advanced Technology, Cardiff, Wales; Ph.D., 1967, University of Birmingham, England; Bell Telephone Laboratories, 1968—. In England, Mr. Owen was engaged in research on space charge varactors for parametric amplifiers. At Bell Laboratories he is involved in the development of broadband mm-wave circulators.

WOLFGANG O. SCHLOSSER, Dr. Ing., 1964, Techn. Hochschule, Darmstadt, Germany; Research Associate, Techn. Hochschule, Braunschweig, Germany, 1963-1966; Bell Telephone Laboratories, 1966—. Mr. Schlosser has been working on microwave solid state oscillators and mm-wave modulators.

HAROLD SEIDEL, B.E.E., 1943, City College of New York; M.E.E., 1947, and D.E.E., 1954, Brooklyn Polytechnic Institute; Bell Telephone Laboratories, 1953—. Mr. Seidel's interests have been in the areas of ferrite propagation studies, parametric amplification, and active networks ranging over the entire radio and optical spectrum, Member, IEEE.

DAVID N. SHERMAN, B.S.E.E., 1963, Polytechnic Institute of Brooklyn; M.S.E.E., 1964, and Ph.D., 1968, University of Southern California; Bell Telephone Laboratories, 1969—. Mr. Sherman's interests are in data insertion in speech and the analysis of data networks. Member, Eta Kappa Nu, Tau Beta Pi.

DAVID T. THOMAS, B.S. in E.E., 1959, and M.S. in Mathematics, 1960, Carnegie Institute of Technology; Ph.D., 1962, The Ohio State University; Assistant Professor and Associate Supervisor, Electrical Engineering Dept., Ohio State University, 1961-1963; Assistant Professor of Electrical Engineering, Carnegie-Mellon University, 1963-1968; Bell Telephone Laboratories, 1968—. Mr. Thomas has done research in radar scattering by dielectric bodies, applications of computer solutions in electromagnetics, and depolarization of electromagnetic waves by rain. He is currently responsible for analysis and design of multiple edge blinders used to reduce unwanted side-lobes in large aperture antennas, and for the design of antennas and feeds for the 18.5-GHz Short Hop Radio Relay System (DRX-18). Member, Sigma Xi, Tau Beta Pi, Pi Mu Epsilon, Phi Kappa Phi.

HAROLD N. WAGAR, S.B. (Physics), 1926, Harvard University; M.A. (Physics), 1931, Columbia University; Bell Telephone Laboratories, 1926-1970. At Bell Laboratories Mr. Wagar was involved primarily in the design and development of electromechanical switching apparatus and in studies of the performance of this apparatus. He also helped develop techniques for transistor manufacture. During World War II, he worked on anti-aircraft equipment for the Air Force. He holds 21 patents for his inventions and is co-author of the book *Switching Relay Design* (Van Nostrand). At the time of his retirement Mr. Wagar was head of the Contact Studies Department. Senior member, IEEE; Registered Professional Engineer.

